Aerodynamic Analysis of Wings in Airborne Wind Energy Applications

A 3D potential flow solver extended with a viscous correction to predict non-linear lift and drag coefficients at high AoA

M.S. Agten BSc
September 2012

Master of Science Thesis

TU Delft Delft University of Technology

Challenge the future

Aerodynamic Analysis of Wings in Airborne Wind Energy Applications

A 3D potential flow solver extended with a viscous correction to predict non-linear lift and drag coefficients at high AoA

Master of Science Thesis

For obtaining the degree of Master of Science in Applied Sciences at Delft University of Technology

M.S. Agten BSc

September 2012

Faculty of Applied Sciences · Faculty of Aerospace Engineering
Delft University of Technology

"The moment you doubt whether you can fly, you cease for ever to be able to do it."

Sir James Matthew Barrie (1860-1937)

TU Delft

Delft University of Technology

Delft University Of Technology
Department Of
Applied Sustainable Science Engineering and Technology

The undersigned hereby certify that they have read and recommend to the Faculty of Applied Sciences for acceptance a thesis entitled **"Aerodynamic Analysis of Wings in Airborne Wind Energy Applications"** by **M.S. Agten BSc** in partial fulfillment of the requirements for the degree of **Master of Science**.

Dated: September 2012

Head of department: _____
Prof.dr. W.J. Ockels

Supervisor: _____
Dr.-Ing. R. Schmehl

Reader (Aerodynamics & Wind Energy): _____
Ir. W.A. Timmer

Reader (Director Ampyx Power): _____
Dr. R. Ruiterkamp

Preface

After graduating for my BSc at the faculty of Aerospace Engineering at the Delft University of Technology, I followed the MSc program of Sustainable Energy Technology at the faculty of Applied Sciences. Learning about all available technologies to work towards a more sustainable future I found both interesting and inspiring. It was, however, not a coincidence that I ended up at the faculty of Aerospace Engineering to find a subject and work on my MSc thesis. Aircraft always intrigued me since I was a child, followed by aerodynamics during my BSc. Being able to combine this knowledge and passion with a sustainable energy technology was all I could wish for.

This report aims to contribute to the understanding of developing an aerodynamic analysis tool for wings in airborne wind energy applications. The PowerPlane of Ampyx Power is considered as a test case, which can be used to improve the design of this remotely controlled sailplane.

The author wishes to thank the following persons, who made everything possible and enjoyable during the time I worked on my thesis. First of all, thanks to Prof.dr. Wubbo Ockels for making the kite project within the ASSET institute possible. Secondly, I would like to thank Dr.-Ing. Roland Schmehl and Dr. Richard Ruiterkamp for their guidance as my graduation supervisors. Not only I have learned about sailplane and kite aerodynamics, but also much about the total airborne wind energy systems of both Ampyx Power and ASSET. I would also like to thank Ir. Nando Timmer, for taking seat in the graduation committee and making wind tunnel data available. I am also grateful to the collaboration with Robin van Kappel and Dr.ir. Leo Veldhuis for the helpfull discussions and handing over wind tunnel data. Furthermore, thanks to Ir. Loek Boermans for his expertise during discussions on sailplane aerodynamics and to Mac Gaunaa and Niels Sørensen for giving their model geometry used for validation. Finally, thanks to management assistant Nana Saaneh for the organization within ASSET.

Delft, The Netherlands
September 2012

M.S. Agten BSc

Summary

During the development of an aerodynamic analysis tool to predict non-linear lift and drag coefficients, research was performed on arbitrary wing configurations focusing on airborne wind energy (AWE) applications. The purpose of this research is to develop and examine the accuracy of computationally fast aerodynamic methods. The non-linear part and maximum value of the lift curve, with the corresponding drag, are of great interest for AWE applied wings, since these fly at high angles of attack. By means of a trail and error procedure, a most promising method is found. This research was performed via ASSET at the faculty of Aerospace Engineering and Ampyx Power, following the MSc Sustainable Energy Technology at the faculty of Applied Sciences at the Delft University of Technology.

Kite technology has been discovered some 3,000 years ago. Since then, kites have been used to for example send messages, pull carts and perform weather measurements. Nowadays, the most advanced kites are used for sports such as kite surfing. Although higher altitudes can be reached with kites and (AWE) have been developed to extract energy from the wind, the wind energy market is dominated by wind turbines. The efficiency of these turbines is reaching the Betz limit, leaving one option to increase power output, which is increasing the operating altitude. However, structural issues will then appear for a wind turbine tower, where a tethered kite can easily fly up to several kilometers altitude. The opportunities of kite power systems have been discovered by scientists, which has resulted in a number of 40 active AWE companies around the world. Ampyx Power is one of these companies, where a tethered rigid sailplane, called the PowerPlane, is used to extract energy from the wind.

The current Ampyx system is designed to generate 10 kW at a design wind speed of 8 m/s. For this, a single 4 mm in diameter tether is used, connected to the 3 m^2 wing surface area PowerPlane. The tether is connected to a drum on the ground station, which drives a generator. A pumping cycle technique is performed to create tension on the tether during the reel out phase. For this, cross-wind figures of 8 are flown such that velocities are reached that are higher than the wind speed. At a certain altitude, the PowerPlane flies back towards the ground station, such that the power consumption during the reel in phase is kept minimal. From a flight model analysis, it showed that the lift coefficient and lift to drag ratio of the system are most important to obtain an optimal power output. The tether generates most of the drag, such that the PowerPlane

should be designed for a high maximum lift.

In order to obtain a fast and reliable tool to predict lift and drag, relatively simple aerodynamic methods are considered, since solvers such as computational fluid dynamics (CFD) tools are expensive and require long computation times. Starting from basic lift theorems, potential flow methods are investigated, including available applications. XFLR5 is considered as the most promising option, containing a two dimensional (2D) viscous solver (XFOIL), a vortex lattice method (VLM) and a three dimensional (3D) panel method.

Since the VLM and 3D panel method are potential flow methods, thus inviscid, no viscous effects are taken into account. Therefore, a fully linear lift curve is obtained, without stall conditions (separation). In literature, methods have been found that make use of 2D viscous lift and drag polars to implement viscosity in 3D calculations. Here, an angle shift is performed on the 3D wing such that it flies at an angle of attack that has the same lift coefficient as the viscous lift coefficient following from 2D lift polars. By means of an iterative process, a converged solution for the viscous lift and corresponding drag can be determined. A set of available methods have been derived, based on literature and aerodynamic theories. Furthermore, several program features have been implemented such as a dihedral effect on the induced angle of attack.

Four different program versions resulted from the previous investigation, on which a trade-off procedure is applied. For this, a set of arbitrary wing configurations was considered, making use of the 2D and 3D wind tunnel data to validate the tool. From the trade-off, 2 versions showed to be most accurate in predicting non-linear lift coefficients with the corresponding drag coefficient and the location and value of the maximum lift coefficient. Also, performance of the software is tested, considering computation time as a function of several program settings. This showed that a cosine and uniform distribution in chordwise and spanwise distribution, respectively, give most accurate results. Furthermore, with the first version, called MG_b, iteration until convergence is used, where a maximum number of 14 iterations was required for the validation cases. The second version, called AK, is used with 1 iteration, since more iterations lead to increasing fluctuations in the induced angle distributions. However, similar results are obtained with both versions, which showed to predict non-linear lift and drag coefficients close to reality.

The two most promising versions of the aerodynamic tool are finally used to analyze the 10 kW PowerPlane of Ampyx Power. Here, XFOIL polars and 3D analyzes are considered, including lift and drag curves/distributions. These results can be used to improve the configuration as such, that the AWE system performance increases. A maximum lift coefficient of $C_{L_{max}} = 1.55$ at $\alpha = 20^o$ was obtained from the performed simulations. This implies an increased accuracy of 30% on the maximum lift and 40% on the corresponding drag coefficient, when compared to results of the original XFLR5 version. Furthermore, a number of sailplane design considerations are treated, taking into account the operating conditions of the PowerPlane, such as high angles of attack and gravitational forces. Improvements can be made on the design of the airfoil, the fuselage and adding winglets to the planform.

Contents

Nomenclature

Latin Symbols

A	Aspect ratio	[-]
a	Speed of sound	[m/s]
a	NACA mean camber line factor	[−]
A_c	Cross-section of cylindrical volume	[m^2]
A_f	Frontal surface area of the fuselage	[m^2]
A_w	Surface area perpendicular to the wind velocity vector	[m^2]
b	Wing span	[m]
c	Chord length	[m]
C_D	Drag coefficient	[-]
C_{D_0}	Profile drag coefficient	[-]
C_{D_f}	Drag coefficient of the fuselage	[-]
$C_{D_{f,rel}}$	Relative drag coefficient of the fuselage	[-]
C_{D_i}	Induced drag coefficient	[-]
C_{D_t}	Drag coefficient of the tether	[-]
$C_{D_{t,rel}}$	Relative drag coefficient of the tether	[-]
C_L	Lift coefficient	[-]
C_{L_f}	Lift coefficient of the fuselage	[-]
C_d	Two dimensional drag coefficient	[-]
C_f	Friction coefficient	[-]
C_l	Two dimensional lift coefficient	[-]
C_p	Pressure coefficient	[-]

c_r	Root chord length	[m]
c_t	Tip chord length	[m]
C_{l_i}	Two dimensional inviscid lift coefficient	[-]
C_{l_v}	Two dimensional viscous lift coefficient	[-]
C_{p_l}	Lower side pressure coefficient	[-]
C_{p_u}	Upper side pressure coefficient	[-]
C_{L_α}	Lift curve slope	[deg^{-1}]
$C_{L_{\alpha=0}}$	Lift coefficient at zero angle of attack	[-]
$C_{L_{max}}$	Maximum lift coefficient	[-]
C_{m_0}	Pitching moment coefficient	[-]
D	Drag	[N]
d	Diameter	[m]
D_i	Induced drag	[N]
D_t	Tether drag	[N]
d_t	Tether diameter	[m]
e	Oswald span efficiency factor	[-]
F_b	Breaking force	[N]
F_P	Operational mode of the PowerPlane	[-]
$F_{P_{max}}$	Maximum value of operational mode	[-]
F_{panel}	Panel force	[N]
F_{wz}	Vertical wind axis projected force	[N]
G_{eff}	Effective glide ratio	[-]
h	Height	[m]
h_{ref}	Reference height	[m]
k	Constant used for fuselage induced lift	[-]
L	Lift	[N]
l_t	Tether length	[m]
L_t	Lift acting on the tether	[N]
L_{eff}	Effective lift	[N]
M	Mach number	[-]
m	Mass	[kg]
M_t	Tether moment at the ground	[Nm]
M_{eff}	Effective Mach number	[-]
$\overline{n}$	Normal velocity	[m/s]
n	Number used for the e^n method	[-]
P	Power	[W]
P_{avg}	Average power output	[W]
P_{down}	Power consumption during the reel in phase	[W]

P_{up}	Power production during the reel out phase	[W]
R	Gas constant	[J/(mol K)]
Re	Reynolds number	[-]
r	Radius	[m]
S	Wing surface area	[m^2]
s	Distance along tether	[m]
S_c	Safety factor	[-]
S_{panels}	Total panel area	[m^2]
S_{wet}	Wet surface area	[m^2]
T	Temperature	[K]
t	Chord thickness	[m]
T_t	Tension force in the tether	[N]
t_{down}	Duration of the reel in phase	[s]
t_{up}	Duration of the reel out phase	[s]
u	Local velocity	[m/s]
$\overline{v}$	Local panel velocity	[m/s]
v	Velocity	[m/s]
V_∞	Free stream velocity	[m/s]
v_{app}	Apparent velocity	[m/s]
v_c	Crosswind velocity	[m/s]
v_i	Induced velocity	[m/s]
v_n	Wind normal velocity	[m/s]
v_{ref}	Reference velocity	[m/s]
v_t	Reel out/in velocity	[m/s]
v_{tether}	Velocity of the tether during flight	[m/s]
v_w	Wind velocity	[m/s]
$v_{w_{eff}}$	Effective wind velocity	[m/s]
W	Weight	[N]
w	Downwash velocity	[m/s]
x	x coordinate (chordwise direction)	[m]
y	y coordinate (spanwise direction)	[m]
z	z coordinate	[m]
z_0	Roughness length	[m]

Greek Symbols

α	Angle of attack	[deg]
α_∞	Free stream angle of attack	[deg]

α_i	Induced angle of attack	[deg]
α_s	Angle shift	[deg]
α_{eff}	Effective angle of attack	[deg]
$\alpha_{eff,original}$	Initial effective angle of attack	[deg]
$\alpha_{eff,new}$	Effective angle of attack after angle shift	[deg]
α_{twist}	Twist angle	[deg]
β	Prandtl-Glauert compressibility factor	[-]
Γ_c	Circulation	[deg]
Γ	Dihedral angle	[deg]
γ	Heat capacity ratio	[-]
ε	Downwash angle	[deg]
ε_b	Wake blockage factor	[-]
η	Airfoil efficiency factor	[-]
θ	Zenith angle	[deg]
Λ	Sweep angle	[deg]
λ	Taper ratio	[-]
$\Lambda_{0.5c}$	Half chord sweep angle	[deg]
Λ_{LE}	Leading edge sweep angle	[deg]
μ	Bank angle	[deg]
$\overline{\mu}_s$	Doublet strength	[-]
ν	Kinematic viscosity	[m^2/s]
ρ	Air density	[kg/m^3]
σ_{max}	Maximum tensile strength	[MPa]
$\overline{\sigma}_s$	Source strength	[-]
τ	Thrust angle	[deg]
φ	Velocity potential function	[-]
ϕ	Azimuth angle	[deg]
$\phi_{l_{TE}}$	Lower side velocity potential at trailing edge	[-]
$\phi_{u_{TE}}$	Upper side velocity potential at trailing edge	[-]

Abbreviations

2D	Two Dimensional
3D	Three Dimensional
AR	Aspect Ratio
ASSET	Applied Sustainable Science Engineering and Technology
AVL	Athena Vortex Lattice
AWE	Airborne Wind Energy

BC	Boundary Condition
CFD	Computational Fluid Dynamics
CP	Center of Pressure
FVM	Finite Volume Method
GUI	Graphical User Interface
L/D	Lift to Drag ratio
LE	Leading Edge
LLT	Lifting Line Theory
MAC	Mean Aerodynamic Chord
MAPD	Mean Absolute Percentage Deviation
LES	Large Eddy Simulation
RHS	Right Hand Side
TAT	Thin Airfoil Theory
TE	Trailing Edge
TG	Tilted Geometry
UAV	Unmanned Aerial Vehicle
VLM	Vortex Lattice Method

Chapter 1

Introduction

1.1 Background

It was in Asia, around 500 B.C., where wind energy applications were discovered and used first for purposes such as sending messages and fishing. The simplest way to do this, was by using tethered kites. Once scientific knowledge grew, people started to build wind turbines to for example grind corn or pump water from flooded areas. Nowadays, and since the end of the 19th century, wind turbines are mostly used for electricity generation, whereas kites are only used for recreational purposes such as kite surfing. As the Betz limit is nearly reached by the most advanced horizontal axis wind turbines these days, improvements in terms of energy conversion efficiency are hardly possible. Scaling up such systems in height to make use of the more constant and larger wind velocities is limited by mainly structural problems and this is where an innovative concept comes into the picture. An airborne wind energy (AWE) system does not consists of a massive tower to support the energy generating parts, but of a flying object that is attached to the ground through a tether. Since the last 12 years, the number of active AWE companies over the world has grown to 40. The flying objects used by these companies are either flexible kite structures, rigid bodies like and auto gyro or airplane and even zeppelin like concepts. These systems are used for energy production or transportation, introducing specific design requirements.

Ampyx Power is such an active AWE company. The PowerPlane is one of the crucial parts of their airborne wind energy system. This system consists of a rigid sailplane flying patterns of 8 at high altitudes, which is connected to a generator on the ground through a tether. While the tether is unwound from the drum due to the resulting tension force, power is generated. When the maximum tether length is reached, the PowerPlane dives towards the ground station and the tether is reeled in with a power consumption that is 1/10th of the generated power during the reel out phase. During the reel in phase, the generator works as an electric motor. Once the desired minimum tether length is obtained, the process starts over again. An important feature of this system is the ability to perform autonomous flights. This adds quite some complexity to the application, but is also one of the most important aspects. This is due to the main purpose of this system, which is to produce energy as cheap as possible.

Ampyx Power will start to scale up their 10 kW PowerPlane system to a commercial

100 kW size. This implies a wing with some 25 m^2 surface area that will constantly operate at high angle of attack. In order to produce a first commercial system that has performance characteristics close to optimal, Ampyx Power will first design and test a re-designed 3 m^2 prototype at the end of 2012. This prototype will be analyzed and optimized using computational analysis starting from an initial design and will be produced mid 2012 by DG Flugzeugbau.

1.2 Thesis objective

The purpose of this thesis is to present the development of a tool to asses the impact of design parameters on the aerodynamics of the Ampyx PowerPlane. For optimal power production, the tension force in the tether during the reel out phase should be as high as possible, which can be obtained by high lift forces. Therefore, the sailplane should constantly fly at high angles of attack. For the purpose of designing this plane for this specific application, a realistic and computationally fast aerodynamic tool is required. Since modern numerical solvers, such as computational fluid dynamics (CFD) software, are expensive and require long computation times, potential flow methods are used. However, such available programs do not take into account viscous effects in 3D simulations, thus neglecting stall behavior and giving unreliable lift and drag coefficients. Therefore, a tool is required that is able to predict non-linear lift and drag coefficients at high angles of attack up to stall conditions. With such a tool, the PowerPlane can be re-designed to increase the aerodynamic performance, which in turn affects the total system performance. Also, lift and drag coefficients can be used as an input for dynamic flight models, increasing accuracy.

From available software, an analysis tool called XFLR5 is used, since it incorporates both XFOIL, a vortex lattice method (VLM) and a 3D panel method. XFOIL is a 2D panel method, which is able to predict transition and separation (stall conditions) by means of boundary layer equations. In the original version of XFLR5, XFOIL is used to predict the profile drag of a 3D wing, but the VLM and 3D panel method calculate an inviscid lift curve, which is in turn used to determine the drag.

Most of the time, the PowerPlane operates at high angles of attack, meaning linear inviscid assumptions are not valid. It is therefore required to add non-linear viscous behavior to the inviscid potential flow methods. This is done by means of an algorithm that uses the sectional XFOIL polars to correct the lift and drag in 3D calculations. Simulation results from the adapted software are validated with the use of 2D and 3D wind tunnel and CFD data of various cases. From these results, it can be concluded whether the new program is able to predict lift and drag at high angles of attack with an acceptable error. The outcome of this study will be an input for the ongoing research within Ampyx Power.

1.3 Thesis structure

First, in chapter 2, the basic principles of airborne wind energy will be discussed as result from a literature study. The main advantages of operating at high altitude with a tethered system are explained, followed by a concise summary of existing airborne wind energy systems. Also, a more elaborate analysis is done on the current 10 kW PowerPlane system.

This concerns the pumping cycle technique, a flight model, aircraft design parameters and the aerodynamic influence of cable drag and other design parameters.

In chapter 3, an elaboration on aerodynamic calculation methods is performed, starting from basic lift theorems. These concern the principles required to explain the used methods in the developed algorithm. Both 2D and 3D theories are discussed, from which a list of available software has been tested. In the final section of this chapter, the most promising tools are shown together with important test results.

In chapter 4, a method to incorporate thickness and viscosity in a VLM and 3D panel method with the use of 2D lift and drag polars is proposed and elaborated. Several methods are compared to come up with a most promising version, that all start from the same basic principle, which is explained first. This is followed by the theories behind each method, including the main differences. The aerodynamic tool XFLR5 is used to implement these methods, next to a number of other attachments/changes to the program. These features are explained together with the main settings available in the original software, focusing on the computational performance.

In chapter 5, the validation process of the developed tool is presented. A set of 2D and 3D wind tunnel data is obtained from literature and tests performed at the Delft University of Technology Low Speed Laboratory. With this collection, it is shown how accurate the tool predicts the aerodynamic behavior of arbitrary wing configurations. Since several versions of the program are made, an extensive trade-off procedure is set up to obtain the version that shows to be most promising. Here, a distinction is made between the VLM and 3D panel method. After the analysis of lift and drag polars/distributions, the performance of the software is discussed.

In chapter 6, the 10 kW PowerPlane design is considered as a test case for the validated software. Here, focus will be laid on final results of 3D simulations, concerning lift and drag polars/distributions. Furthermore, design considerations specifically for sailplane applications are discussed, taking into account the operating conditions at which the PowerPlane normally flies. These should improve the aerodynamic performance and total performance of the system.

Finally, in chapter 7, conclusions are drawn from found results of the validation process and the test case considered. Also, recommendations are done concerning the use of the aerodynamic analysis tool.

In appendix A, validation results of the 2D airfoil sections from XFOIL are shown. These are used for the 3D simulations, of which the validation results are presented in appendix B. For each of the validation cases a section is devoted, containing the corresponding lift and drag polars from wind tunnel experiments and simulations. In appendix C, simulation results of the validation cases performed with the final program versions are shown.

Chapter 2

Airborne wind energy

Modern wind turbines dominate the wind energy market present-day, competing with other sustainable energy technologies, such as solar panels. As a result, the most important feature of a wind energy system is the price per kWh. Until now this price has become cheaper with an increasing size of wind turbines and generators. Larger turbines are beneficial, because they reach higher altitudes, which increases the capacity factor. The prices of these systems are mostly based on farms, while it might also be an advantage to achieve a competitive kWh price for a single system. Airborne wind energy applications are optional for this requirement, which do not make use of a rigid altitude limiting device. In this chapter, the main advantages of high altitude wind and airborne wind energy (AWE) systems will be discussed followed by existing AWE systems, all being in the development phase. Then, the so called pumping cycle technique used by several of these concepts is explained, followed by the definition of a flight model. Finally, a more elaborate analysis will be performed on the PowerPlane concept from Ampyx Power, concerning i.e. a study on aircraft design parameters.

2.1 High altitude wind

Due to viscous effects and obstacles on the Earth's surface, a planetary boundary layer exists. This results in a velocity gradient, which is defined as a distribution increasing with height perpendicular to the surface of the Earth. The importance of this wind gradient can be explained by equation 2.1, which shows the available wind power in a surface area perpendicular to the wind velocity vector.

$$P = \frac{1}{2}\rho A_w v_w^3 \tag{2.1}$$

Here, P is the wind power, ρ is the air density, A_w is the surface area and v_w is the wind velocity. It is directly noted that the available wind power is related to the wind speed to the power 3, which indicates why high altitudes are preferred for wind energy systems. In order to visualize the variation as a function of the altitude, an exponential relation based on a neutral atmosphere is considered. This is shown in equation 2.2, where $v(h)$ represents the wind velocity as a function of the height above the ground. Furthermore, v_{ref} and h_{ref} are a reference velocity and height respectively and z_0 is the

roughness length, which is defined as the height above the ground at which the wind velocity is theoretically zero (Ragheb, 2011). This can also be explained as the thickness of the Earth's boundary layer.

$$v(h) = v_{ref} \frac{\ln \frac{h}{z_0}}{\ln \frac{h_{ref}}{z_0}} \tag{2.2}$$

Depending on the surface roughness, several wind velocity profiles can exist as shown in figure 2.1, where a reference height of 10m is used. The variation in surface roughness shows that the effect is quite large when looking at high values of z_0. In these cases, z_0 = 0.0024 corresponds to a completely open terrain with a smooth surface, z_0 = 0.055 corresponds to an agricultural land with some houses and hedgerows within 1,250m distance and z_0 = 1.6 corresponds to very large cities with high buildings. If for example wind energy would be extracted at an altitude of 80 m (800 kW wind turbine (Hatch, 2009)), for z_0 = 0.055, wind speeds are a factor of 1.4 larger with respect to the reference height. Since the output power is related to v_w^3, this results in a potential power increase factor of 2.7. However, if one would extract wind energy at an altitude of 300 m, the wind speeds are a factor of 1.65 larger, such that a potential power increase factor of 4.5 is obtained. Also, due to more constant wind speeds at high altitudes, the capacity factor (energy produced over available energy) for an airborne wind energy system is higher than for a wind turbine. This shows why operating at an increased altitude is beneficial and concerning structural and economical difficulties for wind turbines to increase their tower height, airborne wind energy is a more interesting alternative.

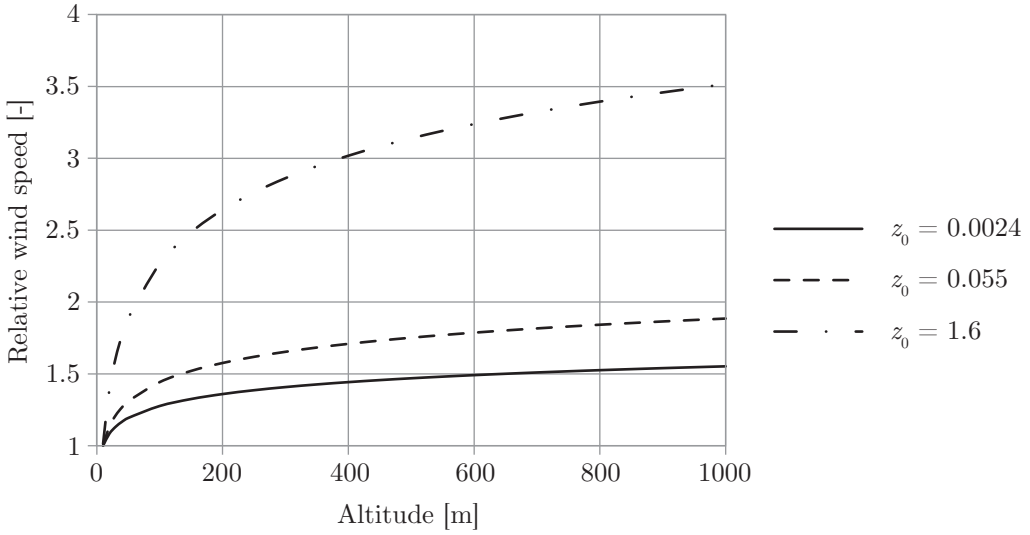

Figure 2.1: Wind velocity profiles for various regions (z_0 values from Ragheb, 2011).

It should be noted that actual measurement data do not fully correspond to the theoretical approach as mentioned. Comparing both results even shows that realistic data gives more promising results, meaning higher relative wind velocities, such that the assumption of a neutral atmosphere is probably not valid (Van den Berg, 2005). Furthermore, equation 2.2 will certainly not be valid anymore for altitudes above 1 km. For this, weather balloons can be used as a measurement device, showing that the increase

of the wind velocity for altitudes up to 10 km becomes even more steep. However, air density will be significantly lower at such altitudes, such that the maximum available wind power will be at lower heights. A weather balloon measurement can be seen in figure 2.2, where the average wind power density is shown as a function of altitude. This is the available wind power per unit area perpendicular to the wind velocity vector measured at De Bilt in the Netherlands.

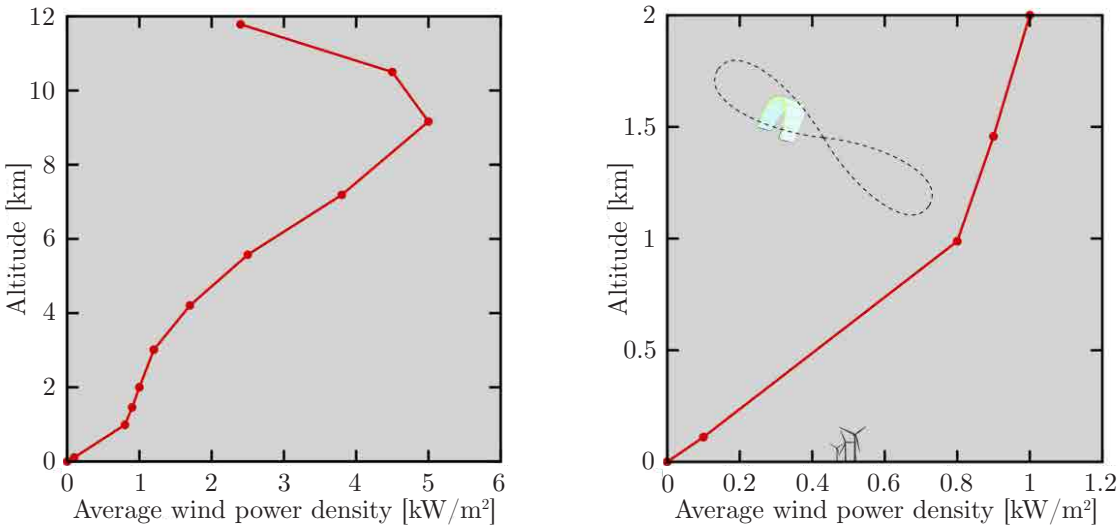

Figure 2.2: Average wind power density as a function of altitude measured at De Bilt in the Netherlands (from Schmehl, 2011).

2.2 Advantages of airborne wind energy systems

Before analyzing airborne wind energy systems, it is important to understand the major advantages compared to existing wind energy systems. The most obvious applications are wind turbines, which have become reliable and economically viable. Therefore, a new concept should have specifications that makes it a cheaper and equally reliable solution. Below, the major advantages of airborne wind energy systems compared to conventional wind turbines are discussed, which are based on a system that is equal in power rating.

One of the major limitations of modern wind turbines is the height at which they operate. This is due to tower construction limits in combination with the enormous forces acting on the rotor blades and thus on the tower. And because wind turbines are fixed to the ground, they can only operate at the installed height. Wind velocities at higher altitudes are steadier, more persistent and of larger magnitude (see section 2.1), thus it would be favorable to have a system that allows to be adjusted in operating height.

For commercial purposes, most important are the costs of the system. Compared to a wind turbine, approximately half of the capital costs are already saved mainly by material costs (Renewable Energy Sources, 2011) within an airborne system. There is for example no need of a tower construction, the required surface area of the tethered flying object is less than that of the wind turbine rotor blades and the required foundation and generator are smaller. Next to that, there are more possible locations to operate with an airborne system. Many inland locations do not provide high enough wind speeds at

wind turbine operating heights, whereas there might be enough at airborne heights. Also, due to the small and lightweight system parts, an airborne wind energy system is much easier to install. This also holds for offshore potential, since there is no need of a large construction on the seabed, making maintenance costs lower. Therefore, more feasible locations at sea are available for airborne systems compared to wind turbines. Other aspects that make airborne wind energy systems more attractive, are the low noise that is produced due to lower operating velocities and a larger operating altitude compared to rotating wind turbine blades. Also, the visibility of an airborne system is less than that of a wind turbine, due to its smaller dimensions and the higher operating height. This also causes shadow effects on the ground to be significantly smaller.

2.3 Existing airborne systems

Since the 1980's, scientists have been studying the possibilities of airborne wind energy (Loyd, 1980), from which several concepts exist nowadays. Each of these systems operate at high altitudes, although their working principle is quite different. On of the main design choices to be made is the location of the generator(s). This can be placed either airborne (flygen concepts) or based on the ground (groundgen concepts), both having its advantages and disadvantages. In this section, a selection of the most well-known airborne wind energy systems will be considered briefly.

2.3.1 Flying wind turbines

This system can be approached as a tethered auto gyro, which consists of a light weight structure and propellers connected to a ground station with a tether, as shown in figure 2.3. The propellers are used to ascend the flying wind turbine up to its operating level. When this position is reached, the propellers are used to both keeping the system floating at a certain height and generating electrical energy at the same time. Since no use is made of the cross-wind possibilities, the auto gyro will approximately remain at a certain location in space. To make this system stable, however, seems to be rather difficult and increases the complexity of the system.

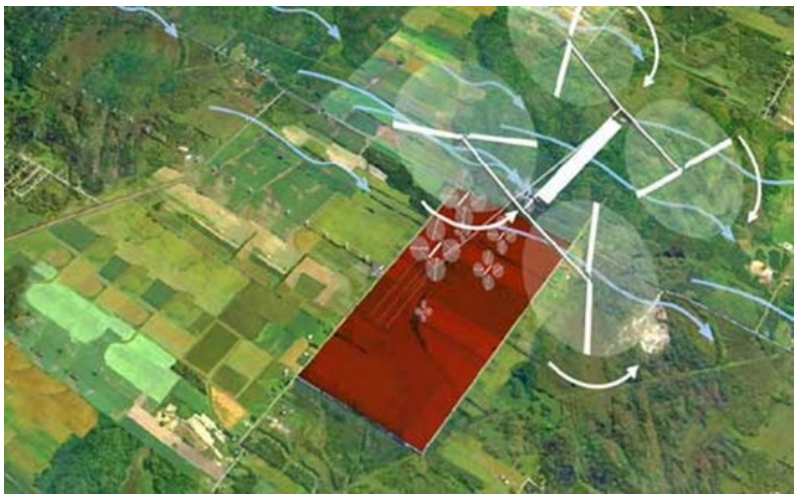

Figure 2.3: A flying wind turbine farm by Sky WindPower (from Levesque, 2007).

2.3.2 Airships

For these applications, a low density gas like Helium is used to create lift on a balloon type device. The main advantage here is the autonomous buoyancy that keeps the system up in the air. One of such concepts uses two separate balloons with a sail connected to each one, which is developed by an Italian company called Twind. An illustration of this concept is shown in figure 2.4a. By alternately opening and closing the sails, the balloons are constantly moving upwind and downwind, in opposite direction to each other. This movement is then used to generate electricity via a tether connected to a ground station.

Another system that uses a low density gas is called the Air Rotor System, developed by Magenn Power, which can be seen in figure 2.4b. In contrast to the previous concept, this system also remains at a certain location in space. It uses the principle of a drag based wind turbine (Savonius type) to rotate the airship around its horizontal axis. This mechanical energy is converted to electricity by generators located at both sides of the airship. Also, this rotation creates a lift force, which is a result of the Magnus effect. This principle states that a rotating object in a fluid generates a lifting force due to a resulting pressure difference. It is this phenomenon that is used as extra lift force and to stabilize the system.

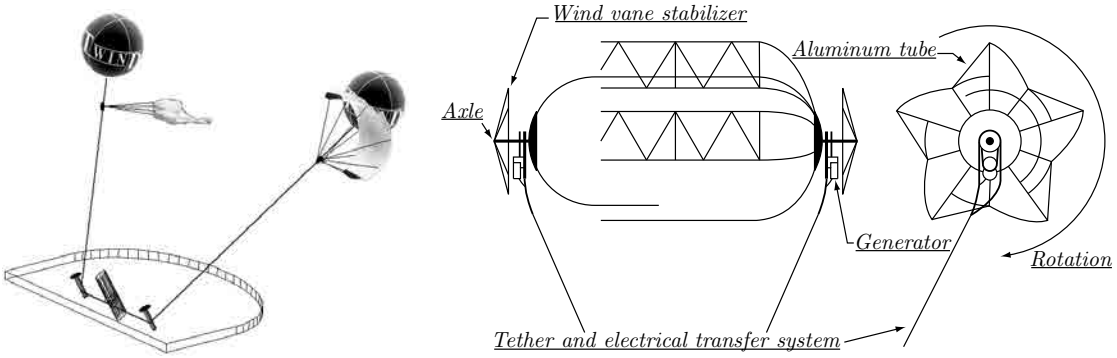

(a) Twind concept (b) Magenn Air Rotor Ship

Figure 2.4: Two airborne wind energy concepts using a low density gas to create autonomous lift (adapted from Twind, 2011; Magenn Power, 2011).

2.3.3 Kites

Well-known is the tethered kite concept, which is for example used for recreational purposes and sport activities such as kite surfing, kite buggying and snow kiting. There are many variations on the design of a kite, leading to for example a kiteplane, which uses the operating principle of a kite and the rigidity of an airplane. An important design consideration for a kite system is whether the generator(s) is/are placed on board of the kite or on the ground. When integrated in the kite, it can also be used as a motor during lift off, but it also makes the system heavier and power cables will be required to transport the electricity to the ground. But the most difficult part of a kite system is the automatic ascending and descending, not forgetting the flight itself. Cross-wind patterns are made during flight to make use of both the wind speed and the velocity of the kite to create a higher tension force on the tether. To make all flight phases autonomous, many test flights

are required during the development phase to obtain a reliable system, which has led to a number of working concepts. Sky Sails is the first commercially available kite traction system, which uses a flexible kite flying autonomous patterns of 8 as a propulsion system for ships. Another concept is the Makani M1, a kiteplane with generators on board (see figure 2.5a), which are also used to hover the plane up into the air as a helicopter.

Next to a single kite, it could also be possible to let several kites operate together at the same time. This concept is called the Laddermill, which is shown in figure 2.5b. Here, a number of kites are used to harvest an enormous amount of wind energy at once. The kites on the ascending side are set at an angle of attack to achieve maximum lift, whereas on the descending side the kites just create enough lift to stay in the air. This results in a tension force on the tether, driving a generator at the ground station. However, due to the complexity of this concept, a more simple system is being developed first by a research group of ASSET, an institute of the Delft University of Technology. A single flexible kite, under which the so called control pod hangs (steering the lines), on a tether flying cross-wind patterns of 8 connected to a ground station is what the system consists of. Their main challenge is making the flights autonomous. Thereafter, the original Laddermill project is supposed to be extrapolated from the existing system.

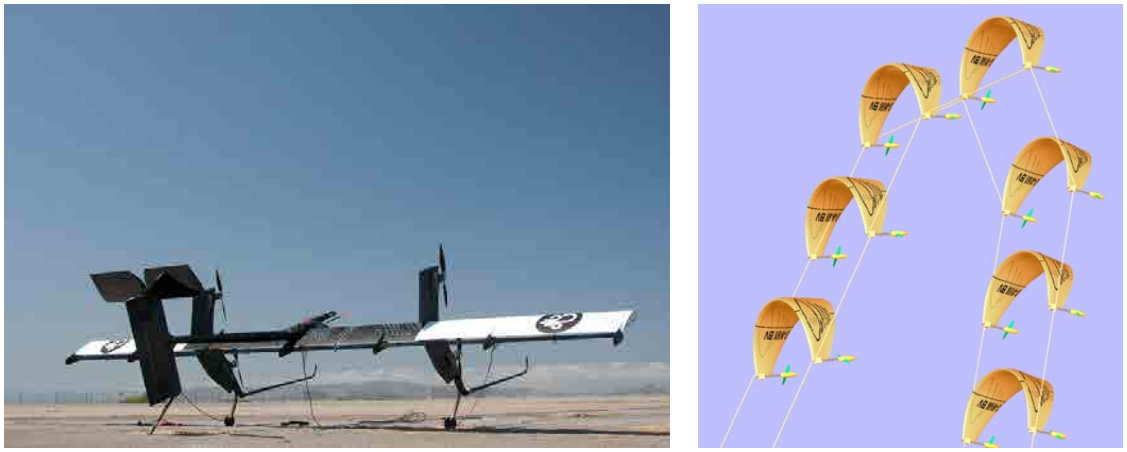

(a) Makani M1 (b) Laddermill

Figure 2.5: Two airborne wind energy kite concepts of which the Makani M1 is a rigid kiteplane with generators on board and the Laddermill consists of flexible kites with a generator on the ground (from Makani Power, 2011; Wind Energy Guide, 2011).

2.4 Pumping cycle technique

A limitation to a tethered kite system that is only ascending and descending, is the local wind speeds on which it depends. Since the output power increases with v_w^3, as seen before in equation 2.1, it would be beneficial to fly cross-wind patterns. This would increase the apparent wind velocity, which increases the tension on the tether such that more energy can be produced. Therefore, effort is gained by flying patterns of 8 during the energy production phase, as shown in figure 2.6. Here, the PowerPlane of Ampyx Power is shown as an example. Once the maximum cable length is reached, the plane flies back towards

the ground station with a negative angle of attack, such that it can be reeled in with a low power consumption. Afterwards, the process starts over again.

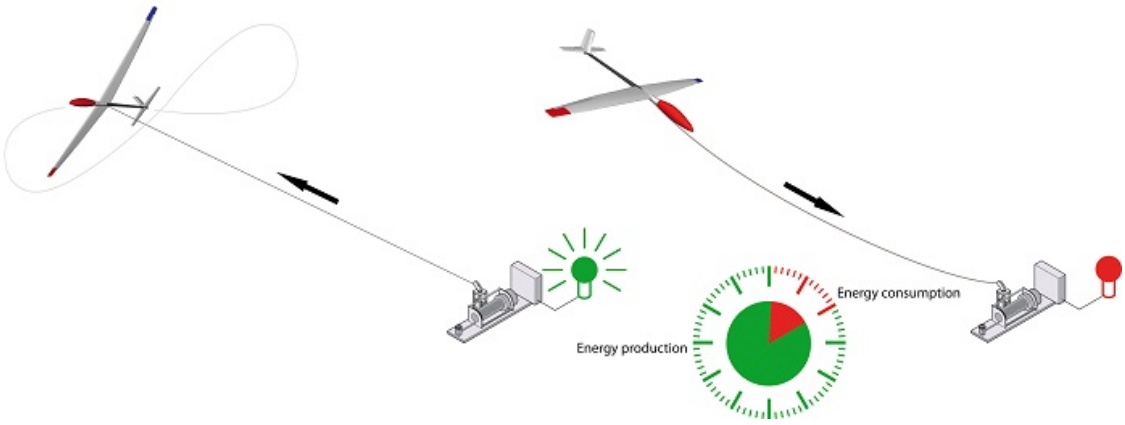

Figure 2.6: Pumping cycle technique performed by the PowerPlane during the energy production and consumption phase (from Ampyx Power, 2011).

The tips of wind turbine blades follow the same procedure (in circles), but here only a small surface area experiences the highest velocities, whereas an airborne wind energy system uses its total surface area in these conditions. This is illustrated in figure 2.7. Only the outermost 20% of wind turbine blades contributes to 80% of the power generation (Schmehl, 2011). Furthermore, light and cheap generators can be used for airborne wind energy systems compared to wind turbines, because high rotational speeds can be reached by decreasing the drum diameter. Wind turbines depend on low rotational velocities and therefore need large and expensive gearboxes.

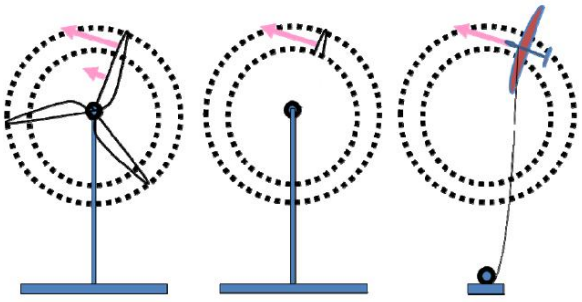

Figure 2.7: Comparison of rotating wind turbine blades and a cross-wind flying PowerPlane (from Ampyx Power, 2011).

2.5 Flight model definition

Understanding all principles of a tethered cross-wind flying system, requires a level of knowledge which can be build by analyzing a simplified model. From this, it also becomes clear which design parameters are the most critical and sensitive to certain changes. Focus should be laid on these numbers, which result in the most efficient way to come up with

optimized designs. In this section, a simplified model of the Ampyx PowerPlane will be analyzed on a performance level. A more elaborate discussion on this rigid sailplane is performed in section 2.6. It should be noted, that the derivations shown in this section also hold for other airborne wind energy systems making use the pumping cycle technique, such as flexible kites.

Once the main operation parameters of the PowerPlane and the cable are known, one can start designing and dimensioning the system. In case of wind energy systems, the baseline parameters are the wind speed conditions. For determining the local wind speeds near the plane, some simplifications are made to come up with a basic model (Schmehl, 2011). It is assumed that the plane flies at constant velocity in a horizontal direction, being stable. Furthermore, only the power production phase is considered and wind speeds are assumed to be dependent on altitude only (see equation 2.2).

In order to determine the power output of the system in terms of cable tension, a relation for the apparent wind speed is needed. In figure 2.8, top and front views of the PowerPlane and cable are shown with the orientation of the wind velocity, v_w, and the lift and drag vectors, L and D respectively. In figure 2.8a, the wind velocity component acting on the PowerPlane is shown as a function of the azimuth angle, ϕ, with respect to the wind direction. It is clear that the angle should be kept as small as possible to obtain an apparent wind speed as high as possible. However, this does not mean that flying small circles is efficient, considering drag and cable twist. Therefore, figures of 8 are flown within an angle of $-30^o < \phi < 30^o$ (Ruiterkamp, 2009). Another angle that does not vary that much is the zenith angle θ, as shown in figure 2.8b, which is 60^o during operation. This is because the PowerPlane flies at an approximately constant height and the tether is quite long. Because of the reeling out of the tether, the effective wind speed, $v_{w_{eff}}$, will be smaller. Therefore, using the reel out speed of the cable, v_t, this can be written as

$$v_{w_{eff}} = v_w \cos(\phi) \sin(\theta) - v_t \tag{2.3}$$

In order to balance the gravity forces working on the plane and cable, a bank angle, μ, will be introduced. This can also be seen as a safety factor, since a negative bank angle will result in a loss in lift and eventually a crash. Furthermore, a thrust angle, τ, is used to balance the drag with the lift force, as shown in figure 2.8c. First, the tension in the cable can be defined by summing up the relevant vectors, as shown in equation 2.4. This relation can be rewritten using the sine rule as in equation 2.5, showing a relation that must be satisfied to balance the system.

$$T_t = L \cos(\tau) - W \tag{2.4}$$

$$\frac{L \cos(\tau)}{\sin(\theta)} - \frac{W}{\sin(\mu)} = 0 \rightarrow L \cos(\tau) \sin(\mu) - W \sin(\theta) = 0 \tag{2.5}$$

Since the apparent wind velocity is perpendicular to the lift force, as shown in figure 2.8b, the geometry of lift and drag vectors can be used to determine a relation for v_{app}. This derivation is shown in equation 2.7-2.8, where the effective glide ratio, G_{eff}, is defined as in equation 2.6. This can also be used to simplify a relation for the thrust angle, which can be derived from figure 2.8b. As a result, equation 2.9 is obtained. It

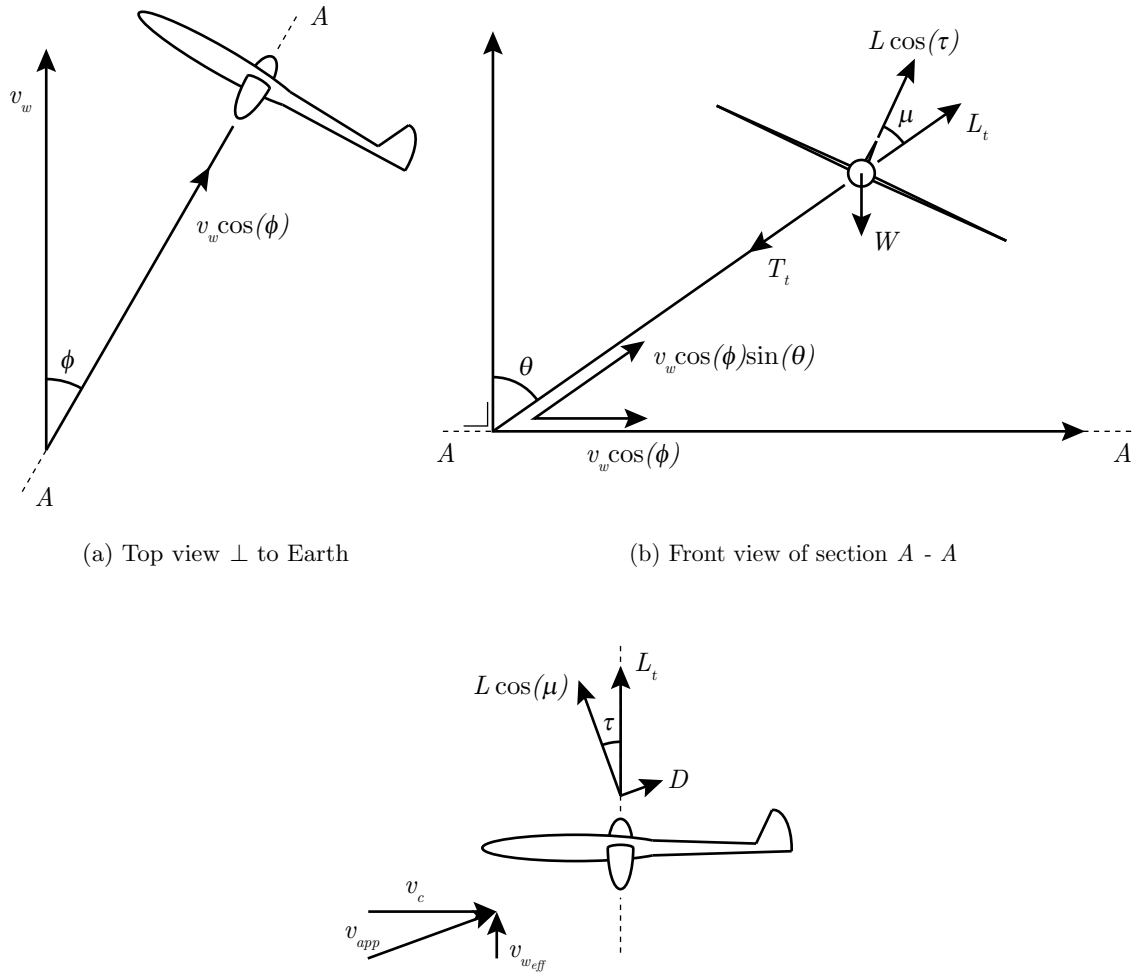

(a) Top view ⊥ to Earth

(b) Front view of section A - A

(c) Top view ⊥ to the cable

Figure 2.8: Top and front views of the PowerPlane flying at constant velocity in horizontal flight conditions.

should be noted that in these relations, L and D are accounting for the total system lift and drag, respectively.

$$G_{eff} = \frac{L}{D} = \frac{C_L}{C_D} \tag{2.6}$$

$$v_p = \frac{L\cos(\mu)}{D} v_{weff} = G_{eff}\cos(\mu) v_{w_{eff}} \tag{2.7}$$

$$v_{app} = \sqrt{v_{w_{eff}}^2 + v_c^2} = v_{w_{eff}}\sqrt{1 + (G_{eff}\cos(\mu))^2} \tag{2.8}$$

$$\tan(\tau) = \frac{D}{L\cos(\mu)} = \frac{1}{G_{eff}\cos(\mu)} \tag{2.9}$$

Finally, the total lift, drag and tension force in the tether can be determined by implementing the apparent wind velocity in the total force relations. This can be seen in equation 2.10-2.12, where the relation for the tension is again obtained from the geometries in figure 2.8b. Here, ρ is the local air density and S is the wing surface area. With the tension force known, the power output of the system can be expressed with the reel out speed as shown in equation 2.13.

$$L = \frac{1}{2}\rho v_{app}^2 S C_L \tag{2.10}$$

$$D = \frac{1}{2}\rho v_{app}^2 S C_D \tag{2.11}$$

$$T_t = L\cos(\mu)\cos(\tau) - W\cos(\theta) + D\sin(\tau) \tag{2.12}$$

$$P = T_t v_t \tag{2.13}$$

According to Sieberling & Ruiterkamp (2011), the power output of a cross-wind flying kite can also be written as shown in equation 2.19. To derive this formula, first of all, the apparent wind speed can be written as follows, such that the lift force can also be rewritten. Here, $(L/D)_P$ represents the lift to drag ratio of the PowerPlane.

$$v_{app} = v_{w_{eff}}\left(\frac{L}{D}\right)_P \tag{2.14}$$

$$L = \frac{1}{2}\rho v_{w_{eff}}^2 \left(\frac{L}{D}\right)_P^2 S C_L \tag{2.15}$$

Assuming v_t is parallel to T_t and L and T_t are equal in magnitude, the produced power can be defined as

$$P = \frac{1}{2}\rho v_w^3 S C_L F_P \tag{2.16}$$

Here, a function F is describing the operational mode of the PowerPlane, which is cross-wind flying in this case. Assuming the PowerPlane flies at 0m altitude and perfectly downwind in cross-wind motion, F_P can be written as (Loyd, 1980)

$$F_P = \left(\frac{L}{D}\right)_P^2 \left(\frac{v_t}{v_w}\right)\left(1 - \frac{v_t}{v_w}\right)^2 \tag{2.17}$$

It is found that the maximum of this function occurs at

$$F_{P_{max}} = \frac{4}{27}\left(\frac{L}{D}\right)_P^2 \tag{2.18}$$

Inserting equation 2.18 into equation 2.16, results in

$$P = \frac{2}{27}\rho v_w^3 S \frac{{C_L}^3}{{C_D}^2} \tag{2.19}$$

From this definition it can be concluded that for a fixed surface area, the wind speed, lift coefficient and drag coefficient are of most significance for a high power output. Since the wind speed is uncontrollable, the term ${C_L}^3/{C_D}^2$ is of most importance when designing the PowerPlane. It is noted that the power output thus depends on the L/D ratio squared and linearly on C_L. Since the maximum values of both parameters do no coincide on the same angle of attack of the sailplane, an optimum in between should be found to fly at. It can, however, be said that high angles of attack are beneficial during the power production phase, since $C_{L_{max}}$ and $(L/D)_{max}$ are normally located at high values of the angle of attack.

Equation 2.19 follows from the derivations made by Loyd (Loyd, 1980), from which also resulted that the optimal reel out speed during the energy production phase (at which $F_{P_{max}}$ occurs) is 1/3 of the wind velocity, or $v_t = \frac{1}{3}v_w$. The reel in phase time should be kept as low as possible, since this is the period where energy is consumed. This can also be made clear by showing the definition of average produced power, as stated in equation 2.20.

$$P_{avg} = \frac{P_{up}t_{up} + P_{down}t_{down}}{t_{up} + t_{down}} \tag{2.20}$$

Here, P_{up} and t_{up} represent the produced power and duration of the reel out phase, respectively. P_{down} and t_{down} represent the consumed power and duration of the reel in phase, respectively.

2.6 Ampyx Power

Ampyx Power is a young and ambitious company that is developing an innovative airborne wind energy system. As shown before, their system also makes use of the pumping cycle technique. In this section, the general concept of the Ampyx system will be explained, followed by a study on the design parameters. Finally, a short overview of the future goals that are set is given.

2.6.1 The PowerPlane

In section 2.3, a selection of the most potential airborne wind energy systems have been discussed. Very similar to the kite or kiteplane concept is the PowerPlane system, where

instead of a flexible kite structure, a rigid airplane is used. The working principle of this plane is similar to a sailplane and can be regarded as a UAV without an active propulsion force. In figure 2.9, the 10 kW prototype PowerPlane is shown during a tethered flight.

Figure 2.9: Prototype of the 10 kW PowerPlane design (from LabS55, 2011).

Compared to a flexible kite or kiteplane, from a performance point of view, the PowerPlane can handle higher wing loadings and generates a higher lift-to-drag (L/D) ratio, resulting in a higher power output. In section 2.5, this will be explained more elaborately. For a 25 m^2 flexible kite the L/D ratio is in the range of 3-6 (Schmehl, 2011), whereas for a sailplane with 5.5 m wing span (3 m^2 wing surface area) this can easily be 20-30 (SailPlane Directory, 2011), which is still low for an ordinary sailplane. Therefore, significantly more surface area is required for a flexible kite system to generate an equivalent amount of power, compared to the PowerPlane system. Next to that, an aircraft is a well known technique, for which durable materials can be used. Flexible kite materials require replacement and maintenance more frequently, increasing the system costs. Furthermore, the automation of an airplane is easier to control and foretell, because of the available and reliable control techniques.

One of the main obstacles in the PowerPlane concept, is the launch and landing technique. During test flights, the PowerPlane is launched with the common sailplane launch principle, where the tether is reeled in fast such that the plane gains enough speed to ascend. For commercial use, however, this is not a feasible method, considering the required space. Therefore, a rotating platform is being designed on which the PowerPlane can launch and land, as shown in figure 2.10. This platform will start rotating when wind velocities are high enough, such that the plane will gain lift and launches. The tether is guided by a mechanical arm, which is decoupled once the PowerPlane reaches its operational height. From this moment on, the system will go in the autonomous mode, where the plane will continuously fly figures of 8 until a certain cable length is reached. The landing of the system is done in the reverse way, where the plane is controlled as such, that the tension in the cable is just enough to keep it up in the air.

2.6.2 PowerPlane design parameters

In section 2.5, definitions of the lift and drag forces were obtained as a function of the operating flight conditions. The only parameters that are not known here, however, are the lift and drag coefficient. In order to determine an approximation of these constants, aircraft design methods can be used from La Rocca (2008). For simplification, the total

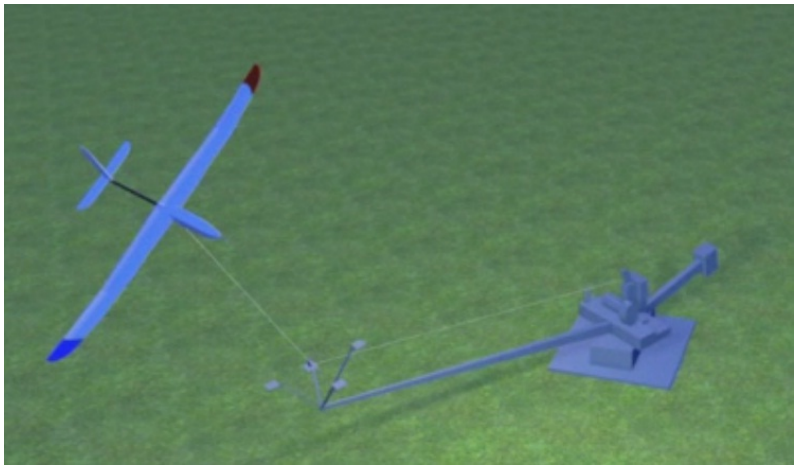

Figure 2.10: Launch and landing platform mechanism (adapted from Ampyx Power, 2011).

drag is considered to be the drag of the wings, since the fuselage is relatively small. The required initial design parameters are shown in table 2.1.

Table 2.1: Initial design parameters main wing 10 kW PowerPlane (data from Ampyx Power, 2011).

Parameter	Symbol	Value	Unit
Wing area	S	3	m^2
Wing span	b	5.5	m
Taper ratio	λ	0.67	-
Sweep angle	Λ	0	deg

First of all, the aspect ratio, A, of the main wing can be computed as

$$A = \frac{b^2}{S} \tag{2.21}$$

Here, b represents the wing span and S is the wing surface area. Then, by making use of the geometry of the wing, the root chord length, c_r, tip chord length, c_t, and mean aerodynamic chord, MAC, can be found as shown in equations 2.22-2.24, respectively.

$$c_r = \frac{2b}{A(1+\lambda)} \tag{2.22}$$

$$c_t = \lambda c_r \tag{2.23}$$

$$MAC = \frac{2c_r}{3}\frac{1+\lambda+\lambda^2}{1+\lambda} \tag{2.24}$$

The mean Reynolds number can be calculated using the MAC as

$$\overline{Re} = \frac{\rho v_{app} MAC}{\nu} \tag{2.25}$$

The lift coefficient can now be determined following the steps from equation 2.26-2.29. In these relations, M_{eff} is the effective Mach number, Λ_{LE} is the sweep angle at the leading edge, a is the speed of sound, γ is the heat capacity ratio, R is the gas constant, T is the air temperature, β represents the Prandtl-Glauert compressibility factor, η is the airfoil efficiency factor, α is the angle of attack, $\Lambda_{0.5c}$ is the sweep angle at half chord position and $C_{L\alpha=0}$ corresponds to the lift coefficient at zero angle of attack.

$$M_{eff} = M\cos(\Lambda_{LE}) = \frac{v_{app}}{a}\cos(\Lambda_{LE}) = \frac{v_{app}}{\sqrt{\gamma RT}}\cos(\Lambda_{LE}) \tag{2.26}$$

$$\beta = \sqrt{1 - {M_{eff}}^2} \tag{2.27}$$

$$C_{L\alpha} = \frac{dC_L}{d\alpha} = \frac{2\pi A}{2 + \sqrt{4 + (A\beta)^2\left(1 + \frac{\tan^2(\Lambda_{0.5c})}{\beta^2}\right)}} \tag{2.28}$$

$$C_L = C_{L\alpha}\alpha + C_{L\alpha=0} \tag{2.29}$$

In order to determine the drag coefficient, several parameters are required. This includes the base drag coefficient, C_{D0}, which is defined as

$$C_{D0} = C_f F Q \frac{S_{wet}}{S} \tag{2.30}$$

where C_f is the viscous drag coefficient, $Q = 1$ for a mid-wing configuration without nacelles, S is the surface area of the plane and S_{wet} is the wet surface area. These unknowns can be determined as shown in equation 2.31-2.33.

$$C_f = \frac{0.455}{(\log_{10}\overline{Re})^{2.58}(1 + 0.144M^2)^{0.65}} \tag{2.31}$$

$$F = \left[1 + \frac{0.6}{(x/c)_{max}}\left(\frac{t}{c}\right) + 100\left(\frac{t}{c}\right)^4\right] 1.34M^{0.18} \tag{2.32}$$

$$S_{wet} = S\left[1.977 + 0.52\left(\frac{t}{c}\right)\right] \tag{2.33}$$

Here, $(x/c)_{max}$ is the chord wise location of the maximum thickness point of the airfoil and (t/c) is the chord thickness to chord length ratio. Finally, the total drag coefficient can be determined as

$$C_D = C_{D0} + \frac{{C_L}^2}{\pi A e} \tag{2.34}$$

where e represents the Oswald span efficiency factor, which is defined as

$$e = 0.98\left[1 - \left(\frac{d}{b}\right)^2\right] \tag{2.35}$$

where d is the fuselage diameter. The 2D airfoil characteristics, such as $C_{L\alpha=0}$, (t/c) and $(x/c)_{max}$ can be determined with for example XFOIL (Drela & Youngren, 2011b). The root airfoil section of the main wing of the PowerPlane has been implemented in XFOIL to predict these parameters. Together with the input and output values, all design parameters can be found in table 2.2. The final results are the lift and drag coefficient as a function of α, obtained as

$$C_L = 0.09\alpha + 0.44 \tag{2.36}$$

$$C_D = 1.78 \cdot 10^{-5} + \frac{(0.09\alpha + 0.44)^2}{9.87\pi} \tag{2.37}$$

2.6.3 Cable drag

So far, flight model definitions and an approximation of the lift and drag coefficient of the PowerPlane are known. However, the total system performance can only be mapped by also taking into account the effect of the cable. Since the major effect of the tether is the addition of drag, this will be treated in this section.

For the PowerPlane system, a Dyneema cable is used, which is made of aramid fibers with a low thickness to strength ratio. A required cable diameter can be found from

$$d_t = \sqrt{\frac{4 S_c F_b}{\pi \sigma_{max}}} \tag{2.38}$$

where S_c is a safety factor, F_b is the breaking force of the cable and σ_{max} is the maximum allowed tensile strength. Lankhorst Ropes (Lankhorst Ropes, 2011) is a company that makes Dyneema cables, of which the relation of the cable diameter and breaking strength is shown in figure 2.11. This is compared to equation 2.38, where an aramid 29 cable with a σ_{max} of 3600 MPa is used. In order to obtain realistic values, a safety factor of 4 is taken into account. From the figure, it can be seen that the theoretical values are close to the Lanko Force data.

Now that the data is known to compute the required tether diameter, a simple drag estimation can be done. To derive an equation for this, the model in figure 2.12 is used (Bontekoe, 2010). In this figure, the ground station is represented by a hinge on which a moment, M_t, is generated at $s = 0$ due to the drag on the cable.

Since drag is a function of the cable speed, a relation for this is required assuming the cable does not bend (see equation 2.39). Here, s denotes the distance along the tether and l_t is the length of the tether. It should be noted that this relation assumes no variation in wind speeds for different altitudes. However, the flight speed is several times larger than the wind speed, such that it is a good approximation.

$$v_{tether}(s) = \frac{s}{l_t} v_{app} \tag{2.39}$$

The tether velocity at the ground station ($s = 0$) is then 0 and at the connection with the PowerPlane it is equal to the apparent wind speed. Making use of a macro analysis, an infinitely small element ds is considered. The drag on such an element is dD_t and by

Table 2.2: Main wing input and output design parameters of the 10 kW PowerPlane resulting in a relation for C_L and C_D using aircraft design methods.

Parameter	**Symbol**	**Value**	**Unit**
Air density	ρ	1.225	$\mathrm{kg/m^3}$
Kinematic viscosity	ν	$1.5 \cdot 10^{-5}$	$\mathrm{m^2/s}$
Heat capacity ratio	γ	1.4	-
Gas constant	R	287.04	J/(kg K)
Air temperature	T	293.15	K
Wind velocity	v_w	10	m/s
Reel out velocity	v_t	3.33	m/s
Azimuth angle	ϕ	0	deg
Zenith angle	θ	60	deg
Effective wind velocity	$v_{w_{eff}}$	5.33	m/s
Crosswind velocity	v_c	30	m/s
Apparent velocity	v_{app}	30.47	m/s
Aspect ratio	A	10.08	-
Root chord length	c_r	0.65	m
Tip chord length	c_t	0.44	m
Mean aerodynamic chord	MAC	0.55	m
Mean Reynolds number	$\overline{Re}$	$1.37 \cdot 10^6$	-
Effective Mach number	M_{eff}	0.09	-
Compressibility factor	β	0.996	-
Lift curve slope	C_{L_α}	0.09	$\mathrm{deg^{-1}}$
C_L *at* $\alpha = 0$ *(XFOIL)*	$C_{L_{\alpha=0}}$	0.44	-
Lift coefficient	$C_L(\alpha)$	$0.09\alpha + 0.44$	-
Thickest point location (XFOIL)	$(x/c)_{max}$	0.282	-
Chord thickness/length ratio (XFOIL)	t/c	0.14	-
Friction coefficient	C_f	$7.51 \cdot 10^{-6}$	-
Profile drag function	F	1.16	-
Wet surface area	S_{wet}	6.15	$\mathrm{m^2}$
Fuselage diameter	d	0.16	m
Profile drag coefficient	C_{D_0}	$1.78 \cdot 10^{-5}$	-
Oswald efficiency factor	e	0.98	-
Drag coefficient	C_D	$1.78 \cdot 10^{-5} + \frac{(0.09\alpha+0.44)^2}{9.87\pi}$	-

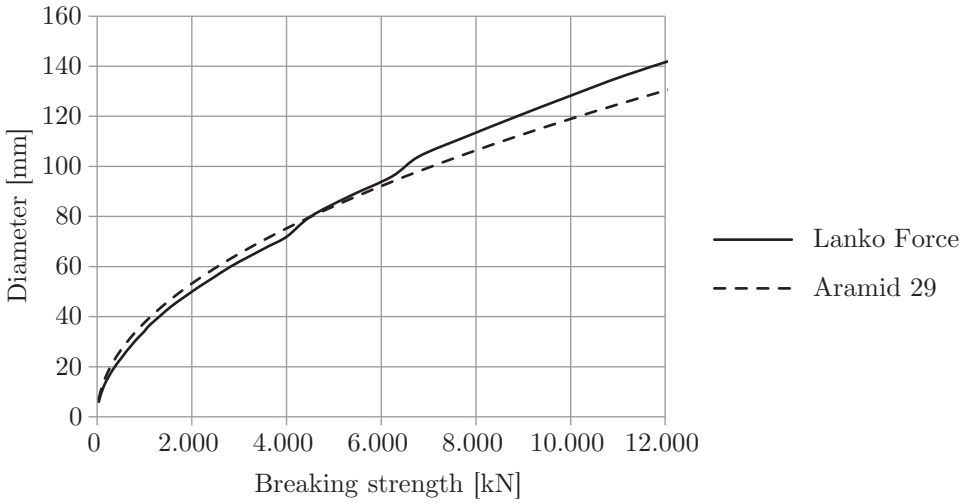

Figure 2.11: Relation between the diameter and breaking strength of an aramid 29 and Lanko Force cable (data from Lankhorst Ropes (2011)).

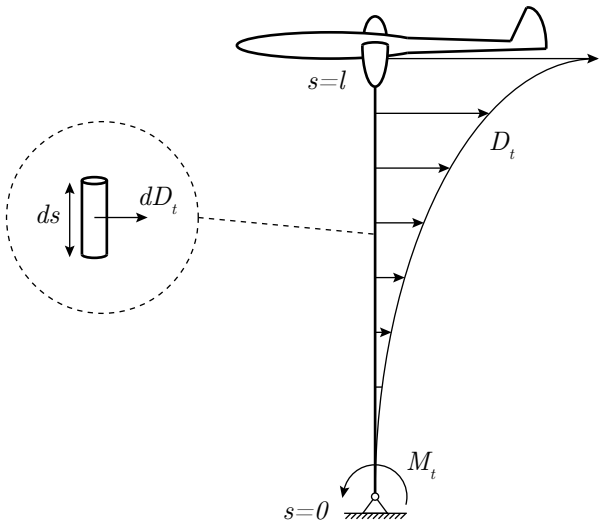

Figure 2.12: Model to calculate an estimation of the tether drag influencing the total system performance.

integrating over the whole length of the cable, the moment on the hinge can be computed as

$$M_t = \int_0^l \frac{1}{2} C_{Dt} \rho d_t \frac{s^3}{l^2} {v_{app}}^2 ds = \frac{1}{8} C_{Dt} \rho d_t l^2 {v_{app}}^2 \tag{2.40}$$

Since the cable can only carry tension forces, the drag force at $s = l$ can be found as

$$D_t = \frac{M_t}{l} = \frac{1}{8} C_{Dt} \rho d_t l {v_{app}}^2 \tag{2.41}$$

From this, the drag coefficient of the cable can be computed and once added to the drag coefficient of the PowerPlane, the total system drag is determined. Assuming a relative drag coefficient, in which the wing surface area, S, of the sailplane is used, one can write

$$C_{Dt,rel} = \frac{\frac{1}{8} C_{Dt} \rho d_t l^2 {v_{app}}^2}{\frac{1}{2} \rho {v_{app}}^2 S} = \frac{C_{Dt} d_t l}{4S} \tag{2.42}$$

However, the actual drag coefficient of the cable is not yet known. Wind tunnel tests and experiments show that for a wide range of Reynolds numbers, the drag coefficient of a smooth cylinder has a value of 1.2 on average (Ohya, 2004). This can be reduced by for example adding grooves to the surface or with the attachment of a straight flap behind the cable. Assuming the value of $C_{Dt} = 1.2$, a tether diameter of 4mm (presently used) and a tether length of 400m, the relative drag coefficient becomes $C_{Dt,rel} = 0.16$. Using equation 2.37, at for example $\alpha = 10^o$, the drag coefficient of the PowerPlane is $C_D = 0.058$. This is almost a factor of 3 times less than the tether drag. This already shows the significant influence of the tether on the total system performance, since the L/D ratio becomes lower when including the tether drag.

A decrease in drag coefficient of the tether would also be beneficial when looking at larger scale. Since the tether diameter is related to the square root of the power output, relatively less tether drag is produced for larger systems. Therefore, a required increase in power production requires a lower increase in the PowerPlane dimensions. Calculated numbers of this phenomena are shown in table 2.3 in section 2.6.5.

2.6.4 Aerodynamic influence

Aircraft aerodynamics are well known and in that respect, the PowerPlane is not a special device. However, considering up scaling effects, the aerodynamic influence becomes of great importance. The major influencing parameters are the maximum lift coefficient and the aspect ratio, with which the wing surface area can be decreased dramatically. For the smaller scale PowerPlane (10-100 kW), an aspect ratio of 10 is chosen, due to several reasons. The most important is the high cable drag with respect to the plane, such that increasing the aspect ratio would only bring the required wing surface area down a little. And since this induces an increase of the wing span, the packing dimensions of the plane becomes larger, which is not preferable for transportation purposes.

Future prospects lie at a competing kWh price system, such that for example a 1 MW system should be optimized for these purposes. In order to come up with some preliminary results, a design wind speed of 8m/s is chosen. According to (Ruiterkamp, 2009), this value is an optimal design estimation from simulations for a 1 MW system.

Using this value as a starting point, the aspect ratio's for different values of C_{Lmax} are shown in figure 2.13. The maximum lift coefficient depends on the airfoil shape, but for the PowerPlane only one airfoil type has been used so far. However, assuming a value of 2 is not unrealistic, since flapped airfoils often have even higher values.

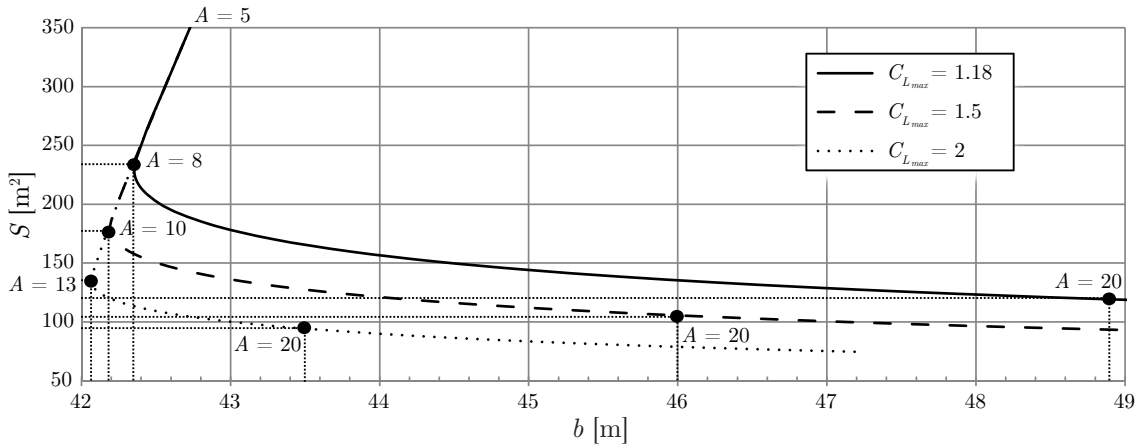

Figure 2.13: Effect of C_{Lmax} and the aspect ratio on the required wing surface area and wing span for a 1 MW PowerPlane system with a design wind speed of 8 m/s (data from Engelen, 2011).

The linear part in figure 2.13 represents the low aspect ratio region where the optimal angle of attack is lower than the maximum angle of attack. It shows that an increase of the aspect ratio will then both decrease the required wing span as well as the wing surface area. Next to that, flying at high angles of attack with an increased aspect ratio will decrease the induced drag relatively. Once the optimal angle of attack coincides with C_{Lmax}, the required wing span increases, visualized by the non-linear part of the graph. However, the scale of the wing span axis is significantly smaller than that of the wing surface area. It already shows for $C_{Lmax} = 1.18$ that an increase of the aspect ratio from 10 to 15 increases the wing span by 6.5%, while the wing surface area decreases by 25%. This effect increases when flying with larger maximum lift coefficient. For $C_{Lmax} = 2$, an increase of the aspect ratio from 10 to 20 increases the wing span by only 3% and decreases the wing surface area by 47%. These results show that using a wing with a high C_{Lmax} and aspect ratio, is of great interest. The most important to realize here, is that the production and transportation of the wing are highly cost effective. A wing surface area as small as possible is therefore preferred.

From a material and construction based view, these aerodynamic optimizations do not go without facing new problems. As a result of an increased aspect ration and decreased wing surface area, the airfoil chord and thickness will decrease, while the wing loading increases (smaller wing surface area). This requires stronger spars and skin construction, such as a larger lay-up thickness. Obviously, this will increase the material costs, so an optimum between this and the wing dimensions should be found. Another way to cope with large aspect ratios, is using a thicker wing profile, as done in wind turbine design. This might be disadvantageous for the aerodynamic behavior, but this way material costs can be kept lower. Again, an optimum in between is to be investigated here.

It can be concluded that the most important parameters to base an aerodynamic

model on, are a high C_{Lmax} and aspect ratio. However, the design wind speed that is used for this, is probably even more important. This holds especially for low design wind speeds, which is for several reasons. First of all, the cable diameter should then be larger, due to lower roll-out velocities. A larger wing surface area is required for lower wind speeds, increasing the PowerPlane costs, but the relative cable drag is lower. This means the aerodynamics of the PowerPlane are of big importance for a low design wind speed, such that an increased aspect ratio is also of interest. A low design wind speed also induces a decreased launching and landing speed, which makes the platform used for this economically more beneficial. Therefore, the design wind speed is a crucial initial input for an aerodynamic model and should be chosen wisely.

2.6.5 Future goals

Up until now, Ampyx Power has been working on an autonomous 10 kW system, which is expected to be finished by the end of 2011. At the same time, the launch and landing platform is being developed and should be operational by the end of 2012. The next step is increasing power production with a 100 kW system, followed by a 1 MW system. A major advantage of scaling up the PowerPlane is the scale at which the dimensions of the plane itself increases. For example, the wing span rises from 5.5 m to 13 m when scaling up from the 10 kW to the 100 kW design. In table 2.3, the main design parameters of these models can be compared, including the 1 MW design.

Table 2.3: Dimensions of the existing 10 kW and designed 100 kW and 1 MW PowerPlane (data from Ampyx Power, 2011).

Parameter	**Unit**	**10 kW**	**100 kW**	**1 MW**
Wing span	m	5.5	13	35-40
Weight	kg	25	300	3000
Operating height	m	300	350	400
Tether diameter	mm	4	10	30
Aircraft loading	kN	4	40	400

Focusing on large scale power production, PowerPlane wind farms are certainly a possibility as well. Because the plane needs to be reeled in at about 1/6 of a full cycle period, there is no continuous power production of one PowerPlane system. Therefore, such wind farm systems should operate in such a way that all the time as much power as possible is produced. This can be done by operating each separate system in phases with each other.

Chapter 3

Aerodynamic calculation methods

The goal of this research is developing a tool for analyzing various design configurations of the PowerPlane, of which the methodology is to be set up first. In the previous chapter, it is explained what the influencing design parameters are. Making use of relatively simple aerodynamic methods already gives more insight in the behavior of these factors. In this chapter, a variety of such available methods will be considered, for which the theory behind these methods should be understood first. Thereafter, potential flow based methods are investigated, since these are the most well-known, reliable and fastest methods. Finally, an available set of programs is tested and evaluated to find a most promising software tool.

3.1 Basic lift theorems

In order to understand and explain the outcomes of certain methods, such as the vortex lattice method (VLM), the fundamental theory behind the aerodynamics is elaborated first in this section (J. D. Anderson, 2007; Gilbert, 2011). For this, several models are considered, each focusing on specific aerodynamic phenomena. This theory is then used further to derive the concept of a 2D and 3D potential flow methods, such as the 3D panel method and the VLM.

3.1.1 Momentum lift theory

Downwash, or downward push, that is created by a deflected airfoil creates lift on the wing. Since the incoming air is deflected downwards, an upward reaction force is acting on the airfoil. In the momentum lift theory, it is assumed that the resulting lift force of a rectangular shaped wing is equal to the downwash momentum, such that the induced drag component is ignored. Also, the downwash is assumed to be equally distributed along the wing span, which is only true for an ideal elliptical wing shape or an infinite wing span.

In the momentum lift theory, a cylindrical volume with a diameter equal to the wing span, b, is considered as the control volume, as shown in figure 3.1. The air speed, v, is deflected downstream of the airfoil with a downwash angle, ε, such that a downwards air velocity, w, rises. This value is assumed to be proportional only to the resulting lift force,

L, on the wing.

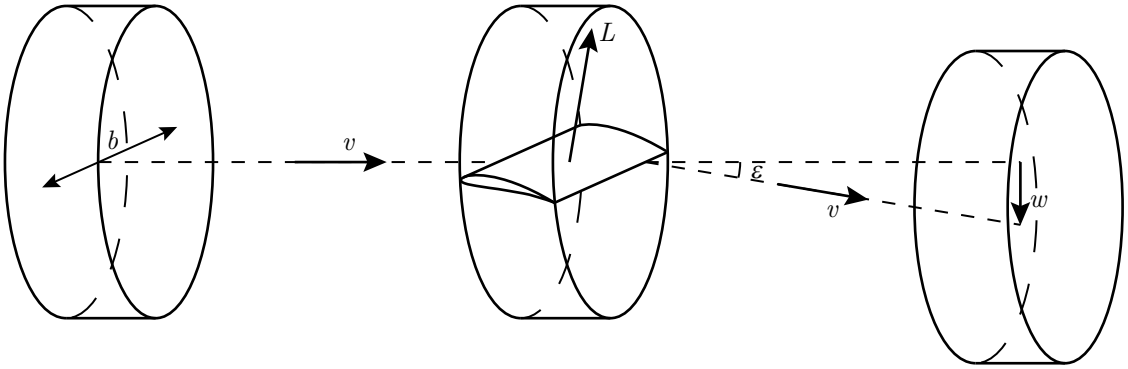

Figure 3.1: Visualization of the momentum lift theory considering cylindrical volumes to analyze downwash.

The lift force is equal to the amount of air crossing the cylindrical volume with cross-section A_c times the downward velocity, w. The transported mass of air per time unit can be written as

$$m = \rho v A_c \tag{3.1}$$

where the cross-sectional area is defined as $A_c = \frac{\pi}{4} b^2$. Substituting this in the lift force equation and assuming small angles, such that $\varepsilon = w/v$, one can write

$$L = \rho v A_c w = \rho v^2 A_c \varepsilon \tag{3.2}$$

From this relation and using the well-known formula to calculate the lift force, the downwash angle can be determined as

$$\varepsilon = \frac{\frac{1}{2}\rho v^2 S C_L}{\rho v^2 A_c} = \frac{S C_L}{2 A_c} \tag{3.3}$$

Rewriting this in terms of the wing span and using a relation for the aspect ratio as $A = \frac{b^2}{S}$, then

$$\varepsilon = \frac{2 C_L}{\pi A} \tag{3.4}$$

From this result, a relation for the induced drag can be derived. The aerodynamic force acting on the wing is deflected by an angle which is assumed to be half of the downwash angle. This force consists in this case of the lift force and the induced drag force. Since these are perpendicular vectors, geometric relations are used such that

$$C_{Di} = \alpha_i C_L = \frac{{C_L}^2}{\pi A} \tag{3.5}$$

where C_{Di} is the induced drag coefficient and α_i is the induced drag angle, which is said to be half the downwash angle. This angle is not effective concerning lift production, such that the angle of attack of an airfoil consists of an effective angle of attack plus this induced angle of attack, such that $\alpha = \alpha_{eff} + \alpha_i$. It is noted that the relation for the induced drag coefficient shows that a high aspect ratio reduces induced drag. This is

beneficial when considering a sailplane, since high aspect ratio's are normally used. For the PowerPlane, this also holds.

3.1.2 Circulation lift theory

Similar to the momentum lift theory is the circulation lift theory, which also assumes the lift force to result only from the downwash. However, this theory goes into more detail concerning the flow behavior around the wing. It assumes an ideal flow regime, known as potential flow, neglecting viscous effects.

Circulation of a fluid states that a particle's velocity, w, depends on the distance to the center of circulation, r (see figure 3.2). Assuming the path of this particle is a circle, the circulation is written as

$$\Gamma_c = 2\pi w r \tag{3.6}$$

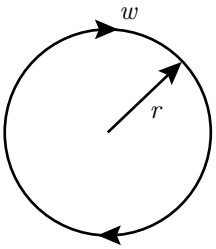

Figure 3.2: Circulation particle in a fluid with velocity w and at distance r from the center of circulation.

For the circulation lift theory of a wing, an infinite wing span is assumed, such that also here a constant downwash distribution holds. The model of this theory is shown in figure 3.3, where c represents the chord length of the airfoil and h is the region where the downwash is acting in. For this case, the circulation is defined as $\Gamma_c = wh$. As can be seen, a portion of the wing with span b is used here, but the infinite wing span assumption still holds. Due to the velocity of the wing through the air, circulation around the airfoil is induced. The lift force is defined as the amount of air that is deflected downstream of the wing times the downwash velocity. The air mass in this case can be determined as the air density times the volume per unit time. This volume is computed as vbh. As a result, the lift force can be written as

$$L = \rho v b h w = \rho v b \Gamma_c \tag{3.7}$$

Since the drag vector is perpendicular to the lift force, the induced drag force is obtained as

$$D_i = \rho w b \Gamma_c \tag{3.8}$$

The lift coefficient can now be derived by using the standard lift force equation and assuming the circulation around the airfoil is a circle with a diameter equal to the chord length, c. Using equation 3.9, the lift coefficient is obtained as in equation 3.10.

$$L = \frac{1}{2}\rho v^2 b c C_L = \rho v b w 2\pi \frac{c}{2} \tag{3.9}$$

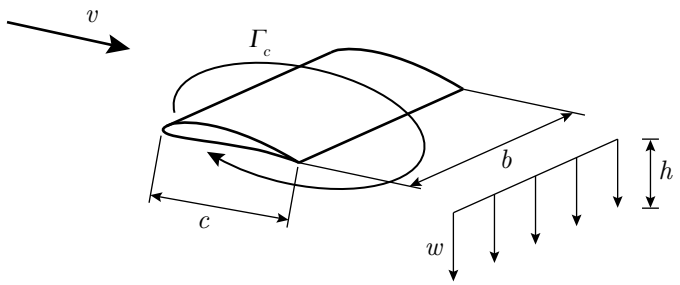

Figure 3.3: Circulation lift theory model of an infinitely long wing.

$$C_L = \frac{2\pi w}{v} \tag{3.10}$$

Another way of rewriting equation 3.9 results in

$$C_L = \frac{2\Gamma_c}{vc} \tag{3.11}$$

From this relation, it can be seen that the lift force depends on the circulation per unit chord length. This explains the reason of using a tapered or elliptical wing shape, such that the lift distribution along the wing span becomes more constant.

Considering a flat plate, as shown in figure 3.4, one can assume the downwash deflection is equal to the angle of attack. A small angle approximation results in $\alpha = w/v$. Using equation 3.10, the lift coefficient can be written as a function of the angle of attack in its simplest form as

$$C_L = 2\pi\alpha \tag{3.12}$$

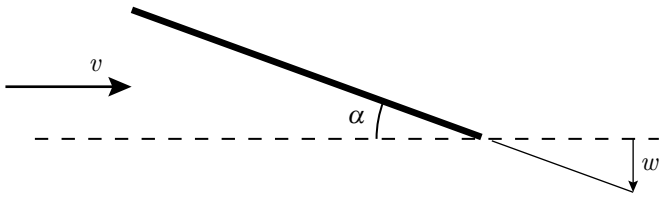

Figure 3.4: Downwash deflection of a flat plate with an angle of attack α.

3.1.3 Lifting line theory

In the circulation lift theory, an infinity wing span was assumed, such that there were no variations in the downwash distribution. The lifting line theory incorporates a finite wing span, which gives rise to other aerodynamic effects. One of them is the appearance of a starting vortex once the wing starts moving upstream, as shown in figure 3.5. This vortex is equal in magnitude to the bound vortex (wing vortex), but in the opposite direction of rotation. Next to this, the wing tips generate so called tip vortices, resulting in a closed vortex system, which is a result of the conservation of circulation. According to the lifting

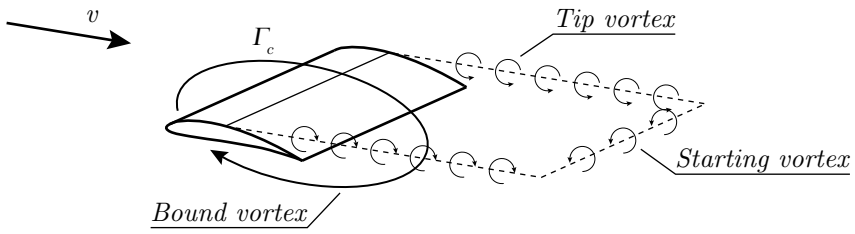

Figure 3.5: Development of a closed circulation vortex system behind a finite wing section.

line theory, the wing is considered to be a single vortex line, at which the bound vortex is bound to.

As a result of the tip vortices, additional downwash is added to the already present downwash due to the bound vortex. Therefore, the downwash magnitude increases towards the wing tips, increasing the induced drag (see equation 3.8). This phenomena is illustrated in figure 3.6, which is also known as Prandtl's wing theory. Here, the equally distributed downwash comes from the bound vortex and the parabolic distribution increasing towards the wing tips is a result of the tip vortices. Since this holds for a rectangular shaped wing, changing this shape results in a different downwash distribution. A said before, an elliptical shaped wing equally distributes the extra downwash due to tip vortices, such that the total downwash is also constant along the wing span. The total induced drag D_i is determined as

$$D_i = \rho v \int_{tip}^{tip} \Gamma sin\left(\alpha_i\right) dy \tag{3.13}$$

where α_i is the induced angle of attack defined as

$$\alpha_i = sin^{-1}\left(\frac{w}{v}\right) \tag{3.14}$$

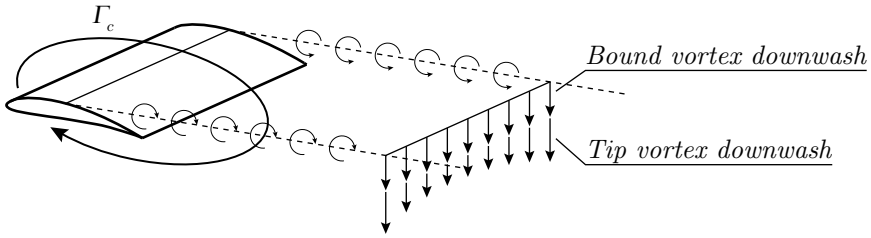

Figure 3.6: Downwash distribution due to the bound vortex (constant) and the tip vortices (parabolic).

It is obvious that the lifting line theory is an easy and fast approach to determine lift and induced drag coefficients. However, compared to realistic values, the expected accuracy is low. Especially considering wings with a low aspect ratio, large sweep or large dihedral. As a matter of fact, the theory assumes that the wing lies in the $x - y$ plane only and sweep, dihedral and twist are not even taken into account for the calculation of the lift distribution. Also inviscid conditions are assumed, which results in significant errors in the drag terms. Lastly, the chordwise position of the center of pressure at each

spanwise station can be defined as shown in equation 3.15. Here, C_{m_0} represents the pitching moment of the wing.

$$x_{CP} = 0.25 - \frac{C_{m_0}}{C_l} \tag{3.15}$$

Non-linear lifting line theory

The classical LLT assumes a linear variation of the lift coefficient versus effective angle of attack. For applications that fly at high angles of attack close to the stall angle, LLT is extended to account for a non-linear lift curve.

With the results of the classical LLT, the induced angles and corresponding effective angles per spanwise station are determined. Now assume that for each spanwise station experimental data for the lift curves (including the non-linear regime) are known. With the effective angles, the lift value for each spanwise station is obtained from the lift curve, from which a new circulation distribution can be determined. This process can be iterated until convergence is reached for which relaxation might be necessary.

About this method, J. Anderson (1980) states that solutions give reasonable preliminary engineering results for the high angle of attack post stall region, though 'it is wise not to stretch the applicability of LLT too far'. The 3D effects at high angles of attack, such as spanwise flow and mushroom shaped flow separation regions, cannot be included in this method.

3.2 Thin airfoil theory

In the lifting line theory, a closed circulation vortex system was determined behind a line representing the wing. The airfoil shape is therefore not taken into account. A 2D method to predict forces, pressures and moments on thin cambered airfoils is called thin airfoil theory (TAT).

A vorticity distribution is placed on the airfoil camber line as shown in figure 3.7. This distribution will be a solution of Laplace's equation and will satisfy the BC's if the vortex induced velocities cancel the free-stream velocity component normal to the airfoil (J. D. Anderson, 2007). The latter is defined as

$$w'(s) = V_\infty \left(\alpha - \frac{dz}{dx} \right) \tag{3.16}$$

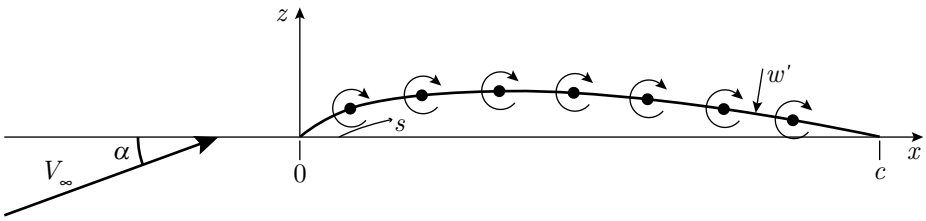

Figure 3.7: Vorticity distribution on the camber line of a thin airfoil.

The velocity induced at location x due to the vorticity at ξ is assumed to be equal to the induced velocity at the same x location due to a vortex projected on the x axis

(see figure 3.8). This is because the camber line of a thin airfoil is close to the chord line. Vortex singularity is used to determine the induced velocity by means of the Biot-Savart law. Combining this with the flow tangency BC, the integral relation of thin airfoil theory is obtained as

$$\frac{1}{2\pi}\int_0^c \frac{\gamma(\xi)d\xi}{x-\xi} = V_\infty\left(\alpha - \frac{dz}{dx}\right) \tag{3.17}$$

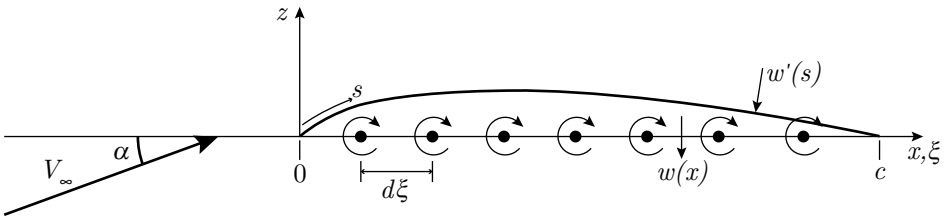

Figure 3.8: Projected vorticity distribution on the x axis of thin airfoil's camber line.

Here, γ represents the strength of the vortex street. With the integral relation, airfoils can also be designed for a desired pressure distribution. This is called the thin airfoil inverse design method. By a Fourier series representation of γ, the use of polar coordinates and trigonometric relations, the unknown constants become

$$\begin{aligned} A_0 &= \alpha - \frac{1}{\pi}\int_0^\pi \frac{dz}{dx}\,d\theta_0 \\ A_n &= \frac{2}{\pi}\int_0^\pi \frac{dz}{dx} cos\, n\theta_0\, d\theta_0 \end{aligned} \tag{3.18}$$

With these expressions, the pressure difference between upper and lower surface, the lift coefficient and moment coefficient about the leading edge can be determined as

$$C_{p_l} - C_{p_u} = 4\left(A_0 cos\,\frac{\theta_0}{2} + \sum_1^w A_n sin\, n\theta_0\right) \tag{3.19}$$

$$C_l = \pi\left(2A_0 + A_1\right) \tag{3.20}$$

$$C_m = -\left[\frac{C_l}{4} + \frac{\pi}{4}\left(A_1 - A_2\right)\right] \tag{3.21}$$

3.3 Potential flow methods

Since the lifting line theory has quit some limitations considering the wing geometry, other potential flow methods are developed that give more accurate results when for example using low aspect ratios, sweep, dihedral, twist and cambered airfoils. It does not include all the characteristics of flows that are encountered in the real world e.g. turbulence and boundary layers. Yet, there are ways to introduce non-potential flow aspects, at least in a certain degree. The 3D version of thin airfoil theory is the vortex lattice method, considering the mean camber line as a thin airfoil. In order to take into account airfoil

thickness, so called panel methods are used, discretizing both upper and lower wing surface.

3.3.1 Fundamentals of potential flow

In potential flow theory the flow field is described as the gradient of the velocity potential function $\varphi = \varphi(x, y, z, t)$ as

$$\vec{v} = \nabla\varphi \tag{3.22}$$

Knowledge of φ directly relates to the velocity components, shown in equation 3.23.

$$u = \frac{\partial\varphi}{\partial x}, \quad v = \frac{\partial\varphi}{\partial y}, \quad w = \frac{\partial\varphi}{\partial z} \tag{3.23}$$

Because the curl of a gradient is equal to zero (see equation 3.24), it follows that vorticity is zero and therefore potential flow is irrotational.

$$\nabla \times (\nabla\varphi) = \nabla \times \vec{v} = 0 \tag{3.24}$$

The assumption of having irrotational flow makes fluid dynamics much simpler, however it is also an important drawback of potential flow theory: it is not able to include vorticity. Therefore in flow regions containing a lot of vorticity, such as wakes and separated flow, potential flow is not able to accurately predict the flow. However, many problems have large regions where the flow behaves irrotational and therefore potential flow is used in many applications. Combining the definition of the velocity potential with the principle of conservation of mass for incompressible flow results in the well-known Laplace equation, which is defined as

$$\nabla^2\varphi = 0 \tag{3.25}$$

A consequence of incompressible, potential flow is that viscous terms vanish, therefore incompressible potential flow implies the absence of viscosity[1]. Therefore, it cannot predict boundary layer behavior.

In many cases potential flow reduces a problem to a linear problem. Incompressible, potential flow results in the well-known Laplace equation. A large advantage of using potential flow lies in the fact that the flow can be analytically solved and therefore is often simple and fast. Linear equations can be superimposed, which makes it possible to add several elementary flows to create more complex flows. The property of superposition has been fundamental for the development of numerical panel methods and vortex lattice methods.

[1] From Stokes (1851), it actually follows that viscous stresses do not have to be zero in irrotational flow. However the terms containing viscous stresses disappear in the Navier Stokes equations since they only contain derivatives of the viscous stresses which are zero in potential flow. Potential flow can be used for considering viscous effects in cases where shear stresses are negligible, but normal stresses exist (where the orientation of the stresses is taken with respect to the orientation of the flow field). This is however only valid in some special cases (Joseph, 2003).

The well known Bernoulli equation is used to determine corresponding pressure values, as shown in equation 3.26, which finally is used to determine the lift, drag and moment coefficient of a wing. Here, gravity is neglected.

$$p + \frac{1}{2}\rho v^2 = constant \tag{3.26}$$

Potential flow theory can also be extended to compressible and unsteady flows resulting in the non-linear full potential equation. The dynamics of wings used for airborne wind energy applications is assumed to be quasi-steady and incompressible, hence the full potential equation is for this thesis not of further interest.

Kutta-Joukowski theorem and the Kutta-condition

The Kutta-Joukowski theorem determines the lift (per unit span) of an airfoil section by determining the circulation in a region of potential flow as

$$L' = \rho_\infty V_\infty \Gamma_\infty \tag{3.27}$$

Here ρ_∞ and V_∞ are the undisturbed flow properties. The circulation Γ_∞ is determined as the line integral around a path c far from and enclosing the airfoil, as shown in equation 3.28.

$$\Gamma_\infty \equiv -\oint_c \vec{V} \cdot d\vec{s} \tag{3.28}$$

For potential flow over an airfoil, an infinite amount of solutions are possible. The value of circulation can be anything and therefore it is not defined where the stagnation points are located. In real life flow the rear stagnation point for a body with a sharp trailing edge is located at that trailing edge. This condition is known as the Kutta-condition and implies which value the circulation should have to satisfy this condition. The fact that this rear stagnation point is at the trailing edge is a result of viscosity, hence the Kutta-condition incorporates an important effect of viscosity while maintaining the advantages that potential flow offers.

Circulation is directly related to vorticity by Stokes' theorem, as shown in equation 3.29. Circulation implies presence of vorticity and hence, rotational flow (a property which should not be present in potential flows). The Kutta-Joukowski theorem can still be valid, however. As can be seen in equation 3.28, circulation is defined as an integral along a closed contour and therefore does not contain information about the contents within that contour. Now consider the elementary potential flow of a free vortex, as shown in figure 3.9. A free vortex is irrotational and velocity is inversely proportional to the radius. It is irrotational everywhere, except at the center where it has infinite strength. If now such a vortex can be placed such that the center is within the airfoil, the flow is everywhere irrotational and therefore potential flow theory is applicable.

$$\Gamma_\infty \equiv -\oint_c \vec{V} \cdot d\vec{s} = -\iint_S \left(\nabla \times \vec{V}\right) \cdot d\vec{s} \tag{3.29}$$

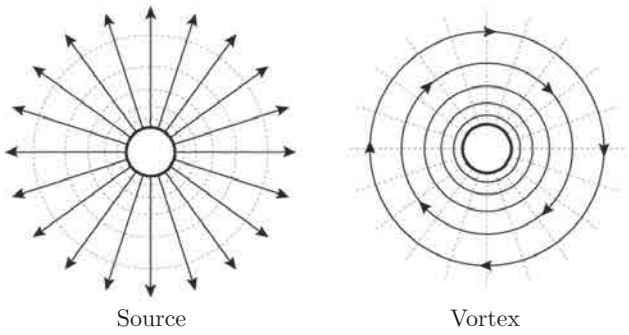

Figure 3.9: Visualization of two elementary flows, which can be used to describe the flow around an airfoil. The source has radially directed induced velocity vectors, while the vortex has induced velocities in the tangential direction.

Vortex filament, Biot-Savart law and Helmholtz's vortex theorems

Expanding the concept of a 2D point vortex to 3D, leads to the vortex filament. A vortex filament can be curved and induces a flow field in the surrounding space. The filament with length $A \leq l \leq B$ has constant circulation Γ and induces a velocity at a distance $\vec{r}$ of

$$\vec{V} = \int_A^B \frac{\Gamma}{4\pi} \frac{\vec{dl} \times \vec{r}}{|\vec{r}|^3} \tag{3.30}$$

This equation is called the Biot-Savart law. Helmholtz's vortex theorems state that strength of a vortex filament is constant along its length. Furthermore, he states that the filament can not end in a fluid. It must extend to the boundaries of the fluid (which can be $\pm\infty$) or form a closed path. These theorems were important building blocks for lifting line theory and the vortex lattice method.

3.3.2 2D panel method

In contrast to the VLM, panel methods take into account the thickness of an airfoil and therefore also give results on pressure distributions on upper and lower surfaces. Furthermore, also fuselage bodies can be modeled with a 3D panel method, such that total aircraft can be analyzed. Programs such as XFOIL are 2D panel methods and only consider an airfoil section, therefore neglecting three-dimensional effects. How an airfoil is discretized in a 2D panel method is shown in figure 3.10.

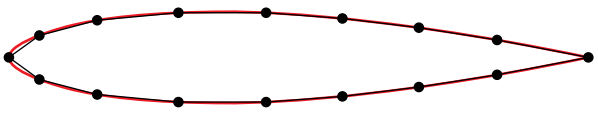

Figure 3.10: Discretization of a 2D airfoil section using a panel method.

Before getting into 3D numerical wing analysis methods it is useful to understand 2D numerical methods. In such methods a distribution of singularities is solved for a specified shape, as shown in figure 3.10. In combination with a uniform stream, the singularities

produce the flow over a given body. These singularities can consist of elementary potential flows, such as sources, sinks, doublets and vortices. Most common is to use a combination of both source (σ) and vortex (γ) panels, which basically simulate respectively airfoil thickness and circulation (instead of vortices also doublets are used). Lets assume the airfoil is discretized in a number of panels, as can be seen in figure 3.10, which contain these two singularities. Each of these singularities induce a velocity potential at a predefined point of each panel, the control points. In order to satisfy the boundary condition of zero normal velocity at the control point, the potential at that point due to all the panels should be equal to the normal velocity component of the free stream, such that

$$V_{\infty,n} + V_n = 0 \tag{3.31}$$

where V_n is the summation of induced normal velocities of all panels. For panel i, this can be written as

$$V_{n,i} = \sum_{j=1}^{N} A_{ij} \cdot \sigma_j + \sum_{j=1}^{N} B_{ij} \cdot \gamma_j + C_i \cdot V_\infty = 0 \tag{3.32}$$

where the coefficients (A_{ij}, B_{ij}) represent the influence of panel j distribution strengths on the control point of panel i and represents the free stream influence. All coefficients are functions of the geometry of the section, i.e. due to orientation and spacing of panels. The resulting system can be written in matrix form, as shown in equation 3.33. To complete the system, the Kutta-condition is used. The tangential velocities leaving at the TE panel have an equal magnitude. This gives a system of linear equations which allow the solution for the required distribution strengths to be found.

$$\begin{bmatrix} A_{1,1} & \dots & A_{1,N} \\ \vdots & \ddots & \vdots \\ A_{N,1} & \dots & A_{N,N} \\ B_{1,1} & \dots & B_{1,N} \\ \vdots & \ddots & \vdots \\ B_{N,1} & \dots & B_{N,N} \end{bmatrix} \begin{bmatrix} \sigma_1 \\ \vdots \\ \sigma_N \\ \gamma_1 \\ \vdots \\ \gamma_N \end{bmatrix} = \begin{bmatrix} C_1 \\ \vdots \\ C_N \\ C_1 \\ \vdots \\ C_N \end{bmatrix} \cdot (-V_\infty) \tag{3.33}$$

Once the distribution strengths have been calculated, surface tangential velocities at the center of each panel can be calculated and then surface pressure coefficients as

$$C_{p,i} = 1 - \left(\frac{V_i}{V_\infty} \right)^2 \tag{3.34}$$

The panel method as described in this section is named a 'first-order' method because it assumes a constant value of singularity over a given panel. Higher order methods can also be used, of which a more thorough discussion can be found in Katz & Plotkin (1991) and J. D. Anderson (2007).

2D boundary layer correction

A relatively efficient way of introducing the effects of viscosity into calculations on airfoils is by adding the effects of a boundary layer to the potential flow solution in an iterative manner, also known as viscous-inviscid interaction. The inviscid outer flow region serves

as input to the boundary layer equations from which a quantity known as the displacement thickness can be determined. With this quantity, the wall streamlines are displaced to obtain a correction on the potential flow solution of the pressure field (see figure 3.11).

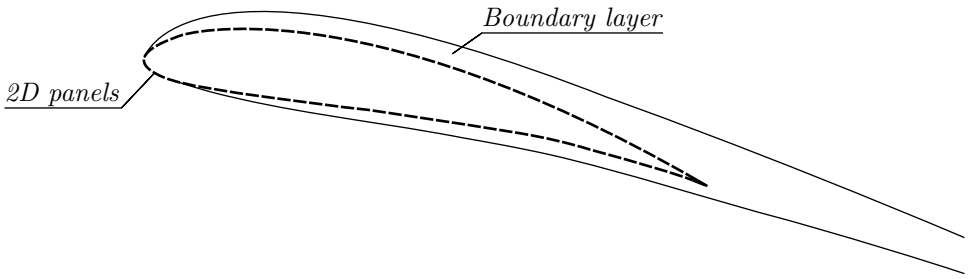

Figure 3.11: The thickness of the boundary layer is added to the airfoil geometry.

Another option to displace the streamlines is to use a source contribution on the contour of such strength that a normal velocity v_n is generated of

$$v_n = \frac{d}{dx}\left(U\delta^*\right) \tag{3.35}$$

Here, x is in the direction of the panel, U is the local outer flow velocity and δ^* is the displacement thickness. The advantage of this procedure is that the geometry of the airfoil remains the same through all iterations (Veldhuis, 2012).

These boundary layer correction methods produce results that for most cases of engineering interest compare well with experiment and this at much lower computational cost than Navier-Stokes simulations. Furthermore, viscous-inviscid interaction methods give clear insight into the behavior of the boundary layer since the integral thicknesses are immediately available (Coenen et al., 2000).

3.3.3 Vortex lattice method

The vortex lattice method (VLM) is used to model the wake behind a wing by means of placing a number of vortices on the wing planform. For each of these vortices, the strength is determined such that the boundary conditions are satisfied. It should be noted that a VLM does not take into account airfoil thickness. Instead, the mean camber line is taken as a basis, such that only the upper surface pressure distribution can be determined.

Two methods are distinguished considering a VLM, which are based on a slightly different theory. The first one is shown in figure 3.12, where a horseshoe vortex is placed on every quarter chord panel with a control point at the three quarter chord panel. This control point refers to the boundary condition that states the non-penetration condition on the surface of the body.

The second method is recommended by Katz & Plotkin (1991) and uses so called ring vortices or quad vortices, as shown in figure 3.13. Also here, the vortex is placed on the quarter chord panel with a control point at the three quarter chord panel. However, in this case only the trailing vortices extend to infinity, which strength is equal to the trailing edge ring vortex. This is due to the condition that the wake is force free. Besides the fact that these methods use a different approach, the outcomes are expected to be similar.

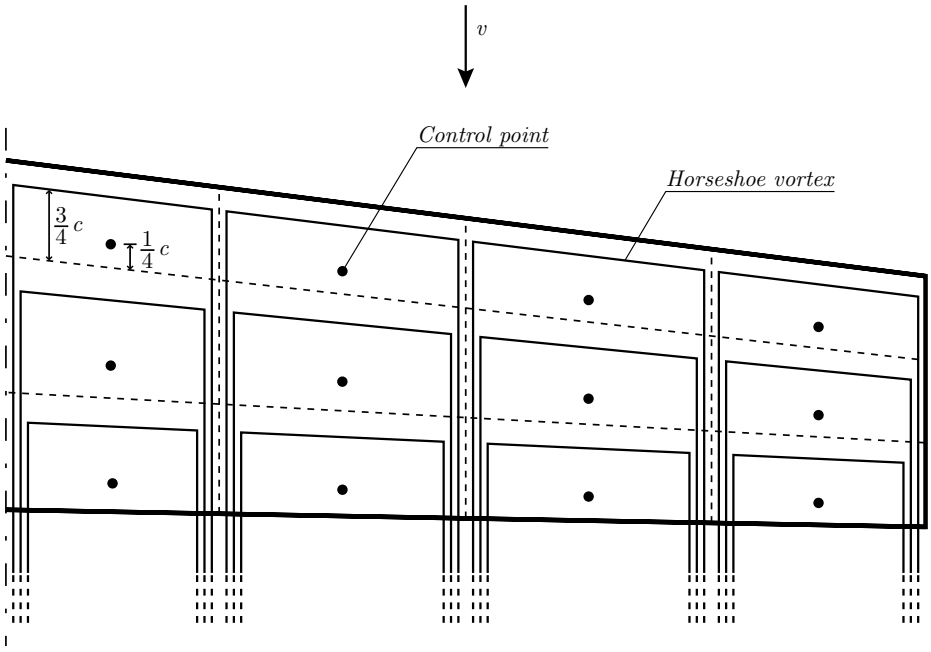

Figure 3.12: Top view of a semi-span wing illustrating the vortex lattice method using the horseshoe vortex method.

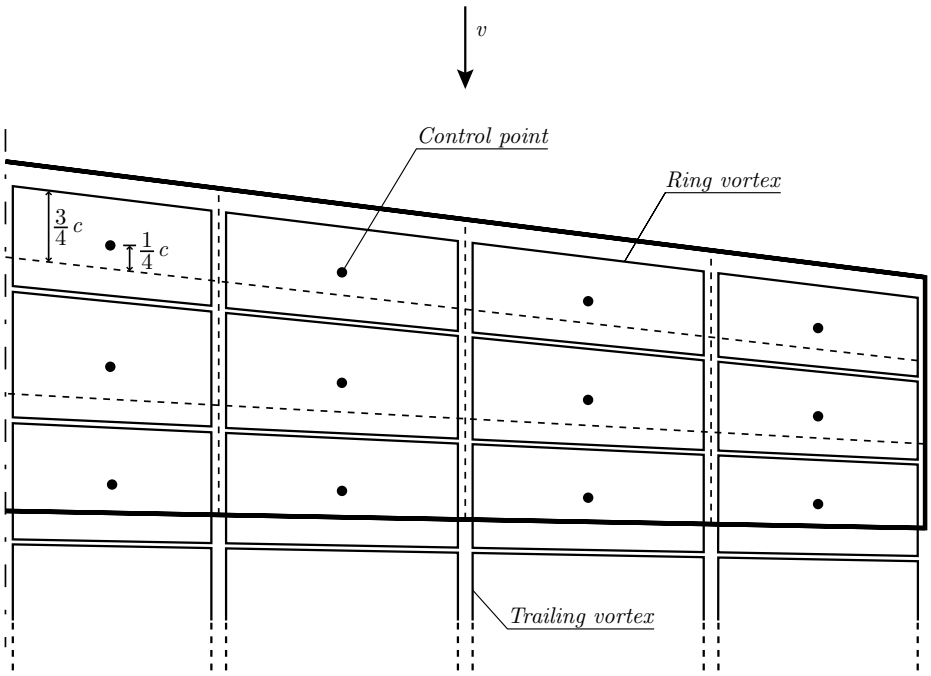

Figure 3.13: Top view of a semi-span wing illustrating the vortex lattice method using the ring vortex method.

As mentioned earlier, the vortex lattice method uses the mean camber line of the considered airfoil to perform calculations on, neglecting thickness effects. In a three-dimensional space, such a lay-up can be visualized as shown in figure 3.14.

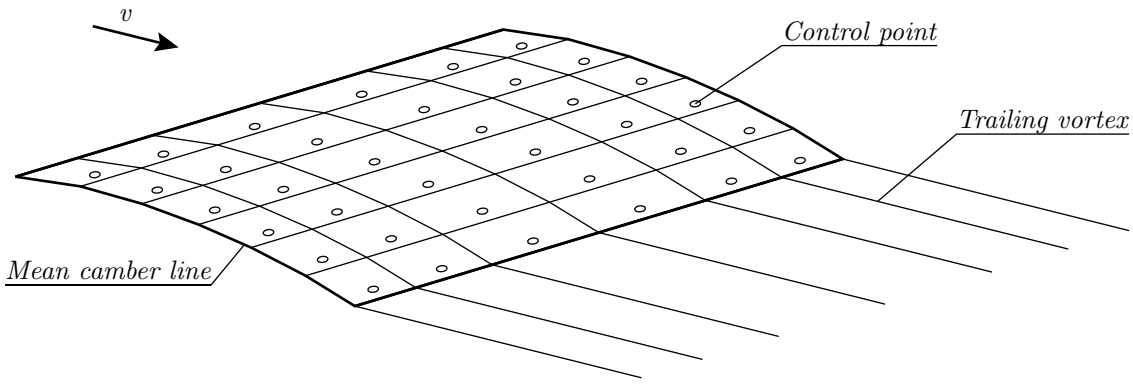

Figure 3.14: Lay-up of a three-dimensional wing using the vortex lattice method.

Considering a single panel on this surface, the lift force and coefficient can be determined from the force acting on this panel. This force is defined as

$$F_{panel} = \rho v \Gamma_c \tag{3.36}$$

Here, Γ_c is the vortex strength multiplied by the vortex length. Therefore, this force is acting in normal direction with respect to the panel. The lift coefficient can then be determined as shown in equation 3.37, where S_{panels} is the total area of all panels and F_{wz} is the force projected on the vertical wind axis. From this, the lift force can be determined, which is in turn used to calculate the position of the center of pressure and pitching moments.

$$C_L = \frac{1}{\rho S_{panels} v^2} \sum_{panels} F_{wz} \tag{3.37}$$

3.3.4 3D panel method

Next to the VLM, which already has significant improvements with respect to LLT, 3D panel methods are developed. These are in principal an extension of the 2D panel method discussed in section 3.4.1. In contrast to the VLM, these methods take into account the thickness and camber of an airfoil and therefore also gives results on pressure distributions on upper and lower surfaces. Furthermore, fuselage bodies can be modeled with a 3D panel method, such that total airplanes can be analyzed.

In a 3D panel method, a wing or plane is discretized into panels distributed over the span and chord of the airfoil. As with the VLM, each panel contains one or multiple singularities and a control point. Popular are sources and doublets; the latter is equivalent to a distribution of vortices and can therefore generate lift, as opposed to sources (Paraschivoiu, 2003).

In addition to covering the body with panels, also the wake behind the body can be modeled with panels (see figure 3.15). The idea is that each of the wing's chordwise strip sheds a column of wake panels. The doublet strength of each panel in this wake strip is

the difference of the doublet strength of the top and bottom panels of the wing's strip. This is a consequence of the fact that the wake cannot sustain load. In addition, being a thin surface, the wake panels have a zero source strength. Again here, the singularity strengths are determined, satisfying the boundary conditions.

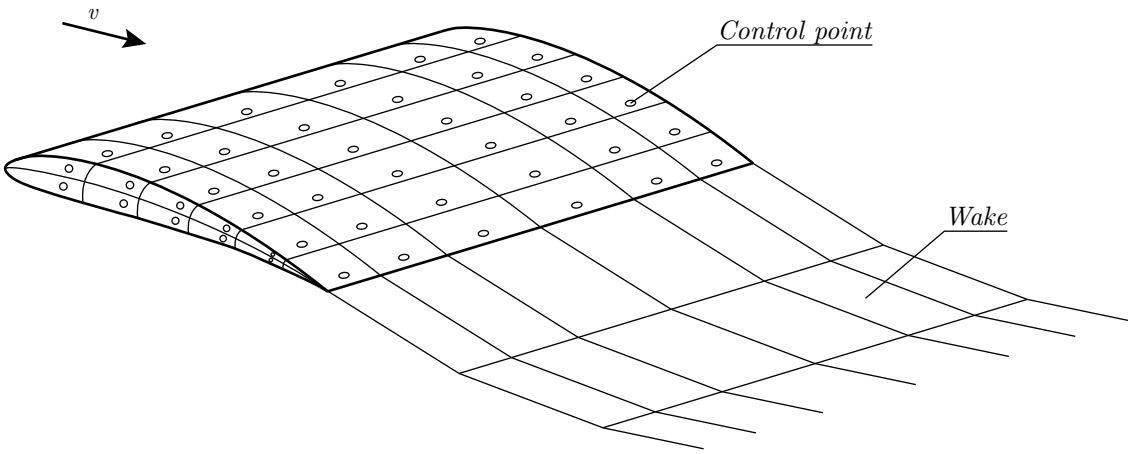

Figure 3.15: Lay-up of a three-dimensional wing using a panel method.

The resulting equations which are solved in case Neumann boundary conditions are applied, are principally the same as described in equations 3.31, 3.32 and 3.33. However, for multiple programs, such as XFLR5 and VSAERO, the format of the equation is somewhat different. The boundary condition considers sources and doublets on each surface panel (σ_s and μ_s) and only doublets on each wake panel (μ_{wake}), such that the induced velocity v_i is obtained for the Neumann boundary condition as

$$\overline{v}_i = [A]\overline{\mu}_s + [B]\overline{\sigma}_s + [C]\overline{\mu}_{wake} = -\overline{V}_\infty \cdot \overline{n} \tag{3.38}$$

The singularities represent the jump in conditions across the boundary; the doublet density represents the local jump in potential and the source density represents the local jump in the normal component of velocity. For the Dirichlet boundary condition, the equation is slightly different when rewritten. This results in

$$[D]\overline{\mu}_s + [E]\overline{\sigma}_s + [F]\overline{\mu}_{wake} = 0 \tag{3.39}$$

In the relations above, the matrices $A - F$ represent influence matrices completely determined by the geometry of the surface. Furthermore, the doublets and sources are defined as

$$\mu = \frac{1}{4\pi}\left(\phi - \phi_0\right) \tag{3.40}$$

$$\sigma = -\frac{1}{4\pi}\left(\overline{V}_\infty \cdot \overline{n}\right) \tag{3.41}$$

In the definition of σ, it is assumed that no transpiration velocity is used (which can be the case when coupling boundary layer calculations). In the case of a VLM, only vortices are placed on each surface panel, such that no wake panels exist (no sources). The wake therefore completely consists of shedded horseshoe vortices, where there is no jump in

velocity across the wake. In the case of a panel method, the source strength on each wake panel is zero. Furthermore, the definition of μ implies the Kutta-condition at the trailing edge, such that $(\phi_{u_{TE}} - \phi_{l_{TE}})$ is constant on the wake shedded by these panels. Finally, a full-matrix equation is obtained as

$$\begin{bmatrix} A_{1,1} & \dots & A_{1,N} \\ \vdots & \ddots & \vdots \\ A_{N,1} & \dots & A_{N,N} \end{bmatrix} \begin{bmatrix} \mu_1 \\ \vdots \\ \mu_N \end{bmatrix} = \begin{bmatrix} RHS_1 \\ \vdots \\ RHS_N \end{bmatrix} \tag{3.42}$$

$$\text{influence matrix (geometry)} \cdot \mu = \sigma,\ V_\infty,\ \alpha \text{ (boundary conditions)}$$

Once the doublet and source strengths in spanwise and chordwise direction are known, the associated derivative is used to determine the pressure distribution.

3D boundary layer correction

Despite the success in two dimensions, results obtained with 3D inviscid-viscous interaction are still limited (Lock & Williams, 1987). The development of a 3D boundary layer correction method proves difficult due to the complexity of the boundary layer equations. Furthermore, in the presence of flow separation these methods run into difficulties: the algorithm becomes instable and ceases to converge as a singularity is encountered in the boundary layer formulation. There are some methods which overcome these problems, but when significant separation is present, the inviscid and viscous solutions are mismatched and an efficient update procedure for rectifying this has yet to be developed (Coenen et al., 2000).

3.3.5 Boundary element method

Panel methods and boundary element methods are similar in the way that they both use a surface mesh with singularities and are based on potential flow theory. The boundary element method is however not restricted to determination of flow properties on only the surface. It uses Green's Second Identity, depicted in equation 3.43, to map a potential flow problem from dimension x to dimension $x-1$.

$$\int_A \left(\varphi \nabla^2 \lambda - \lambda \nabla^2 \varphi\right) \mathrm{d}V = \oint_{\partial A} \left(\varphi \frac{\partial \lambda}{\partial n} - \lambda \frac{\partial \varphi}{\partial n}\right) \mathrm{d}S \tag{3.43}$$

Using this identity, each point in the domain is expressed in terms of the boundary values. Once all boundary values are known, any potential value within the domain can be found. The resulting system is the boundary integral equation, which is defined as

$$C(P)\varphi(P) = \oint_{\partial A} K_2\left(P,Q\right) \frac{\partial \varphi}{\partial n} \mathrm{d}S(Q) - \oint_{\partial A} K_1\left(P,Q\right) \varphi(Q) \mathrm{d}S(Q) \tag{3.44}$$

Here, $K_1(P,Q) = \frac{\partial \lambda(P,Q)}{\partial n}$, $K_2(P,Q) = \lambda(P,Q)$ and $C(P) = \frac{\theta}{2\pi}$. These three parameters are solely determined by geometry.

The boundary element method is often more efficient than other volume-discretization methods in terms of computational resources for problems where there is a small surface/volume ratio. However, for many problems boundary element methods are significantly less efficient than volume-discretization methods. This method can give insight in

flow characteristics around a wing, however, it is based on potential flow theory and has therefore the same limitations.

3.4 Potential flow based applications

Now that the theory behind panel methods and vortex lattice methods is known, one is able to understand the working principles and outcomes of software programs which use these methods. In order to gain experience with such tools, a variety of programs has been tested. In this section, a selection of these software packages is shown, with a number of results. From this evaluation, conclusions are drawn concerning which tool seems most promising.

3.4.1 2D Panel Method

A Matlab based panel method, or 2D potential flow simulator is tested, which only gives an ideal streamline representation and ideal performance curves (Jayaraman, 2006). However, these results do give a rough estimation on the actual output that is required in the end. For the purpose of comparing each method discussed in this section, the main wing profile will be considered. In figure 3.16a, the 10 kW PowerPlane main wing profile (Kiteplane 14) is shown, with a thickness to chord ratio of $t/c = 0.14$ at $c = 0.282$. Running the Matlab simulation results in a vector plot, in which the air velocity vectors can be simulated over time, following the airfoil shape. The Kutta condition is implemented here, to obtain smooth trailing edge streamlines. A simulated velocity vector field around the airfoil with $\alpha = 10^o$ is shown in figure 3.16b. It should be noted that the outer part of the main wing with dihedral has a profile thickness of $t/c = 0.12$.

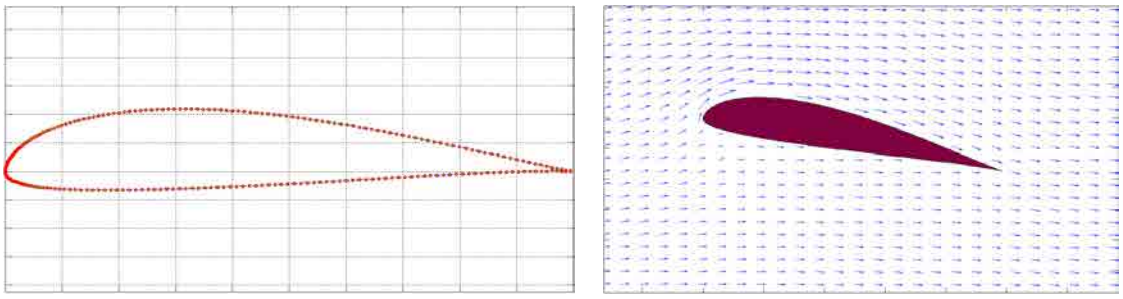

(a) Discretized airfoil section

(b) Simulated velocity field

Figure 3.16: Main wing profile with velocity vector field of the 10 kW PowerPlane with $t/c = 0.14$ at $c = 0.282$ (obtained with Matlab 2D potential flow simulator).

In this program one can also generate a $C_l - \alpha$ curve and a C_p distribution of upper and lower surface with respect to x/c. These curves are shown in figure 3.17 and 3.18, where for the pressure distribution the angle of attack was set to $\alpha = 10^o$. From these results, it is noted that the lift curve is purely inviscid (linear), meaning C_l values for high angles of attack are too high. The pressure distribution also shows the smooth inviscid behavior, but the values near the trailing edge do not coincide nicely.

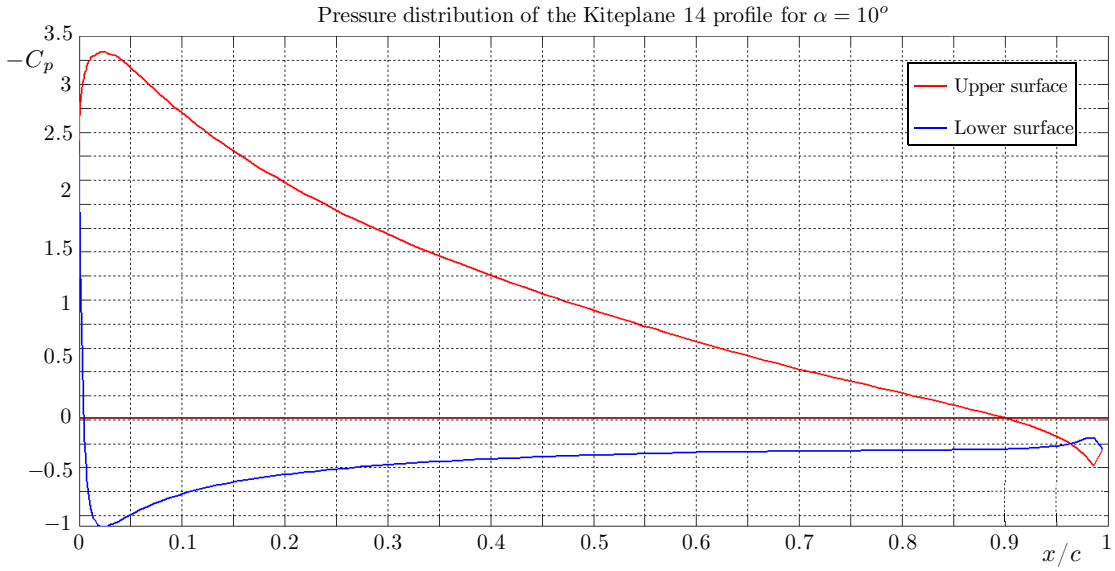

Figure 3.17: C_p as a function of x/c of the 10 kW PowerPlane main wing profile for $\alpha = 10^o$ (obtained with Matlab 2D potential flow simulator).

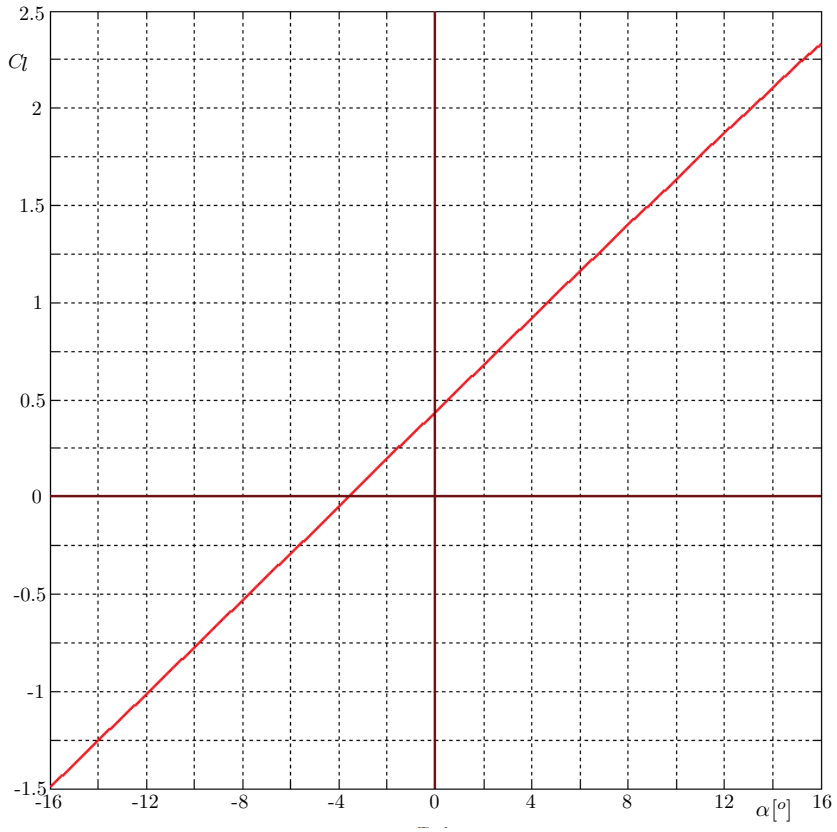

Figure 3.18: The $C_l - \alpha$ curve of the 10 kW PowerPlane main wing profile (obtained with Matlab 2D potential flow simulator).

3.4.2 XFOIL

Another 2D panel method based program is XFOIL, used for the design and analysis of subsonic airfoils. In comparison with the previous discussed tool, with XFOIL viscous calculations can be performed. For this, boundary layer theory and a turbulence model (e^n method) are integrated. The boundary layer and transition equations are solved with the inviscid flow field by a global Newton method. In addition to calculating the total drag from the wake momentum thickness, XFOIL also determines the friction and pressure drag components. A notation to the program is given: "The procedure is especially suitable for rapid analysis of low Reynolds number airfoil flows with transitional separation bubbles" (Drela & Youngren, 2011b). Since the 10 kW PowerPlane flies at low Reynolds numbers, this assumption should hold for this application.

In order to compare with the results of the Matlab 2D panel method simulator (see section 3.4.1), the C_p distribution with respect (x/c), the $C_l - \alpha$ curves and $C_l - C_d$ curves from XFOIL are discussed in this section. In these analysis, a range of $(0.2 < Re < 1.4) \cdot 10^6$ is used. In figure 3.19, the pressure distribution of the Kiteplane 14 profile can be seen, obtained with XFOIL. Here, the inviscid and viscous solution are shown separately. The inviscid distribution is similar to that obtained with the Matlab tool, but the viscous distribution shows a lower pressure on both upper and lower surface, which is due to the added boundary layer to the airfoil surface. Also, a laminar separation bubble can be seen in the viscous C_p distribution, affecting lift and drag of the airfoil.

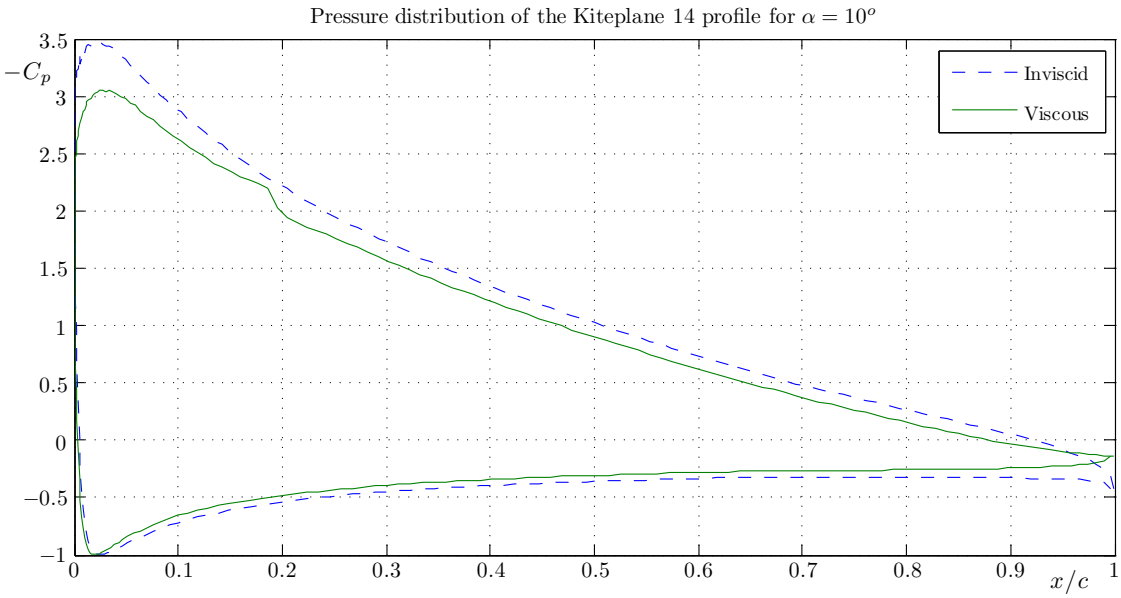

Figure 3.19: C_p as a function of x/c of the 10 kW PowerPlane main wing profile for $\alpha = 10^o$ and $Re = 1 \cdot 10^6$ (obtained with XFOIL).

Regarding the lift curves obtained with XFOIL (see figure 6.3) and the one from the Matlab tool (see section 3.4.1), a small difference is noted in the slope of the $C_l - \alpha$ curve for low angles of attack. For the Matlab 2D Panel Method this is 0.12 deg^{-1} and XFOIL gives a value of 0.11 deg^{-1}, which is close $2\pi\alpha$, known from lifting line theory. The lift coefficient values at zero angle of attack are also quite similar, which is 0.44. Therefore, the angle of attack at zero lift is also found to be approximately the same,

which is $\alpha = -3.5^o$. However, the maximum lift coefficient can not be compared, since the Matlab based panel method gives a purely inviscid/linear solution. As shown with the pressure distribution, XFOIL takes into account viscous effects resulting in a lift curve that reaches separation conditions, giving a value of $C_{l_{max}} = 1.8$ for $Re = 1.4 \cdot 10^6$.

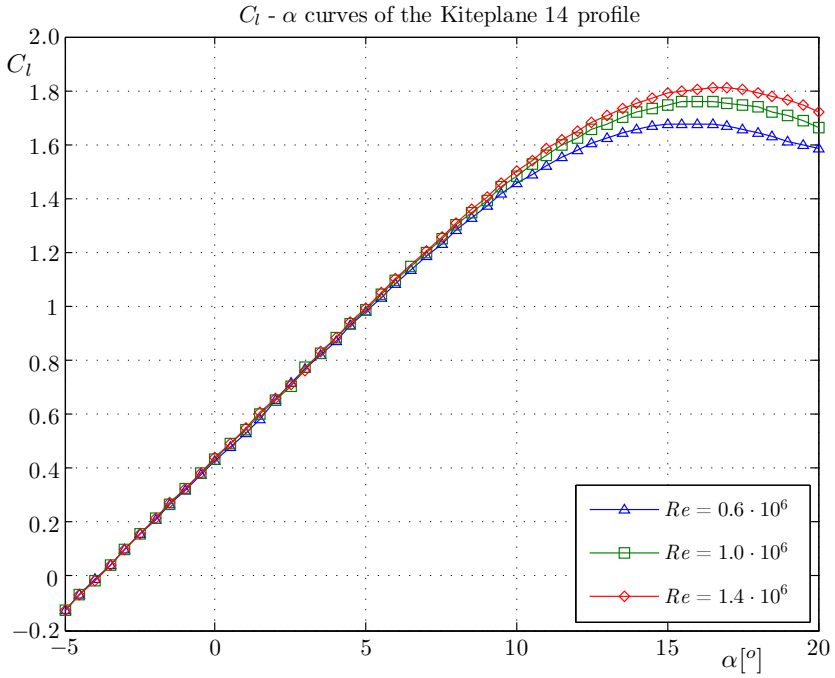

Figure 3.20: $C_l - \alpha$ curves of the 10 kW PowerPlane main wing profile (obtained with XFOIL).

Next to the effect on the lift curve due to viscosity, the drag of the airfoil is also influenced. Since XFOIL concerns a 2D panel method, only the profile drag is determined with the added boundary layer. For the Kiteplane 14 profile, the $C_l - C_d$ curves are shown in figure 6.4. In the next section, it will be explained how these results can also be used as a drag correction in a 3D environment.

3.4.3 Tornado

Tornado is an open-source VLM and is intended for linear aerodynamic wing design applications in conceptual aircraft design or in aeronautical education. The code is implemented in the user-friendly technical computing language Matlab, which makes it relatively easy to understand and adapt. Tornado is widely used at universities and corporations and new functionalities are continuously added. The program was written as a Master thesis by Melin (2000).

Tornado offers the user to choose the direction of the wake: fixed (direction of the chord) or free (direction of the free stream). For discretization, 7 vortex segment panels or standard horseshoe vortices can be used. Multiple wing sections and asymmetrical wings can be defined. A Trefftz-plane analysis tool is implemented. Airfoil sections can be read in via coordinate files (.dat). When Tornado generates output, many screens open simultaneously, which makes it less user-friendly than XFLR5.

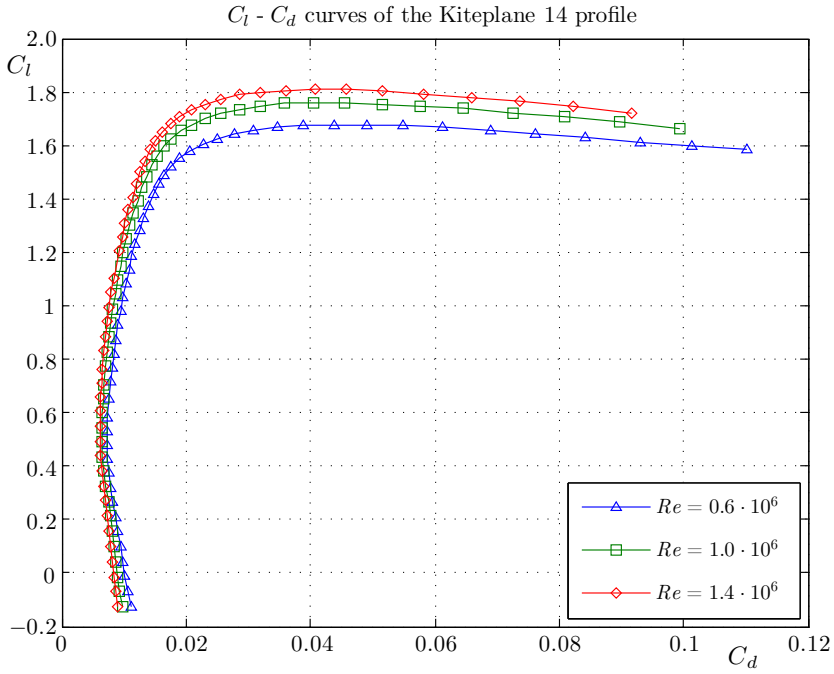

Figure 3.21: $C_l - C_d$ curves of the 10 kW PowerPlane main wing profile (obtained with XFOIL).

3.4.4 XFLR5

A tool that is widely used in the regime of sailplanes is XFLR5 (XFLR5, 2011b). Integrated in this program is XFOIL, which allows one to analyze airfoil sections separately (see section 3.4.2). Originally, Miarex (Sivells & Neely, 1947) was used as the 3D wing analysis program, which is based on LLT corrected with non-linear section lift data as was discussed in 3.1.3. In the last decade the 3D wing analysis feature of XFLR5 expanded and currently incorporates LLT, a VLM as well as a 3D panel method. The code is programmed in C++, one of the most popular programming languages nowadays (TIOBE Programming Community Index, 2009).

XFLR5 offers the possibility to either use horseshoe or quad vortices when using VLM. In the 3D panel method, the wake is modeled as a series of flat panels which extend 100 x MAC (Mean Aerodynamic Chord) behind the wing. Lift and induced drag values are obtained from a Trefftz-plane analysis. The viscous drag is estimated by interpolation of XFOIL pregenerated polars, by using the spanwise lift coefficients resulting from the linear 3D analysis. The wake can be chosen to be fixed or free, as in Tornado.

Considering the meshing of a wing (plus tail), either for the VLM or 3D panel method, several methods are recommended in the guidelines manual that comes with the program (XFLR5, 2011a). In the case of the VLM, an analysis is performed on the mean camber line of the wing and in case of the 3D panel method, an analysis is performed where the wing is modeled as a thick surface. It is advised to consider the following approaches when defining a wing:

- Use a panel distribution where the mesh density near geometrical breakpoints is higher, such as the root and tips of the wings. There is, however, a lower limit size

for the panels. Below this limit, non-physical and unstable results are obtained, by for example using a sine spanwise panel distribution.

- An increased mesh density at the leading and trailing edges can be obtained by using a cosine panel distribution in the chordwise direction. In general, more precise calculations and shorter computational times are obtained with a well refined mesh.
- The aspect ratio of the panels should be low, since large panel length differences in streamwise and chordwise directions can result in numerical instabilities for a 3D panel method analysis.
- Considering a panel method, all corners of each panel should be in the same plane, since first order panels are used. This would imply twisted geometries cannot be analyzed, but since small downwash angles are assumed, the accuracy should still be acceptable.
- Considering the VLM, use the same amount of chordwise panels along the wing span with a similar distribution. This way, all connected panels have the same edges and nodes. The reason for this is because the surface velocity is determined from the gradient of doublet strengths between adjacent panels.

Next to the availability of either the LLT, VLM and 3D panel method, one can also choose to implement inertia properties, viscosity (interpolated from XFOIL curves) and tilted geometry effects. Next to this, 3 polar types can be chosen, considering either fixed speed, fixed lift or fixed angle of attack. One can also choose between 2 different VLM types, which are the horseshoe vortex method (VLM1) and the ring vortex method (VLM2), which are explained in section 3.3.3.

Since these methods are all potential flow based and thus inviscid, only the induced drag part can be determined directly. For this, a Trefftz plane analysis is used, which is a far field method based on the balance of the momentum on a control surface far downstream of the body. As mentioned in the guidelines of XFLR5 (XFLR5, 2011a), it is generally reported that the drag and lift results from near field analysis are significantly higher and less representative than those resulting from a calculation in the Trefftz plane. This is reported for almost all VLM and panel codes (Smith, 1996). The implementation in XFLR5 for the calculation of lift and drag is therefore the far field method.

The main wing profile was already analyzed separately using the XFOIL Direct Analysis tool as shown in section 3.4.2. In order to illustrate the working environment of XFLR5, this airfoil is used to analyze a flat wing with $A = 7.5$ and $Re = 1 \cdot 10^6$. For this, the VLM is used including the profile drag correction where induced drag is determined from a Trefftz plane analysis. For each spanwise station, the 2D profile drag is interpolated from the XFOIL polars with the angle of attack and local Reynolds number. The final result is shown in figure 3.22. Here, the spanwise distribution of lift is indicated in green, downwash in red, induced drag in yellow and profile/viscous drag in pink. Furthermore, pressure distributions per span station, spanwise distributions of each aerodynamic parameter and lift and drag polars can be visualized in the program. Important to mention here, is that the lift curve in the VLM and 3D panel method is inviscid and thus linear, since the viscous correction is only applied to the drag coefficient. For the LLT the lift curve is corrected, but since this method is less accurate and does not take into account effects such as dihedral, sweep and twist, results are expected to be unreliable.

As an extension, a horizontal and vertical tail can be modeled behind the main wing. Also fuselages can be implemented, but it is not recommended, since these are not lifting bodies on which the VLM and 3D panel methods are based (XFLR5, 2011a). Results are therefore expected to be unrealistic, so wing tail configurations are preferred.

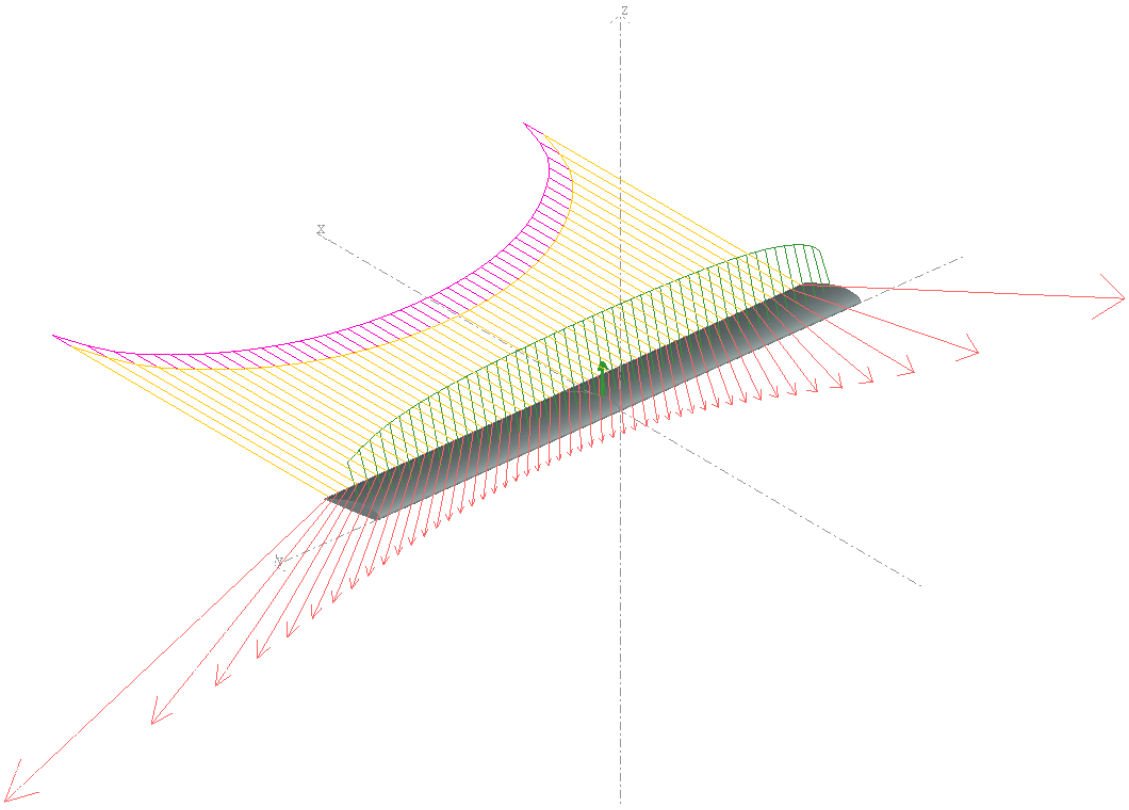

Figure 3.22: Result from a VLM analysis of a flat wing configuration with $A = 7.5$ and $Re = 1 \cdot 10^6$ (obtained with XFLR5).

3.4.5 Athena Vortex Lattice

Athena Vortex Lattice (AVL) is a program used for the analysis of aerodynamics and flight dynamics of rigid aircraft, considering arbitrary configurations (Drela & Youngren, 2011a). It consists of an extended vortex lattice method for lifting surfaces, including a slender body model to analyze fuselages and nacelles. For the purposes of this research, the latter model will be neglected and a wing tail configuration will be considered again. The software is written in FORTRAN77 and can be run as an executable in Windows. XFLR5 models can be exported as an AVL file, saving time on generating all geometry input files, since this is necessary using AVL. As an illustrative example, a wing tail design of the 10 kW PowerPlane is shown in the AVL environment in figure 3.23.

AVL uses horseshoe vortices for surfaces and sources and sinks for bodies. Airfoil sections can be defined for NACA (4 and 5) profiles or coordinate files can be loaded. Using the AVL code, lift and induced drag distributions can be visualized, also resulting from a Trefftz-plane analysis. Comparing these results with those obtained with XFLR5 gives similar results, of which several examples are also shown in the guidelines (XFLR5, 2011a).

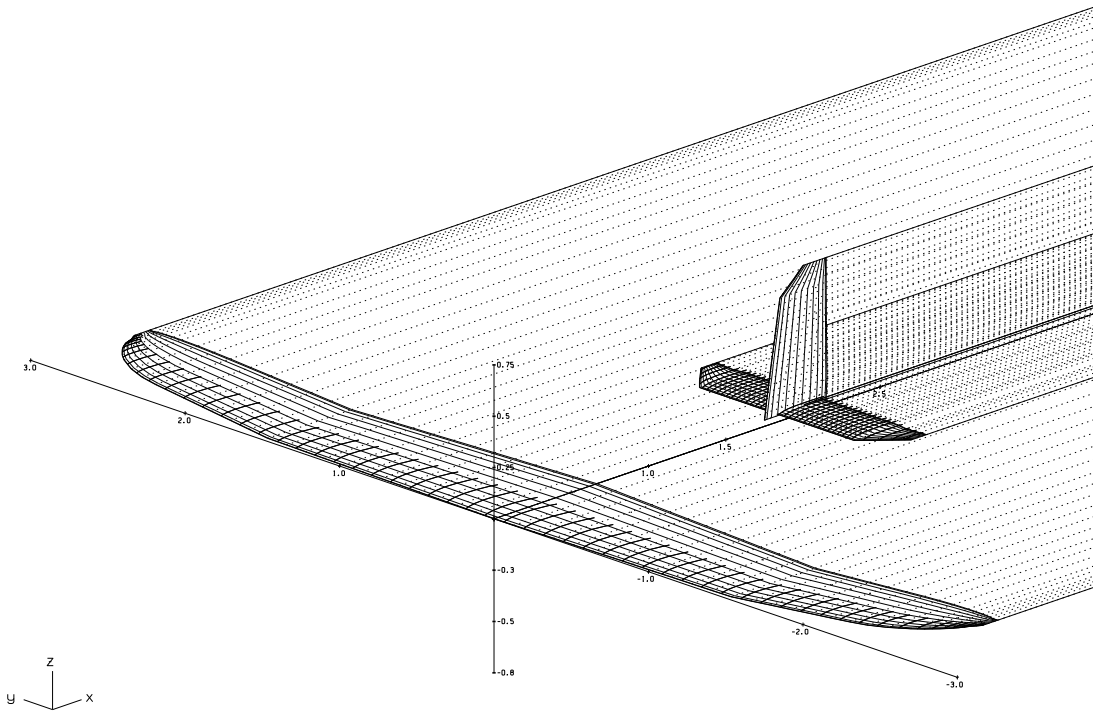

Figure 3.23: Main wing plus tail design of the 10 kW PowerPlane in the AVL environment.

In contrast to XFLR5, AVL does not take into account a profile/viscous drag correction and the results are therefore purely inviscid. Also, calculations can only be performed for one angle of attack, such that obtaining a lift or drag polar requires significantly more effort when compared to XFLR5. And since a GUI is build in XFLR5, models are easier to create, calculate with and analyze.

3.4.6 Project Falcon

Project Falcon is a 2D and 3D wind tunnel simulation program, designed to be used in early conceptual design stages (Autodesk Inc., 2011a). The program is Autodesk software, claiming that Project Falcon uses a revolutionary meshing technique. It should be able to automatically generate a mesh for any geometry at any design stage. Changing the wind speed and direction of the incoming flow should result in an almost real-time update of velocity and pressure distributions around the design.

The solver of this program uses several CFD techniques as stated in the validation manual (Autodesk Inc., 2011b). These contain for example a transient (changing velocity and pressure over time), incompressible (divergence of the fluid velocity is zero) fluid flow solver. Next to this, the Finite Volume Method (FVM) is used in combination with a full 2D and 3D Navier-Stokes fluid solution. Furthermore, a Large Eddy Simulation (LES) turbulence model is used for the turbulent flow behavior. In the validation manual, several examples are shown to compare results with published drag coefficient values of for example the flow around a sphere. These lie within a precision of 93% and higher for these particular examples.

In the program, the inputs are the particular design and the wind velocity and di-

rection. Results can be visualized in 2D or 3D view, being the velocity or pressure distribution. In 3D mode, the stream lines of the flow can be visualized as well. In case of the PowerPlane, or any aircraft, the interest lies in numerical values as resulting from velocity and pressure distributions. Project Falcon, however, gives in the 3D modus only the resulting drag forces and coefficient of the analyzed design. This is probably due to the application of cars, where drag is the most important aerodynamic factor to be reduced. However, as can be seen in figure 3.24, there are examples of aircraft available to analyze with the program, so there might be goals to extend the software with calculations of lifting bodies. But since it does not give any lift forces at the moment and the reliability is doubtful since real-time updating in a CFD solver seems unrealistic, Project Falcon is not useful for this research.

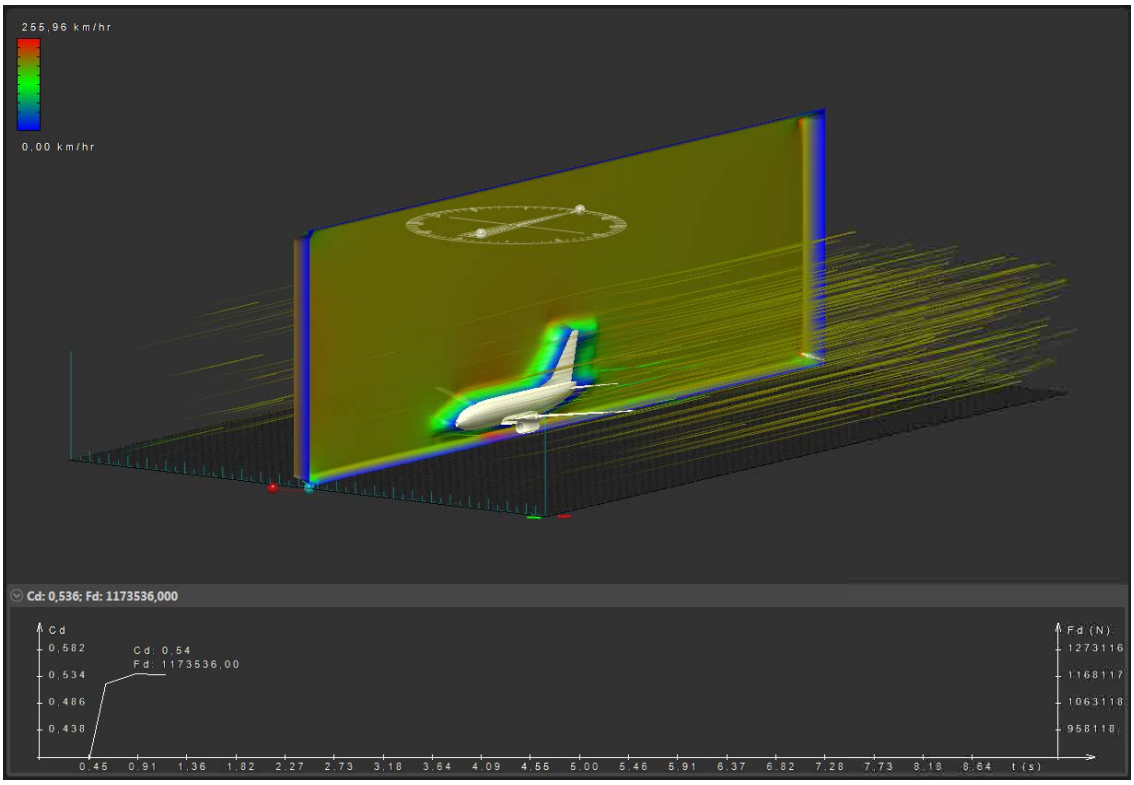

Figure 3.24: Example of an aircraft analyzed in 3D mode with Project Falcon.

Chapter 4

Methodologies to correct for thickness and viscosity

Regarding the aerodynamic tool study in the previous chapter, XFLR5 is chosen to work with. By default, the VLM and 3D panel method ignore profile drag, though XFLR5 uses interpolation on predetermined 2D viscous lift to drag polars. This determination of profile drag is dependent on the calculated lift values of the 3D analysis method, since lift and drag are directly related to each other. Certainly for the PowerPlane, which mostly flies around its maximum lift coefficient, it is of great importance to accurately determine the aerodynamics in the non-linear range of the lift curve. In this chapter, methodologies that use a lift correction to implement this non-linear behavior are investigated. Two methods are found in literature, on which several interpretations resulted in a set of different algorithms. The main differences are the use of induced angles and one iteration of the proposed angle shift (Horsten & Veldhuis, 2009) and avoiding to calculate induced angles every iteration and iterate until convergence (Gaunaa et al., 2010; Carqueija et al., 2010). Also, the profile drag in these methods is determined in another manner.

4.1 Implementing non-linearity by using lift correction

Since 3D panel methods and VLM's are inviscid methods, significant viscous phenomena such as boundary layer transition and separation are neglected. In the VLM a mean camber line is used and thus thickness effects are neglected. The assumption of neglecting viscosity and thickness will affect lift and drag values. Especially when non-linear behavior occurs, such as separation in the high angle of attack region, calculated values will deviate significantly from reality. By making use of viscous 2D airfoil calculations, lift corrections on multiple spanwise sections can be implemented in a 3D analysis. Though any 2D airfoil data source could be used, in the validation of the methods a 2D panel method called XFOIL is used (Drela & Youngren, 2011b). In this tool, boundary layer equations and a turbulence model (e^n method) are used to take into account viscous effects, such as a boundary layer thickness, transition, separation and laminar separation bubbles. Before explaining the method used to perform such a correction, the definition of the effective angle of attack is explained, which is required for the lift correction methods.

4.1.1 Effective angle of attack

By definition, the lift force acting on a wing is directed perpendicular with respect to the velocity vector. In case the wing is under an angle of attack, the lift vector should not be taken perpendicular with respect to the free stream velocity vector, V_∞, but with respect to the induced velocity vector, v_i. This is the vector which is deflected with a downwash angle (or induced angle of attack). As a result, the direction of the lift force is also deflected by this angle, as illustrated in figure 4.1. It can be seen that this will reduce the magnitude of the lift force, which is therefore called the effective lift. Since the airflow has already been deflected with the induced angle, this angle is not effective in terms of lift production. Therefore, the effective lift is caused only by the difference between the airflow direction and the airfoil, which is called the effective angle of attack.

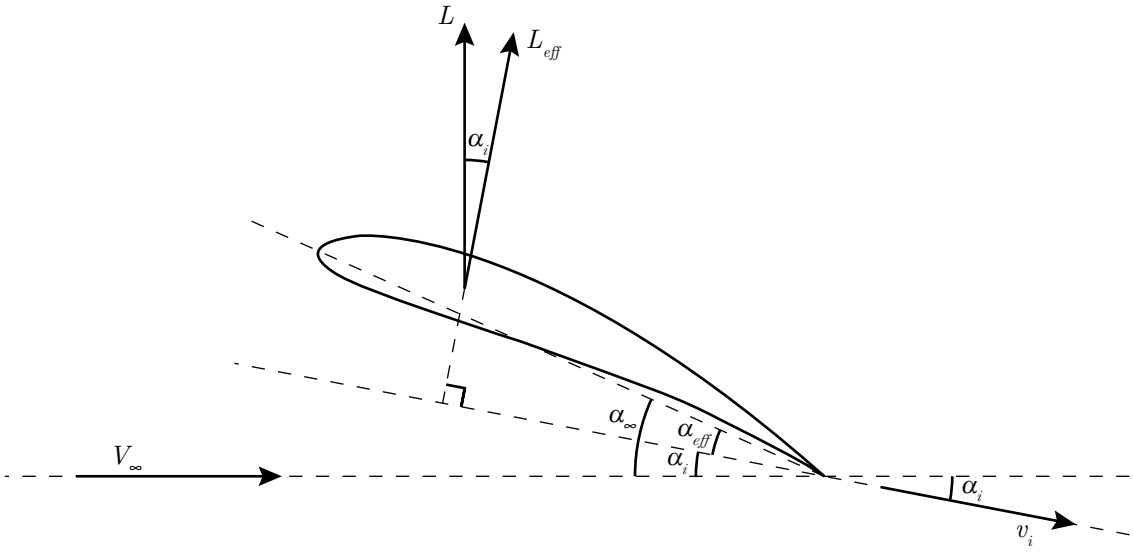

Figure 4.1: Definition of the effective angle of attack, induced angle of attack and effective lift vector.

Adding a spanwise twist distribution to the wing can be used to reduce the lift and induced drag near the tips. Taking this into account, the effective angle of attack of an airfoil is defined as

$$\alpha_{eff} = \alpha_\infty - \alpha_i + \alpha_{twist} \tag{4.1}$$

4.1.2 Angle shift on lift curve

For the effective angle of attack seen by a section, which is dependent of the downwash created by the trailing wake, the inviscid and viscous lift coefficients can be determined by making use of XFOIL. In figure 4.2, an example is shown of such an inviscid and viscous $C_l - \alpha$ polar. To account for viscosity in a 3D analysis, a shift on the initial effective angle, $\alpha_{eff,original}$, is performed. Now, the airfoil works at an angle of attack which has the same lift coefficient as the viscous lift coefficient before the angle shift, called $\alpha_{eff,new}$. This can also be defined as shown in equation 4.2, where $\alpha_{eff,original}$ is defined as in equation 4.1 and α_s represents the angle shift.

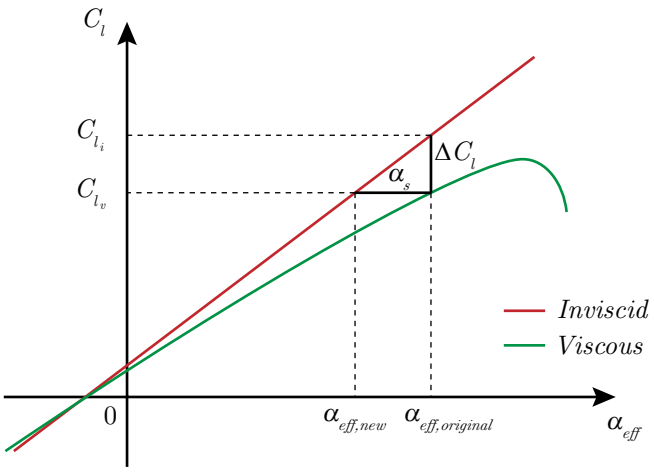

Figure 4.2: Angle shift correction method on 2D lift polars to account for viscous effects in a 3D analysis.

$$\alpha_{eff,new} = \alpha_{eff,original} - \alpha_s \tag{4.2}$$

This method assumes implicitly that the airfoil's behavior on a finite wing is not very different than on an infinite XFOIL wing. There is no real background, neither theoretical nor experimental, to support this approach, so it should be used with caution. However, the results of Horsten (initial proposer of this method) and Gaunaa show improvement on the results when compared to experimental and CFD data.

4.2 3D analysis methodology

In the previous section, the principle of using angle shifts to correct 3D potential flow methods is explained. Both Horsten (Horsten & Veldhuis, 2009) and Gaunaa (Gaunaa et al., 2010) use this method to correct a VLM, each having different characteristics. In this section, these variants are discussed followed by the explanation of the newly developed algorithm.

4.2.1 Reference literature on lift correction methods

As mentioned before, two papers are found that consider the use of angle shifts for lift correction: Horsten (Horsten & Veldhuis, 2009) was the initial proposer of this method, followed by Gaunaa et al. (2010) who developed an equivalent algorithm in coorporation with Carqueija et al. (2010), though based on different calculations.

The applications used to validate their methods are a planar wing in the case of Horsten and a highly non-planar (circular arc shaped) kite in the case of Gaunaa. They use different programs for the implementation of their methods: Horsten uses Athena Vortex Lattice (AVL) with a 2D viscous airfoil calculation in XFOIL, while Gaunaa combines a VLM written earlier by himself with XFOIL. However, Gaunaa states that 2D airfoil data from any other source works as well. This is shown in his validation, where he actually uses CFD results. The use of XFOIL is on the one hand fast and accurate in

the low angles of attack range. On the other hand, it uses models for transition, separation and boundary layer behavior, which can be inaccurate in certain cases. Therefore, the possibility to use other 2D airfoil data seems useful when for example CFD or experimental data is available.

To account for viscosity, a shift on the initial effective angle is performed (see section 4.1.2). Therefore, the calculation of the effective angle will have large impact on the quality of results. The definition, as shown in equation 4.1, is based on geometrical input, free stream input and resulting induced angles. Horsten determines the induced angles with a Trefftz plane calculation. Gaunaa bases the induced angles on the spanwise lift distribution and thin airfoil theory. Furthermore, they use different implementations of the angle shift: Horsten uses a geometrical change by applying twist, while Gaunaa changes the local inflow angle on every spanwise section. The latter method is significantly more efficient in terms of computational effort. In the method of Gaunaa, iteration until convergence is used, whereas Horsten only uses one iteration of the correction. For the determination of the viscous drag, Horsten uses the final effective angle of attack after the angle shift. Gaunaa, however, uses the initial effective angle of attack, before the angle shift.

4.2.2 Determination angle shift: 3D panel method vs VLM

The proposed correction method by Horsten is to correct a VLM for viscosity effects. Gaunaa states that his correction method introduces the effect of airfoil thickness and viscosity.

The angle correction is based on the difference between a viscous and inviscid 2D panel method calculation. Both these calculations include the thickness of a profile and thus the difference does not include a thickness correction. If, however, thin airfoil theory (TAT) would be used to calculate the inviscid lift curve, Gaunaa's statement is correct in the sense that there is a correction for both thickness and viscosity. Therefore, such a method would in theory be more appropriate when correcting a VLM, since it is only applicable for thin surfaces. The method where only viscosity is corrected would be appropriate for a 3D panel method. This viscous/thickness effect methodology is illustrated in figure 4.3.

4.2.3 Implementation in XFLR5

From the discussed methods and theories, several options for using angle shifts are available. These combinations are not purely theoretical, but represent artificial methods to correct for thickness and viscosity. One can choose between the following options concerning the method of angle shift correction:

- Angle shift calculation:
  - TAT vs XFOIL
  - Induced angle calculation
- Potential flow method: VLM vs 3D panel method
- Number of iterations: convergence vs limited
- Implementation angle shift: RHS vs geometry

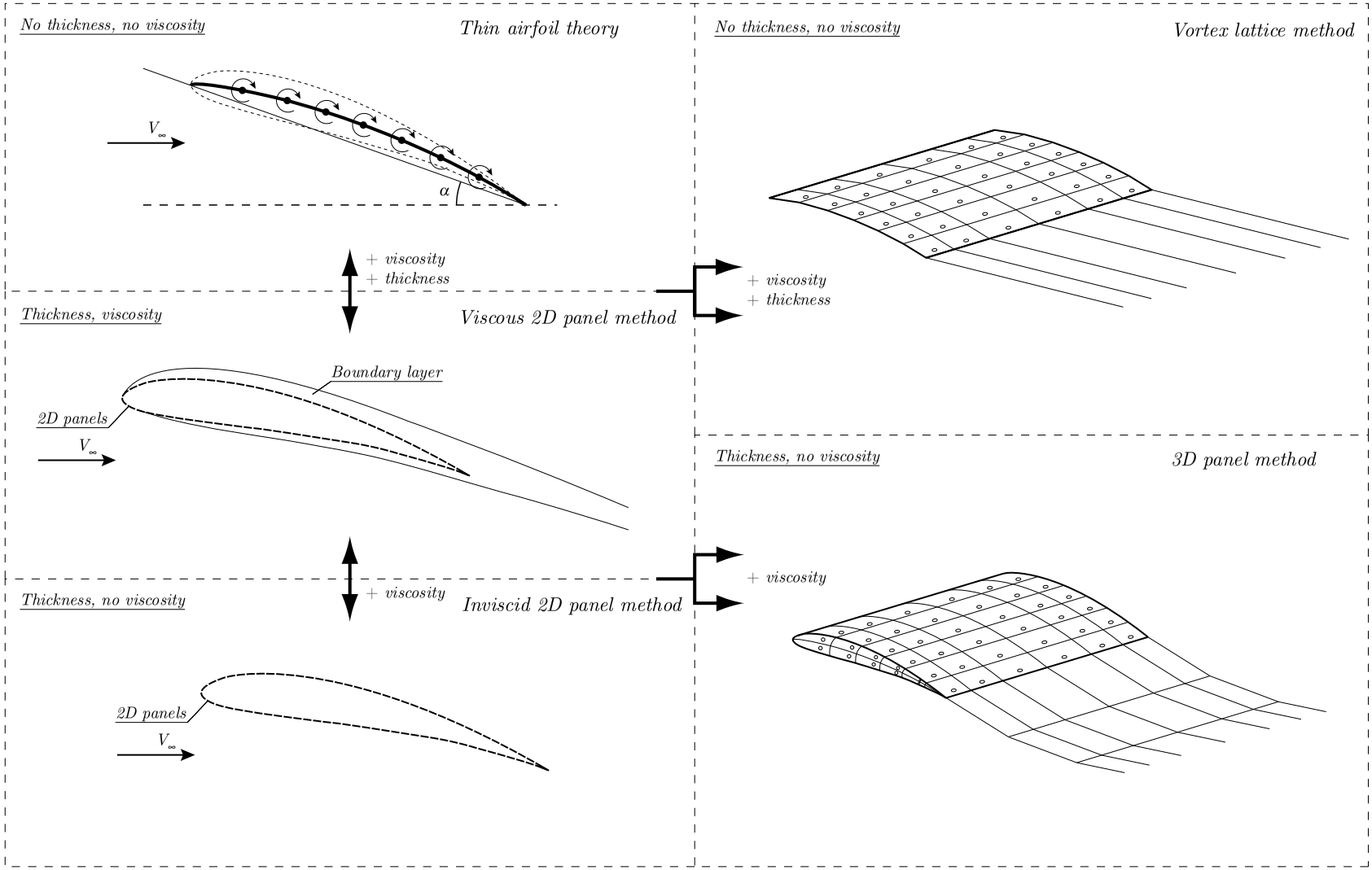

Figure 4.3: Correction methods concerning viscous and thickness effects using thin airfoil theory and a 2D panel method for a 3D VLM and panel method.

- Viscous drag calculation: initial vs final α_{eff}

The angle shift method is implemented in XFLR5 and above mentioned options are made available, except for the angle shift implementation. For this, changing the local inflow angle defined at the RHS is used, because it is more efficient in terms of computational effort. The determination of the angle shifts is the core of the program, therefore two algorithms similar to Horsten and Gaunaa's methods are constructed in which the remaining options can be adjusted. The used program structures by Gaunaa and Horsten are given below. Furthermore, the complete program overview in XFLR5 is visualized in figure 4.4. As mentioned before, Gaunaa uses thin airfoil theory, hence $C_{l_\alpha} = 2\pi$.

Method of Horsten

1 Perform an inviscid VLM calculation and calculate the induced angles in the Trefftz plane

2 Calculate $\alpha_{eff} = \alpha_\infty + \alpha_i + \alpha_{twist}$

3 Determine angle shift $\alpha_s = \frac{\Delta C_l}{C_{l_\alpha}}$

4 Add α_s to RHS

5 Return to step 1 and iterate until convergence or a predefined iteration limit

6 Use final α_{eff} to calculate profile drag

Method of Gaunaa

1 Perform an inviscid VLM calculation and save the $C_{l,original}$ for each section along the span

2 Initialize $\Delta\alpha_i$ as equal to zero

3 Find α_{eff} each section, from: $\alpha_{eff} = \frac{C_{l,original}}{C_{l_\alpha}} + \alpha_0 - \Delta\alpha_i$

4 Calculate angle shift $\alpha_s = \frac{\Delta C_l}{C_{l_\alpha}}$

5 Add α_s to RHS

6 Perform new VLM calculation and save for each section along the span the new lift coefficient $C_{l,final}$

7 Calculate $\Delta\alpha_i = \frac{C_{l,original} - C_{l,final}}{2\pi} - \alpha_s$

8 Return to step 3 until convergence or a predefined iteration limit

9 Use initial/final α_{eff} to calculate profile drag

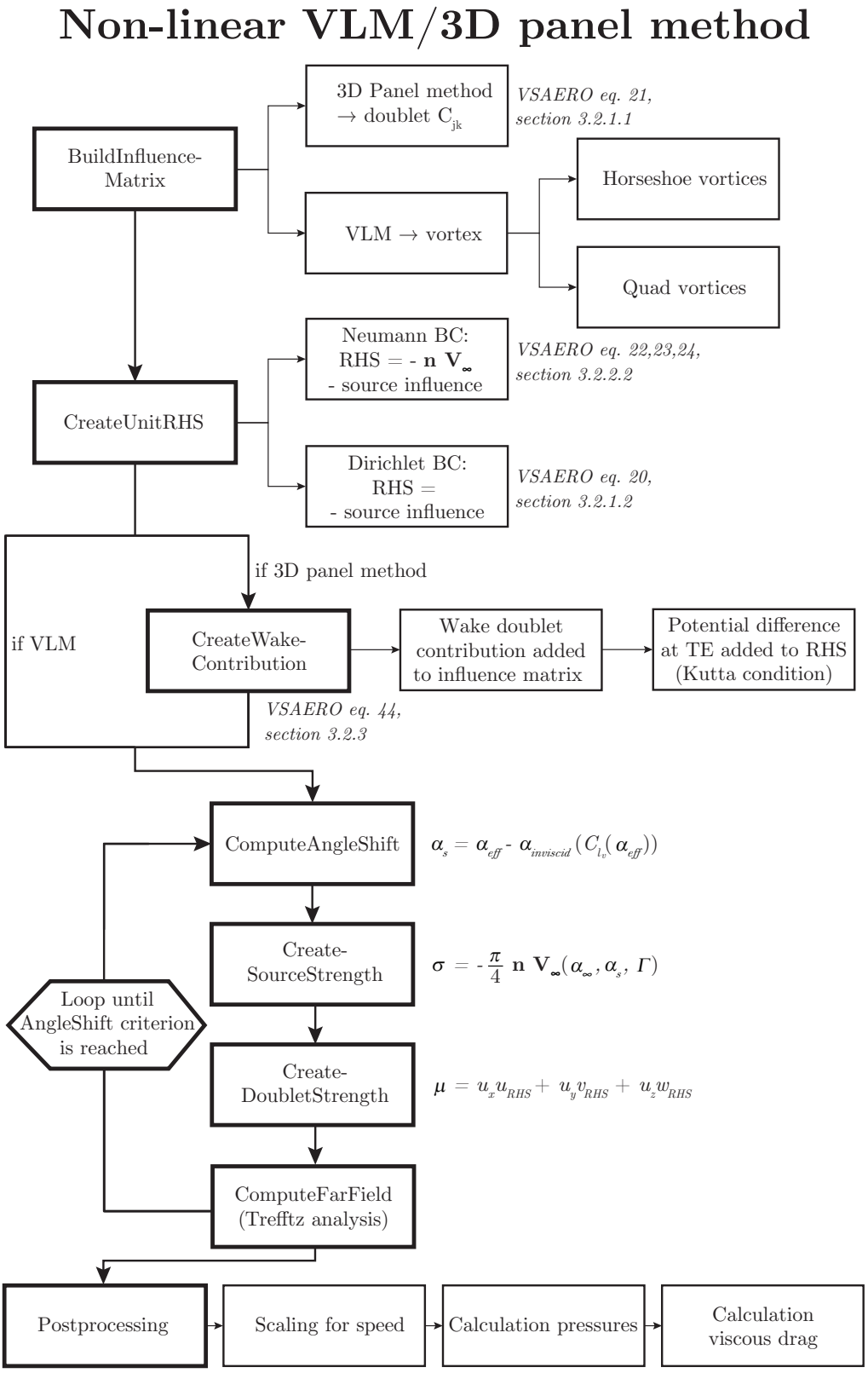

Figure 4.4: Flow diagram of the adapted XFLR5 program structure.

4.3 Program features of the adapted XFLR5 software

Besides the implementation of the angle shift methods, a number of other features have been included in the adapted XFLR5 program. In this section, these adjustments are presented.

4.3.1 Inviscid 2D lift curve

When determining the angle shifts, both viscous as inviscid lift curves of the airfoils are required. A practical issue is that the build in XFOIL version in XFLR5 is not capable of determining inviscid lift values and polars, though the stand alone version of XFOIL is capable. This feature has been added in the adapted XFLR5 version such that also the inviscid lift value and inviscid $C_l - \alpha$ curve are automatically generated when doing viscous XFOIL calculations. The function for linear interpolation between different airfoil curves and Reynolds numbers is also added for the inviscid lift curves.

When using TAT for the determination of angle shifts, an external program was used, written in Matlab. XFLR5 is adapted such that external inviscid lift values can be imported from simple text files. The theory of the TAT programs can be found in section 3.2.

4.3.2 Trefftz plane calculations

By standard, the induced angles in XFLR5 are measured in the $x-z$ plane, therefore not taking into account out of plane sections. In the adapted version, the induced angles are calculated normal to a section. The induced angle is determined as shown in equation 4.3, where w represents the downwash and v is the induced velocity. In this section, it is explained what procedure is used to adapt the induced velocity components.

$$\alpha_i = \frac{w}{v} \tag{4.3}$$

An incoming airflow under some angle of attack, α, can be decomposed in two dimensional velocity vectors in the x and z direction, as shown in figure 4.5.

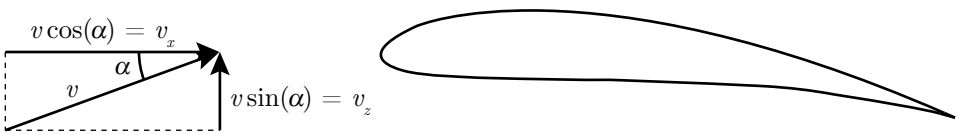

Figure 4.5: Two dimensional airflow acting on an airfoil with a local angle of attack, α.

In case of dihedral on the wing, the components of the velocity vector acting perpendicular to this deflected geometry are required to obtain the exact three dimensional total velocity vector. This can be determined with a simple model in the $y-z$ plane (front view), as shown in figure 4.6. Here, the two dimensional z component is projected on a wing section with a certain dihedral, Γ, together with its perpendicular component with respect to the wing surface.

Using the geometry, one can find relations for the y and z components of this perpendicular velocity vector. Now, including the effect of dihedral, the total velocity vector (or

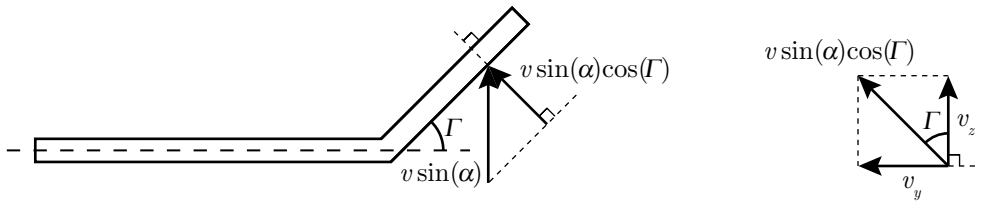

Figure 4.6: Perpendicular velocity vector projected on the wing dihedral.

wind direction) is defined as

$$\mathbf{v_w} = \begin{bmatrix} vcos(\alpha) \\ vsin(\alpha)cos(\Gamma)sin(\Gamma) \\ vsin(\alpha)cos^2(\Gamma) \end{bmatrix} \begin{bmatrix} x \\ y \\ z \end{bmatrix} \tag{4.4}$$

From this, the vector perpendicular to the wind direction and the wing surface can be determined, which is called the wind normal vector. Considering a spanwise section of the dihedral wing as a two dimensional vector (no sweep), the wind normal vector can be computed by means of the cross product method. In other words, this is solving the determinant of the three dimensional velocity vector matrix for both vectors. Considering all three components ($\mathbf{i}$, $\mathbf{j}$, $\mathbf{k}$) of two vectors, which are in this case the wind direction vector and spanwise dihedral wing, the wind normal vector acting in perpendicular direction on both vectors can be determined as

$$\begin{aligned}
\mathbf{v_n} &= \mathbf{v_w} \times \mathbf{\Gamma} \\
&= \begin{vmatrix} \mathbf{i} & \mathbf{j} & \mathbf{k} \\ cos(\alpha) & sin(\alpha)cos(\Gamma)sin(\Gamma) & sin(\alpha)cos^2(\Gamma) \\ 0 & cos(\Gamma) & sin(\Gamma) \end{vmatrix} \\
&= \begin{vmatrix} sin(\alpha)cos(\Gamma)sin(\Gamma) & sin(\alpha)cos^2(\Gamma) \\ cos(\Gamma) & sin(\Gamma) \end{vmatrix} \mathbf{i} + \begin{vmatrix} cos(\alpha) & sin(\alpha)cos^2(\Gamma) \\ 0 & sin(\Gamma) \end{vmatrix} \mathbf{j} \\
&+ \begin{vmatrix} cos(\alpha) & sin(\alpha)cos(\Gamma)sin(\Gamma) \\ 0 & cos(\Gamma) \end{vmatrix} \mathbf{k} \\
&= \left[sin(\alpha)cos(\Gamma)\left(sin^2(\Gamma) - cos^2(\Gamma)\right)\right] \mathbf{i} + \left[cos(\alpha)sin(\Gamma)\right] \mathbf{j} + \left[cos(\alpha)cos(\Gamma)\right] \mathbf{k}
\end{aligned} \tag{4.5}$$

Thus, the velocity vector normal to the section and to the free stream velocity vector is defined as

$$\begin{aligned}
\mathbf{v_x} &= sin(\alpha)cos(\Gamma)\left(sin^2(\Gamma) - cos^2(\Gamma)\right) \\
\mathbf{v_y} &= cos(\alpha)sin(\Gamma) \\
\mathbf{v_z} &= cos(\alpha)cos(\Gamma)
\end{aligned} \tag{4.6}$$

The wind normal vector effects the induced angle of attack (or downwash angle), and will therefore change the effective angle for panels with dihedral.

From performed simulations on a flat wing configuration, results from the VLM showed induced angle distributions with values twice as large with respect to the 3D panel method. From theory, the LLT should give rather accurate results for a flat wing. Therefore, the induced angle distributions are compared with LLT and it showed that the 3D panel method results were similar. An error was present in the calculation of the induced angles and was solved by dividing the induced angle calculations in the VLM code by 2.

4.3.3 Local effective angle of attack

As given in equation 4.1, the definition of the effective angle of attack is

$$\alpha_{eff} = \alpha - \alpha_i + \alpha_{twist}$$

Here, α is the local free stream angle of attack and therefore dependent on dihedral, as shown in equation 4.7.

$$\alpha_{local} = atan(tan(\alpha)cos(\Gamma)) \tag{4.7}$$

The induced angle of attack is already defined perpendicular to the panel normal as described in section 4.3.2. Note that side slip angles are not included in the equations. This is because these are by default implemented in XFLR5 by changing the geometry.

4.3.4 Implementation angle shift

In section 4.3.2, a dihedral effect was implemented on the induced angle calculations. A similar approach is used to add the angle shift to the RHS. The RHS represents the free stream velocity normal to a panel. This is normally defined as a scalar V_∞ multiplied by a vector containing all panel normals. By adding an angle shift to each spanwise station, the scalar V_∞ becomes a vector acting as a local free stream velocity vector varying in spanwise direction. Here, the local velocity is changed by including an angle shift and is therefore dependent on dihedral. This results in a new local velocity as shown in equation 4.8, where α_s represent the angle shift.

$$\begin{aligned} \mathbf{u_x} &= cos\left(\alpha_s sin(\Gamma)\right) cos\left(\alpha + \alpha_s cos(\Gamma)\right) \\ \mathbf{u_y} &= cos\left(\alpha + \alpha_s cos(\Gamma)\right) sin\left(\alpha_s sin(\Gamma)\right) \\ \mathbf{u_z} &= cos\left(\alpha_s sin(\Gamma)\right) sin\left(\alpha + \alpha_s cos(\Gamma)\right) \end{aligned} \tag{4.8}$$

4.3.5 Viscous drag calculation

In the original version of XFLR5, the profile drag is based on an interpolation of the $C_l - C_d$ curves from a 2D analysis. This can result in difficulties at high angles of attack, since at certain lift values it is possible to have two solutions of the viscous drag: one corresponding to the value before stall and the other beyond stall. Therefore, in the adapted version, it is avoided to use the lift coefficient when determining profile drag. Instead, the effective angle of attack is used to determine the viscous drag in the $C_d - \alpha$ curve.

In his method, Gaunaa (Gaunaa et al., 2010) calculates the profile drag for the original (initial) effective angle of attack, thus also using the original induced angle of attack. It is however preferred to incorporate the induced values based on calculations including viscous effects and thus the final induced angle of attack should be used when computing the sections effective angles of attack (similar to Horsten's algorithm). Similar as mentioned in sections 4.3.2 and 4.3.4, the effective angle is determined perpendicular to each spanwise section.

4.4 Program settings

A number of adjustments have been performed on the original XFLR5 program so far. In the uncorrected version, several settings significantly affect the results of 3D analyzes. The most important are discussed in this section, using knowledge both from the XLFR5 guidelines and by testing the software.

4.4.1 Grid discretization study

How grid size influences computational time is visualized in figure 4.7. VLM2 is slightly faster than VLM1, since it has less computational heavy horseshoe vortices to calculate. The 3D panel method requires significantly more processing time than the VLM's, probably because it uses paneling of the wake. The curves of the 3D panel method extend further than the VLM's, since for the same discretization roughly twice the number of panels is required (upper and lower camber lines). Regarding accuracy, as shown in figure 4.7, it can be stated that not much gain can be obtained by using grid sizes of more than 1,000 panels. From investigations followed that the type and number of paneling used in chord and spanwise direction can significantly influence lift values. Note that in these considerations 'Tilted Geometry', i.e. a free wake, was used (except for the determination of lift values for the 3D panel method since this was not working in the investigated version of XFLR5). When this option is disabled the gains of using VLM2 instead of VLM1 for full angle sweeps is many times higher.

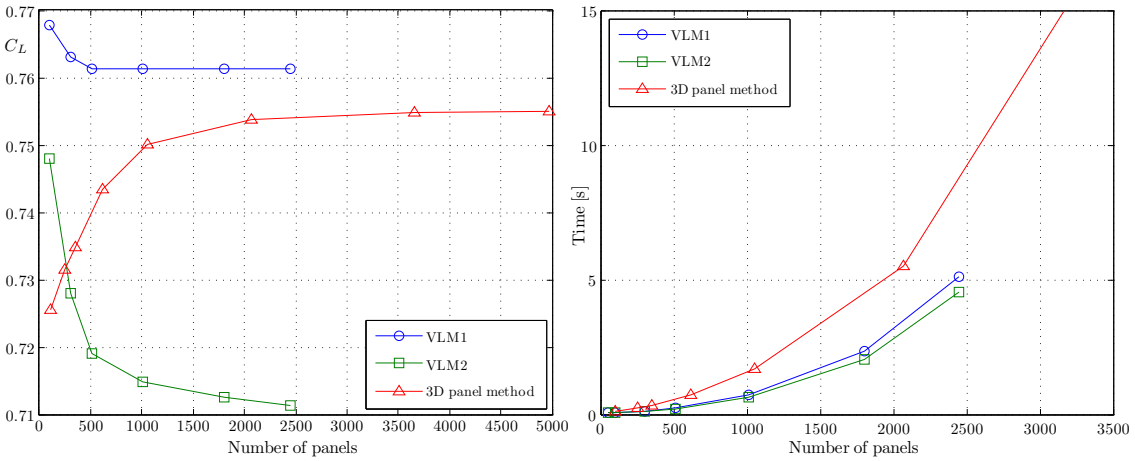

Figure 4.7: Effect of the number of panels on the accuracy and computational time for a flat wing (see section 5.2.1), using inviscid calculations.

4.4.2 Boundary condition

For the VLM, the Neumann BC is the only option. Considering available BC's for the 3D panel method, the options are the Neumann BC and the Dirichlet BC. There is no significant difference in calculation time and lift and drag values are approximately the same (less than 1% smaller). The guidelines of XFLR5 say: "After a trial and error process, the Dirichlet BC have been preferred to the Neumann BC. The latter method is more sensitive to local geometry changes, and leads to less convincing results. This is also the choice which is implied in reference (Maskew, 1987)." Therefore Dirichlet BC will be used in future calculations.

4.4.3 Wake direction

Another calculation setting which can be altered is to use 'Tilted Geometry' (TG) which means the wake is in the direction of the flow and not simply parallel to the body's x-axis (see figure 4.8). When applied in the 3D panel method, all values are totally off. This bug has been reported and is fixed in the new version XFLR5 6.07. It was observed from simulations, that the inviscid VLM lift curves were slightly non-linear without using the TG option. With TG on, the lift slope became more linear. The remaining non-linearity is probably due to discretization errors. Since TG on is more realistic, this option will be used for the VLM.

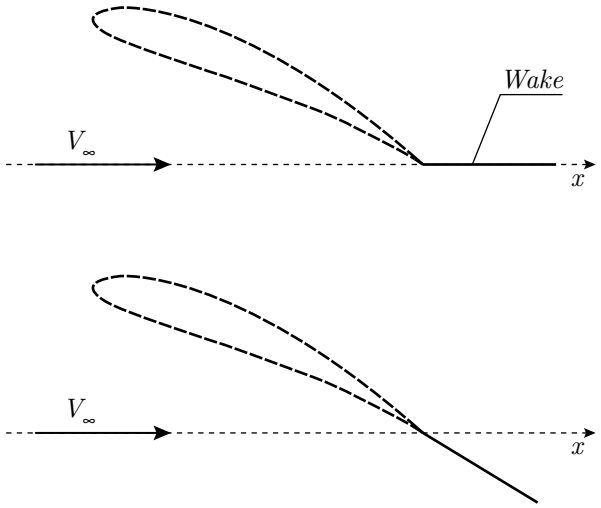

Figure 4.8: Placement of wake direction with (bottom) and without (top) using the tilted geometry setting.

4.4.4 Applying twist

A new definition of applying twist to the wing is implemented in the code, since the definition was incorrect for out of plane sections. In the definition, it is assumed twist is applied linear to the panel.

In the XFLR5 version used to implement the algorithms, it was noticed that applying twist makes the chord length smaller and thus local C_l larger. This is a small error in the software, which is fixed in the new version XFLR5 6.07.

Chapter 5

Software validation and selection

In order to prove the quality of the adapted aerodynamic tool, the software needs to be validated to evaluate the performance on different wing configurations. Considering a sailplane, the most important configuration parameter is a high aspect ratio. Furthermore, dihedral effects become important in case winglets are considered as an addition. Considering a surf kite, configurations with dihedral, small aspect ratio and sweep are of high interest. Multiple cases are found in literature from which experimental wind tunnel data is known. As a result of different theories, 4 versions of the program are created, which gives a great number of simulation data. In this chapter, the trade-off process performed to come up with the most promising method(s) is explained, with a more detailed validation for the final version(s).

5.1 Program versions

Several options are considered with use of the methods described by Gaunaa (Gaunaa et al., 2010) and Horsten (Horsten & Veldhuis, 2009). Four different versions are investigated:

1. Methods of Gaunaa with original effective angle of attack used for viscous drag calculation, as is proposed by Gaunaa. In these methods, induced angles are implicitly determined from lift values. Also, iteration until convergence is used for these versions.

   (a) Version MG: based on difference between inviscid and viscous lift curve, where a inviscid lift slope value of 2π is used corresponding to thin airfoil theory. This version is therefore equivalent to that of Gaunaa. For the inviscid lift curve Gaunaa originally uses XFOIL's calculation, this will be indicated with version MG (XFOIL). Another possibility is to use TAT to determine the inviscid lift curve, this will be indicated by version MG (TAT).

   (b) Version MG_a: based on interpolation between inviscid and viscous lift curve and corresponding inviscid lift slope, which can be different than 2π since XFOIL's inviscid calculation includes thickness. Using TAT for the inviscid lift curve would be equivalent to version MG (TAT) and is therefore omitted.

2. Version MG_b: same as method of Gaunaa, version MG, but with final effective angle of attack used for viscous drag calculation. Using TAT for the inviscid lift curve would be equivalent to version MG (TAT) and is therefore omitted. Also, iteration until convergence is used in this version.

3. Version AK: this version is based on the method of Horsten, for which the inviscid lift curve from XFOIL is used (as in MG_a). The viscous drag is determined as done with version MG_b, using the final effective angle of attack. Induced angles are determined with Trefftz plane calculations and 1 iteration of the angle shift loop is used.

5.2 Experimental wind tunnel data

From experimental wind tunnel data and CFD results found in literature, four cases are selected to validate the aerodynamic analysis tool and choose the most promising version(s). First of all, a simple flat wing with no taper, twist or dihedral is used to also compare results with the algorithm of Horsten. This is followed by a set of 4 swept wings, which differ in airfoil section (symmetrical and cambered) and aspect ratio. The third case is again a straight wing on which a winglet is mounted in a range of different dihedral angles. This could be seen as a step towards an arc shaped (induced drag minimizing) wing, which is treated in the fourth case. Since this is the model used by Gaunaa to validate his work, the version in which his algorithm is processed (MG) can be validated.

5.2.1 Flat wing

The first validation case is the wing configuration found in the work of Horsten (Horsten & Veldhuis, 2009), and used for academic experiments at the Delft University of Technology. It concerns a planar wing with no sweep, twist and taper. Experimental data from this configuration is obtained for $Re = 1 \cdot 10^6$. The wing profile used is the NACA - 64_2(A)015, from which the coordinates and 2D wind tunnel data for $Re = 1 \cdot 10^6$ are known (Wirsing, 1999). The wing properties are shown in table 5.1 and a 3D model in XFLR5 can be seen in figure 5.1.

Table 5.1: Flat wing configuration parameters.

Parameter	**Value**
Airfoil	NACA - 64_2(A)015
Reynolds number	$1 \cdot 10^6$
Wing span	1.28 m
Chord length	0.24 m
Surface area	0.31 m^2
Aspect ratio	5.3

Wind tunnel data from this configuration is uncorrected for wake blockage effects due to wall interference. This could have an impact on the resulting lift coefficient. Therefore,

a correction factor for 3D models in a rectangular closed wind tunnel is considered to verify the influence for this particular case. The wake blockage factor is defined as (Garner et al., 1966)

$$\varepsilon_b = \frac{1}{4}\left(\frac{S}{bh}\right)\frac{1}{\beta^2}C_D \tag{5.1}$$

Here, S is the wing surface area, b and h are the width and height of the wind tunnel, respectively, β is the Prandtl-Glauert compressibility factor and C_D is the corresponding drag coefficient. Inserting the required parameters results in

$$\varepsilon_b = \frac{1}{4}\left(\frac{1.28 \cdot 0.24}{1.25 \cdot 1.80}\right)\frac{1}{1-\left(\frac{62.5}{340}\right)^2}C_D = 0.0353C_D$$

The drag coefficient is in the range of $0.006 < C_D < 0.12$, so the correction factor is of negligible value ($< 0.5\%$). Thus no adjustments have been done on the lift curve values. The drag coefficient polar, however, shows an increased constant value. This is due to the profile drag of the plate where the model is attached to. Wind tunnel tests have been performed while covering this plate, which showed a drag reduction of 0.0092 and is verified by Veldhuis. This value is therefore subtracted from the wind tunnel data. A significant increase in accuracy of the XFLR5 simulations was obtained due to this correction.

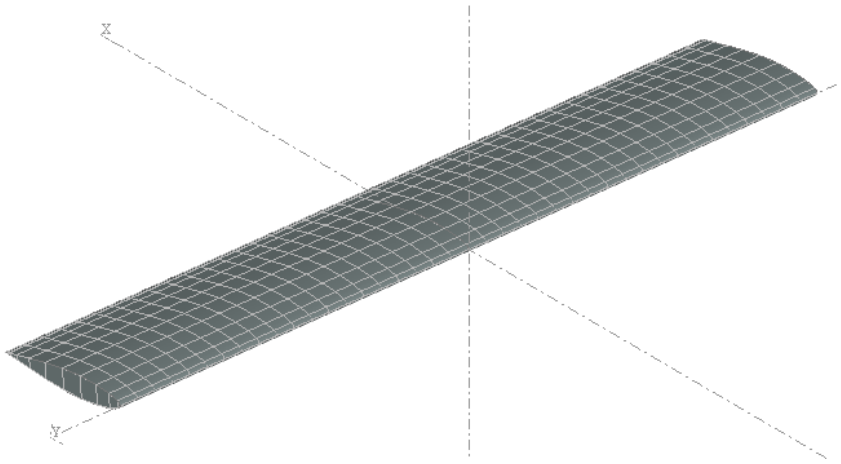

Figure 5.1: Flat wing configuration in XFLR5.

5.2.2 Swept wings

The second case considers 4 planar wings (Tinling & Kolk, 1951), which all have the same sweep angle of 35^o, but vary in aspect ratio ($A = 5$ and $A = 10$), and in airfoil section, namely the NACA - 65_1(A)012 (uncambered) and NACA - 64_1(A)612 (highly cambered). The considered airfoil sections are shown in figure 5.2. With these configurations, the effect of sweep, aspect ratio, as well as the effect of camber are taken into account. Both Reynolds number as Mach number are variated in these cases, which are $2 \cdot 10^6 < Re < 10 \cdot 10^6$ and $0.25 < M < 0.92$. For the application of sailplanes and surf kites only low Mach numbers are present. In case of the 10 kW PowerPlane, Reynolds numbers are in

general between $0.3 < Re < 1 \cdot 10^6$, whereas the 25 m^2 surf kite of ASSET considers a region of $1 \cdot 10^6 < Re < 3 \cdot 10^6$. Therefore, only the case where $M = 0.25$ and $Re = 2 \cdot 10^6$ is considered for validation.

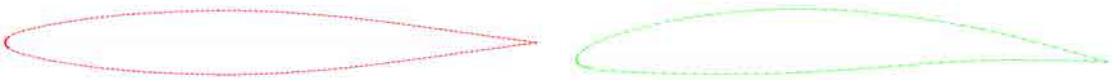

(a) Symmetrical airfoil (b) Cambered airfoil

Figure 5.2: A symmetrical NACA - 65_1(A)012 and highly cambered NACA - 64_1(A)612 airfoil section used for the swept wing configurations.

The configuration parameters of each aspect ratio wing are shown in table 5.2 and the 3D model in XFLR5 of the configuration with $A = 10$ and cambered profile is shown in figure 5.3. The cambered profile is a modified version of the NACA - 64_1(A)612 section, where for the mean camber line NACA $a = 0.8$ was used. Furthermore, the thickness distribution in spanwise direction for each model is constant and no twist is applied. The models are placed on a horizontal turntable, which is connected to a force-balance system directly. Also, wind tunnel wall interference corrections are applied to the data.

Table 5.2: Four swept wings configuration parameters.

Parameter	**AR5_012**	**AR5_612**	**AR10_012**	**AR10_612**
Airfoil (NACA)	65_1(A)012	64_1(A)612	65_1(A)012	64_1(A)612
Reynolds number	$2 \cdot 10^6$		$2 \cdot 10^6$	
Wing span	1.80 m		3.10 m	
Root Chord length	0.41 m		0.41 m	
Tip chord length	0.29 m		0.21 m	
Quarter chord line	0.36 m		0.32 m	
Taper ratio	0.71		0.5	
Surface area	0.32 m^2		0.48 m^2	
Sweep angle	35^o		35^o	

Since sweep is applied to this configuration, the aerodynamic coefficients are determined from wing sections perpendicular to the quarter-chord line. These sections have a thickness of 14% and a design lift coefficient of 0 and 0.73 for the symmetrical and highly cambered profile, respectively. The use of a swept-back wing is only preferred for high subsonic flight speeds, since it delays the rise in drag approaching the speed of sound (Jones, 1946). For low velocities as used in this case ($Re = 2 \cdot 10^6$), sweep has a negative effect such as spanwise flow due to a larger reaction time to push the air towards the tips and a loss in effective aspect ratio since the span is smaller compared to a straight wing. The spanwise flow will result in earlier tip stall, since the effective angles become the largest here. The effect of a lower effective aspect ratio at low speeds is an increase in drag. The effect of increasing the aspect ratio (in this case from 5 to 10), on the other hand,

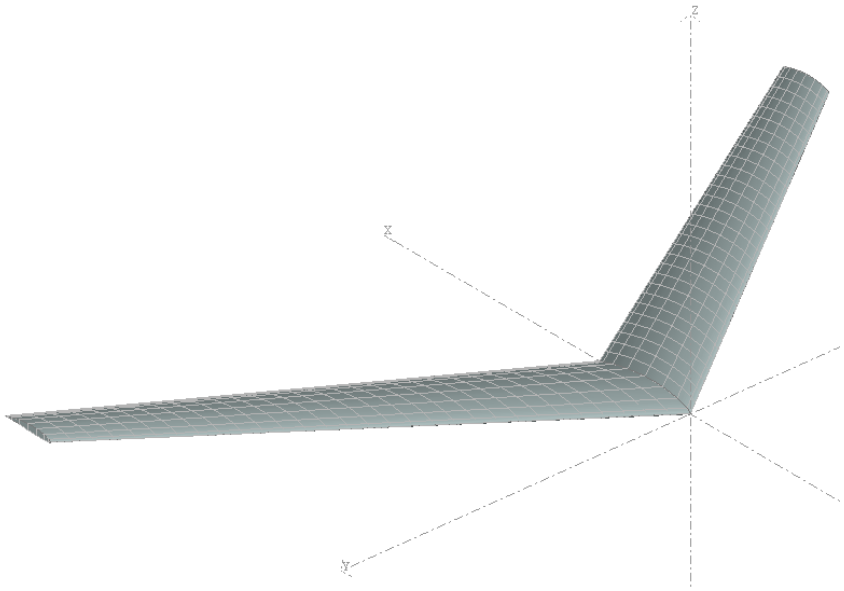

Figure 5.3: Swept wing configuration in XFLR5, with $A = 10$, $\Lambda = 35^o$ and a highly cambered profile.

should result in a higher slope of the lift curve. Furthermore, the main difference between the symmetrical and (highly) cambered profile added to the wing planforms should be an increase in lift coefficient at $\alpha = 0$ and therefore has an effect on the zero lift angle. Also, the value and region of $C_{L_{max}}$ and stall conditions are expected to change. The maximum lift coefficient should be higher for a cambered profile, but occurs at a lower angle of attack. It should also be noted that the wing tip of the wind tunnel model is formed by a half body with a radius equal to the half thickness of the wing tip section. In case of a VLM analysis, thickness is not taken into account, so there the shape of the wing tip is neglected. The 3D panel method does include thickness, but in the analysis the wing tip is simply defined by the last section. This assumption will most likely have impact on the tip characteristics, but for the total lift and drag curves this effect should not be significant.

5.2.3 Winglet configurations

The third case discusses a straight flat wing with $A = 10$ on which multiple winglets are applied with different dihedral angles (Yen & Fei, 2011). Only data for one Reynolds number value is considered, which is $Re = 80,000$. The dimensions of the winglets are significant, namely 20% of the baseline wing span, thus it is expected the winglets have significant effect on the aerodynamic behavior. This validation case could be considered as one step towards an arc shaped kite.

For the wind tunnel model, a stainless-steel symmetric NACA - 0012 airfoil is used for both baseline wing and winglets with a winglet dihedral varying from -30^o to 135^o (Yen & Fei, 2011). The baseline wing parameters are shown in table 5.3. This leads to several wing configurations, of which 5 are shown in figure 5.4, where also surface oil-flow patterns from the wind tunnel experiments are shown for an angle of attack $\alpha = 15^o$. The aerodynamic

performance that is required for the validation, is measured with a JR^3 force-moment balance system in an open-loop wind tunnel. Lift and drag measurement accuracies are $\pm 1.5\%$ and $\pm 2.0\%$, respectively. For the lift and drag coefficients, these are $\pm 4.5\%$ and $\pm 5.1\%$, respectively.

Table 5.3: Baseline wing configuration parameters excluding winglets.

Parameter	**Value**
Airfoil	NACA - 0012
Reynolds number	80,000
Wing span	0.6 m
Chord length	0.06 m
Surface area	0.036 m^2
Aspect ratio	10

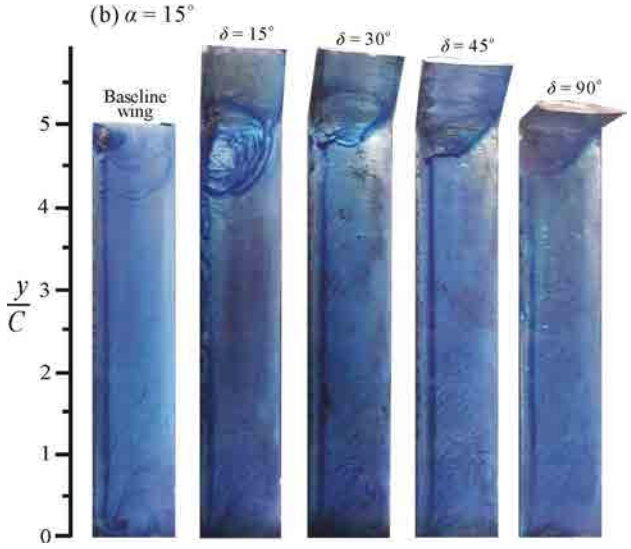

Figure 5.4: Oil flow patterns during a wind tunnel test on five different wing configurations, considering a baseline wing and added winglets under various dihedral angles at $\alpha = 15^o$ and $Re = 80,000$.

It is expected that winglets will effect the aerodynamic performance such, that there will be a decrease in both induced drag and loss of lift (Smith, 1996). These effects will increase the lift to drag ratio. Furthermore, an increasing dihedral angle for the winglet should decrease the major axis of the tip vortex and therefore its strength. However, the wind tunnel experiments showed this only holds for dihedral angles larger than 15^o. For values between 0 and 15, the vortex even grows stronger and therefore negatively influences the aerodynamic coefficients. Apparently, the flow momentum here is still high enough to expand the tip vortex to the winglet.

5.2.4 Arc shaped kite

The fourth and last configuration does not include experimental data, but is considered to validate the algorithm of Gaunaa (Gaunaa et al., 2010). In his work, the algorithm is compared with CFD results from an arc shaped kite. Both profile coordinates and 3D model of this kite are obtained to be able to perform a proper validation. The available results are performed at $Re = 3 \cdot 10^6$. In table 5.4, the kite main dimensions can be found. The planform is of elliptical shape, which is chosen due to the expected induced drag minimization (Munk, 1923). The 3D model in XFLR5 can be seen in figure 5.5.

Table 5.4: Kite configuration main parameters.

Parameter	Value
Airfoil	NACA - 64-418
Reynolds number	$3 \cdot 10^6$
Wing span	1.0 m
Root chord length	0.3 m
Surface area	0.3 m^2
Aspect ratio	3.33

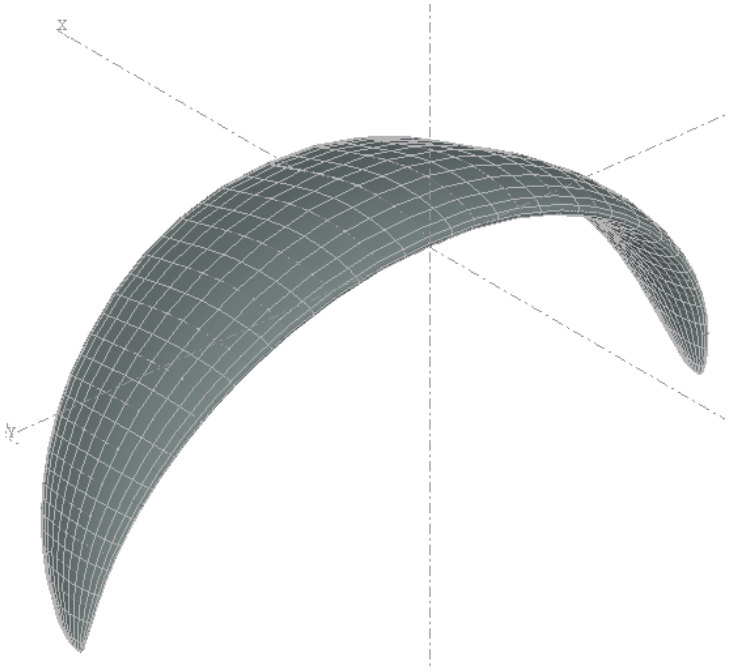

Figure 5.5: Circular arc shaped kite configuration in XFLR5, used to validate the method of Gaunaa.

5.2.5 Model discretization in XFLR5

In table 5.5, the type of discretization and number of panels are given for every validation case. A cosine panel distribution means a higher concentration of panels near the tips and leading/trailing edges for respectively spanwise and chordwise distribution.

All, but one, used discretizations are equivalent for VLM and 3D panel method, where the latter uses chordwise panels on the upper and lower camber line and extra panels on the tip sides. Only in the swept wing configurations variations are made between both MG vs AK and VLM vs 3D panel method. For version AK there is a calculation error due to discretization for induced angles in VLM calculations, which makes the values at the root unrealistic. Therefore, a *cos* spanwise panel distribution is used for the 3D panel method to avoid dense paneling at the root. However, when there are an equal numbers of panels as used in other versions, the values of the induced and effective angles are too extreme at the tips. Hence, too dense paneling is not favorable at both the root as the tips, therefore only half the number of panels are used with respect to the MG versions.

This type of discretization does, however, not work for the VLM in version AK, since then again there is unrealistic behavior at the tips due to too dense paneling. In the spanwise distribution, the induced angle slope towards the tips suddenly flips from negative to positive. Therefore, for the VLM in version AK a uniform distribution is used with the same amount of panels as in the 3D panel method in version AK. These extreme and unrealistic values could be the result of too high aspect ratio panels, which should be avoided according to the XFLR5 manual.

Table 5.5: Discretization parameters used for the validation cases, where *cos* means cosine and *uni* is uniform.

Method →	**VLM**			**3D panel method**		
Configuration ↓	*Chordwise*	*Spanwise*	*Panels*	*Chordwise*	*Spanwise*	*Panels*
Flat wing	*cos*/13	*uni*/30	390	*cos*/13	*uni*/30	806
Swept wing AR5 MG	*cos*/12	*uni*/36	432	*cos*/12	*uni*/36	888
Swept wing AR5 AK	*cos*/12	*uni*/18	216	*cos*/12	*cos*/18	456
Swept wing AR10 MG	*cos*/12	*uni*/72	864	*cos*/12	*uni*/72	1,752
Swept wing AR10 AK	*cos*/12	*uni*/36	432	*cos*/12	*cos*/36	888
Baseline wing	*cos*/10	*uni*/24	240	*cos*/10	*uni*/24	500
Winglet, $\Gamma = 90°$	*cos*/10	*uni*/32	320	*cos*/10	*uni*/32	660
Arc shaped kite	*cos*/20	*cos*/30	600	*cos*/20	*cos*/30	1,240

5.3 Program trade-off

Before validating the algorithms, it should be noted that the results from 3D simulations are highly dependent on the 2D XFOIL polars. Therefore, the airfoil sections of each validation case are first validated by comparing 2D wind tunnel data with XFOIL results. This way, the most promising validation can be performed with 3D simulations.

5.3.1 Procedure

Since there are 4 methods available to perform 3D simulations with, which have been discussed earlier in this chapter, a trade-off scheme will be maintained during the comparison of results. All considered options are shown in figure 5.6. For each version, the VLM and 3D panel method are used. In case of the VLM, the 2D inviscid lift curves of XFOIL and TAT can be chosen.

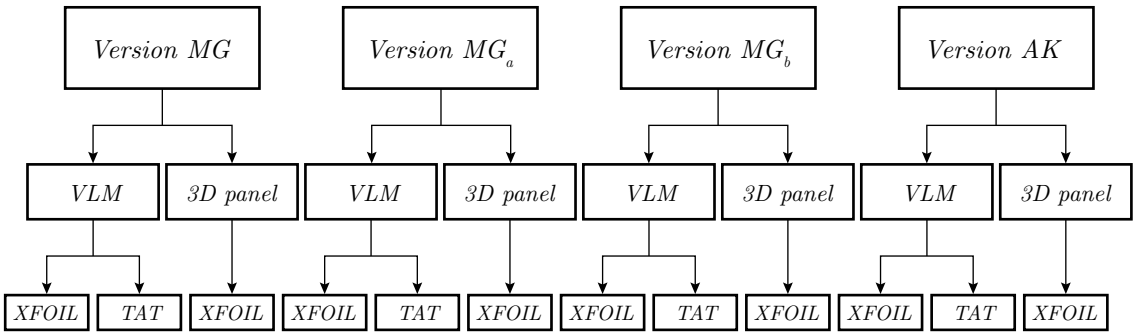

Figure 5.6: Option tree of available methods for each program version.

The trade-off procedure will be performed as follows. First, separate comparisons with experimental data will be done for the MG based VLM's and the AK based VLM's for the flat and swept wing configurations. From this, a most promising VLM will be chosen. A similar analysis will be done with the 3D panel methods based on the methods of MG and AK, from which a most promising version is chosen. These versions are used to analyze the dihedral and arc shaped kite configuration with, to investigate for example the influence of dihedral/winglets. These cases are not used in the program validation, because of uncertainties with respect to wind tunnel, airfoil and CFD data.

5.3.2 Trade-off criteria

Due to the large number of polars that resulted from simulations, a trade-off process has been performed to decide which of the program versions gives the most accurate results. In appendices A and B, all polars can be found which are used to do this analysis. For the trade-off procedure, 3 criteria are selected at which the tool should be as accurate as possible. These concern:

- The linear part of the lift curve with the associated part of the drag curve
- The non-linear part of the lift curve with the associated part of the drag curve
- The determination of $C_{L_{max}}$ (location and value)

These criteria are also visualized in figure 5.7. The non-linear part of the lift curve starts when the lift curve slope deviates more than 10% from the lift curve slope at $C_L = 0$. For the first 2 criteria, a mean absolute percentage deviation (MAPD) is used to determine the error with respect to the wind tunnel data. For the third criteria, the values of $C_{L_{max}}$ and α at $C_{L_{max}}$ are normalized with respect to the values of the wind

tunnel data. The absolute distance of these 2-dimensional points is considered to be the error.

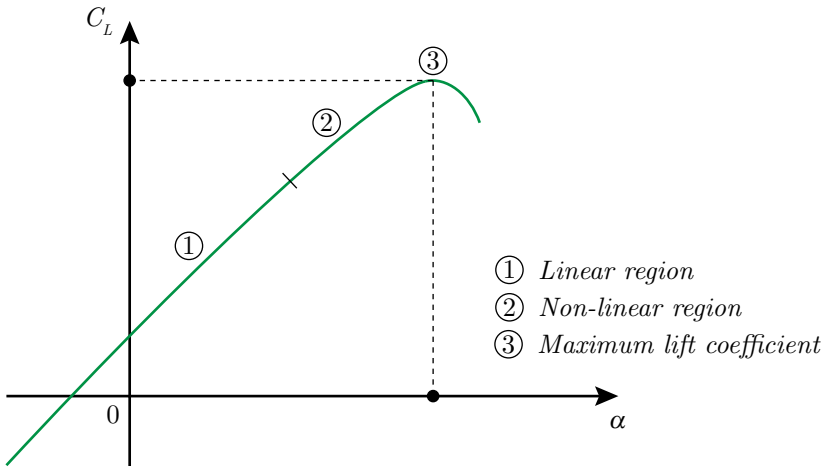

Figure 5.7: Trade-off criteria used for validation.

5.3.3 Choosing the value of n

Since the value used in the e^n method is of significant influence of the 2D polars, and no wind tunnel data was found for all the airfoil sections used for the sweep cases, a trade-off on the 3D simulation data is performed first with 2 different values of n. In appendix A, the considered XFOIL polars can be found. From the trade-off, a most promising value of n will be chosen to be used in the following trade-off procedures. In figure 5.8, the error results of the linear and non-linear regions of the lift and drag curves, averaged over the 4 sweep cases, are shown for $n = 9$ and $n = 12.4$.

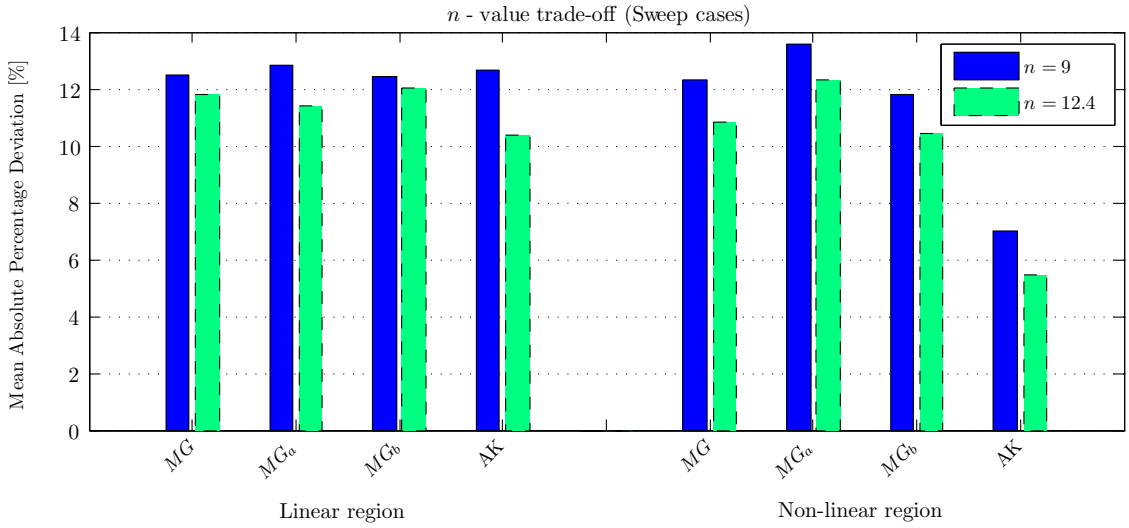

Figure 5.8: Error of the linear and non-linear region for 2 different n-values of all versions for the swept wing configurations.

From this bar diagram, it can be seen that the differences in error between the 2 values of n are not significantly large. However, if one would have to choose, $n = 12.4$ seems to be more promising. The results in this graph do, however, not take into account the range of the simulated data. Therefore, the third criteria is chosen to be important as well. For the sweep cases, it showed that for a value of $n = 9$, 37 out of 48 stall points are reached. For $n = 12.4$, this value is 19 out of 48 stall points. Since there is a significantly larger discrepancy between the amount of reached stall points than the MAPD difference for the linear and non-linear regions of the lift and drag curves, $n = 9$ is chosen to be most promising. This value is therefore used in the following trade-off process, where the flat wing configuration is also taken into account to choose the most accurate program version(s).

5.3.4 VLM and 3D panel method trade-off

In figure 5.9 and 5.10, the trade-off results of criteria 1 and 2 are shown for all validation cases calculated with all VLM and 3D panel method versions, respectively. From both bar diagrams, it can be seen that there is no large discrepancy in error between all versions regarding the linear region of the lift curve. Considering the non-linear region, AK (XFOIL) shows the lowest error percentage for both VLM and 3D panel method. From the versions based on Gaunaa, MG_b shows the lowest error with a small difference. This is expected, since the drag is determined in a manner that would theoretically be better founded.

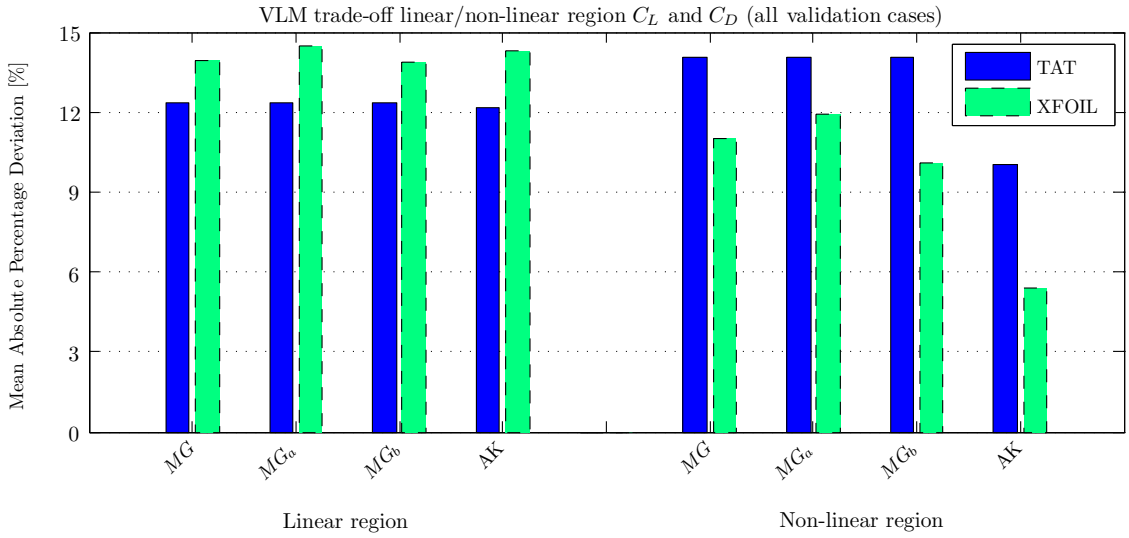

Figure 5.9: Error of the linear and non-linear region of the lift and drag curves of all VLM versions for all validation cases.

In figure 5.11, the accuracy of stall point predictions (criteria 3) of each version is shown, averaged over the flat wing and swept wings validation cases. Also, the amount of reached stall points are depicted above the bar diagrams. It is directly noted that the XFOIL based methods show a higher accuracy than the TAT based methods for the VLM. Also, the Gaunaa based versions determine all stall points, from which MG and MG_b show the lowest error. However, MG_b showed a better performance in criteria 2 and

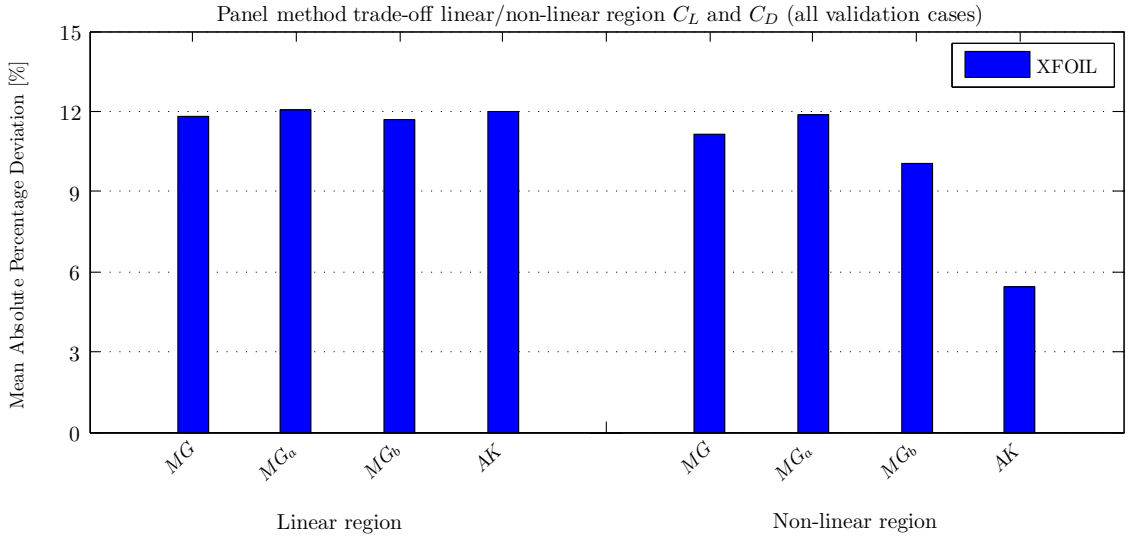

Figure 5.10: Error of the linear and non-linear region of the lift and drag curves of all 3D panel method versions for all validation cases.

is therefore chosen as the most promising version based on Gaunaa's method. AK shows a similar accuracy in stall point prediction, but not all points are reached. Due to the significant higher accuracy in criteria 2, AK is also chosen as a most promising method.

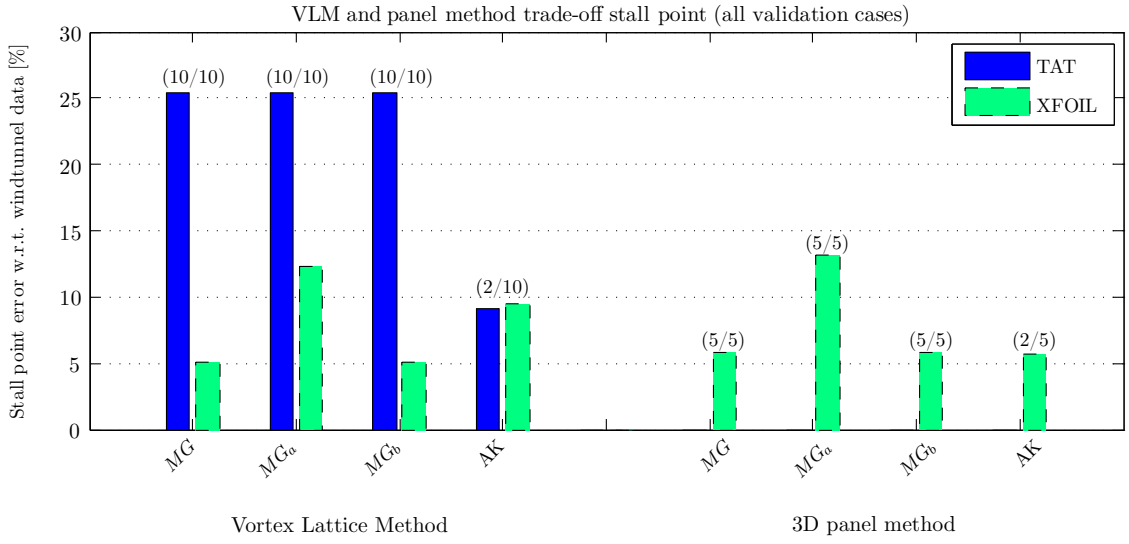

Figure 5.11: Error of the location and value of $C_{L_{max}}$ of all VLM and 3D panel method versions for all validation cases, including the number of reached stall points.

5.4 Results of validation cases

From an extensive trade-off procedure, the versions MG$_b$ and AK came out to be most accurate in predicting lift and drag coefficients up to stall conditions. Although all valida-

tion results can be found in appendix B, in this section the lift and drag polars of version MG_b and AK are shown for all validation cases. From these results, conclusions can be drawn regarding specific phenomena for each different configuration. Also, improvement with respect to the original XFLR5 version is of major importance. Therefore, an analysis is performed on the trade-off criteria (see section 5.3.2) between the original and adapted versions.

5.4.1 Lift and drag coefficient

In figure 5.12 and 5.13, the lift and drag curve results of the flat wing configuration (Horsten case) are shown for the most promising versions. It can be seen that the results from the adapted programs deviate from the values of Horsten. This is due to the use of a different VLM and implementation of the angle shift and the implementation of interference effects in Horsten's algorithm. In general, the solutions are close to the wind tunnel data, although a non-linearity occurs at $\alpha = 6^o$. This follows from the XFOIL polars, which show a higher decrease in lift slope than the wind tunnel data.

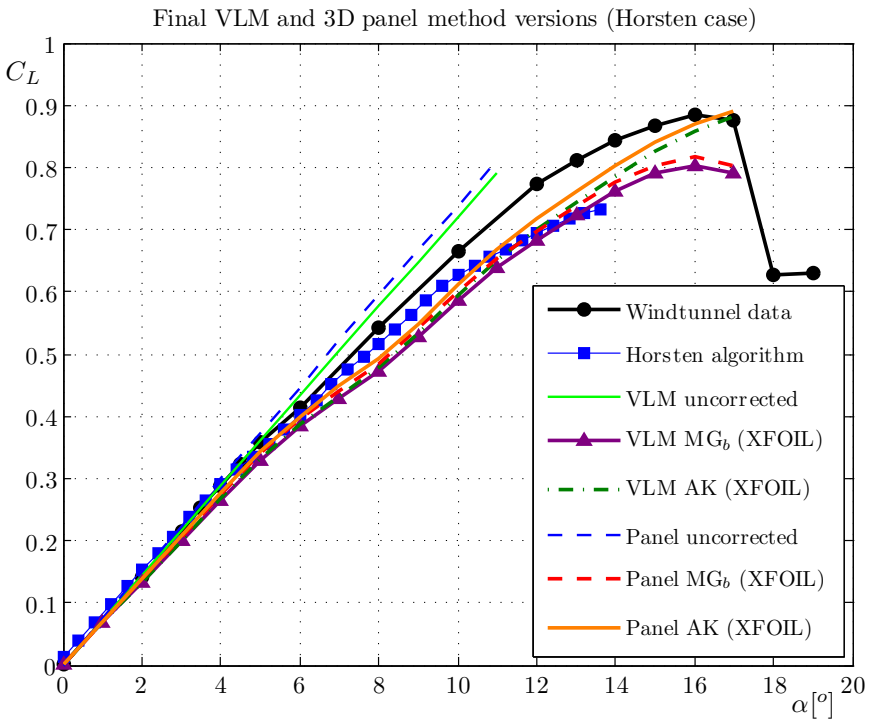

Figure 5.12: The $C_L - \alpha$ curves obtained from wind tunnel experiments and XFLR5 simulations of the flat wing where $Re = 1.0 \cdot 10^6$.

In the experimental data, a kink is observed in the lift curves for the swept wing configurations. This is probably due to sudden movement of the transition point, which can be caused by a dirty wind tunnel model for example. In figure 5.14, 5.15, 5.16 and 5.17 the lift, drag, profile drag and induced drag curves of the AR10_012 wing configuration are shown for the most promising versions. The lift and drag curves from each adapted version show a good resemblance with the experimental data. The lower accuracy of the drag for high lift values is due to the profile drag, which shows an increase in value in

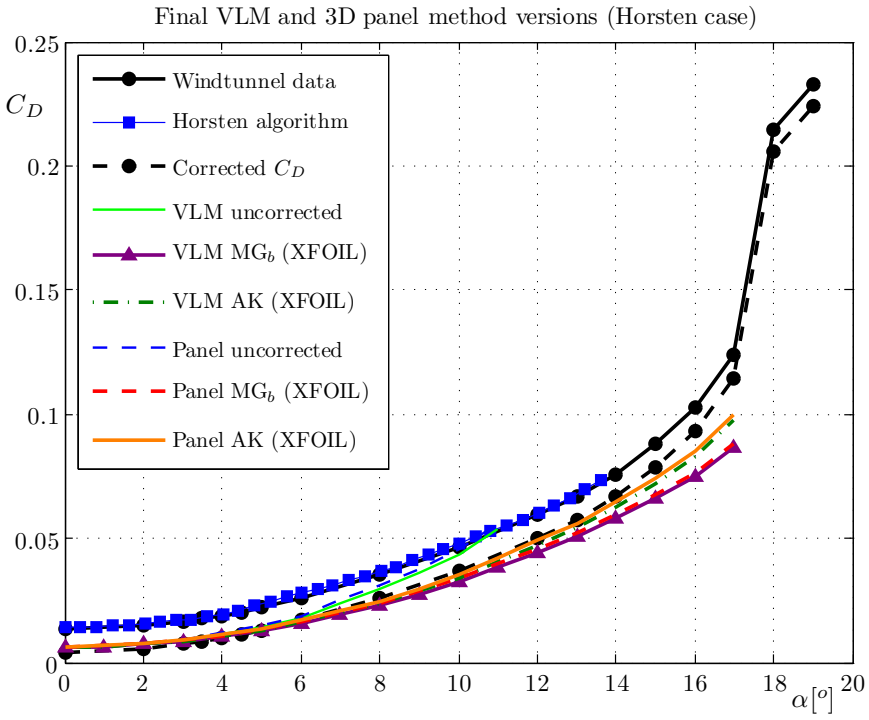

Figure 5.13: The $C_D - \alpha$ curves obtained from wind tunnel experiments and XFLR5 simulations of the flat wing where $Re = 1.0 \cdot 10^6$.

this region. The induced drag coefficients are, however, predicted accurately. It should be noted that the wind tunnel data in figure 5.17 has a value larger than 0 at $C_L = 0$. This is an error due to low resolution figures from literature. The remaining results of the swept wing configurations can be found in appendices C.2-C.4.

5.4.2 Improvement on original XFLR5

In figure 5.18, the mean absolute deviation of the linear and non-linear region of the lift curves are shown of the original XFLR5 program and the adapted versions. An average of all validation cases is used here. In the linear region, negligible differences are observed. In the non-linear region, however, an increased accuracy of approximately 0.1 is obtained with respect to the uncorrected XFLR5 version. Since all validation cases have stall points around or below $C_L = 1$, an average error decrease of 0.1 is significant. The MAD of the adapted versions is in the order of 0.03, which is acceptable.

In figure 5.19 and 5.20, the mean absolute deviation of the linear and non-linear region of the drag curves are shown of the original XFLR5 program and the adapted versions. Here, the profile and induced drag coefficient are considered separately and an average of 2 swept wing configurations (AR5_012 and AR10_012) is used. From figure 5.19, it can be seen that the total drag coefficient shows to be increased in accuracy with the adapted versions. In profile drag there seems to be a small increase in error, but in overall results are similar. More significant increases in accuracy are shown in the non-linear region (see figure 5.20). Most profit is gained in the total drag with the AK method. But also MG$_b$ shows to produce lower errors for both total drag and profile drag. Thus, concerning

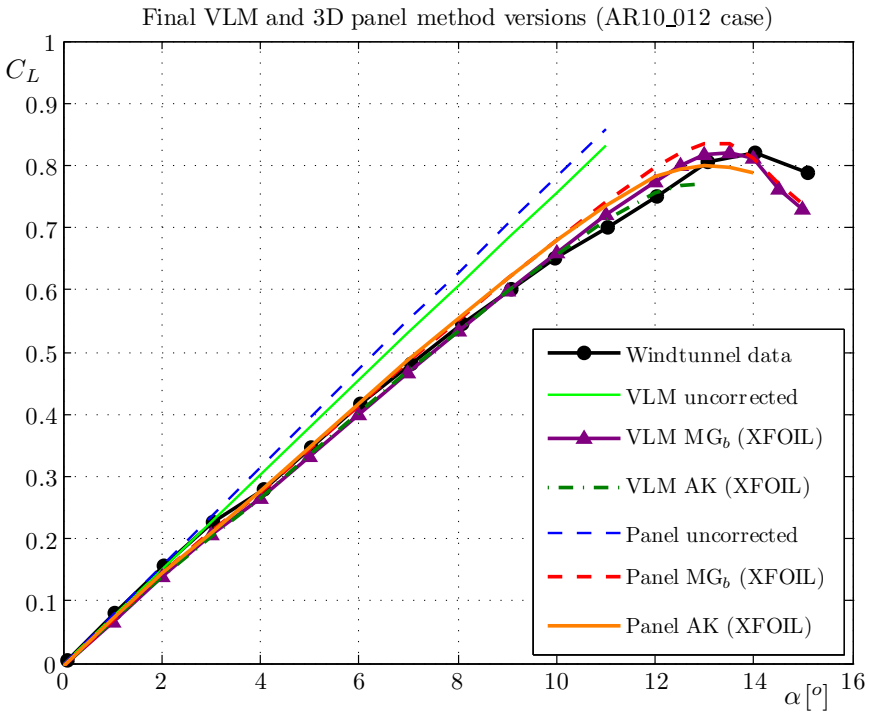

Figure 5.14: The $C_L - \alpha$ curves obtained from wind tunnel experiments and XFLR5 simulations of the AR10_012 wing where $Re = 2.0 \cdot 10^6$.

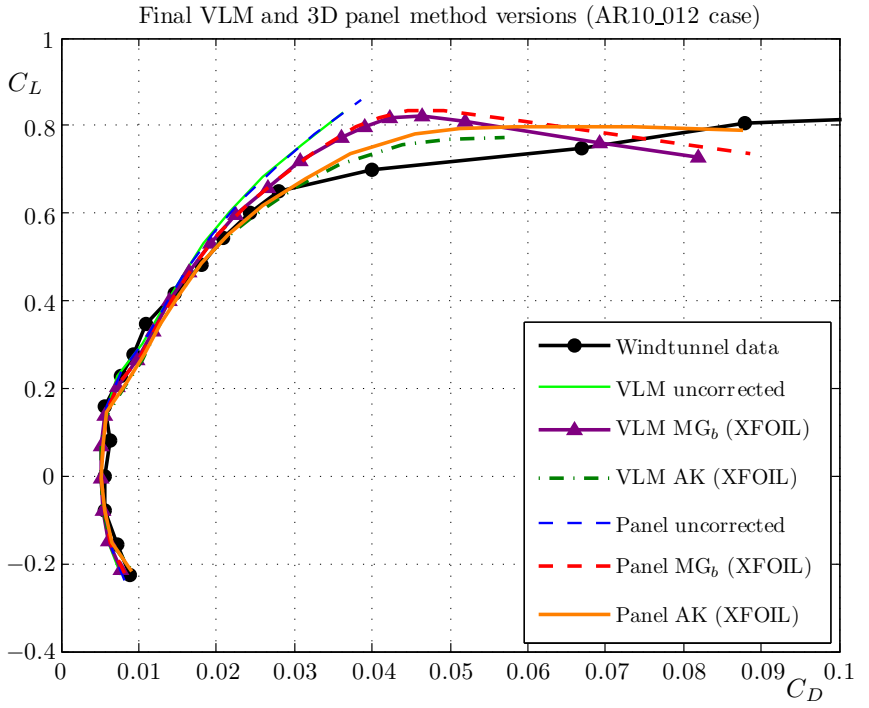

Figure 5.15: The $C_L - C_D$ curves obtained from wind tunnel experiments and XFLR5 simulations of the AR10_012 wing where $Re = 2.0 \cdot 10^6$.

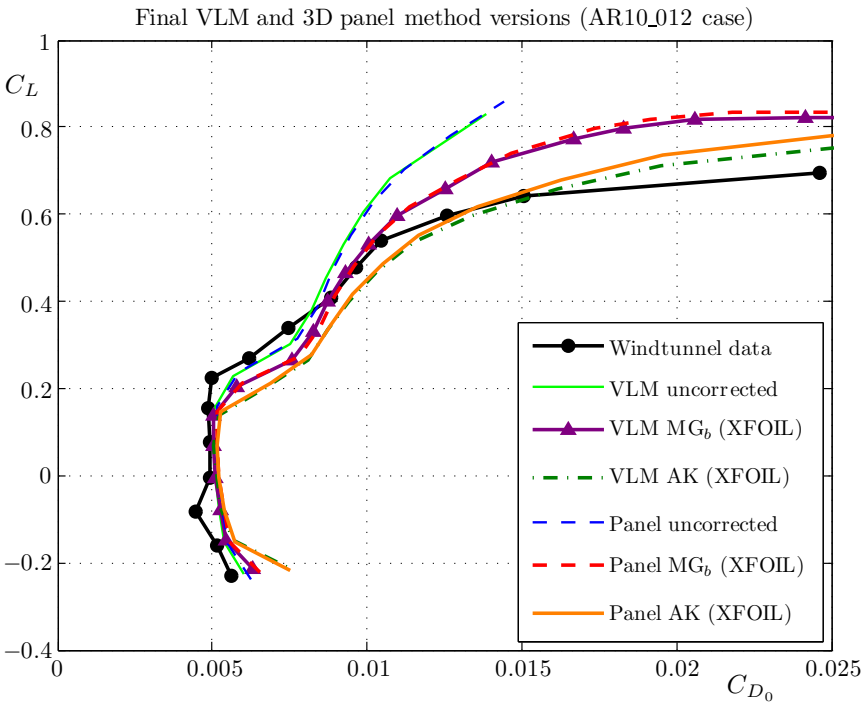

Figure 5.16: The $C_L - C_{D_0}$ curves obtained from wind tunnel experiments and XFLR5 simulations of the AR10_012 wing where $Re = 2.0 \cdot 10^6$.

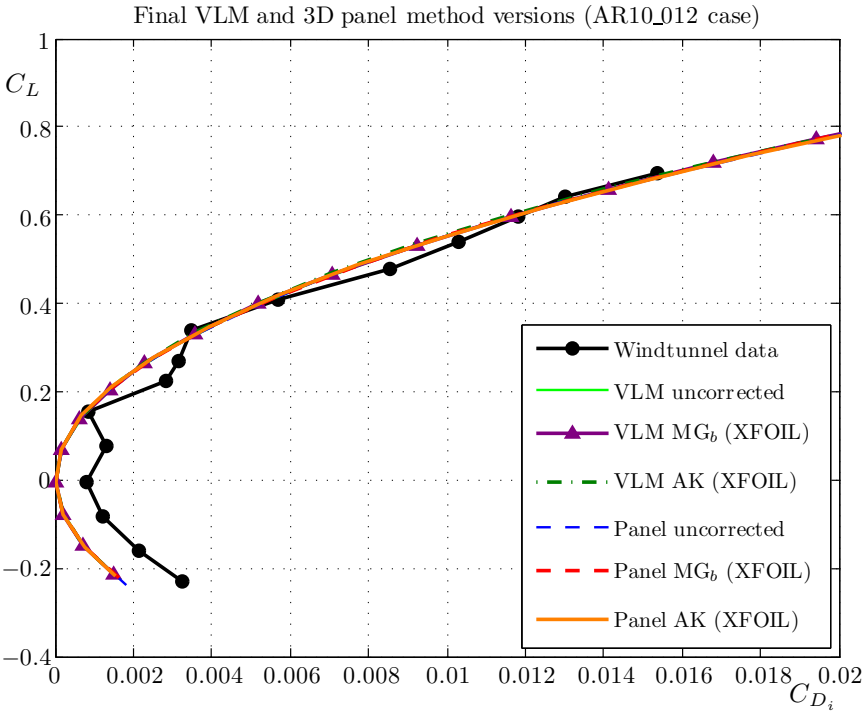

Figure 5.17: The $C_L - C_{D_i}$ curves obtained from wind tunnel experiments and XFLR5 simulations of the AR10_012 wing where $Re = 2.0 \cdot 10^6$.

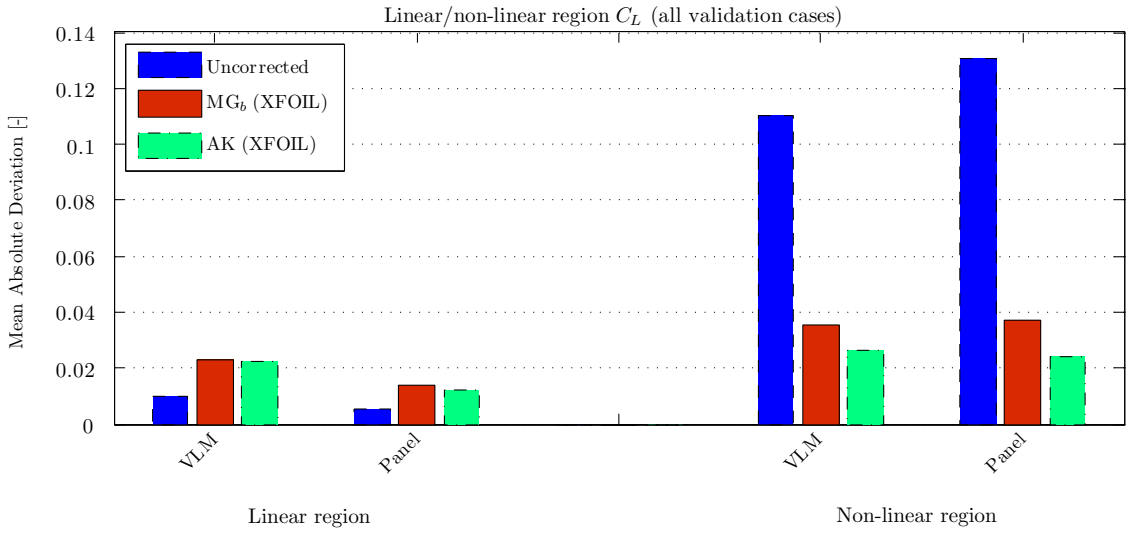

Figure 5.18: MAD of the linear and non-linear region of the lift curves of the uncorrected XFLR5 version and adapted versions for all validation cases.

criteria 1 and 2, significant profits are obtained with the adapted XFLR5 programs.

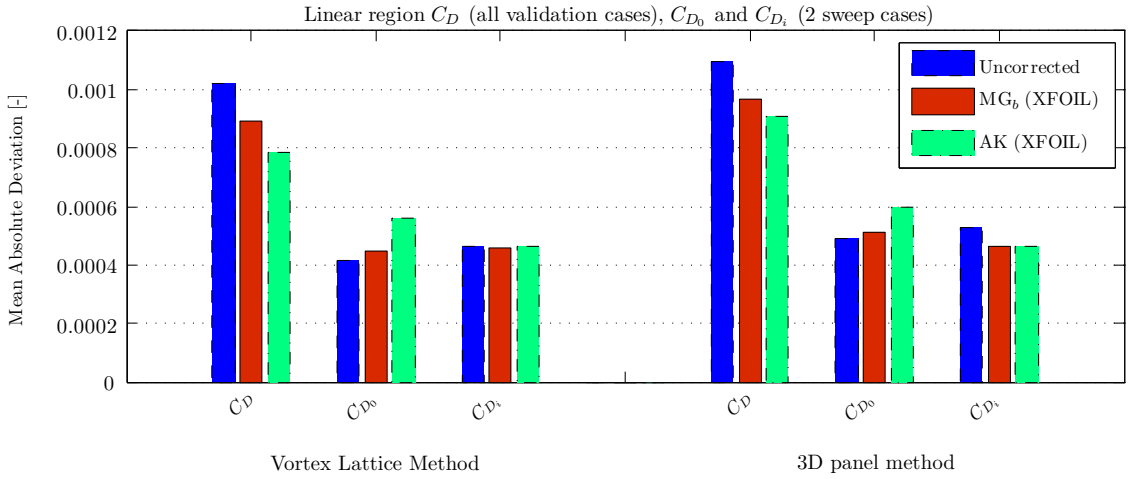

Figure 5.19: MAD of the linear region of the drag (total, profile and induced part) curves of the uncorrected XFLR5 version and adapted versions for all validation cases.

In figure 5.21 and 5.22, the normalized errors w.r.t. the wind tunnel data of the value and location of the stall points are shown. Here, each marker denotes a single validation case. It can be seen that each obtained stall point is predicted within an error of 10%.

5.4.3 Spanwise distributions

In figure 5.23, the lift and angle shift distributions of the AR10_012 wing are shown for $\alpha = 6^o$ and $\alpha = 13.3^o$. In appendix C.1, spanwise distribution results of the flat wing configuration can be found. The results of the swept wing AR10_012 show a significant deviation for the uncorrected VLM and 3D panel method. It is also noted that the different

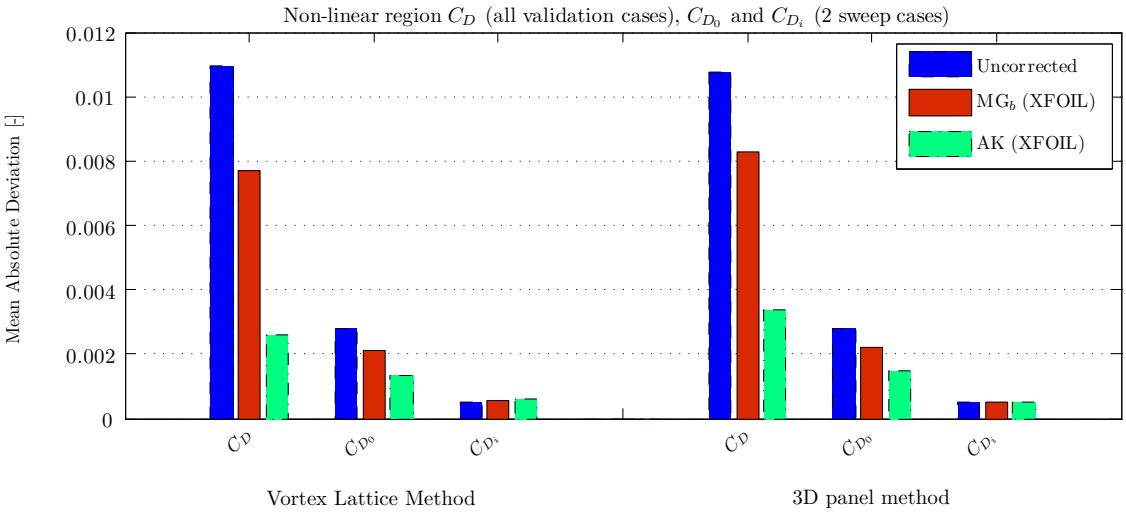

Figure 5.20: MAD of the non-linear region of the drag (total, profile and induced part) curves of the uncorrected XFLR5 version and adapted versions for all validation cases.

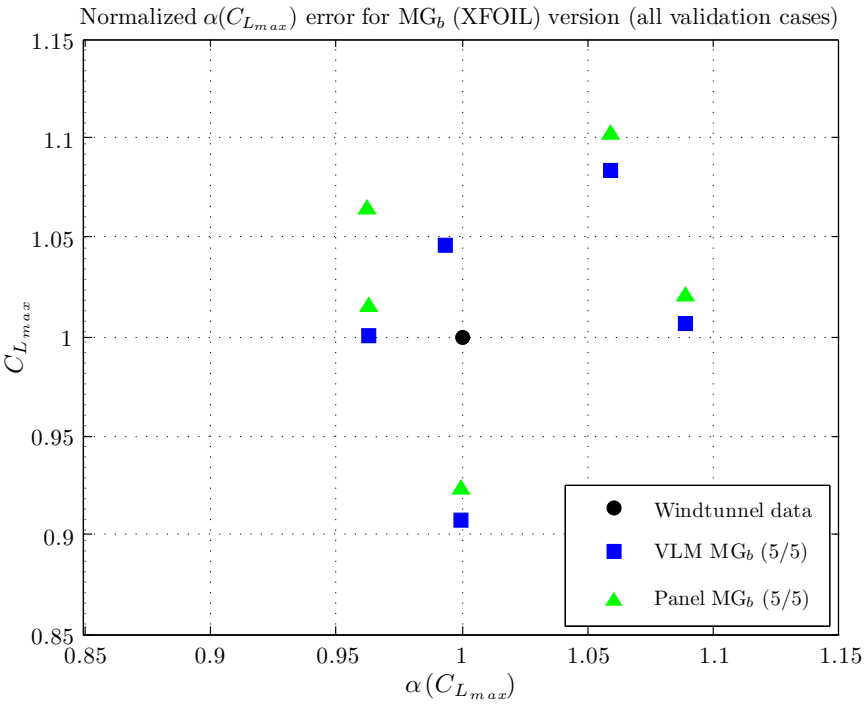

Figure 5.21: Normalized error of the value and location of $C_{L_{max}}$ of version MG$_b$ for all validation cases.

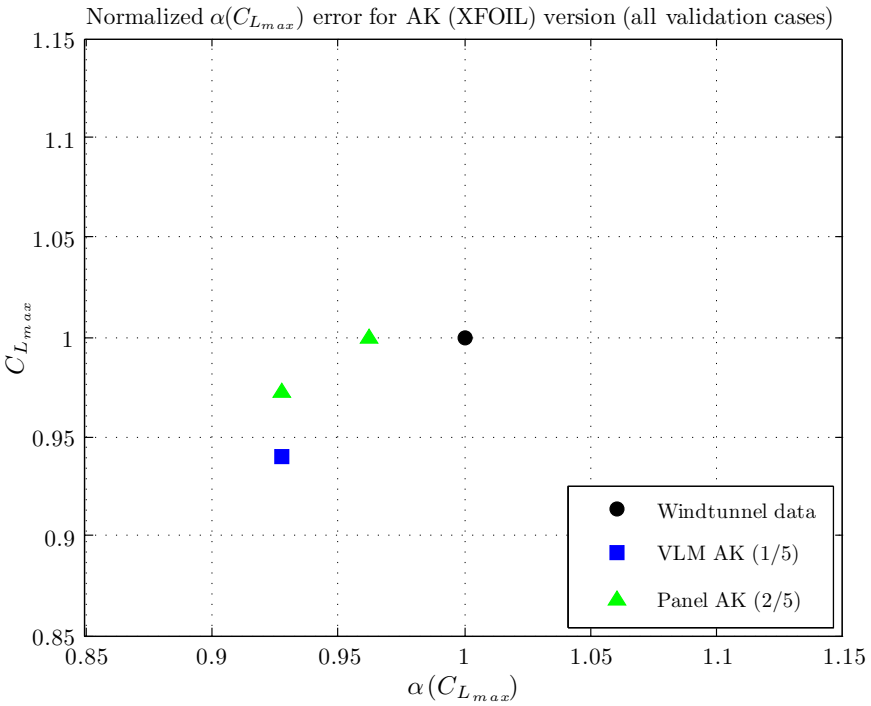

Figure 5.22: Normalized error of the value and location of $C_{L_{max}}$ of version AK for all validation cases.

adapted version show different results, especially for the angle shift distribution. This is expected, since the AK version uses induced angles in the iteration loop to determine the angle shift and the MG_b version does not. For an increasing angle of attack, this effect becomes more and more visible.

In figure 5.24, the effective angle and drag distributions of the AR10_012 wing are shown for $\alpha = 6^o$ and $\alpha = 13.3^o$. Similar differences are observed as in figure 5.23. Concerning the drag distributions for $\alpha = 13.3^o$, the uncorrected VLM and 3D panel method results are not shown, since the drag coefficient could not be interpolated anymore at this angle.

5.4.4 Winglet configurations

When using the 3D Panel Method for the winglet configurations unrealistic peaks in the induced angles originate at the winglet attachment points, which gets even worse when refining the grid. It was found that the inviscid solution already contains these peaks and enlarge when applying angle shifts. Before stall is reached these peaks are so high that the corresponding effective angles can not be interpolated on the airfoil curves to obtain angle shifts. Apparently, the 3D panel method has difficulties with sharp variations in dihedral. Because these peaks are not present in the VLM results, only the VLM results will be used for comparison. Two notifications should be made to the performed simulations on the winglet configurations:

- A very low Reynolds number is used, $Re = 80,000$, and thus viscous forces are relatively higher. They can strongly influence the flow behavior around the profile

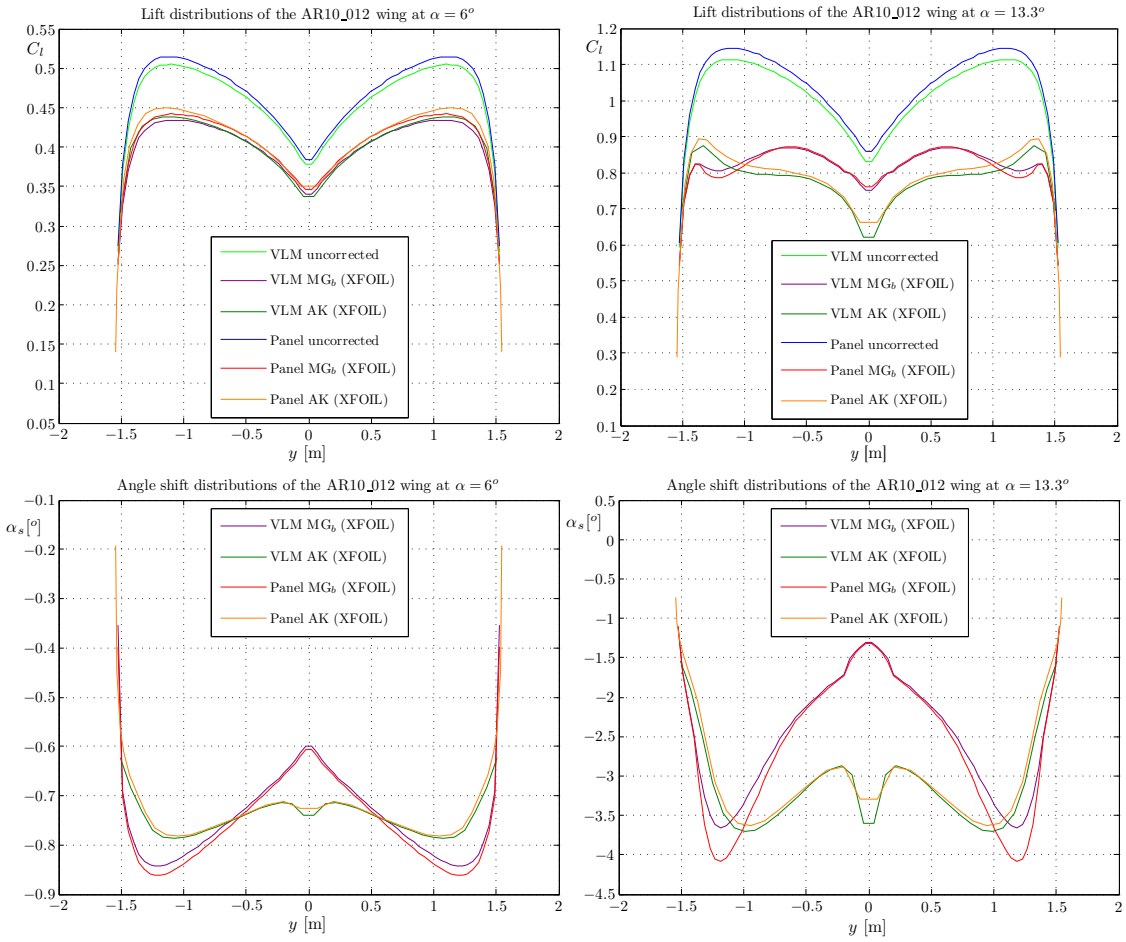

Figure 5.23: The $C_l - y$ and $\alpha_s - y$ distributions obtained from XFLR5 simulations (original, MG$_b$ and AK) for the AR10_012 wing with $\alpha = 6^o$ and $\alpha = 13.3^o$.

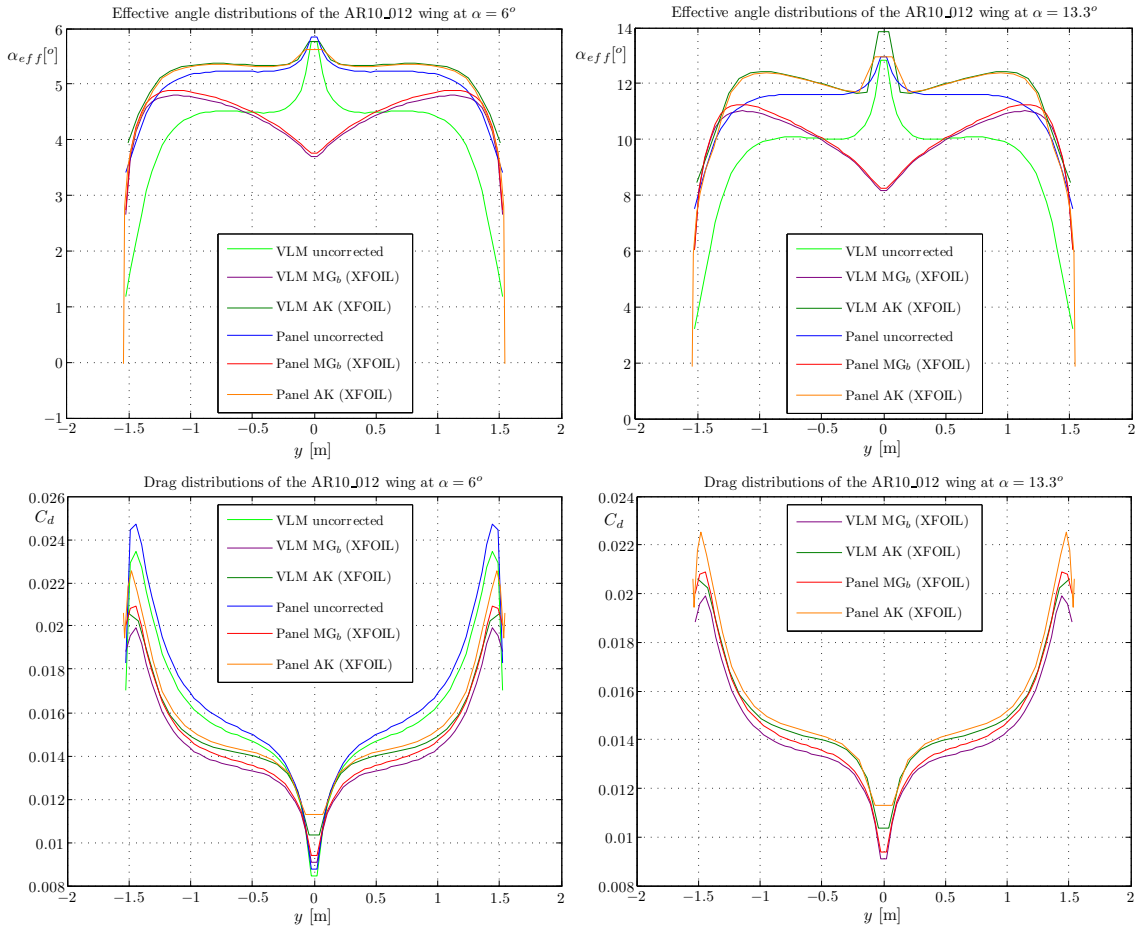

Figure 5.24: The $\alpha_{eff} - y$ and $C_d - y$ distributions obtained from XFLR5 simulations (original, MG$_b$ and AK) for the AR10_012 wing with $\alpha = 6^o$ and $\alpha = 13.3^o$.

and the wake. As a result, deviations can be expected in the used profile data.

- The deviations in profile drag, at $C_D(\alpha = 0)$, between the experimental and simulated data arouse suspicion that the experimental drag coefficients are not corrected for wind tunnel effects. Another explanation could be wind tunnel flow quality or that the NACA profile has a different surface roughness and/or camber lines which can significantly affect friction drag and transition point. The NACA - 0012 profile is also known for the many variations in measured lift and drag values at different wind tunnel measurements, as mentioned by aerodynamicist Veldhuis from the Delft University of Technology.

The $C_D - \alpha$ curve of the simulated values moves upward when winglets are applied. For $\alpha = 0^o$, the induced drag is zero (symmetric profile), which means that the shift is a result of increased profile drag. This is simply because the drag coefficient is calculated with respect to the projected area which remains constant after the addition of winglets of 90^o dihedral (while the total profile drag increases).

The increase in profile drag is proportionally less compared to the experimental values: 18% vs 38%. The 18% of the simulated values corresponds approximately to the 20% increase in total wing area. The remaining 18% increase in the wind tunnel values is therefore due to viscous 3D effects such as cross flow at the junction.

The shape of the simulated $C_D - \alpha$ curve remains approximately the same (see figure 5.26), whereas it would be expected that the wing with winglets would have relatively less resistance as lift increases, because of reduction in induced drag. This reduction in drag is indeed visible in the experimental data. After inspection, the simulated data did show a reduction in induced drag for increasing angle of attack, but this difference in induced drag is only a fraction of the profile drag and has therefore almost no effect on the total drag, see also figure 5.27. Apparently, the lift distribution, and thus lift slope, is significantly more influenced by the winglets in reality than the potential flow code predicts (see figure 5.25). This is not surprising, because this theory is not able to simulate viscous 3D effects, which play an important role for wings with winglets.

Next to the winglet with $\Gamma = 90^o$, a number of other dihedral angles where used for experiments (Yen & Fei, 2011). Here, also a negative dihedral was used of which lift and drag curves deviated significantly from the same positive dihedral. This is due to the wake interference of the negative dihedral winglet with that of the main wing. In simulations, a similar non-symmetrical effect was observed using the tilted geometry option. However, the deviations were less notable, similar to the results in figure 5.25.

5.4.5 Arc shaped kite

Before discussing the results of the new program some notes should be made on this validation case, where originally the algorithm of Carqueija et al. (2010) was compared with CFD results (FVM) from an arc shaped kite:

- It is difficult to determine how accurate the FVM results are, since it is not known whether a convergence study was performed and what the quality of the mesh is. This is however one of the few cases in which an arc shaped kite is analyzed with a FVM for which the results can be expected to have higher accuracy than a VLM or 3D panel method. Therefore, this comparison is still interesting.

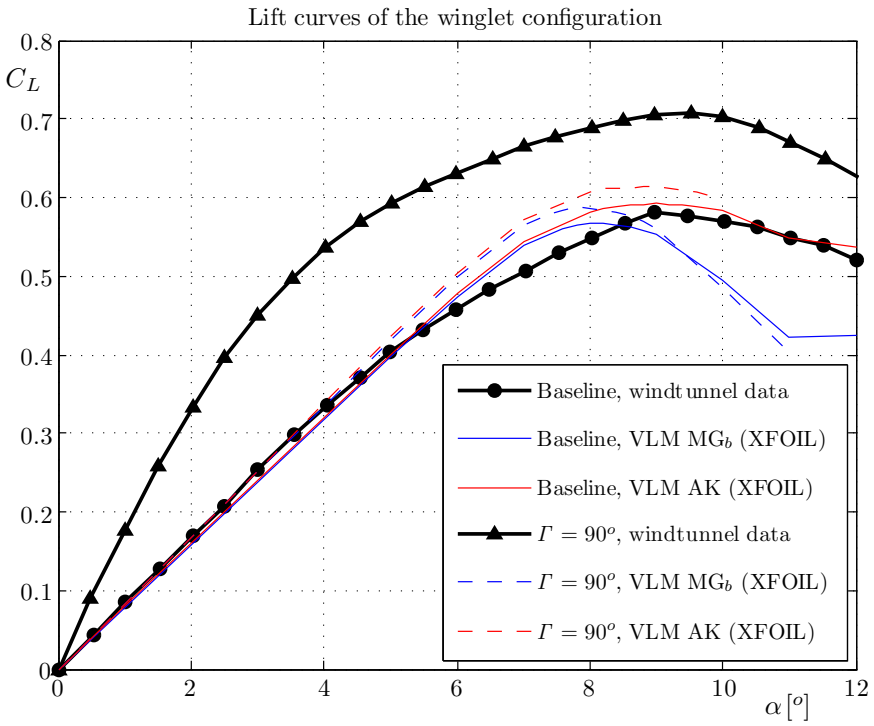

Figure 5.25: The $C_L - \alpha$ curves obtained from wind tunnel experiments and XFLR5 simulations of the winglet configuration without winglet and with $\Gamma = 90^o$ where $Re = 80,000$.

- For the lift and drag curve of the NACA - 64-418 airfoil, results were obtained from a CFD analysis only for $Re = 6\cot 10^6$. Therefore, Carqueija makes the wrong assumption that the Reynolds number is constant over span, while it should change, since the chord length varies in this direction. The local Reynolds numbers are smaller towards the tips and lower Reynolds numbers generally means lower maximum lift. As a result it is expected that the maximum lift predicted by his algorithm is too high.
- Carqueija uses a different VLM, which was not available to investigate. Therefore, small differences in the inviscid VLM calculations can already be expected. It is only known that it uses ring vortices, a free wake (similar as VLM2 with tilted geometry in XFLR5) and TE shed lines of only 1 local chord length opposed to 100 MAC lengths used in XFLR5. Carqueija states that the influence of the TE shed lines is not significant.
- For the calculation of the effective angles, the spanwise lift distribution is used, however it is not known how the local lift coefficient in his VLM is calculated. It is also not clear whether he uses the local normal force coefficient instead of the local lift coefficient. The first one would be more logical to use, since the local effective angles of attack and angle shifts should be defined normal to the airfoil section. If not, these algorithms would not be able to apply the angle shifts to a vertical wing (for example an aircraft tail).

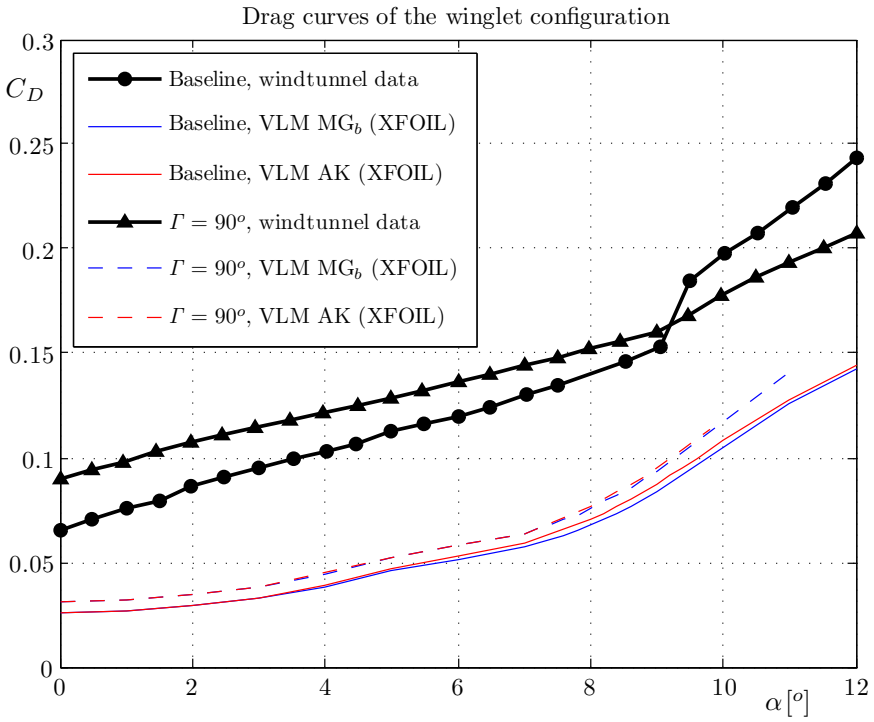

Figure 5.26: The $C_D - \alpha$ curves obtained from wind tunnel experiments and XFLR5 simulations of the winglet configuration without winglet and with $\Gamma = 90^o$ where $Re = 80,000$.

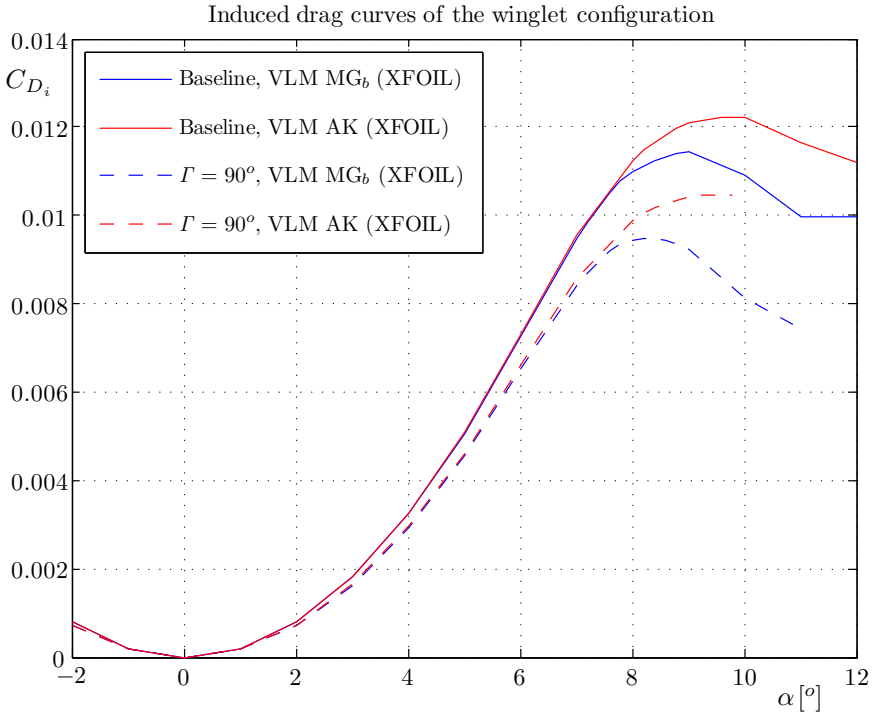

Figure 5.27: The $C_{D_i} - \alpha$ curves obtained from XFLR5 simulations of the winglet configuration without winglet and with $\Gamma = 90^o$ where $Re = 80,000$.

To transform the coordinates along the span y, which are used in XFLR5, to coordinates along the projected span Y, which are used by Carqueija, the following transformation is used:

$$Y = cos\left(\frac{\pi}{2} - \frac{\pi}{2} \cdot \frac{y}{y_{max}}\right) \tag{5.2}$$

This transformation is based on the geometry of the kite, in which the spanwise camber was defined with a cosine function. Furthermore, Carqueija used a different definition for the spanwise lift distribution than the one used in XFLR5: he uses the mean aerodynamic chord instead of the local chord. The values from XFLR5 are therefore transformed such that they match the definition of Carqueija. In figures 5.28-5.33, the results from XFLR5 simulations (VLM MG (XFOIL)) and Carqueija et al. (2010) of the arc shaped kite are shown. From these results, it is observed that the lift curve from the adapted XFLR5 program reaches a higher maximum value. This can be explained by looking at the spanwise lift distributions, which covers a larger area for VLM MG (XFOIL). The shape of the distributions are similar in general, although some differences are visible due to the use of different VLM's. The drag coefficients (induced and profile drag) and the lift to drag ratio curves correspond well to the values of Carqueija. It can thus be concluded that this particular adapted version of XFLR5 resembles his algorithm accurately.

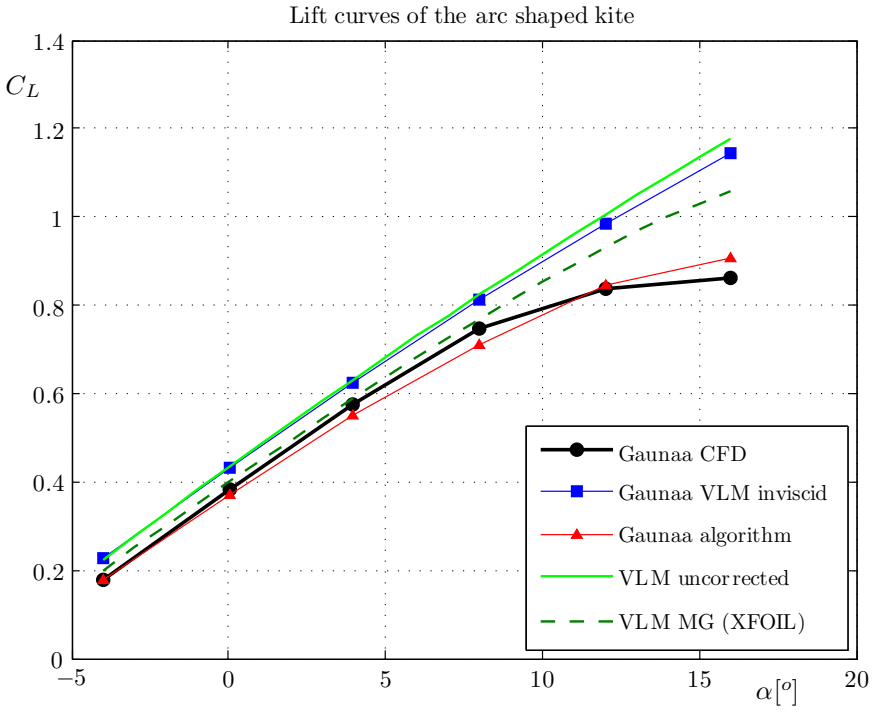

Figure 5.28: Comparison of $C_L - \alpha$ curves obtained from XFLR5 simulations (VLM MG (XFOIL)) and Carqueija et al. (2010) of the arc shaped kite.

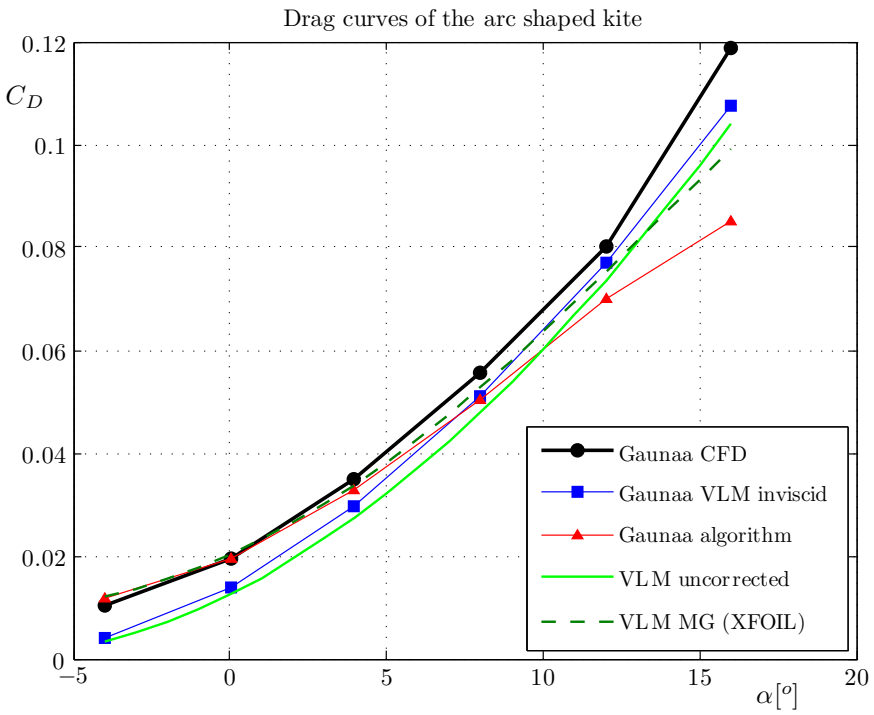

Figure 5.29: Comparison of $C_D - \alpha$ curves obtained from XFLR5 simulations (VLM MG (XFOIL)) and Carqueija et al. (2010) of the arc shaped kite.

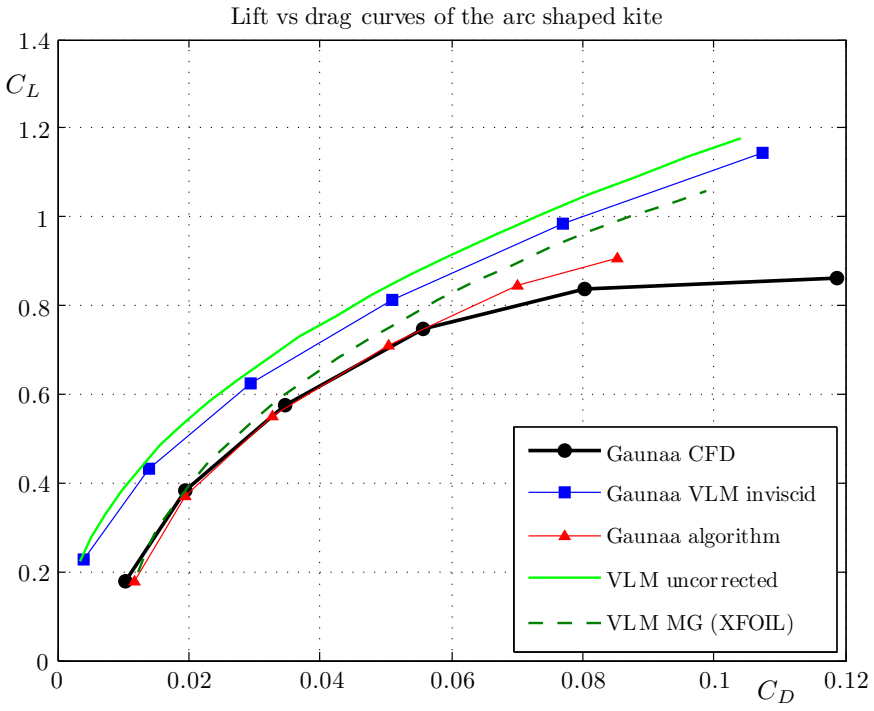

Figure 5.30: Comparison of $C_L - C_D$ curves obtained from XFLR5 simulations (VLM MG (XFOIL)) and Carqueija et al. (2010) of the arc shaped kite.

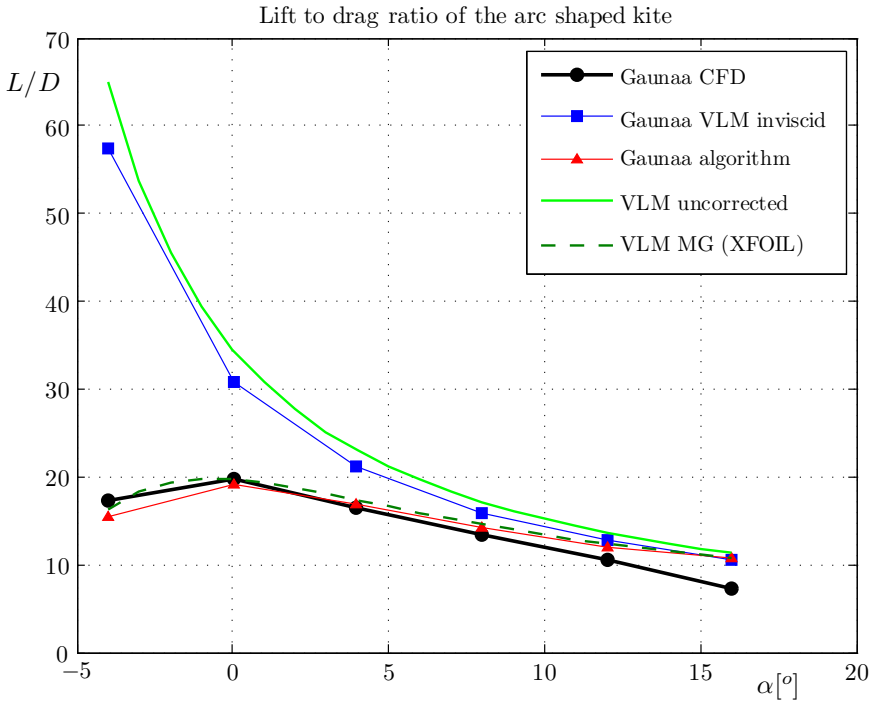

Figure 5.31: Comparison of $L/D - \alpha$ curves obtained from XFLR5 simulations (VLM MG (XFOIL)) and Carqueija et al. (2010) of the arc shaped kite.

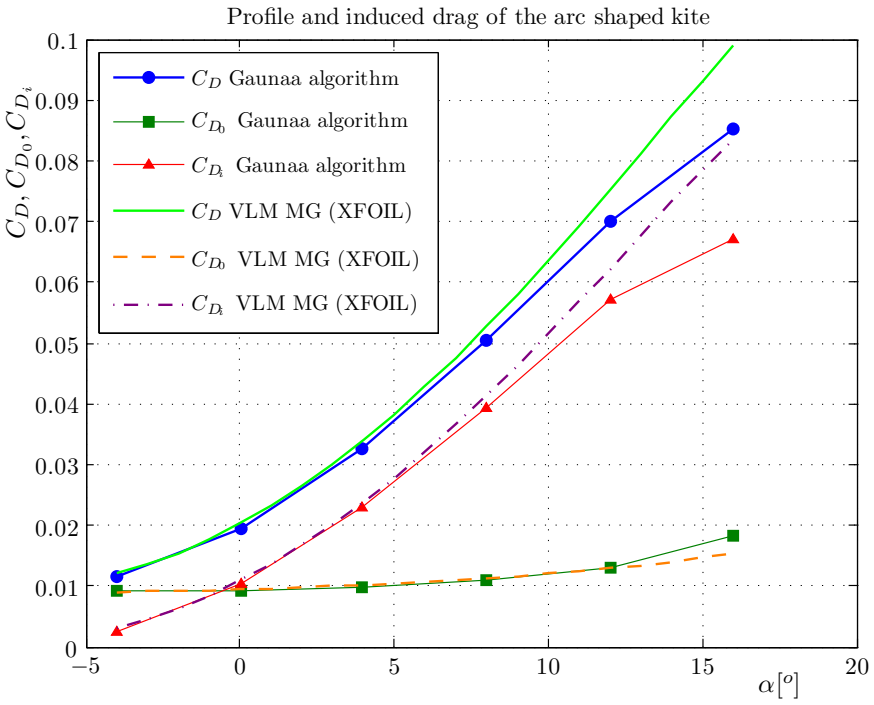

Figure 5.32: Comparison of C_D, C_{D_0} and C_{D_i} as function of α obtained from XFLR5 simulations (VLM MG (XFOIL)) and Carqueija et al. (2010) of the arc shaped kite.

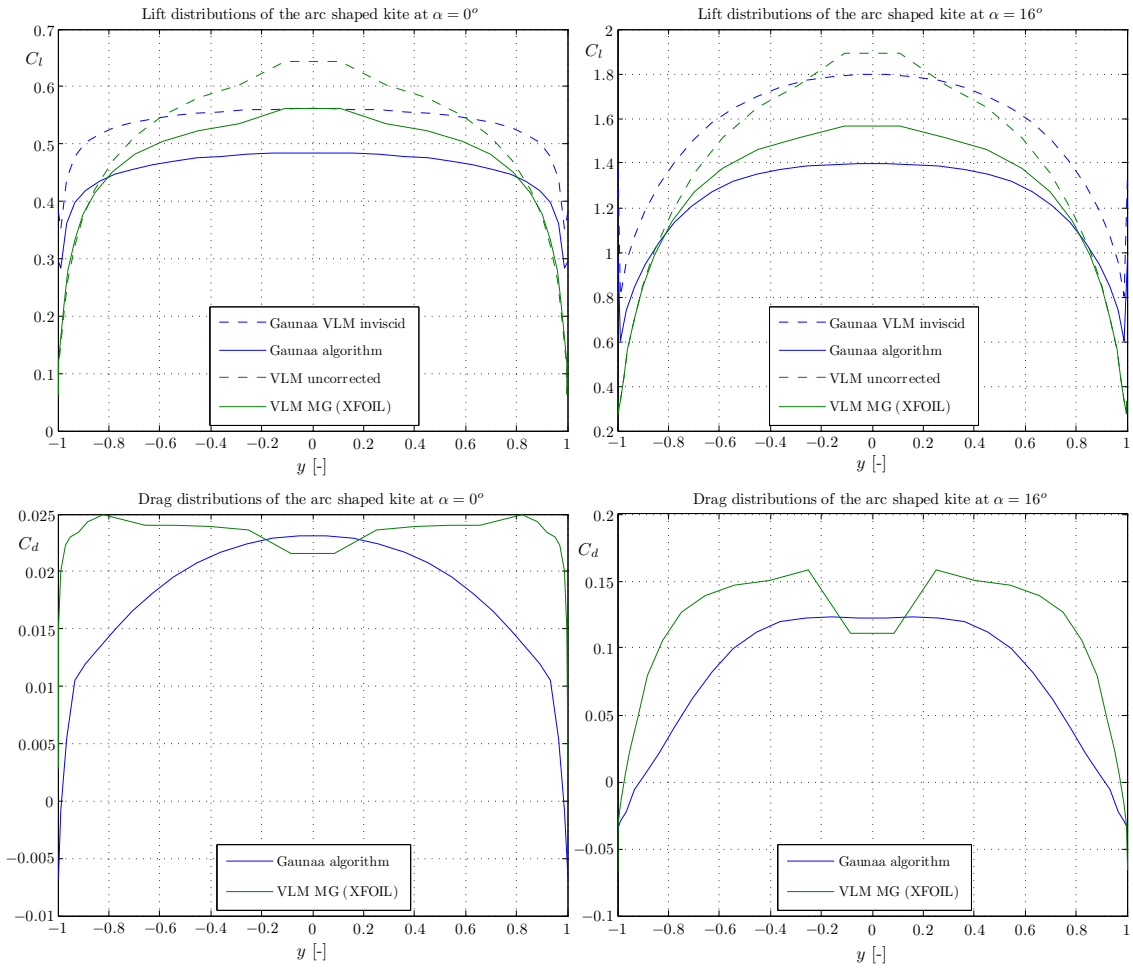

Figure 5.33: The $C_l - y$ and $C_d - y$ distributions obtained from XFLR5 simulations (VLM MG (XFOIL)) and Carqueija et al. (2010) of the arc shaped kite with $\alpha = 0^o$ and $\alpha = 16^o$.

5.5 Software performance

So far, the quality of the adapted aerodynamic analysis tool has been proven. Since it concerns a computational program, performance is an important feature. In this section, focus will be laid on the impact of the number of iterations on computational time in an analysis.

5.5.1 Impact of number of iterations

The influence of the number of iterations on the accuracy of the results is investigated with the flat wing configuration (see section 5.2.1), as shown in figure 5.34. Only the lift coefficient around stall is considered, since there the angle shifts and effect of number of iterations is the highest.

Results are similar for the AK and MG versions, though the AK version diverges for high angles of attack. This is caused by the peaks in spanwise induced angle distributions that become visible after two iterations (see figure 5.35). The combination of angle shift and the induced angle determination in the Trefftz plane results in fluctuating distributions and occurs for every type and number of paneling. The MG version determines the induced angles from the lift distribution and does not show this behavior.

A logarithmic decrease in the relative error is observed: the error with respect to the converged value is already less than 3% after two iterations. Using one iteration with AK is sufficient for having a maximum error of about 10% at stall and less for smaller angles. Two iterations would result in higher accuracy but, as mentioned above, peaks will become visible in spanwise distributions.

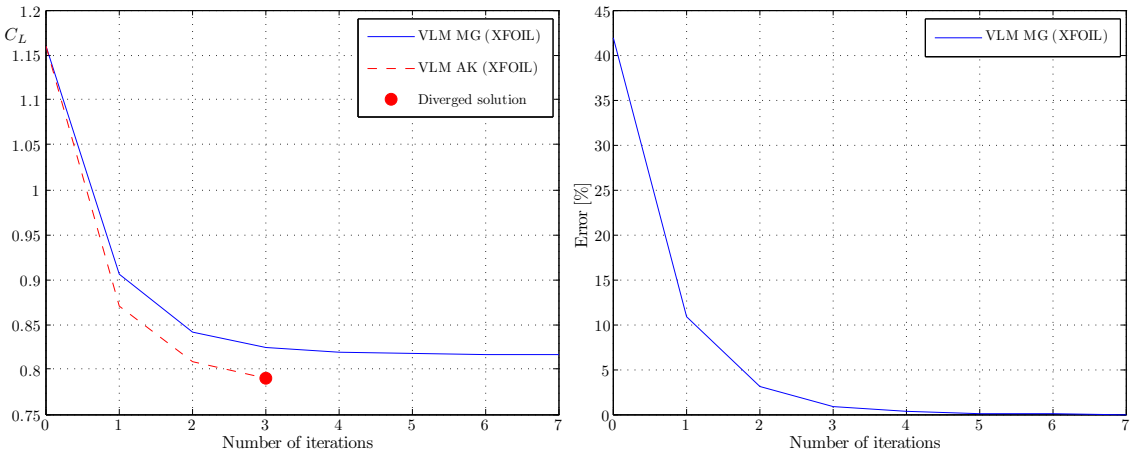

Figure 5.34: Convergence and accuracy of C_L vs number of iterations of the flat wing for $\alpha = 16^o$.

5.5.2 Computational time

The computational times are determined at both discrete angles of attack, thus for a different number of iterations, and by doing a full angle of attack sweep from which an average time per angle of attack follows. The results are given in table 5.6 for which the arc shaped kite with 600 panels is used.

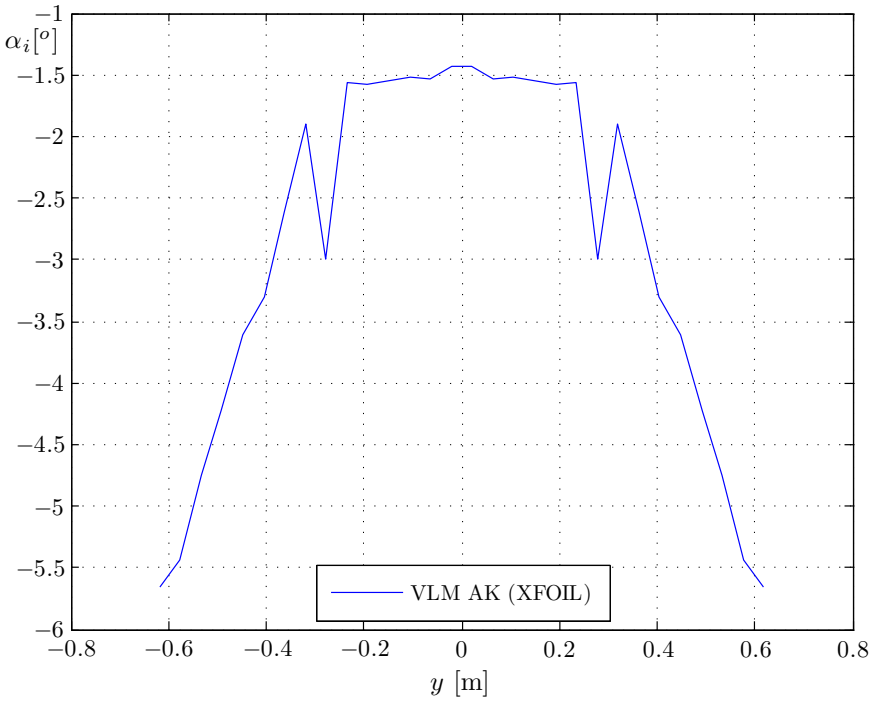

Figure 5.35: Induced angle distribution (VLM AK (XFOIL)) of the flat wing for $\alpha = 16^o$.

Carqueija et al. (2010) states about the computational time of his VLM algorithm: "In average, the algorithm takes around 1.5 minutes to compute one angle". The algorithm presented in this method, which is written in c++, uses only about **100 ms** to compute one angle in VLM2 and therefore presents a huge reduction in computational time (with a clock resolution of 15 ms). The same computation time per angle of attack was observed when doing a full angle of attack sweep. It was found that the number of iterations had no observable influence on the computational time.

For VLM1 computational times are higher, since it uses trailing vortices instead of quad vortices. For 6 and 14 iterations, required calculation times are respectively 307 ms and 561 ms, hence an increase in computational time with increasing iterations is observed. This is probably caused by the relatively time consuming process of calculating the influence of the trailing edge vortices.

The 3D panel method uses 1,240 panels and as a result computational times are significantly higher: 1,148-1,196 ms for 7-13 iterations. The influence of the number of iterations is very small. The average time per angle of attack of an angle sweep gives a much lower value of 680 ms. For the 3D panel method, the TG option (free wake) was not available, therefore the influence coefficients of the wake do not change for varying angle of attack. Thus it can be said that the calculation of the wake influence consumes a significant portion of computational time.

Table 5.6: Effect of the number of iterations on the computational time for the flat wing, using version MG_b.

	VLM1		**VLM2**		**3D panel method**	
discrete α						
α [^{o}]	Iterations	Time [ms]	Iterations	Time [ms]	Iterations	Time [ms]
0	6	307	6	109	7	1,148
3	6	306	7	105	6	1,147
6	5	273	6	108	6	1,173
9	6	306	6	104	6	1,150
12	7	329	6	103	8	1,158
15	14	561	8	106	13	1,196
18	-	-	12	109	-	-
20	-	-	22	115	-	-
α-sweep for [0:1:20]						
Time [ms]	7,614		2,162		14,285	
Average time per α [ms]	363		103		680	

Chapter 6

Aerodynamic analysis of the PowerPlane

From the validation process performed in the previous chapter, the most promising developed methods are chosen. The calculations were performed on regular planar and non-planar wing configurations including a circular arc shaped design. Considering the PowerPlane, a common sailplane configuration is recognized, making the validation cases a reliable basis. In this chapter, the 10 kW PowerPlane model will be used as a test case for the newly developed program. First, the wing profile(s) analysis in XFOIL will be discussed. Then, the most important results are shown from VLM and 3D panel method analyzes performed with the new algorithms. Also, a selection of PowerPlane design considerations is discussed considering the operating conditions and sailplane knowledge. Finally, the effect of gravitational forces is discussed.

6.1 XFOIL analysis

Results from XFOIL analyzes are of great influence on the results in 3D mode, as explained before. The main parameters that couple the 2D and 3D data are the effective angle of attack, α_{eff} and the local Reynolds number. Also, the range of the 2D polars is important, since the non-linear part of the lift curve from 3D analyzes is of great interest for the PowerPlane application. The program should therefore be able to find values in the 2D polars at least up to stall conditions.

6.1.1 Airfoil sections and planforms

The main wing planform airfoil section was designed specifically for this aircraft, which is mainly based on low Reynolds numbers and sailplane experience. A top view of the 10 kW PowerPlane semi-span main wing is shown in figure 6.1. The root airfoil section has a thickness to chord ratio of 14% with the maximum thickness position at $0.282c$. Up to 1.5 m span, the wing is planar with a taper ratio of 0.82 and a decreasing profile thickess of 12.9% at $y = 1.5$ m. From this spanwise station up to the wing tip, a constant dihedral angle of 5^o is applied. A circular shaped wing tip is designed mainly to avoid manufacturing issues, but also lowers induced drag. For 1.5 m $< y <$ 2.25 m, profile

thickness decreases from 12.9% to 12.4%. Then, since the wing tips are rounded off and do not have a constant profile along the wing span, a data set consisting of several spanwise profile locations is used to obtain a tip design that is more realistic. The profile thickness of the last spanwise section (end of wing tip) is 12%.

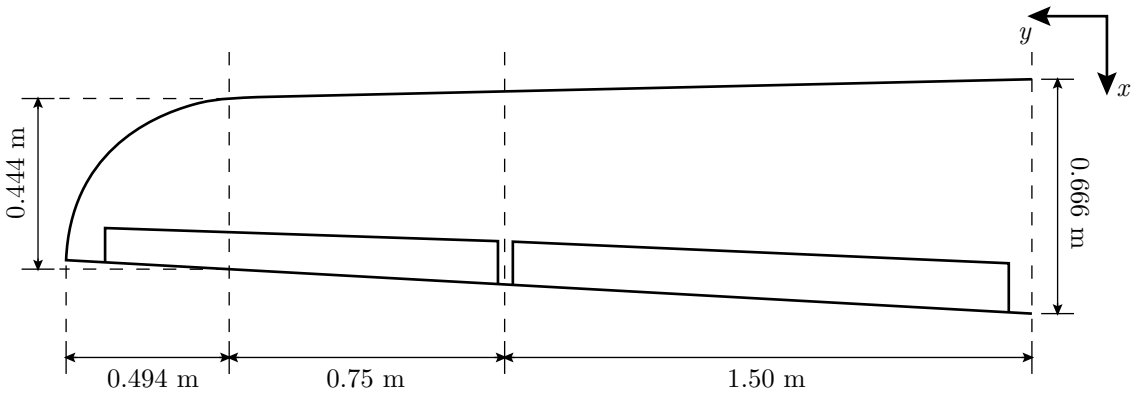

Figure 6.1: Dimensions of the 10 kW PowerPlane main wing.

Dimensions of the horizontal and vertical tail can be seen in figure 6.2. The airfoil used for these tails is the NACA - 0012 profile.

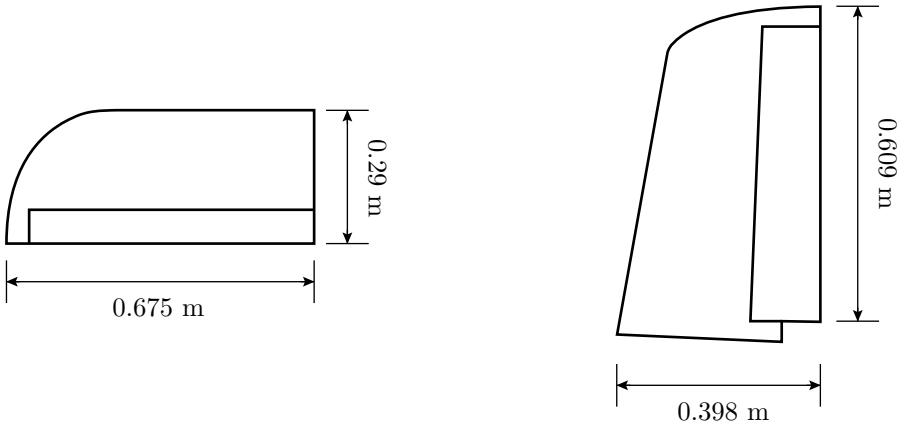

(a) Horizontal tail

(b) Vertical tail

Figure 6.2: Dimensions of the 10 kW PowerPlane horizontal and vertical tail.

6.1.2 2D polars

Settings in XFOIL used for the generation of the 2D lift and drag curves are of great influence on the results. It was shown in chapter 5 that for the turbulence model, a value of $n = 9$ should be chosen. Furthermore, forced upper and lower transition of the airfoil can be set. Calculations showed that the main wing and tail profiles of the PowerPlane have transition locations early due to the presence of a laminar separation bubble. This occurs when forced transition is set at $x/c = 1.0$, meaning no forced transition is used. By setting this value as such, that the boundary layer becomes turbulent before the

separation bubble occurs, results will change. For the following analyzes, however, no forced transition is set. Also, compressibility effects can be included by setting the Mach number. A flight speed of 30 m/s is used in the simulations, thus a value of $M = 0.088$ is considered. Furthermore, the weight of the main wing is 12.7 kg and the total PowerPlane weighs 28 kg. The position of the center of gravity in the x-direction is set at 32.5% MAC, or 0.212 m.

In order to know what Reynolds numbers should be used for the XFOIL calculations, the 3D model of the PowerPlane is build first. From this, the Reynolds number at the root of the main wing showed to be $Re = 1,332,000$ and at the tip $Re = 110,000$. Therefore, a sequence of $(0.1 < Re < 1.4) \cdot 10^6$ is used for the 2D lift and drag polars of the main wing profile, with an increment of $Re = 300,000$. The results are shown in figures 6.3 and 6.4. Here, only the exact Reynolds numbers of root and tip of the used 2D polars are shown, meaning the other polars lie just above/under or in between these curves.

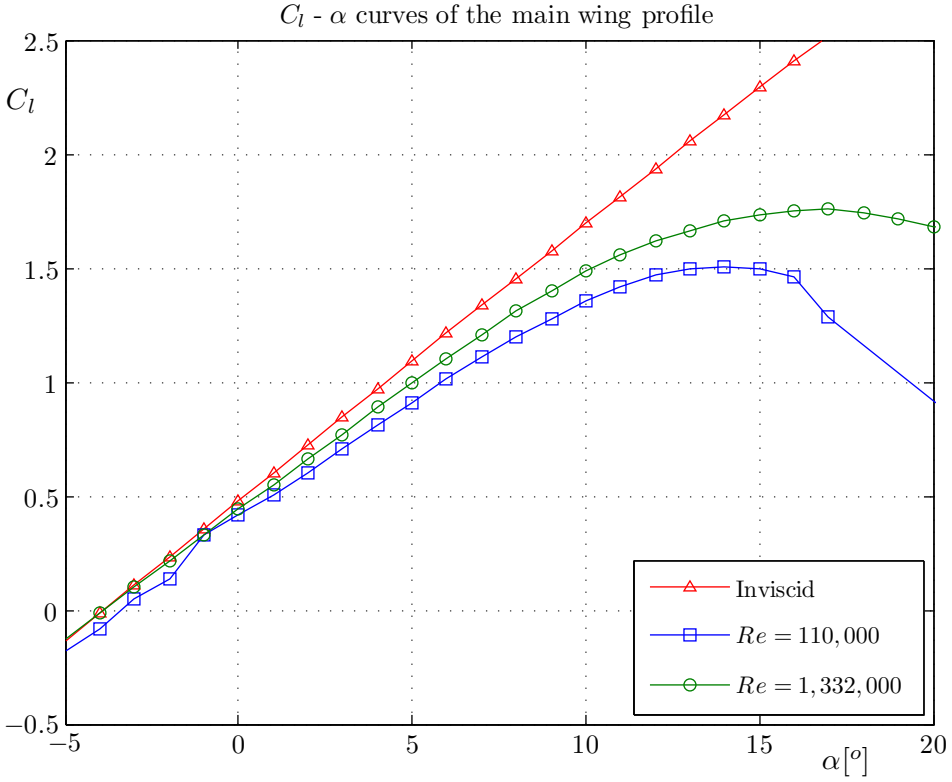

Figure 6.3: $C_l - \alpha$ curves of the 10 kW PowerPlane main wing profile (obtained with XFOIL).

Considering the horizontal tail, at the root $Re = 580,000$ and at the tip $Re = 200,000$. For the vertical tail, at the bottom $Re = 800,000$ and at the tip $Re = 300,000$. Therefore, a sequence of $(2.0 < Re < 8.0) \cdot 10^5$ is used with an increment of $Re = 200,000$. Results of the 2D lift and drag polars of the tail profile are shown in figures 6.5 and 6.6, respectively. Again, only the outer limits of the Reynolds numbers are shown. The other generated polars lie in betweens. It is observed from the lift curve for $Re = 200,000$, that for low angles of attack, non-linearity is introduced where the other curves show to be linear. This phenomena is caused by viscous effects, which are much more effective at such low Reynolds numbers and should therefore be treated with caution.

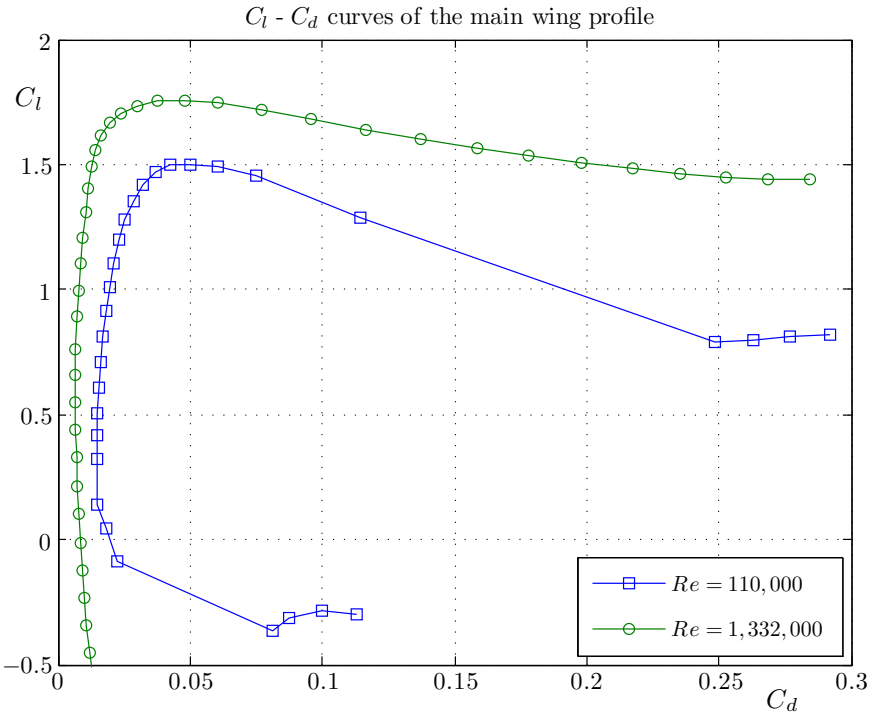

Figure 6.4: $C_l - C_d$ curves of the 10 kW PowerPlane main wing profile (obtained with XFOIL).

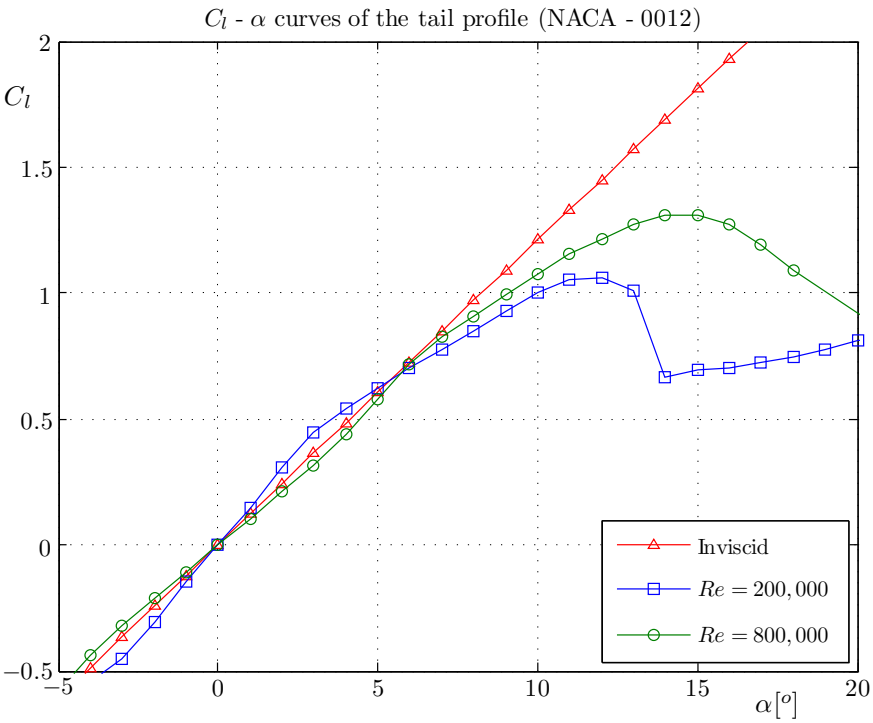

Figure 6.5: $C_l - \alpha$ curves of the 10 kW PowerPlane horizontal and vertical tail profile NACA - 0012 (obtained with XFOIL).

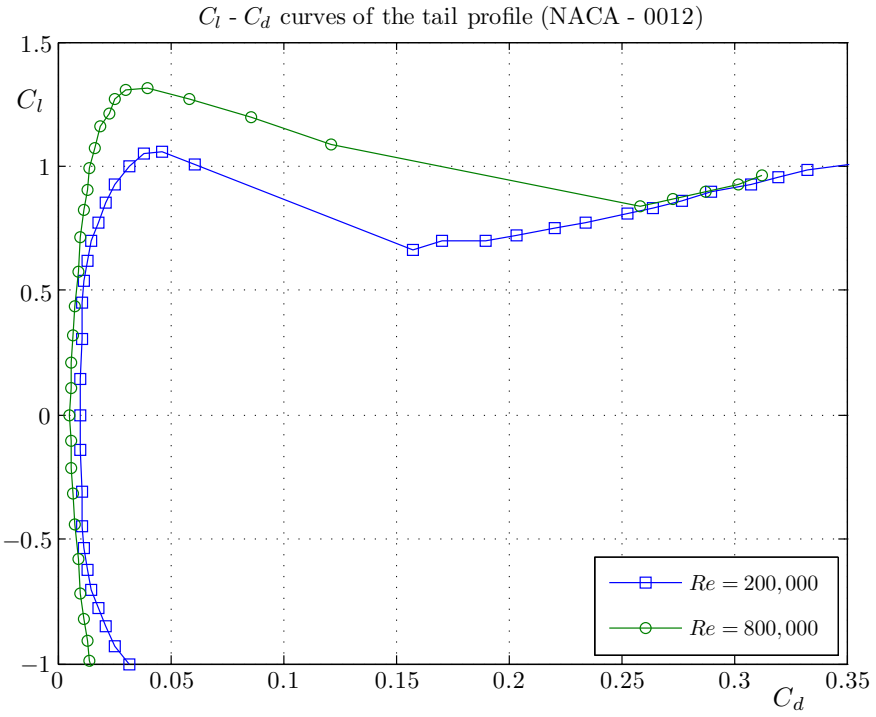

Figure 6.6: $C_l - C_d$ curves of the 10 kW PowerPlane horizontal and vertical tail profile NACA - 0012 (obtained with XFOIL).

6.2 PowerPlane 3D analysis

Now that the required 2D polars are set, a 3D model of the 10 kW PowerPlane main wing can be analyzed with the adapted XFLR5 versions. Here, the methods MG_b and AK are used, considering both VLM and 3D panel method. For the purposes of this report, the exact model which is currently flown with will be treated. Further designing of an improved model will be performed within Ampyx Power, since this is the main interest in the aerodynamic analysis tool.

6.2.1 Model settings

In reality, the wing tip is ending with a sharp edge (no chord). Since modeling this will result in extremely low Reynolds numbers, a small chord length is applied to the end of the wing tip instead. Further, the wing taper, dihedral and offset of the main wing have been implemented. It should be noted that a tilt angle of 4^o is given to the main wing in the complete model. As a result, this angle should be added to the angle of attack in the analysis, such that an angle of attack of 6^o is actually a total angle of attack of 10^o for the main wing. In figure 6.7, the 3D model of the 10 kW PowerPlane in XFLR5 can be seen, including the fuselage and tail configuration.

Next to the main wing and tail, the fuselage is also designed specifically for the PowerPlane, with the main requirement of fitting the hardware/electronics as efficient as possible. However, in the guidelines manual of XFLR5 that comes with the program (XFLR5, 2011a), it is stated that the implementation of a fuselage body will most likely give unrealistic results. This is because the determination of the parameters are based on vortex

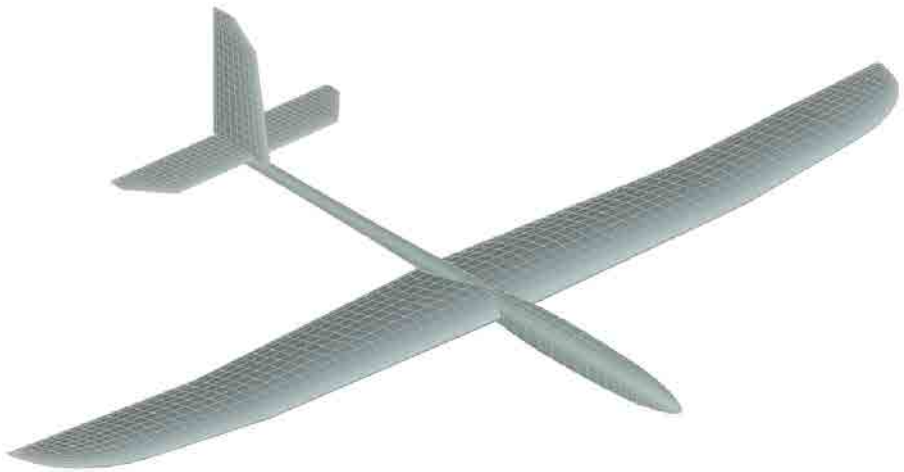

Figure 6.7: Total 10 kW PowerPlane design in XFLR5.

lattice methods and panel methods, which are used to analyze lifting bodies. Since a fuselage is not part of this regime and the additional drag is relatively low compared to the main wing, it is assumed that the most reliable results are obtained with a model that includes only the main wing, horizontal tail and vertical tail. Due to the inability of using the adapted program versions for a wing tail configuration, only the main wing is considered. Since this is the lift generating part of the sailplane, this is of most importance for the design of for example a high maximum lift coefficient. However, a brief discussion on the impact of the fuselage and tail on the lift and drag will be discussed in section 6.2.4.

For the 3D simulations, a free stream velocity of 30 m/s, an air density of 1.225 kg/m^3 and a kinematic viscosity of $\nu = 1.5 \cdot 10^{-5}$ m^2/s are set. A panel discretization is chosen as such, that low aspect ratio panels are obtained with a cosine distribution in chordwise direction to increase panel density towards leading and trailing edge, using 12 panels per section. A uniform distribution is used in the spanwise direction, using a total of 42 sections. Furthermore, the VLM (1,008 panels) with TG option and the 3D panel method (2,040 panels) without TG option are used for the analyzes.

6.2.2 Visualization of results

From using the considered program settings, the most important results are shown in this section. The wing configuration used is shown in figure 6.8, where some interesting results are visualized for $\alpha = 10^o$. First of all, the green distribution on top of the main wing represents the lift forces. The red arrows pointing downwards at the trailing edge of the wing are the downwash velocities, increasing towards the wing tips. The yellow area behind the main wing is the (lift) induced drag and the pink area is the profile/viscous drag. When the latter two areas are added up, the total drag of the wing is obtained. Furthermore, the pressure distribution over the wing is shown, from which the low pressure area is clearly seen at the leading edge. Apart from these results, one can also visualize the panel forces, aerodynamic moments, transition lines, surface velocities and streamlines or animate the visualized results for a certain range of angles of attack.

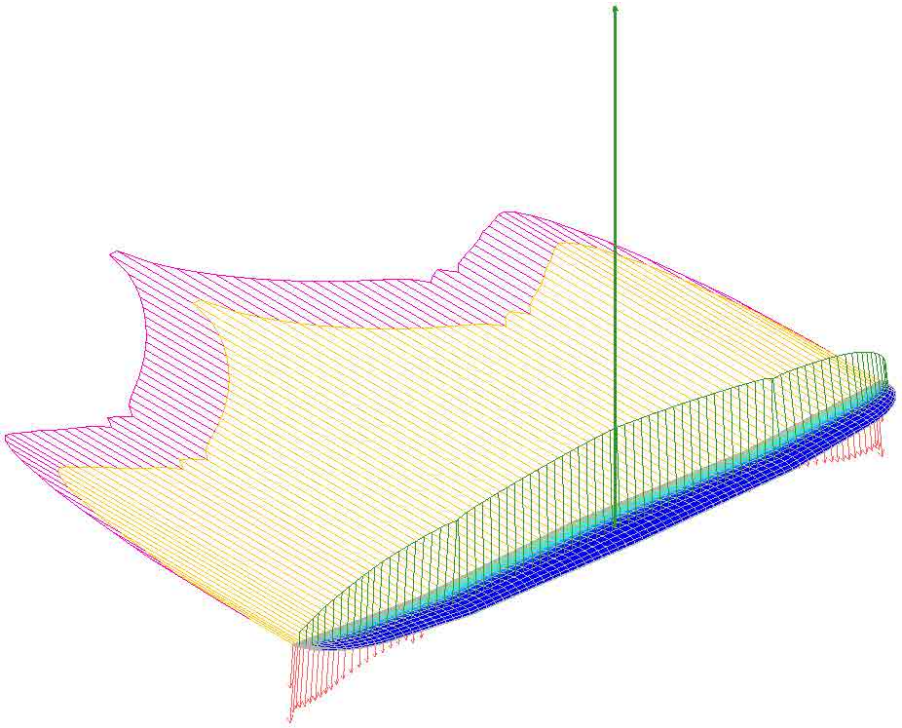

Figure 6.8: Main wing of the 10 kW PowerPlane design in an adapted XFLR5 simulation.

6.2.3 Lift and drag coefficient

The most interesting results are the lift and drag coefficients of the PowerPlane. These values are of great influence of the total system efficiency, but can also be used in dynamic flight models as input. In figure 6.9, the lift curves are shown obtained from the versions MG_b and AK, including the original XFLR5 program. From this figure, it can be clearly seen that the adapted versions approximately give the same results and deviate from the original XFLR5 version. A maximum lift coefficient of $C_{L_{max}} = 1.55$ is obtained at $\alpha = 20^o$. It should be noted that the additional lift of the horizontal tail is not included in figure 6.9. From a separate analysis in the original XFLR5 program, negligible increases in the total lift were observed when including the tail to the wing configuration. Furthermore, it is known that the tail has the purpose of stabilizing the sailplane and not increasing total lift.

The lift vs drag curves resulting from 3D simulations are shown in figure 6.10. Here, the influence of the non-linear lift curve can be clearly seen due to the significant increase in drag at high lift coefficient values. Again, it is observed that the adapted versions give similar results, although VLM MG_b (XFOIL) calculates more values, as can also be seen in figure 6.9.

Finally, the lift to drag ratio curves are shown in figure 6.11. These results show a maximum L/D ratio for the main wing of approximately 35 at $\alpha = 2^o$. The value of L/D will, however, decrease when the drag coefficients of the fuselage and tail would be included. This will be discussed in the following section.

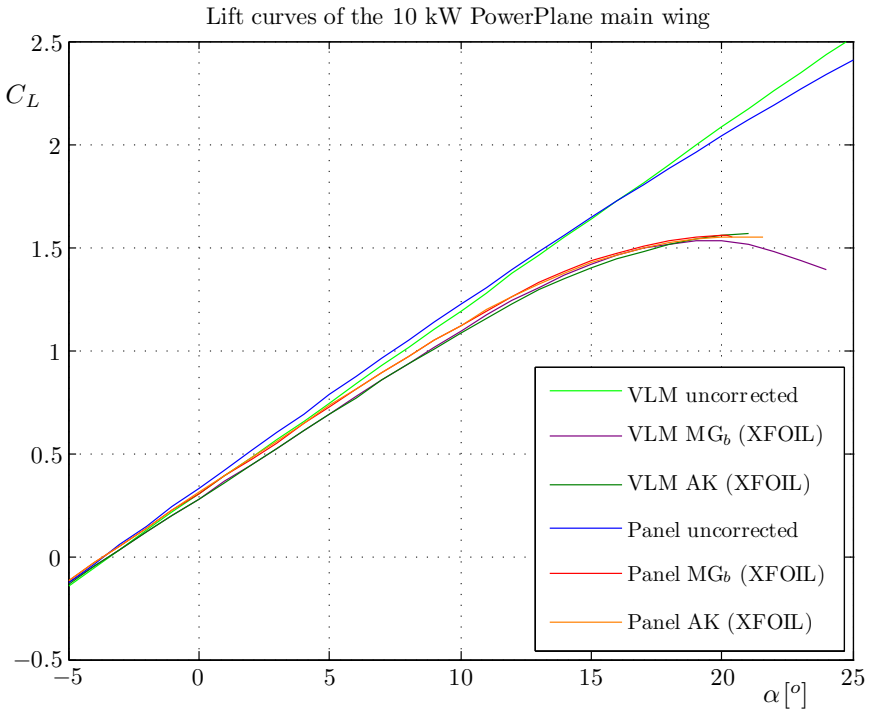

Figure 6.9: The $C_L - \alpha$ curves obtained from XFLR5 simulations (original, MG$_b$ and AK) of the 10 kW PowerPlane main wing.

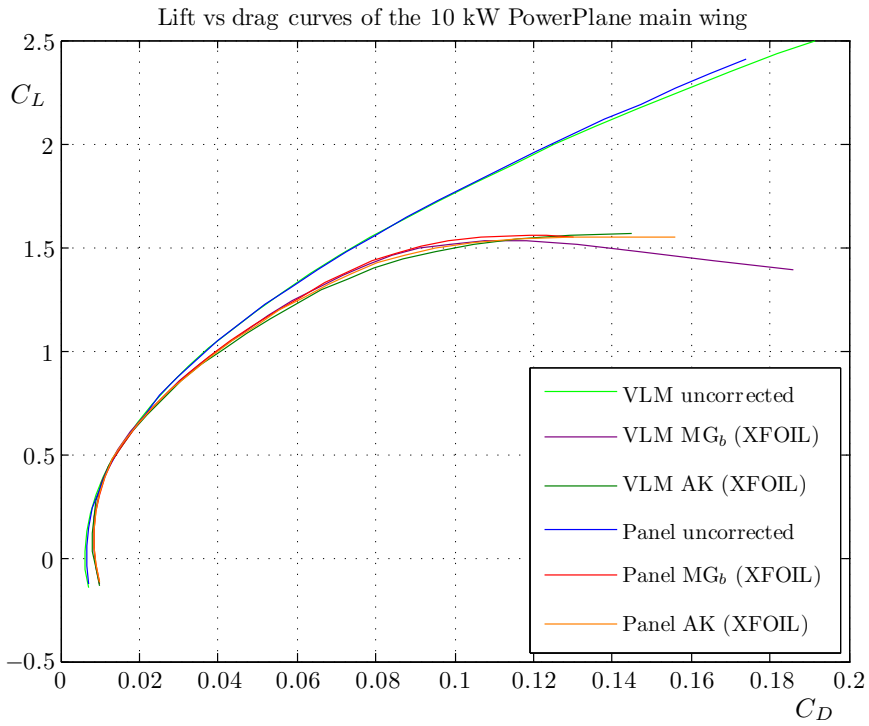

Figure 6.10: The $C_L - C_D$ curves obtained from XFLR5 simulations (original, MG$_b$ and AK) of the 10 kW PowerPlane main wing.

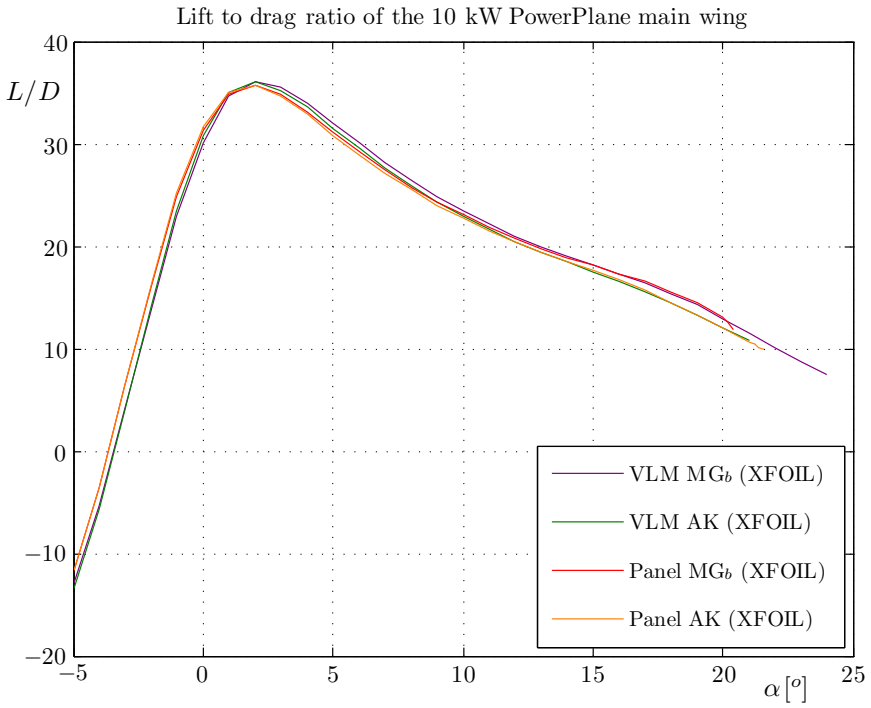

Figure 6.11: The $L/D - \alpha$ curves obtained from XFLR5 simulations (MG_b and AK) of the 10 kW PowerPlane main wing.

6.2.4 Spanwise distributions

Total lift and drag coefficients, as shown in the previous section, are a result of the integrated spanwise lift and drag distributions. With these results, one can for example find issues such as locations where early stall occurs. Since the PowerPlane flies at high angles of attack, spanwise distributions of the non-linear part of the lift curve until stall conditions are interesting. In figure 6.12, the lift distribution of the main wing at $\alpha = 10^o$ is shown. The deviation from the original XFLR5 version is clearly seen here. Also, a fluctuation near the dihedral inflection point at $y = 1.5$ m is observed for the 3D panel method. This can be smoothened by using less panels near this area.

Since only a wing configuration is considered, the effect of the fuselage on the lift distribution is not taken into account. Although the wing will induce lift on the body, it will not generate lift by itself. Therefore, a den will be present in the lift distribution where the fuselage is located. The induced lift on the fuselage can be determined as shown in equation 6.1 (Hoerner, 1946).

$$C_{L_f} = 2kC_L \tag{6.1}$$

Here, $k \approx 0.25$ and C_L represents the lift coefficient that would be present on a single wing configuration near the root. For the viscous lift distributions shown in figure 6.12, this means that for -0.08 m $< y <$ 0.08 m, where the fuselage is located, the local lift coefficient would have a value of 0.85. This would decrease the total (integrated) lift coefficient by approximately 2%.

In figure 6.13, the drag distribution of the main wing at $\alpha = 10^o$ is shown. As with the lift distribution, fluctuations are present near the dihedral inflection point, especially

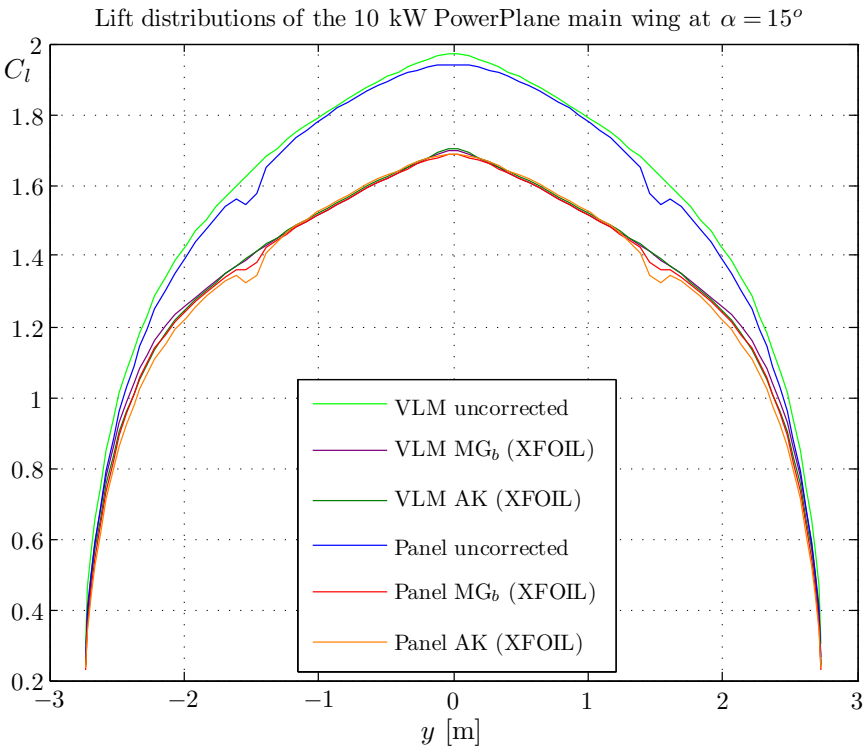

Figure 6.12: The $C_l - y$ distributions obtained from XFLR5 simulations (original, MG$_b$ and AK) for the 10 kW PowerPlane main wing with $\alpha = 15^o$..

for the 3D panel method. Also near the wing tips, fluctuations are visible, which is due to discretization issues. This could be solved by using less panels near the wing tip.

Both the effect of the fuselage and tail are not taken into account for the drag calculation. The relative drag coefficient of the fuselage with respect to the main wing can be determined as shown in equation 6.2, where C_{D_f} represents the drag coefficient of the fuselage and A_f is the frontal surface area of the fuselage.

$$C_{D_{f,rel}} = \frac{C_{D_f} A_f}{S} \tag{6.2}$$

From Thomas (1979), a value of $C_{D_f} = 0.08 C_D$ is found for a lift coefficient of $C_L = 1.0$. This corresponds to a value of $C_D = 0.04$, as can be seen in figure 6.10. From equation 6.2, and using $A_f = 0.0256$ m^2 and $S = 3$ m^2, it follows that $C_{D_{f,rel}} = 2.73 \cdot 10^{-5}$. This value is assumed to be negligible when compared to the drag coefficient of the main wing.

In order to take into account the drag of the horizontal and vertical tail, these have been analyzed separately with the original XFLR5 program. It showed that adding the tail to the wing configuration, increased the drag coefficient by a value of 0.0036. This implies an increase of the total drag coefficient of 5% with respect to the main wing configuration.

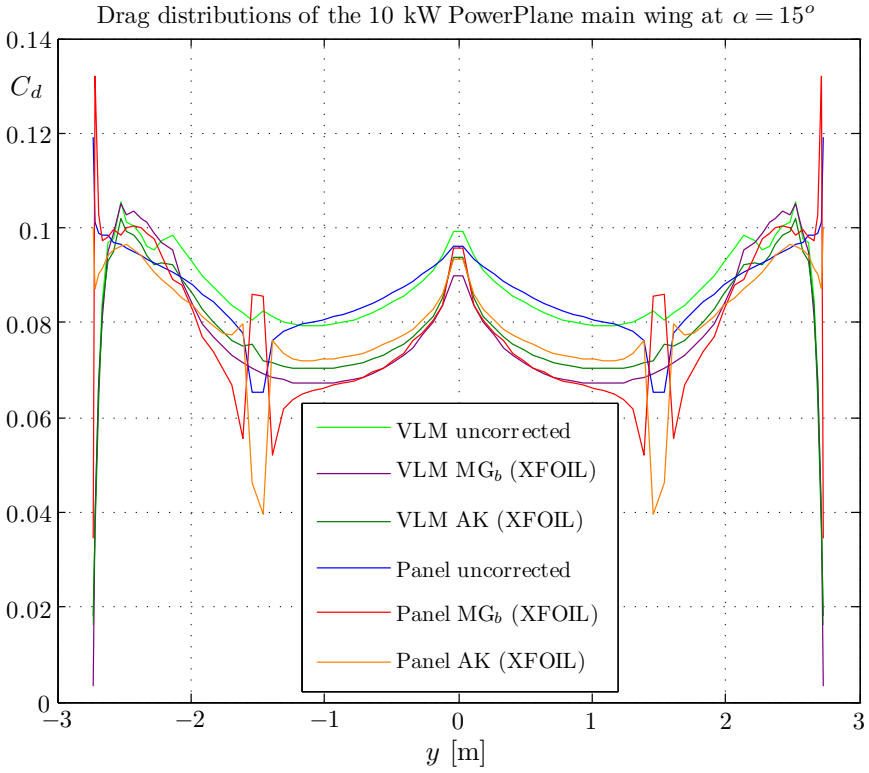

Figure 6.13: The $C_d - y$ distributions obtained from XFLR5 simulations (original, MG$_b$ and AK) for the 10 kW PowerPlane main wing with $\alpha = 15^o$.

6.3 Design considerations

Calculations have been performed on the present 10 kW PowerPlane design. This is, however, far from an optimal design. The main focus in the starting phase of Ampyx Power was laid on creating a working airborne wind energy system. Therefore, a regular sailplane configuration was used with dimensions that are based on required wing surface area for a 10 kW system. At this point, optimization of the PowerPlane aerodynamics become of great interest. In this section, several design considerations are discussed making use of common sailplane aerodynamic knowledge and taking into account the operating conditions of the PowerPlane. These theories are collected from Veldhuis (2012) and discussions with sailplane aerodynamics expert Boermans from the Delft University of Technology.

6.3.1 Airfoil

Depending on the requirements, a laminar or turbulent airfoil can be chosen. Laminar airfoils are typically used to obtain a constant favorable pressure gradient, resulting in laminar flow and low drag. A turbulent airfoil has a more blunt leading edge, that creates a long steep favorable pressure gradient causing earlier transition (see figure 6.14).

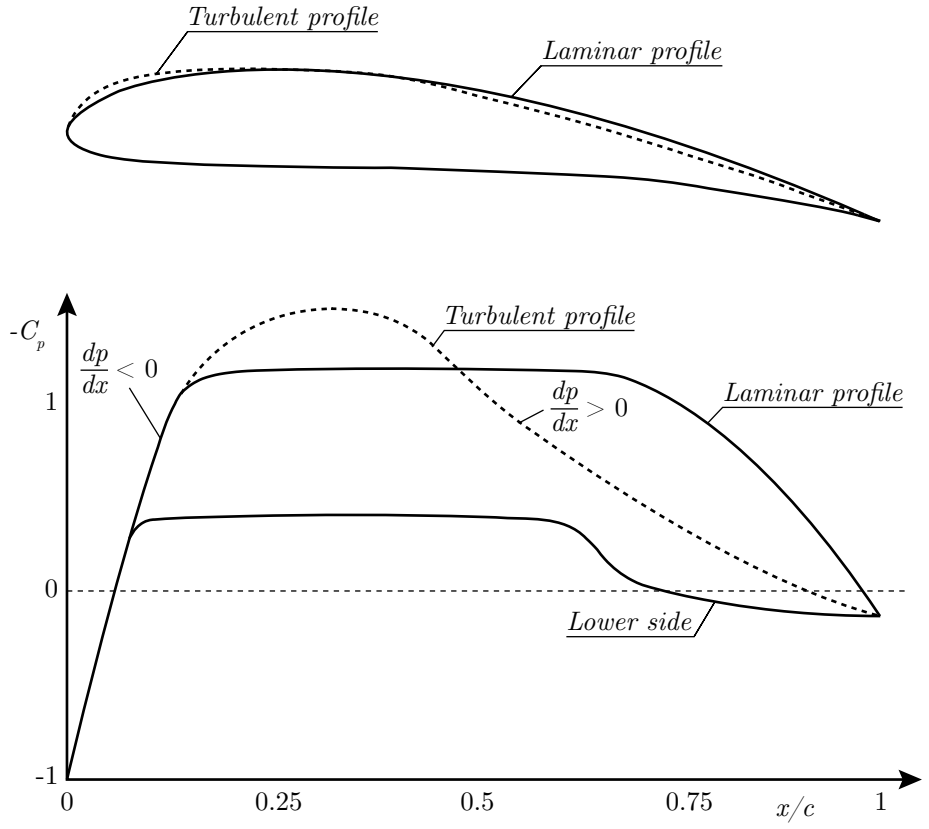

Figure 6.14: Laminar and turbulent airfoil with corresponding pressure distributions.

Turbulence causes turbulent fluctuations to increase shear stresses, known as Reynolds stress. This can be seen from the Prandtl boundary layer equation, shown in equation 6.3.

Here, the last term is the Reynolds stress term and only applies to turbulent boundary layers.

$$\rho u \frac{\partial u}{\partial x} + \rho v \frac{\partial u}{\partial y} = -\frac{dp}{dx} + \mu \frac{\partial^2 u}{\partial y^2} + \frac{\partial}{\partial y}\left(-\rho \overline{u'v'}\right) \tag{6.3}$$

Although a longer turbulent boundary layer exists on a turbulent profile, a higher minimum pressure peak can be obtained, resulting in a higher $C_{L_{max}}$. Other typical characteristics of a turbulent airfoil are low cruise drag and a high climb L/D. Since the PowerPlane is used to produce power and flies at high angles of attack, a turbulent airfoil would be more efficient since higher maximum lift coefficient can be reached.

Another way to increase the lift of an airfoil and improve land and climb performance is by means of adding elements to the leading and/or trailing edge. Most commonly used are slats and flaps, both increasing camber and chord length. Since multi-element airfoils increase complexity, for example slotted flaps would already increase lift significantly. Delaying transition and stabilizing the boundary layer also improves lift. Possibilities to do so are applying surface roughness, surface cooling and boundary layer suction. However, such applications again bring complexity to the design.

6.3.2 Fuselage

When designing an airfoil, the main parameter to taken into account is the curvature. The hand rule is to keep the third derivative of the curvature constant to prevent discontinuities in the pressure distribution. The curvature is defined as the inverse of the local radius of curvature. In principle, the same holds for fuselage design. Air flow is bent due to an inclined wing, which increases with a higher angle of attack. A fuselage would induce the lowest amount of profile drag when the shape in streamwise direction is curved such that it follows the streamlines of the flow. Since the PowerPlane flies at high angles of attack, applying such a shape would be beneficial in terms of lower drag.

Currently, the PowerPlane fuselage consists of a cylindrical beam and shell around the electronics on the nose. When a total fuselage would be considered, the connection with the main is of importance. Near the wing root, turbulent flow occurs due to the interference of the fuselage. In order to prevent early separation, a turbulent profile can be used here. Also, a turbulent boundary layer might grow in the spanwise direction. This can be averted by adapting the leading edge near the fuselage connection as shown in figure 6.15.

6.3.3 Wing tips

The other end of the wing is also important in terms of aerodynamic performance. Since the induced drag coefficient is a function of ${C_L}^2$ and the PowerPlane flies at high lift coefficients, C_{D_i} will increase rapidly relatively to C_{D_0}. This can also be explained with the fact that the airspeed is a function of the inverse of C_L. High lift will therefore induce a low airspeed, at which C_{D_i} is certainly not negligible with respect to C_{D_0}.

Most effective to lower induced drag are increasing the aspect ratio and efficiently designing the wing tips. There is a limit to the aspect ratio due to structural reasons. Therefore, several wing tip designs are invented to increase performance without increasing the wing span. First of all, scientists discovered that using a triangular wing tip lowered induced drag due to smaller existing wing tip vortices. From experiments, it

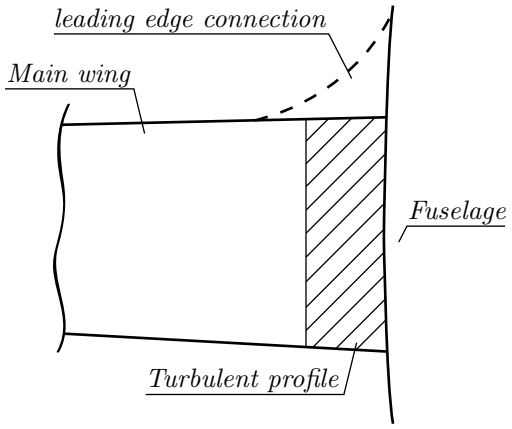

Figure 6.15: Connection between fuselage and main wing.

showed that rounding of the wing tip increases efficiency slightly, but the curvature is not important. Another option is to use so called Hoerner tips, which are known as oblique cut wing tip edges. By principle, this shape pushes the wing tip vortex away from the wing, causing less disturbance in the trailing wake. However, the impact is expected to be low.

Winglets are the most well known devices to lower induced drag of aircraft. These devices suppress the effect of tip vortices, by preventing the vortex reaching the upper surface (low pressure side) of the wing. This will decrease the downwash as such, that a more constant downwash distribution is obtained. Furthermore, winglets allow steeper climb and reduce noise. On the other hand, for a fixed span wing plus winglet with height h, a wing semi-span increase of $0.45h$ produces the same drag as the wing plus winglet combination. An increase in span, however, will increase the root bending moment significantly. Ampyx Power will design an exchangeable wing tip, such that easily can be switched between a rounded off wing tip and a winglet.

Design parameters of winglets are important to take into account. The height is limited to the allowable bending moment of the wing. Certainly for aircraft that are designed without winglets, this parameter is of importance, since it will change the total performance. The sweep angle of a winglet should be larger than that of the wing, to ensure no Mach effects occur near the wing tip. Also, a winglet is normally set backwards, as shown in figure 6.16. This is to prevent the thickest point of the winglet airfoil to coincide with that of the main wing. Otherwise, the lowest pressure areas would increase air velocities, such that higher Mach numbers are obtained than without a winglet. The set back and swept back winglet therefore has a small chord at the tip, resulting in low Reynolds numbers and large viscous effects. Zigzag tape is used for low speed sailplanes to prevent separation here. Also, a toe-out angle is normally applied to compensate for bending of the wing. Still, effects such as boundary layer interaction occurs with a sharp connection between wing and winglet. Therefore, blended wings are designed to prevent this phenomena (see figure 6.16). Furthermore, parameters to take into account are the incidence angle, twist and airfoil selection of the winglet.

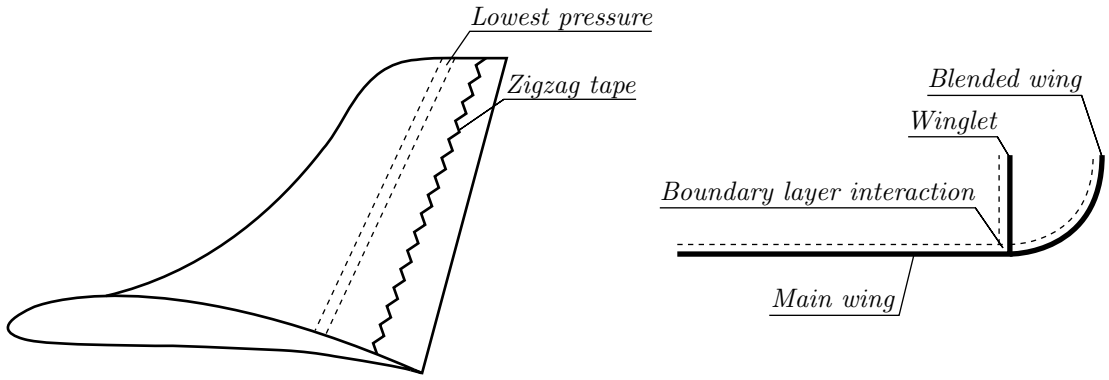

Figure 6.16: Side view (left) and front view (right) of a winglet configuration.

6.4 Gravitational forces

Different from ordinary sailplanes, the PowerPlane flies continuously at high angle of attack (not on $(L/D)_{max}$). But since the PowerPlane is connected to a tether all the time, gravitational forces act on the plane during the power production phase. Measurements showed that during turns, forces of 3-5 G are reached. The flight speed can be determined as

$$v = \sqrt{\frac{W}{S}\frac{2}{\rho}\frac{1}{C_L}} \tag{6.4}$$

Here, W is in principle the aircraft weight at 1 G. But the PowerPlane is actually several times larger during most of the flight time. It is, however, not known what the effects are precisely and how these forces should be incorporated in for example equation 6.4. This also holds for the induced drag, which is proportional to the weight and wing span as

$$D_i \propto \left(\frac{W}{b}\right)^2 \tag{6.5}$$

From this relation, it can be seen that the induced drag is not dependent on the chord, thus aspect ratio, but on the wing span. Since profile drag is dependent on wing surface area, high aspect ratio's are still preferred. But again for the induced drag relation in equation 6.5, it is uncertain if gravitational forces play a role in the weight term.

Chapter 7

Conclusions and recommendations

During the performed research, the goal was to develop a tool to asses the impact of design parameters on the aerodynamics of the Ampyx PowerPlane. Requirements are that this tool should be computationally fast and give realistic values. The most important values are the lift and drag coefficients at high angles of attack, up to stall conditions. During the process, it became clear that a variety of methods were available to include viscosity in 3D simulations. These methods are derived from previously performed research, but were either not completely validated or only used for straight non-planar wings.

A study has been performed on aerodynamic calculation methods that are widely used in the field of wing and plane design. In order to obtain realistic results, without the cost of long computation times, two potential flow based methods are selected: the VLM and 3D panel method. The downside of these methods, however, is that the results are inviscid and thus stall (separation) conditions are neglected. Therefore, methodologies are investigated that use a viscous lift correction to implement non-linear behavior. These methods are based on the principle of performing a shift on the effective angle of attack on 2D lift polars from airfoil analysis, to account for viscous effects in 3D analyzes. For each spanwise station, these angle shifts are performed, such that the 3D wing works at an angle of attack that has the same lift coefficient as the viscous lift coefficient before the angle shift. It should be noted that these methods use 2D viscous effects applied in a 3D environment, while 3D viscous effects are not taken into account.

Since a number of methods were available to implement the effect of viscosity in 3D calculations, four different program versions were obtained, tested and compared to each other. A well known sailplane aerodynamics tool called XFLR5 is used for this, due to the proper user interface, the integration of XFOIL and the possibility to choose between both the VLM and 3D panel method. A trade-off procedure is performed, with the main focus on the linear and non-linear part of the lift and associated drag curve and the location and value of the stall point. For this, 2D and 3D wind tunnel data and CFD results have been used, consisting of a variety of wing configurations.

From the trade-off, it showed that a value of $n = 9$ for the turbulence model in XFOIL gave more useful results than $n = 12$ considering the combination of accuracy and reached stall points. For the VLM, the effect of thickness was artificially included by performing angle shifts on inviscid 2D lift polars following from thin airfoil theory. Since the viscous 2D XFOIL polars contain thickness (2D panel method), taking the difference between

these polars would include a thickness effect in 3D calculations. The use of inviscid 2D lift polars with and without a thickness effect are compared with each other by means of VLM simulations. This showed that the use of inviscid XFOIL polars gives more accurate results than using thin airfoil theory. This shows a limitation to the practical use of a correction based on 2D characteristics in a 3D simulation.

The angle shifts are implemented by changing the local free stream angle of attack at the RHS, as proposed by Gaunaa. The method of Horsten in combination with this method (AK) showed the most accurate results in the non-linear lift and corresponding drag region. This holds for both the VLM and 3D panel method. However, the use of induced angles to determine the angle shift results in peaks in the spanwise distributions of induced and effective angle of attack. Therefore, version AK often does not reach the stall point, since the solution is diverged due to the expanded peaks. This weakness is not noticed when using the MG based versions, resulting in more predicted stall points. Therefore, next to version AK, a second version is chosen to be most promising. From the performed trade-off, it showed that using the final effective angle of attack to determine the profile drag is most accurate. This corresponds to version MG_b. Since Gaunaa originally uses the initial effective angle, this is an improvement on his work. Both most promising program versions predict non-linear lift and associated drag coefficients within an error of 10%. The values and locations of the stall points lie within an error of 10% when compared to experimental data. Lift and drag coefficients beyond stall should, however, be treated with caution.

Simulations showed that the wing discretization and number of iterations are of great influence on the accuracy of results and computational time. Most promising and efficient results were obtained by using a cosine distribution in the chordwise direction and a uniform distribution in the spanwise direction with low aspect ratio panels. For the MG_b version, a maximum number of 14 iterations was required for the validation cases, corresponding to the results that showed to be most accurate. For the AK version, 1 iteration is used, since more iterations results in unstable fluctuations in the induced angle distributions, leading to a diverged solution. However, similar results are obtained with both adapted versions, following from a rapidly converging solution. Simulation times for an angle of attack sweep of 21 steps to obtain complete 3D lift and drag polars are 2, 7 and 14 seconds for the quad vortex lattice method, horseshoe vortex lattice method and 3D panel method, respectively. The large amount of trailing vortices in the horseshoe vortex method and the double amount of panels in the 3D panel method makes these methods slower. For one single angle of attack, approximately 100 ms is required using the quad vortex method. Comparing total lift and drag curves, no significant differences are observed between both VLM's and therefore the quad vortex method is used.

Significant improvements are observed when comparing results of the adapted programs with the original XFLR5 version. In the linear region of the lift and associated drag curve, negligible differences are observed. This is expected, since the VLM and 3D panel method are known to be accurate in the inviscid region. In the non-linear region, however, the average deviation in lift of the uncorrected version is $12 \cdot 10^{-2}$, whereas the adapted versions show a deviation of $3 \cdot 10^{-2}$. The validation cases all have a maximum lift coefficient of approximately 1, thus the increase in accuracy can be said to be significant. Also, concerning the drag coefficients in the non-linear lift region, a significant decrease in deviation on the drag coefficient value is obtained when compared to the uncorrected XFLR5 version: $11 \cdot 10^{-3}$ compared to $3 \cdot 10^{-3}$. It can be concluded that one of the

two most promising versions shows a higher accuracy in predicting non-linear lift and associated drag coefficients and the other predicts more stall points. Therefore, one can choose to consider both versions and use their results to have solutions that are accurate on all defined criteria.

From simulations performed on the 10 kW PowerPlane, a maximum lift coefficient of $C_{L_{max}} = 1.55$ was obtained at $\alpha = 20^o$. This implies an increased accuracy of 30% on the maximum lift and 40% on the corresponding drag coefficient, when compared to results of the original XFLR5 version. Furthermore, it was observed that the discretization around the dihedral inflection point and wing tip have a significant effect on the lift and drag distributions, especially using the 3D panel method. This can be treated by using less panels near these regions, preventing calculations errors on fine panels. Furthermore, the influence of the fuselage and tail on the total lift and drag of the PowerPlane showed to be small. The fuselage induces a decrease in total lift coefficient of 2% and the tail increases the total drag coefficient by 5%.

Although realistic aerodynamic coefficients are predicted fast with the developed tools, there are some improvements that could be made to increase accuracy of the results. First of all, there seem to be discretization problems when using dense panels near area such as the root, tip and dihedral inflection points. Therefore, improvements can be made on the discretization of the VLM and 3D panel method in XFLR5. Furthermore, the use of XFOIL polars showed to differ from 2D wind tunnel data regularly. Especially for very low Reynolds numbers, this seemed to be the case. Since the 2D lift and drag polars are of great influence on the 3D results, it is recommended to use 2D data either from wind tunnel measurements or CFD simulations.

During the development of the aerodynamic analysis tool, a newer version of XFLR5 (6.07) was published. In this version, the free wake option is made available for the 3D panel method, which should increase accuracy. Since this option was not available in version 6.06, the effect on accuracy of using a free wake instead of a fixed wake in a 3D panel method is to be investigated. Also, using a wing tail configuration is not possible in the adapted versions, since a combination of VLM and 3D panel method is used here. Although the tail has a small influence on total lift and drag, this option could be made available. It should be noted that this mixture of methods only uses the VLM for the wings. A fuselage can be analyzed with the 3D panel method, but because of the inefficient connection to the main wing and since it is a non-lifting body with relatively low drag, this option is not considered. Improvement can be obtained by implementing a complete 3D panel method in XFLR5, such that a full sailplane configuration can be analyzed with the adapted versions. Furthermore, the PowerPlane often flies with extended flaps during the power production phase, increasing the maximum lift coefficient. The resulting lift and drag polars can be obtained by applying flaps to the airfoil in XFOIL. Further investigation is required to determine the accuracy and influence on the results of such modifications.

Bibliography

Ampyx Power. (2011). *The PowerPlane Concept.* www.ampyxpower.com. (Accessed 10 October 2011)

Anderson, J. (1980). Numerical lifting line theory applied to drooped leading-edge wings below and above stall. *Journal of Aircraft*, *17*, 898-904.

Anderson, J. D. (2007). Fundamentals of Aerodynamics. *McGraw-Hill, USA*.

Autodesk Inc. (2011a). *Project Falcon, Model using wind direction/strength and resultant airflow/pressure.* labs.autodesk.com/utilities/falcon/. (Accessed 1 December 2011)

Autodesk Inc. (2011b). Project Falcon Validation.

Bontekoe, E. (2010). Up! How to Launch and Retrieve a Tethered Aircraft. *Master of Science Thesis, Faculty of Aerospace Engineering, Delft University of Technology*.

Carqueija, P. F. P., Eca, L. R. da Cunha de, Gaunaa, M., Carvalho Gato, L. M. de, & Campos Henriques, J. C. de. (2010). Aerodynamic Investigations of a High-altitude Wind Energy Extraction System. *Dissertation, Mechanical Engineering, Risø National Laboratory, Denmark*.

Coenen, E., Veldman, A., & Patrianakos, G. (2000). Viscous-inviscid interaction method for wing calculations. *Proc Euro. Congr. Comp. Meth. in Appl. Sc. and Eng., ECCOMAS 2000*.

Cyberiad. (1981). *Airfoil: NACA 0012.* www.cyberiad.net/library/airfoils/foildata/n0012cl.htm. (Accessed 20 April 2012)

Drela, M., & Youngren, H. (2011a). *AVL Overview.* web.mit.edu/drela/Public/web/avl/. (Accessed 20 December 2011)

Drela, M., & Youngren, H. (2011b). *XFOIL Subsonic Airfoil Development System.* web.mit.edu/drela/Public/web/xfoil/. (Accessed 3 November 2011)

Engelen, S. P. J. (2011). Up-scaling of airborne wind energy systems. *Ampyx Power internal document, The Hague*.

Garner, H. C., Rogers, E. W. E., Acum, W. E. A., & Maskell, E. C. (1966). Subsonic Wind Tunnel Wall Corrections. *AGARD (Advisory Group for Aerospace Research & Development), North Atlantic Treaty Orginzation*.

Gaunaa, M., Carqueija, P. F. P., Rethore, P. E., & Sørensen, N. N. (2010). A computationally efficient method for determining the aerodynamic performance of kites for wind energy applications. *Risø National Laboratory, Denmark*.

Gilbert, L. (2011). *Technical and theoretical aspects of RC yacht racing.* www.onemetre.net. (Accessed 10 January 2012)

Hatch, G. (2009). *Why Are Wind Turbines Getting Bigger?* www.terramagnetica.com/2009/08/01/why-are-wind-turbines-getting-bigger/. (Accessed 6 October 2011)

Hoerner, R. T. (1946). Fluid Dynamic Lift. *NACA Technical Note 1033, Langley Memorial Aeronautical Laboratory, Langley Field, Washington*.

Horsten, B. J. C., & Veldhuis, L. L. M. (2009). A New Hybrid Method to Correct for Wind Tunnel Wall- and Support Interference On-line. *World Academy of Science, Engineering and Technology*, *vol. 58*.

Jayaraman, D. (2006). *Panel Method Based 2-D Potential Flow Simulator.* www.mathworks.com/matlabcentral/fileexchange/12790. (Accessed 13 December 2011)

Jones, R. T. (1946). Wing Plan Forms for High-Speed Flight. *NACA Technical Note 1033, Langley Memorial Aeronautical Laboratory, Langley Field, Washington*.

Joseph, D. (2003). Viscous potential flow. *Journal of Fluid Mechanics*, *479*, 191-197.

Katz, J., & Plotkin, A. (1991). Low-Speed Aerodynamics - From Wing Theory to Panel Methods. *San Diego State University*.

La Rocca, G. (2008). Aircraft Design. *AE3-021 lecture slides, Faculty of Aerospace Engineering, Delft University of Technology*.

LabS55. (2011). *Ampyx Power: Airborne Wind Energy competitive with fossil fuels.* www.labs55.nl/unit_28-29.html. (Accessed 20 October 2011)

Lankhorst Ropes. (2011). *High performance ropes Lanko Force.* www.lankhorstropes.com/Maritime/Products/ropes/LANKOFORCE. (Accessed 6 November 2011)

Levesque, T. (2007). *Flying Wind Turbines.* www.inhabitat.com/flying-wind-turbines. (Accessed 12 October 2011)

Lock, R., & Williams, B. (1987). Viscous-inviscid interactions in external aerodynamics. *Progress in Aerospace Sciences*, *24*(2), 51-171.

Loyd, M. L. (1980). Crosswind Kite Power. *Journal of Energy*, *vol. 4*(no. 3), pp. 106-111.

Magenn Power. (2011). *Magenn Air Rotor System.* www.magenn.com/technology.php. (Accessed 17 October 2011)

Makani Power. (2011). *Update: First unconstrained flight.* www.makanipower.com/company/news/page/2. (Accessed 10 October 2011)

Maskew, B. (1987). Program VSAERO Theory Document. *NASA Contractor Report 4023*.

Melin, T. (2000). A vortex lattice MATLAB implementation for linear aerodynamic wing applications. *Master's Thesis, Royal Institute of Technology (KTH)*.

Munk, M. M. (1923). The Minimum Induced Drag of Aerofoils. *NACA Technical Report R-121*.

Ohya, Y. (2004). Drag of circular cylinders in the atmospheric turbulence. *Fluid Dynamics Research*, *vol. 34*, pp. 135-144.

Paraschivoiu, I. (2003). *Subsonic Aerodynamics.* Presses inter Polytechnique.

Ragheb, M. (2011). Wind shear, roughness classes and turbine energy production. *Wind Power Systems, University of Illinois at Urbana-Champaign*.

Renewable Energy Sources. (2011). *Airborne Wind Turbines - Can They Change The Wind Energy Industry.* www.renewable-energy-sources.com/2011/11/22/airborne-wind-turbines-can-they-change-the-wind-energy-industry. (Accessed 10 October 2011)

Ruiterkamp, R. (2009). Powerplane Sizing and Optimization. *Ampyx Power internal document SO0902, The Hague*.

SailPlane Directory. (2011). www.sailplanedirectory.com. (Accessed 26 October 2011)

Schmehl, R. (2011). Traction and energy generation with kites. *AE4T40 lecture slides, Faculty of Aerospace Engineering, Delft University of Technology*.

Sieberling, S., & Ruiterkamp, R. (2011). The Powerplane an Airborne Wind Energy System Conceptual Operations. *Ampyx Power, The Hague*.

Sivells, J., & Neely, R. (1947). *Method for calculating wing characteristics by lifting-line theory using nonlinear section lift data* (Tech. Rep.). DTIC Document.

Smith, S. C. (1996). A Computational and Experimental Study of Nonlinear Aspects of Induced Drag. *NASA Technical Paper 3598, Ames Research Center, Moffett Field, California*.

Stokes, G. (1851). On the Effect of the Internal Friction of Fluids on the Motion of Pendulums. *Transactions of the Cambridge Philosophical Society*, *9*, 8.

Thomas, F. (1979). *Grundlagen für den Entwurf von Segelflugzeugen.* Motorbuch Verlag, Stuttgart.

Tinling, B. E., & Kolk, W. R. (1951). The effects of Mach number and Reynolds number on the aerodynamic characteristics of several 12-percent-thick wings having 35^o of sweepback and various amounts of camber. *National Advisory Committee for Aeronautics, Washington*.

TIOBE Programming Community Index. (2009). www.tiobe.com/index.php/content/paperinfo/tpci/index.html. (Accessed 3 August 2011)

Twind. (2011). *High Altitude Wind Power*. www.twind.eu. (Accessed 12 October 2011)

Van den Berg, G. P. (2005). Wind gradient statistics up to 200 m altitude over flat ground. *First International Meeting on Wind Turbine Noise: Perspective for Control, Berlin*.

Veldhuis, L. L. M. (2012). Aircraft Aerodynamics. *AE4130 lecture slides, Faculty of Aerospace Engineering, Delft University of Technology*.

Wind Energy Guide. (2011). *Laddermill Kites Wind Energy*. www.windenergy1.com/?p=179. (Accessed 17 October 2011)

Wirsing, E. (1999). De prestaties van het profiel NACA64$_2$A015 gemeten in drie verschillende windtunnelconfiguraties. *Master of Science Thesis, Faculty of Aerospace Engineering, Delft University of Technology*.

XFLR5. (2011a). Analysis of foils and wings operating at low Reynolds numbers. *Guidelines for XFLR5 v6.03*.

XFLR5. (2011b). *XFLR5 downloads*. www.xflr5.com. (Accessed 24 November 2011)

Yen, S. C., & Fei, Y. F. (2011). Winglet Dihedral Effect on Flow Behavior and Aerodynamic Performance of NACA0012 Wings. *Journal of Fluids Engineering*, *vol. 133*.

Appendix A

Airfoil section validation

This appendix contains the simulation results of 5 different airfoil sections used for the validation cases, performed with XFOIL and obtained from literature.

A.1 NACA - 64_2(A)015

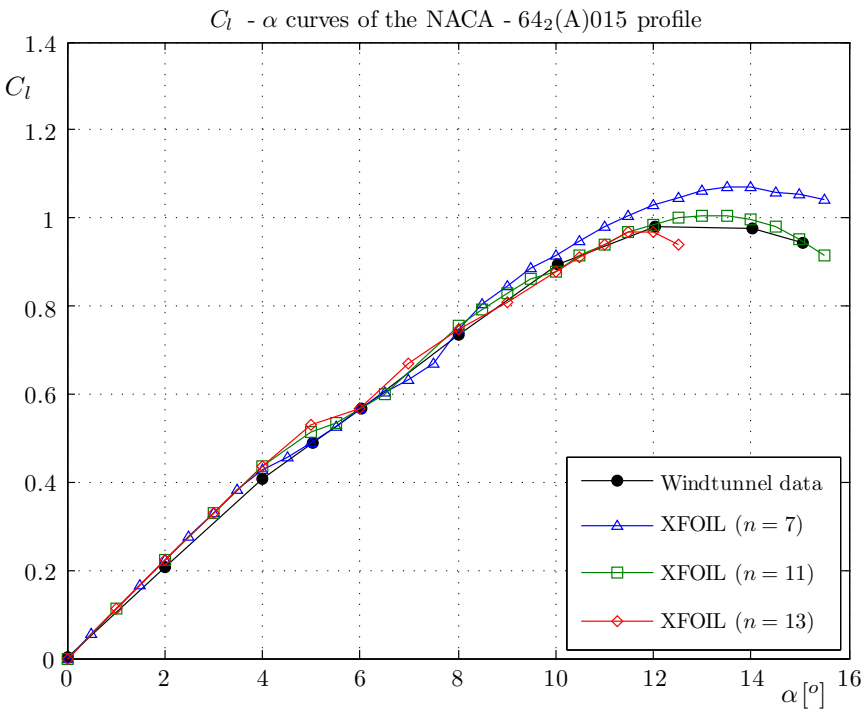

Figure A.1: The $C_l - \alpha$ curves obtained from windtunnel experiments and XFOIL simulations with 3 different values of n for the NACA - 64_2(A)015 profile used for the flat wing configuration where $Re = 1.0 \cdot 10^6$.

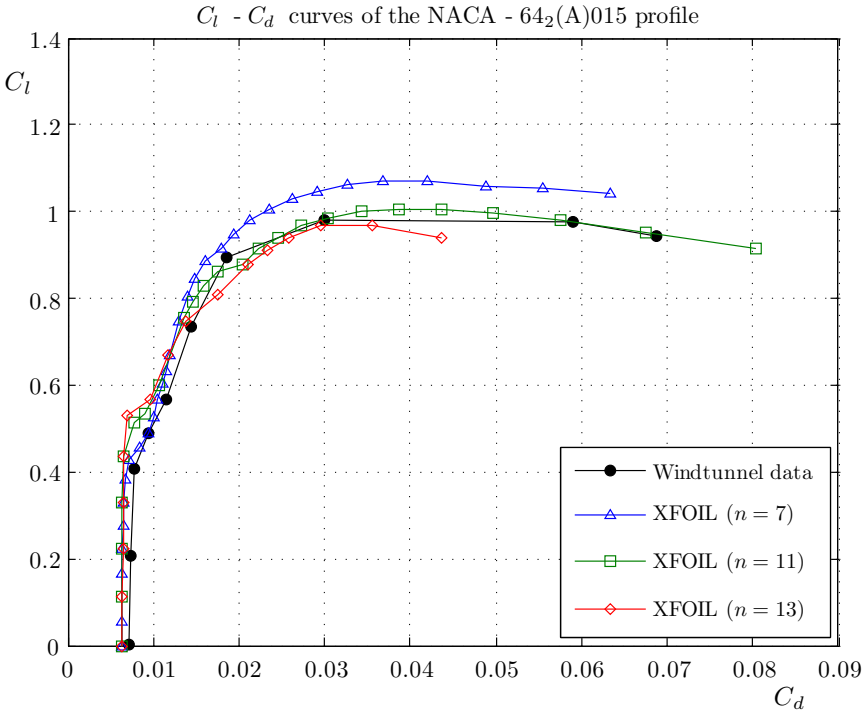

Figure A.2: The $C_l - C_d$ curves obtained from windtunnel experiments and XFOIL simulations with 3 different values of n for the NACA - 64_2(A)015 profile used for the flat wing configuration where $Re = 1.0 \cdot 10^6$.

A.2 NACA - 65_1(A)012

See next page.

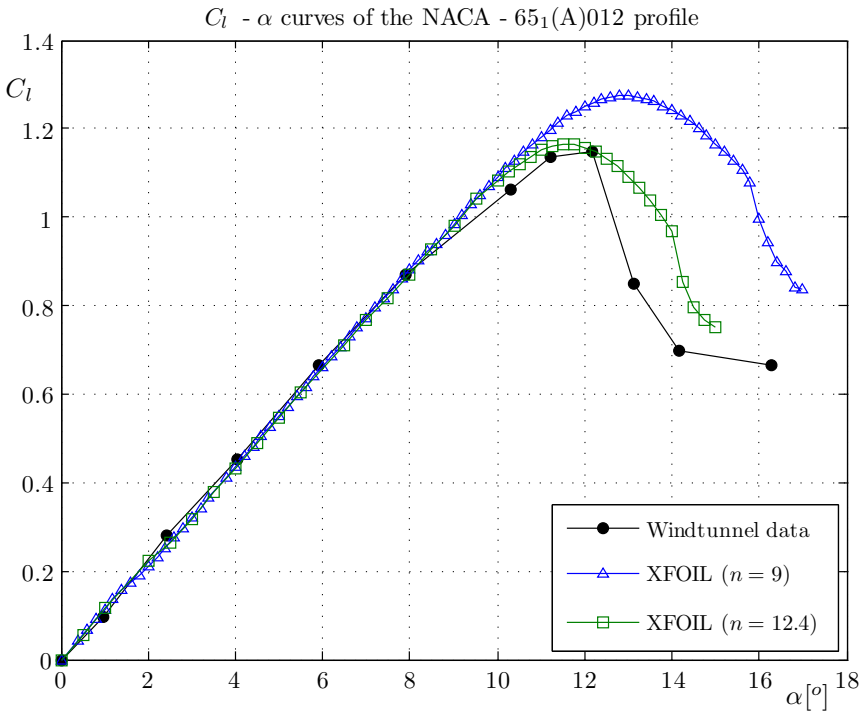

Figure A.3: The $C_l - \alpha$ curves obtained from windtunnel experiments and XFOIL simulations with 2 different values of n for the NACA - 65_1(A)012 profile used for the swept wing configurations where $Re = 3.0 \cdot 10^6$.

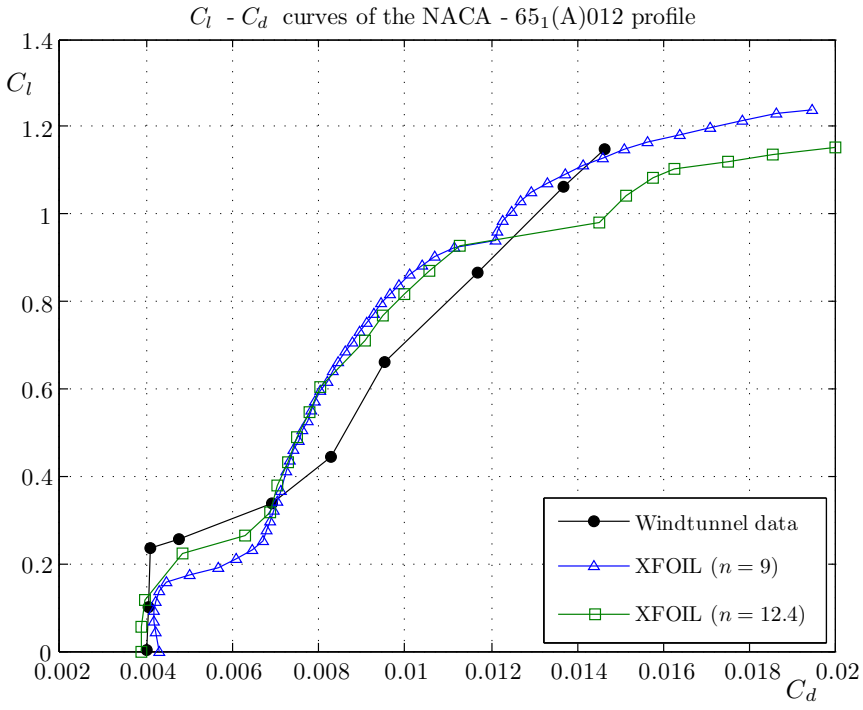

Figure A.4: The $C_l - C_d$ curves obtained from windtunnel experiments and XFOIL simulations with 2 different values of n for the NACA - 65_1(A)012 profile used for the swept wing configurations where $Re = 3.0 \cdot 10^6$.

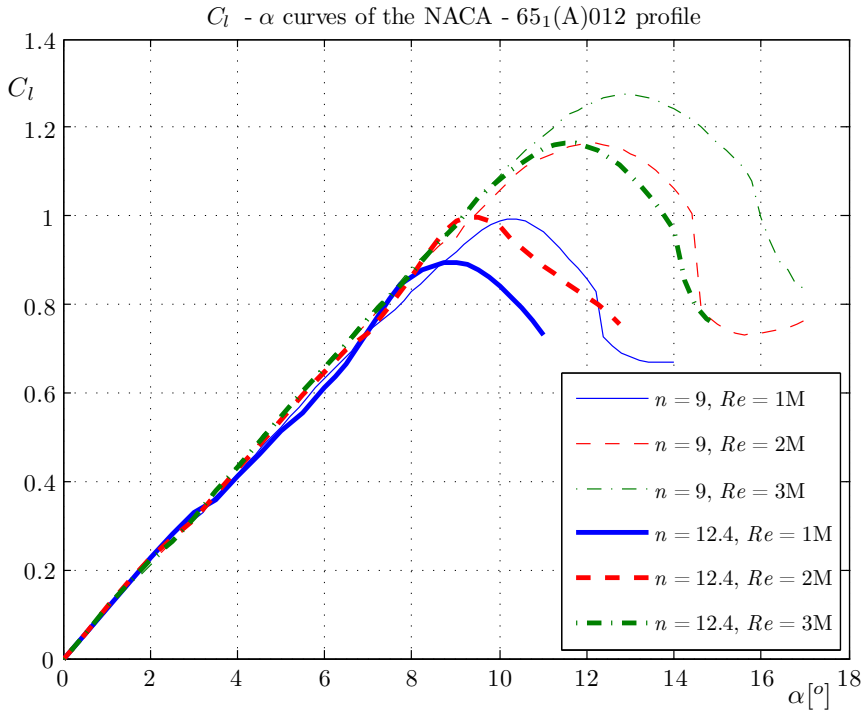

Figure A.5: The $C_l - \alpha$ curves obtained from XFOIL simulations with 3 different values of n for the NACA - 65_1(A)012 profile used for the swept wing configurations where $Re = (1.0 - 3.0) \cdot 10^6$.

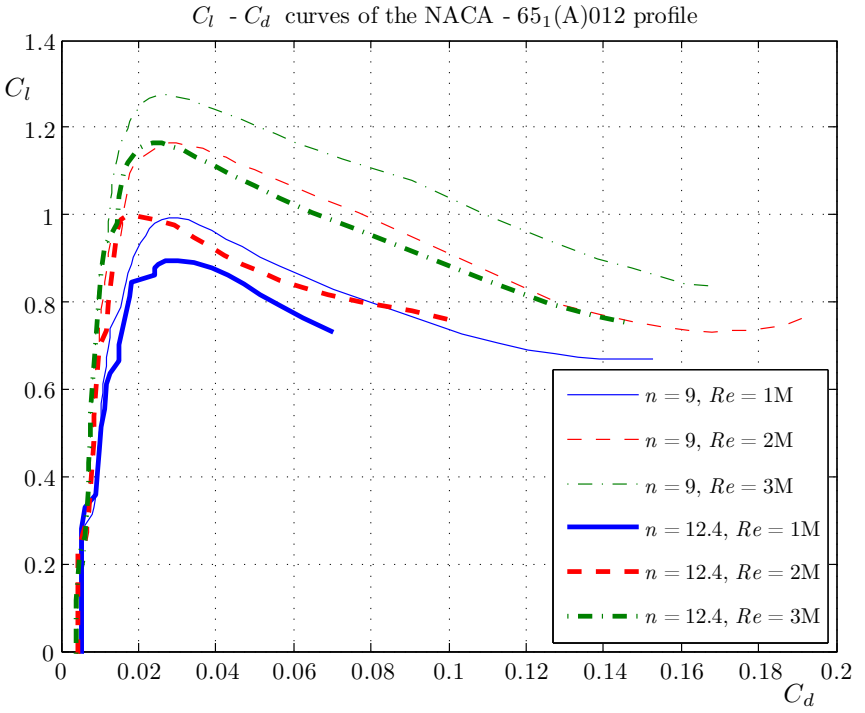

Figure A.6: The $C_l - C_d$ curves obtained from XFOIL simulations with 3 different values of n for the NACA - 65_1(A)012 profile used for the swept wing configurations where $Re = (1.0 - 3.0) \cdot 10^6$.

A.3 NACA - 64_1(A)612

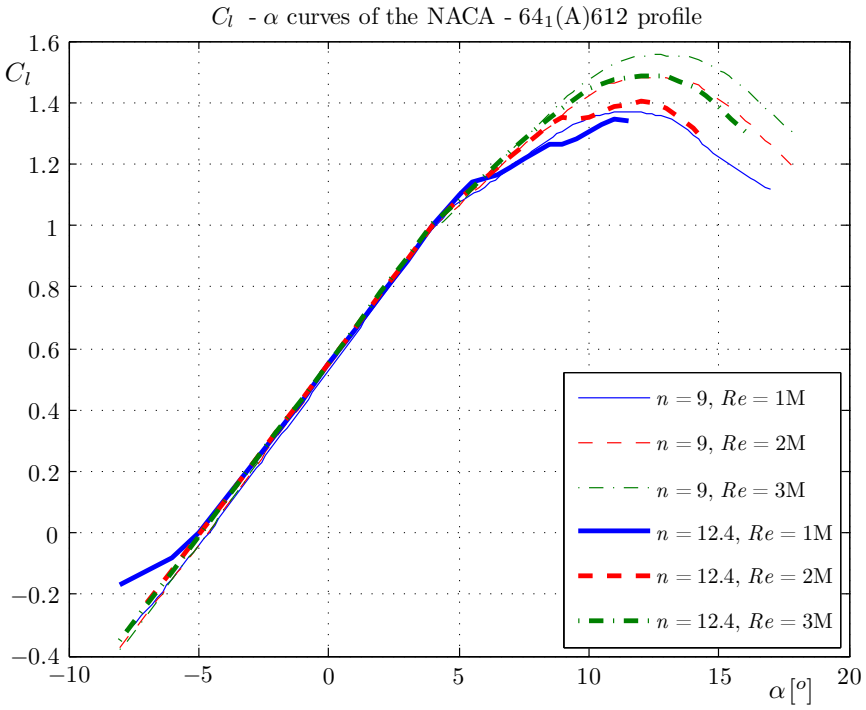

Figure A.7: The $C_l - \alpha$ curves obtained from XFOIL simulations with 3 different values of n for the NACA - 64_1(A)612 profile used for the swept wing configurations where $Re = (1.0 - 3.0) \cdot 10^6$.

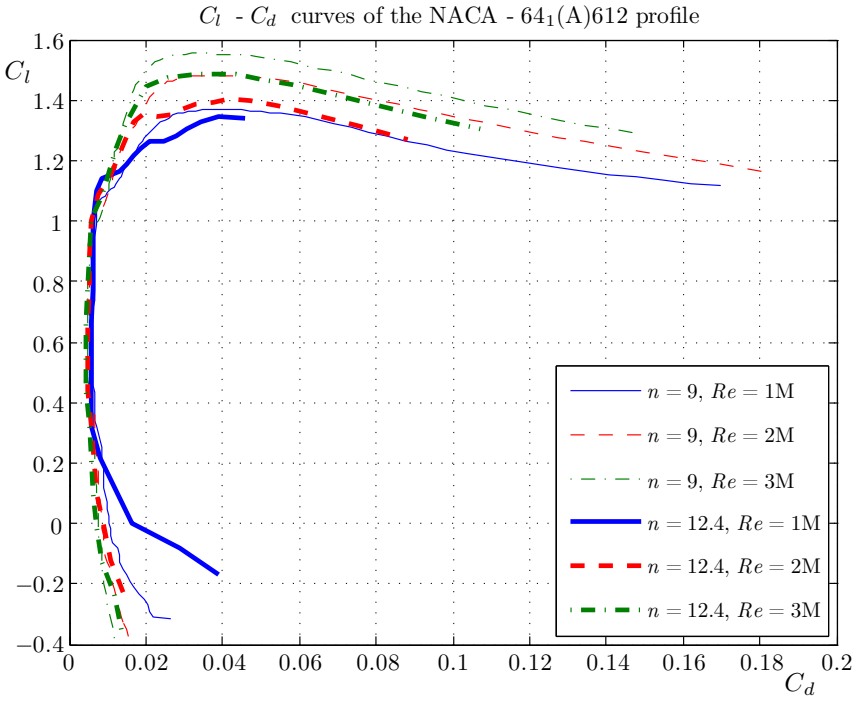

Figure A.8: The $C_l - C_d$ curves obtained from XFOIL simulations with 3 different values of n for the NACA - 64_1(A)612 profile used for the swept wing configurations where $Re = (1.0 - 3.0) \cdot 10^6$.

A.4 NACA - 0012

See next page.

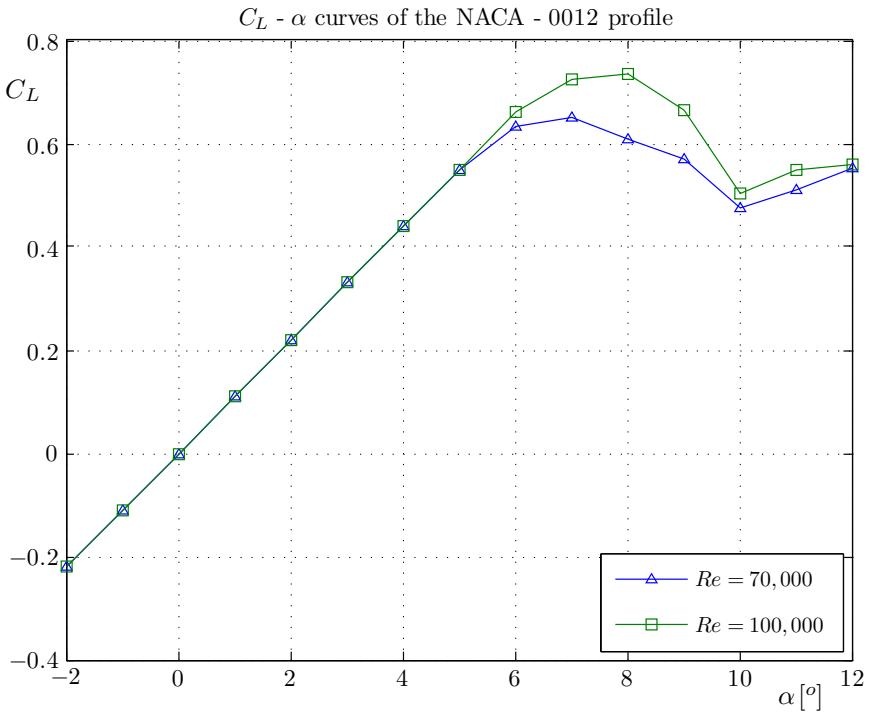

Figure A.9: The $C_l - \alpha$ curves obtained from Cyberiad (1981) for the NACA - 0012 profile used for the winglet configuration where $Re = 80 \cdot 10^3$.

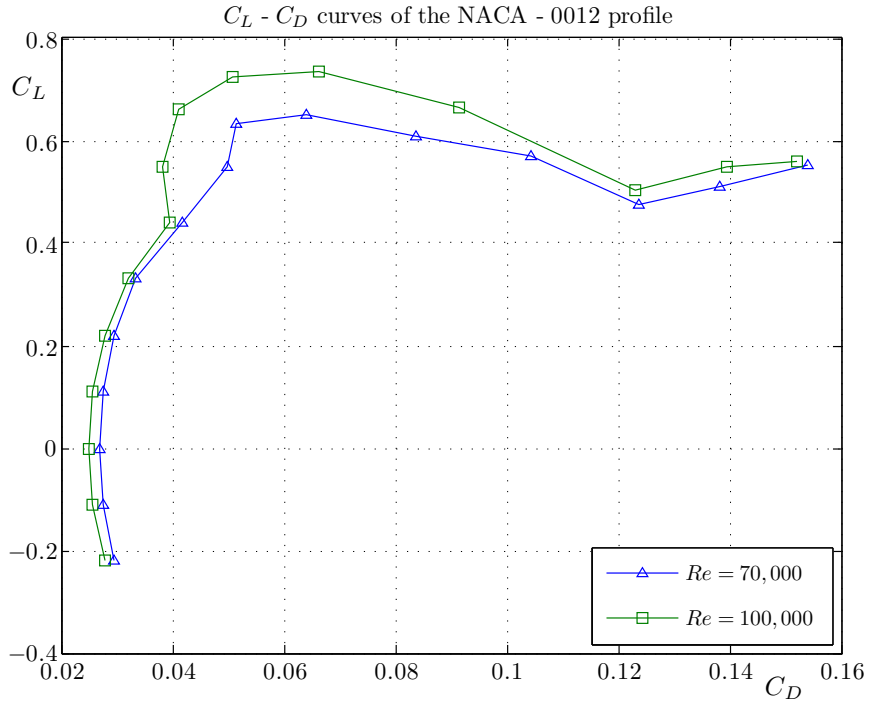

Figure A.10: The $C_l - C_d$ curve obtained from Cyberiad (1981) for the NACA - 0012 profile used for the winglet configuration where $Re = 80 \cdot 10^3$.

A.5 NACA - 64-418

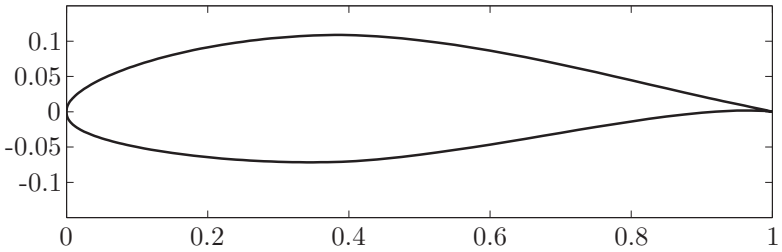

Figure A.11: The NACA - 64-418 airfoil section used for the arc shaped kite.

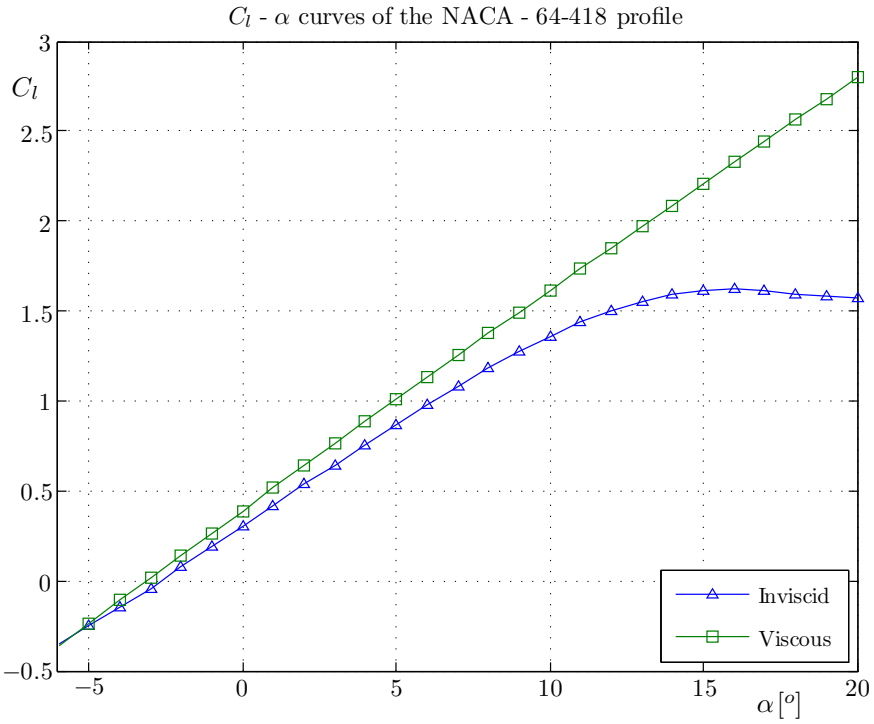

Figure A.12: The inviscid and viscous $C_l - \alpha$ curves obtained from Carqueija et al. (2010) for the NACA - 64-418 profile used for the arc shaped kite where $Re = 6 \cdot 10^6$.

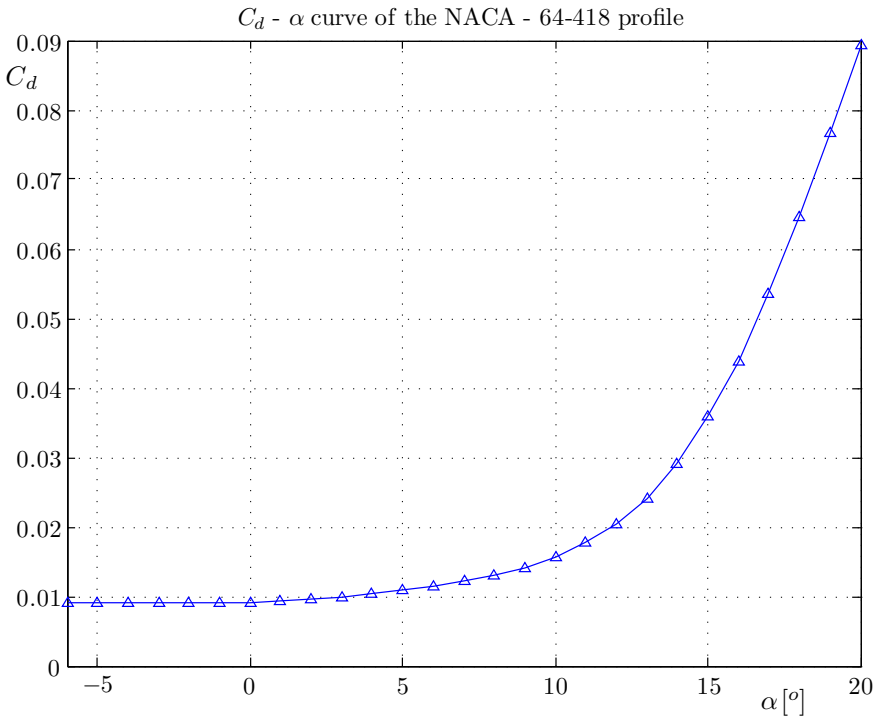

Figure A.13: The $C_d - \alpha$ curve obtained from Carqueija et al. (2010) for the NACA - 64-418 profile used for the arc shaped kite where $Re = 6 \cdot 10^6$.

Appendix B

VLM/3D panel method validation

This appendix contains the simulation results of each validation case performed with 4 different versions of the adapted XFLR5 program. A trade-off procedure is performed on these results, as explained in section 5.3.

B.1 Flat wing

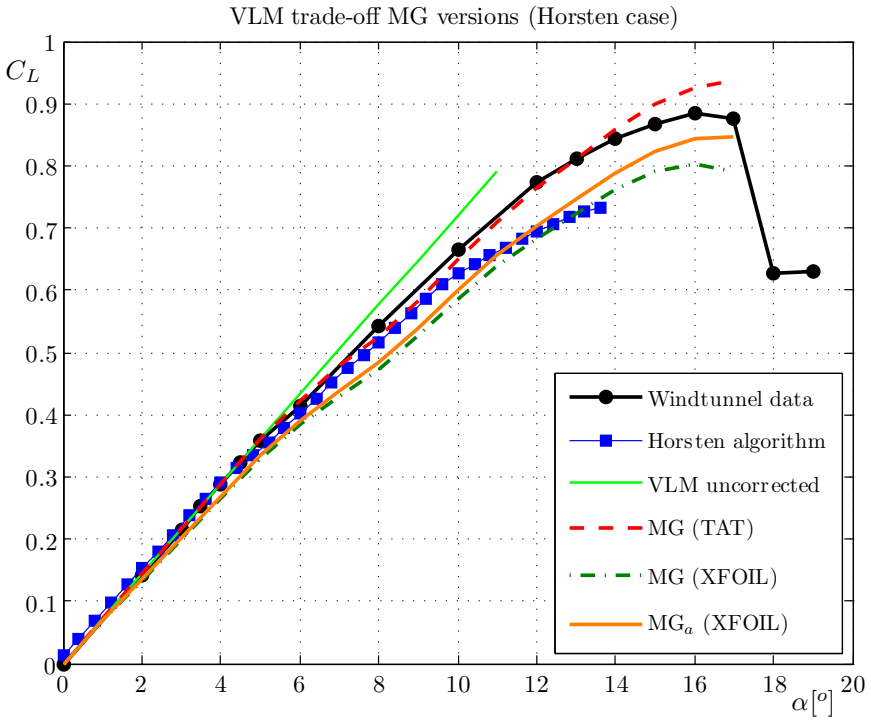

Figure B.1: The $C_L - \alpha$ curves obtained from windtunnel experiments and XFLR5 simulations (VLM MG versions) for the flat wing where $Re = 1.0 \cdot 10^6$.

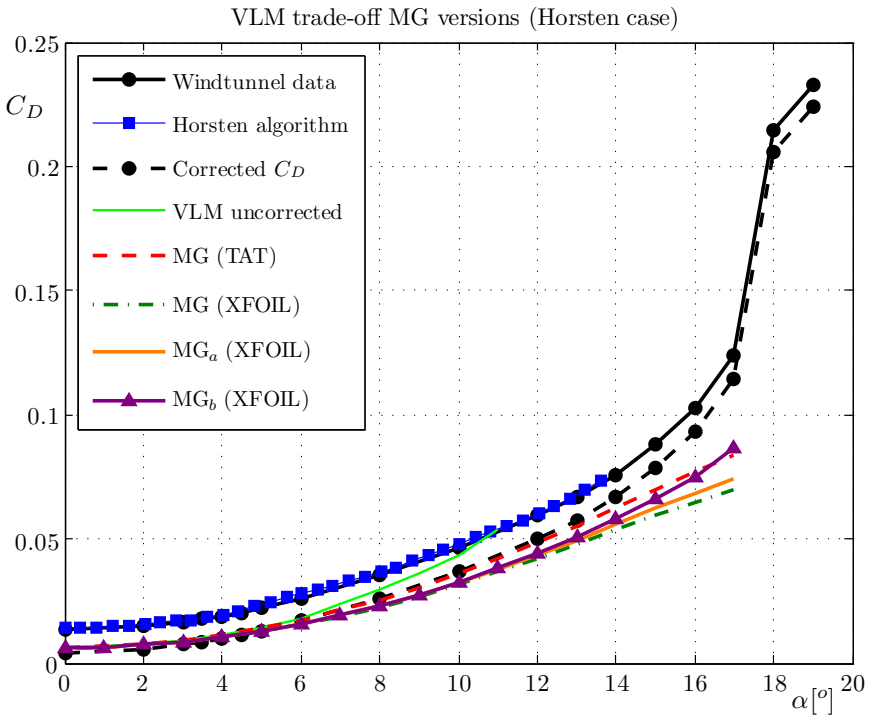

Figure B.2: The $C_D - \alpha$ curves obtained from windtunnel experiments and XFLR5 simulations (VLM MG versions) for the flat wing where $Re = 1.0 \cdot 10^6$.

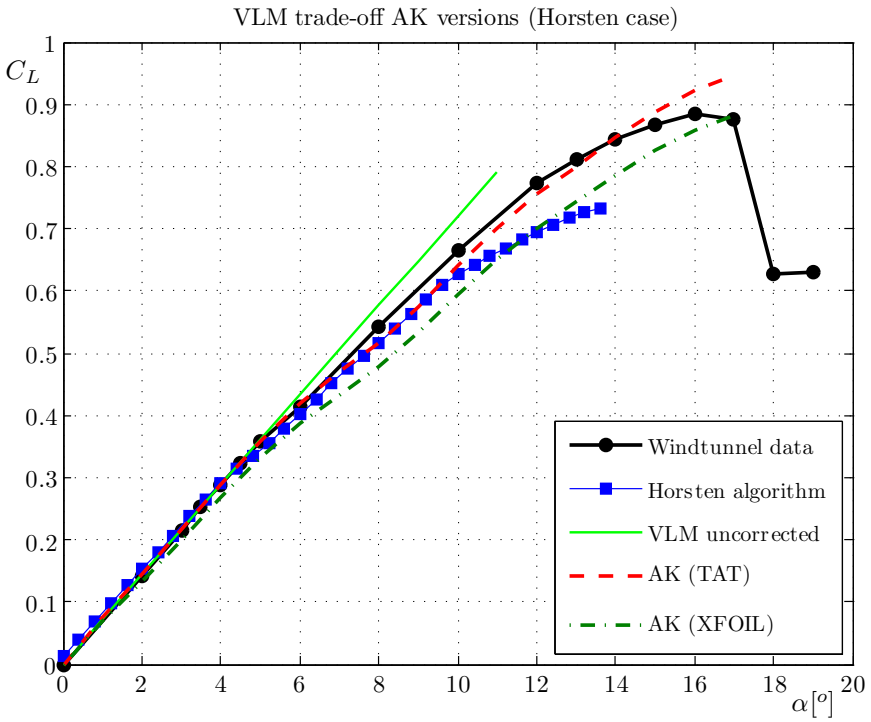

Figure B.3: The $C_L - \alpha$ curves obtained from windtunnel experiments and XFLR5 simulations (VLM AK versions) for the flat wing where $Re = 1.0 \cdot 10^6$.

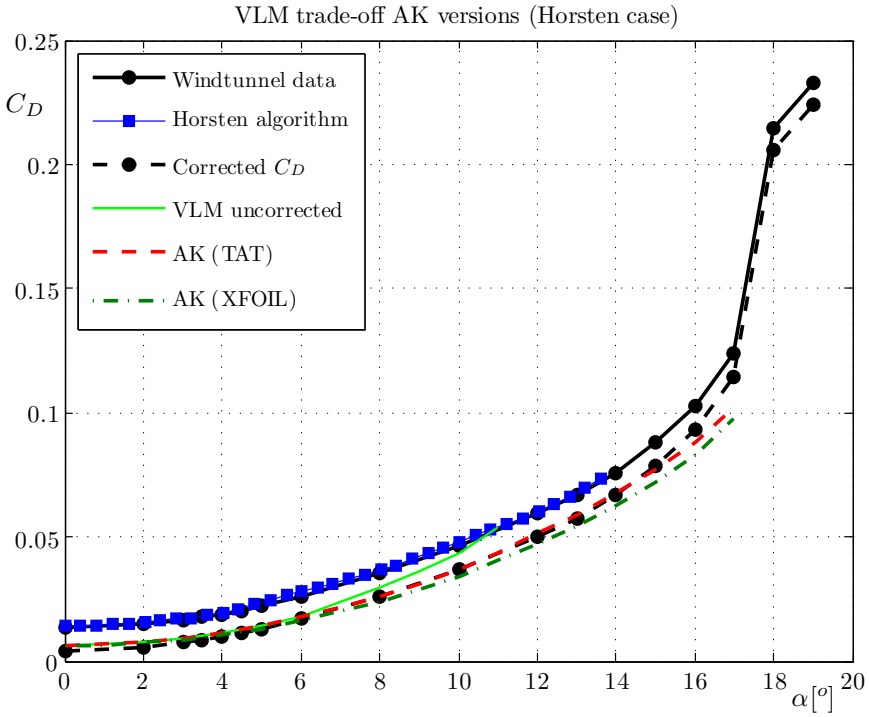

Figure B.4: The $C_D - \alpha$ curves obtained from windtunnel experiments and XFLR5 simulations (VLM AK versions) for the flat wing where $Re = 1.0 \cdot 10^6$.

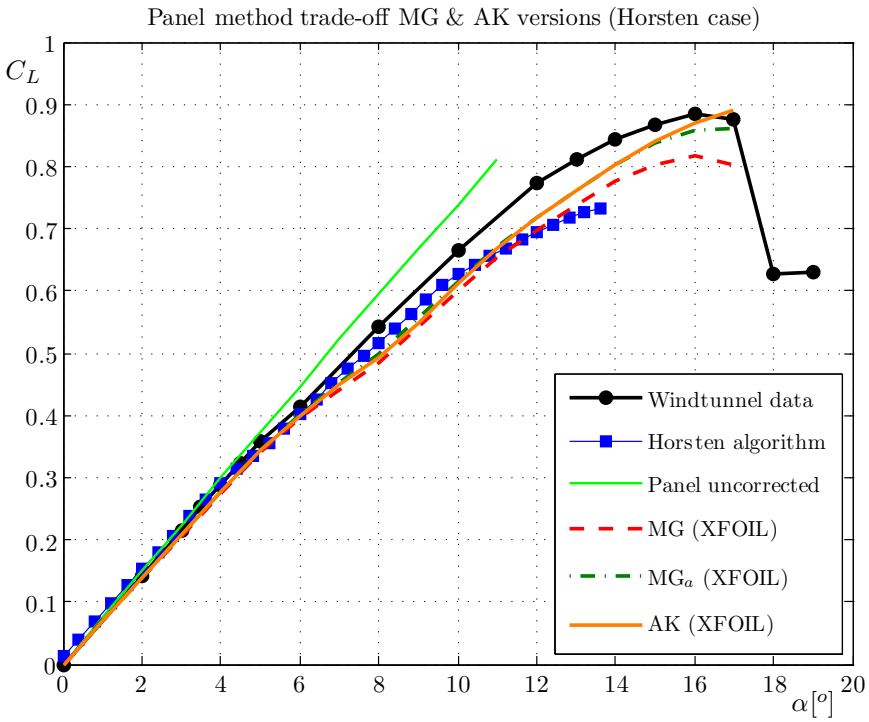

Figure B.5: The $C_L - \alpha$ curves obtained from windtunnel experiments and XFLR5 simulations (Panel versions) for the flat wing where $Re = 1.0 \cdot 10^6$.

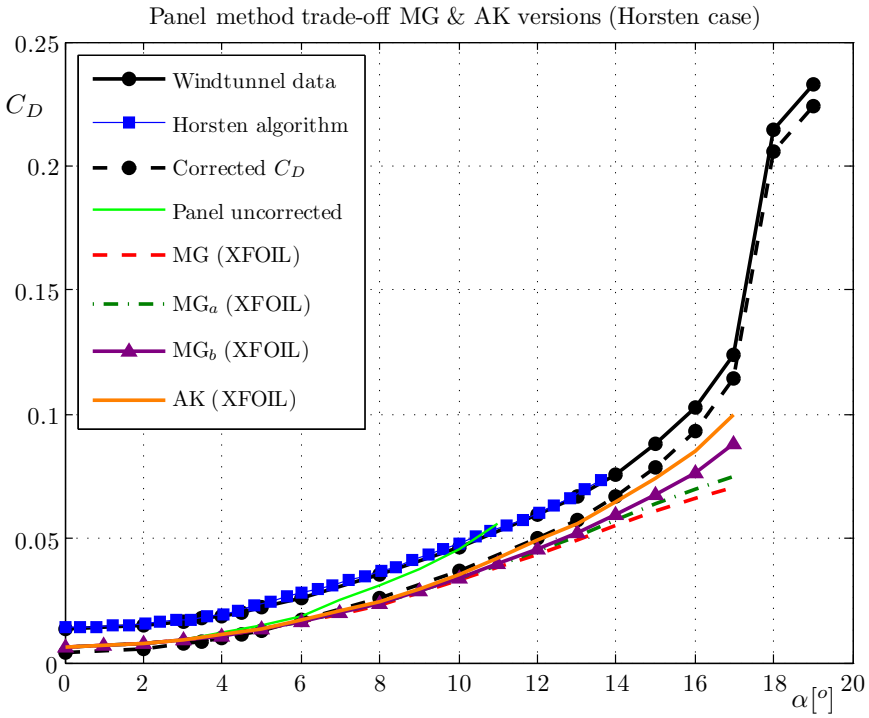

Figure B.6: The $C_D - \alpha$ curves obtained from windtunnel experiments and XFLR5 simulations (Panel method versions) for the flat wing where $Re = 1.0 \cdot 10^6$.

B.2 Swept wing AR5_012

See next page.

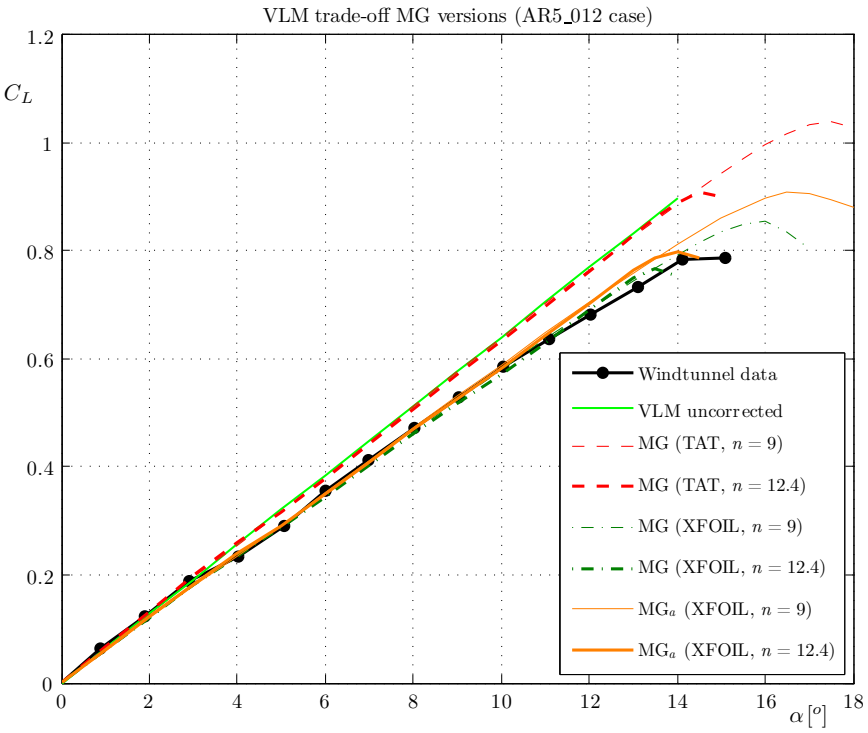

Figure B.7: The $C_L - \alpha$ curves obtained from windtunnel experiments and XFLR5 simulations (VLM MG versions) for the AR5_012 wing where $Re = 2.0 \cdot 10^6$.

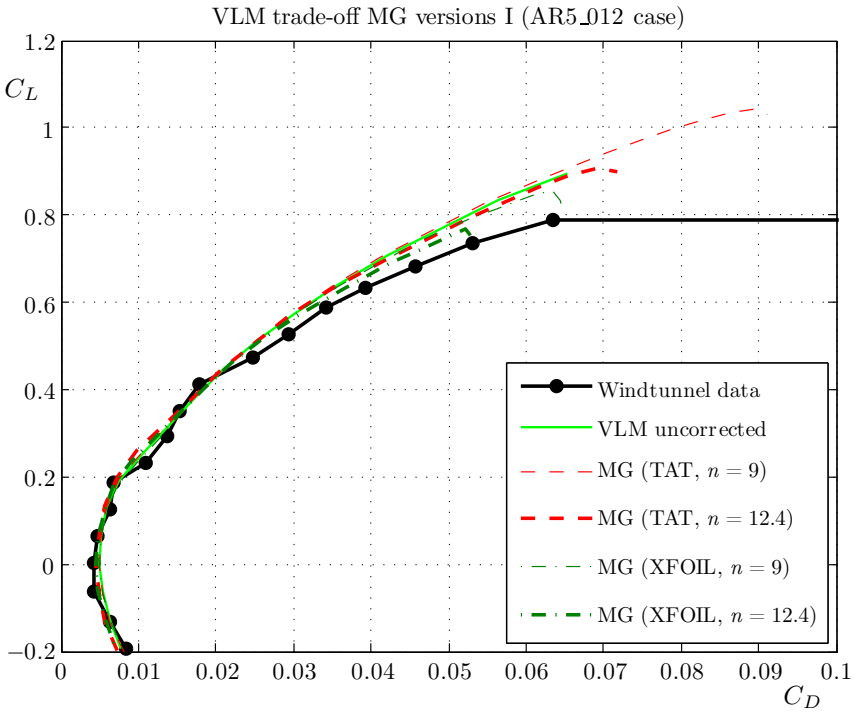

Figure B.8: The $C_L - C_D$ curves obtained from windtunnel experiments and XFLR5 simulations (VLM MG versions) for the AR5_012 wing where $Re = 2.0 \cdot 10^6$.

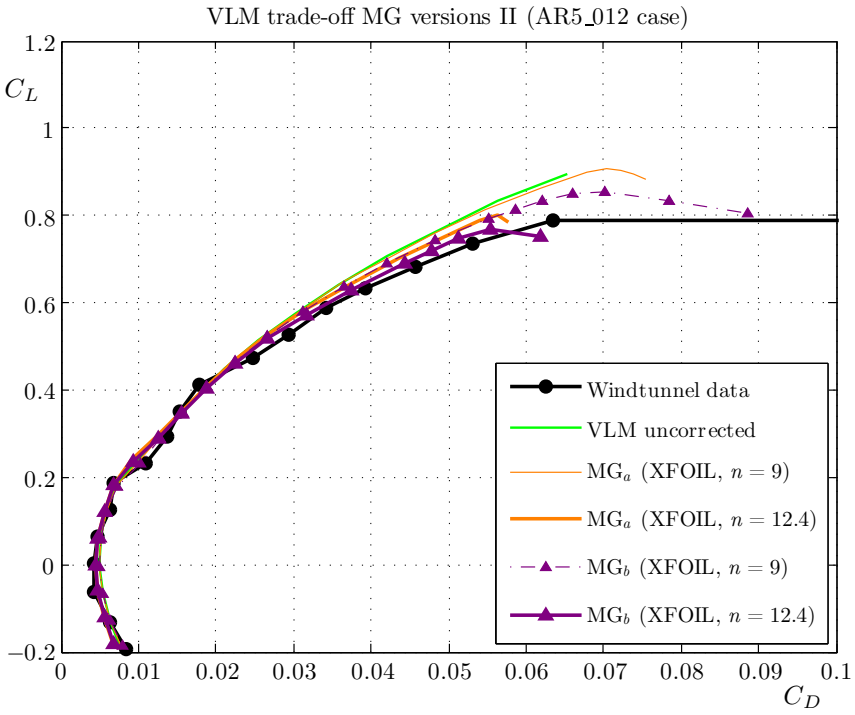

Figure B.9: The $C_L - C_D$ curves obtained from windtunnel experiments and XFLR5 simulations (VLM MG versions) for the AR5_012 wing where $Re = 2.0 \cdot 10^6$.

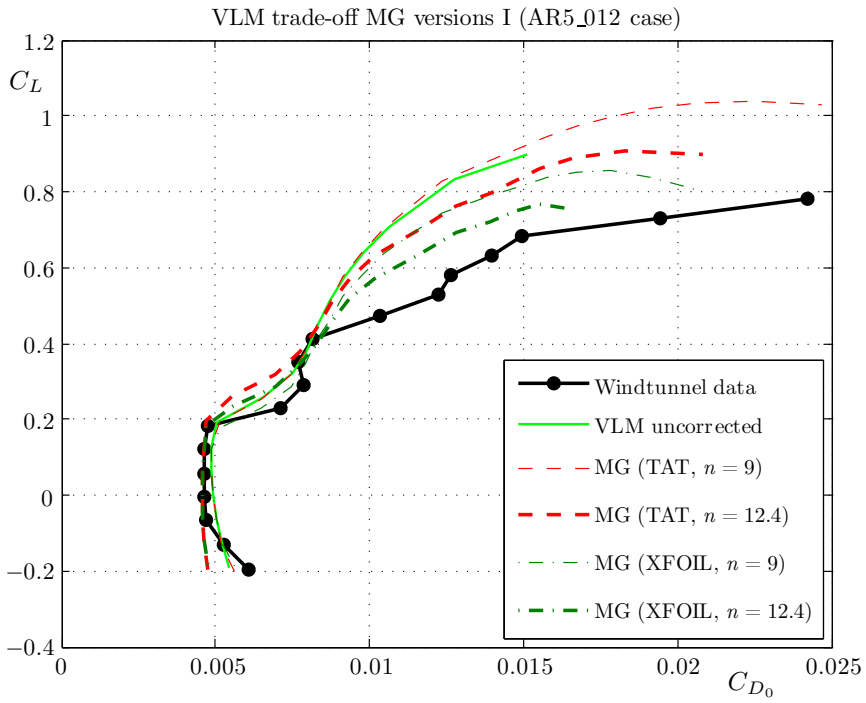

Figure B.10: The $C_L - C_{D_0}$ curves obtained from windtunnel experiments and XFLR5 simulations (VLM MG versions) for the AR5_012 wing where $Re = 2.0 \cdot 10^6$.

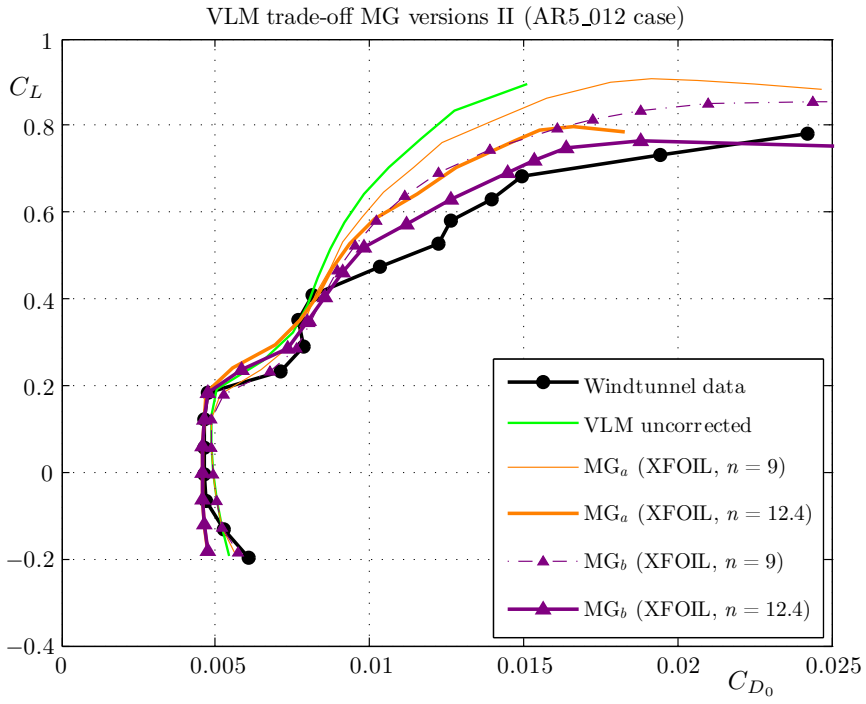

Figure B.11: The $C_L - C_{D_0}$ curves obtained from windtunnel experiments and XFLR5 simulations (VLM MG versions) for the AR5_012 wing where $Re = 2.0 \cdot 10^6$.

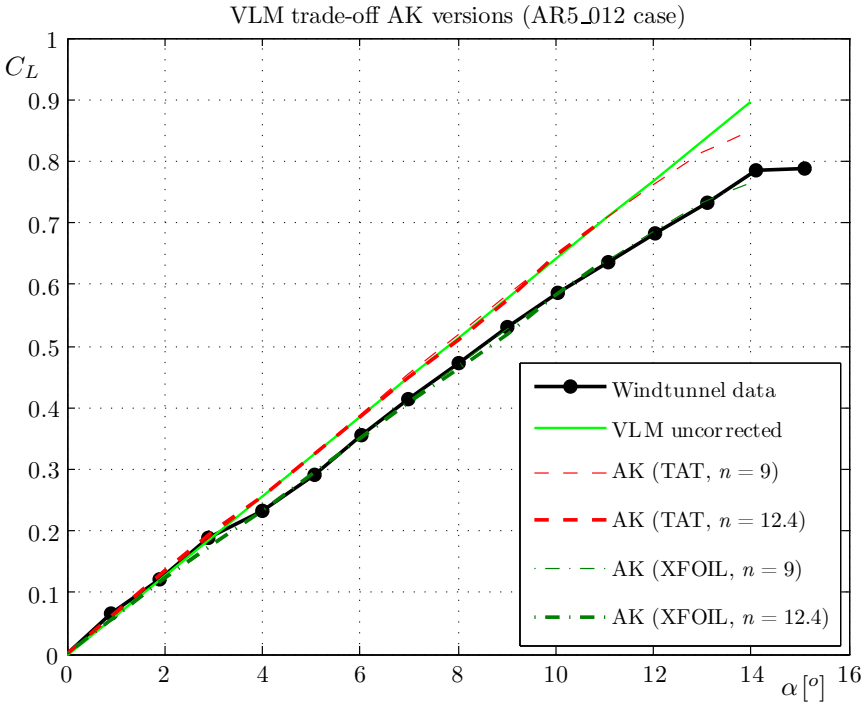

Figure B.12: The $C_L - \alpha$ curves obtained from windtunnel experiments and XFLR5 simulations (VLM AK versions) for the AR5_012 wing where $Re = 2.0 \cdot 10^6$.

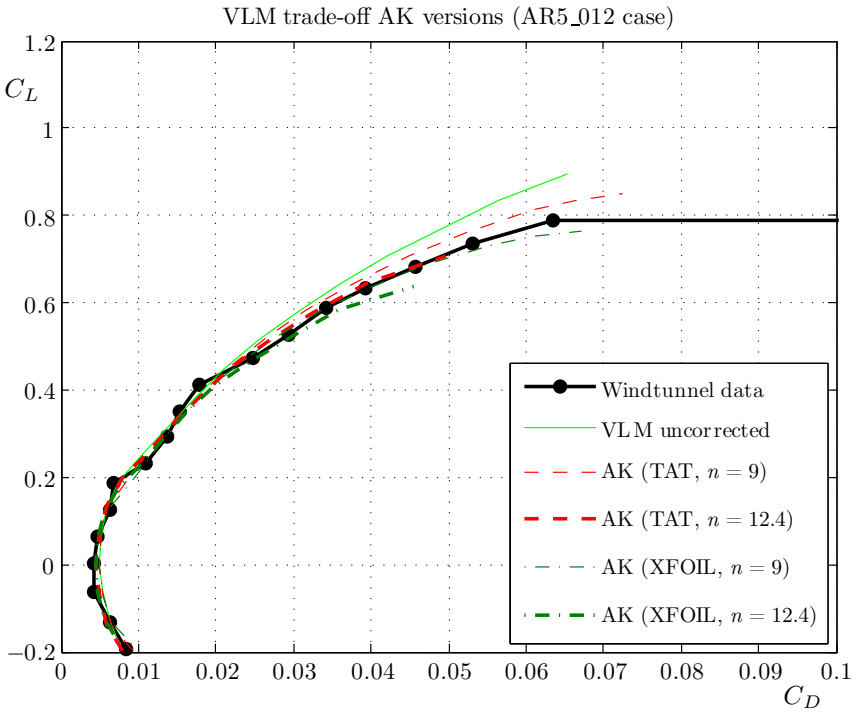

Figure B.13: The $C_L - C_D$ curves obtained from windtunnel experiments and XFLR5 simulations (VLM AK versions) for the AR5_012 wing where $Re = 2.0 \cdot 10^6$.

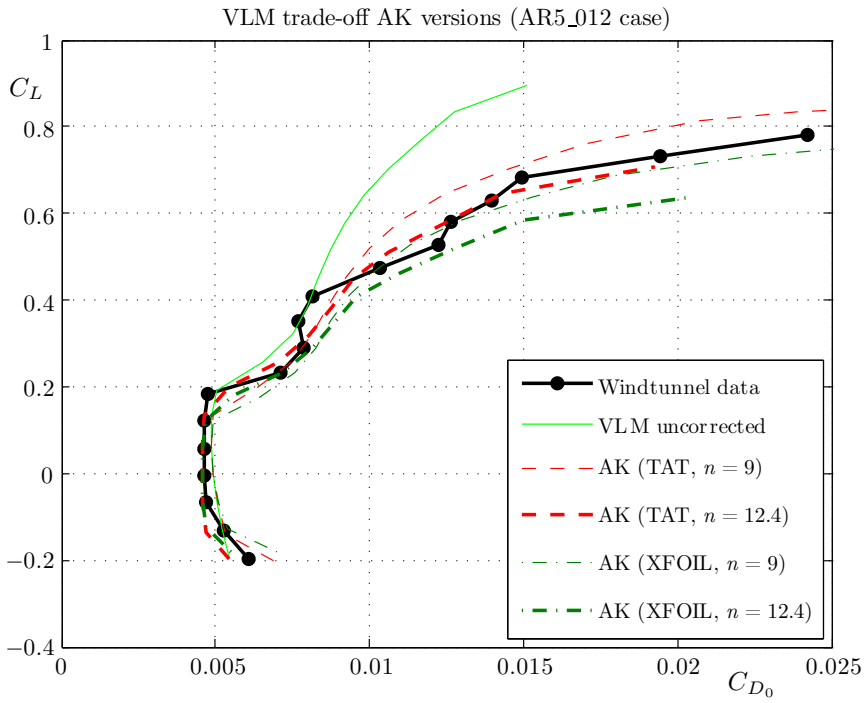

Figure B.14: The $C_L - C_{D_0}$ curves obtained from windtunnel experiments and XFLR5 simulations (VLM AK versions) for the AR5_012 wing where $Re = 2.0 \cdot 10^6$.

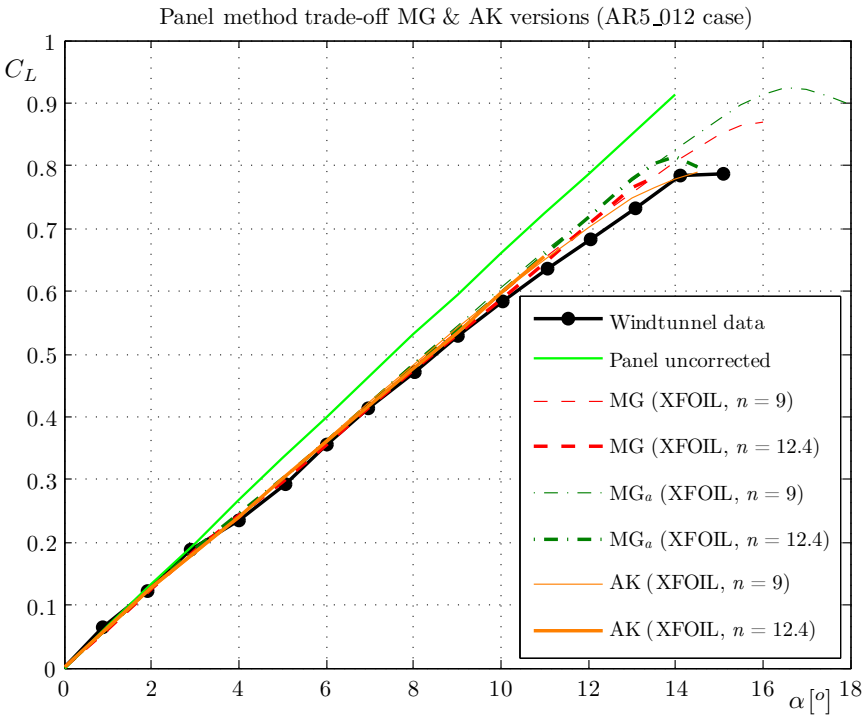

Figure B.15: The $C_L - \alpha$ curves obtained from windtunnel experiments and XFLR5 simulations (Panel method versions) for the AR5_012 wing where $Re = 2.0 \cdot 10^6$.

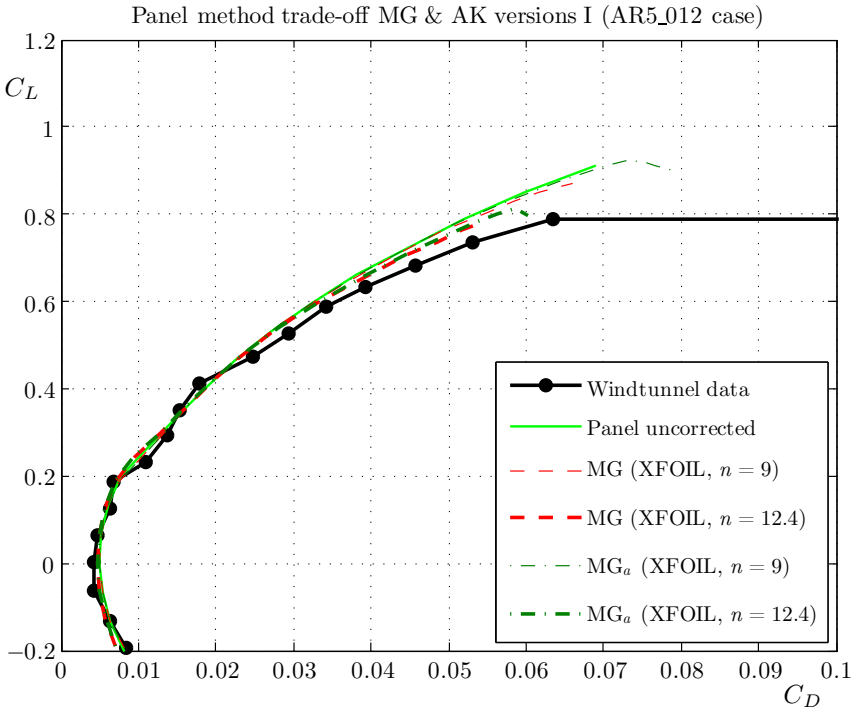

Figure B.16: The $C_L - C_D$ curves obtained from windtunnel experiments and XFLR5 simulations (Panel method versions) for the AR5_012 wing where $Re = 2.0 \cdot 10^6$.

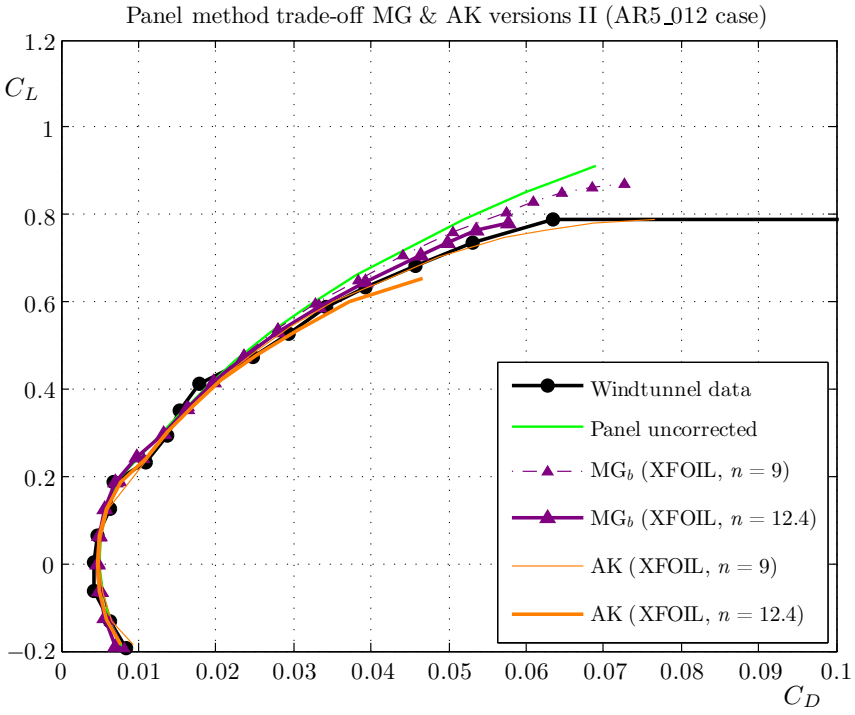

Figure B.17: The $C_L - C_D$ curves obtained from windtunnel experiments and XFLR5 simulations (Panel method versions) for the AR5_012 wing where $Re = 2.0 \cdot 10^6$.

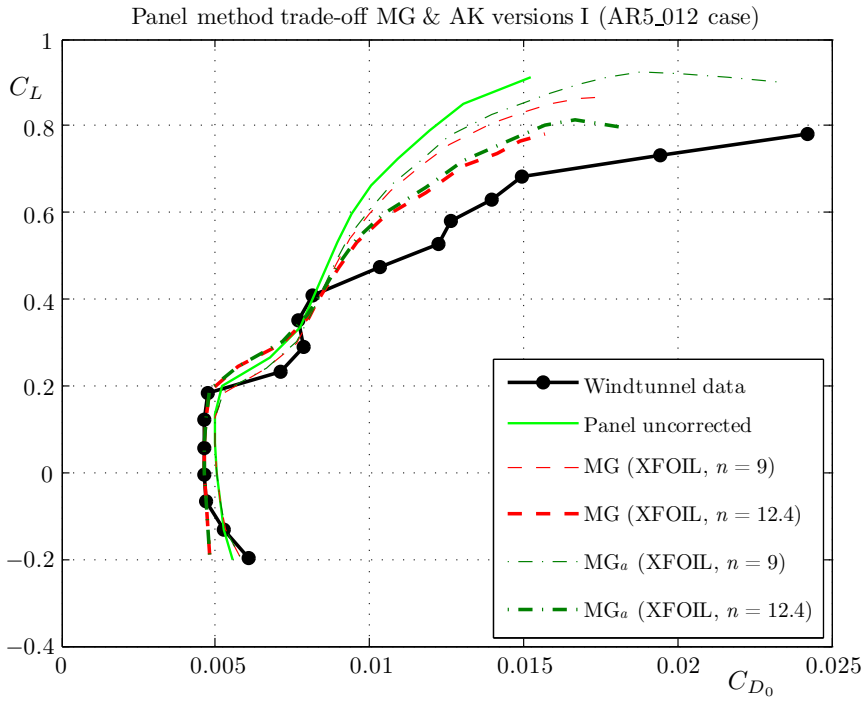

Figure B.18: The $C_L - C_{D_0}$ curves obtained from windtunnel experiments and XFLR5 simulations (Panel method versions) for the AR5_012 wing where $Re = 2.0 \cdot 10^6$.

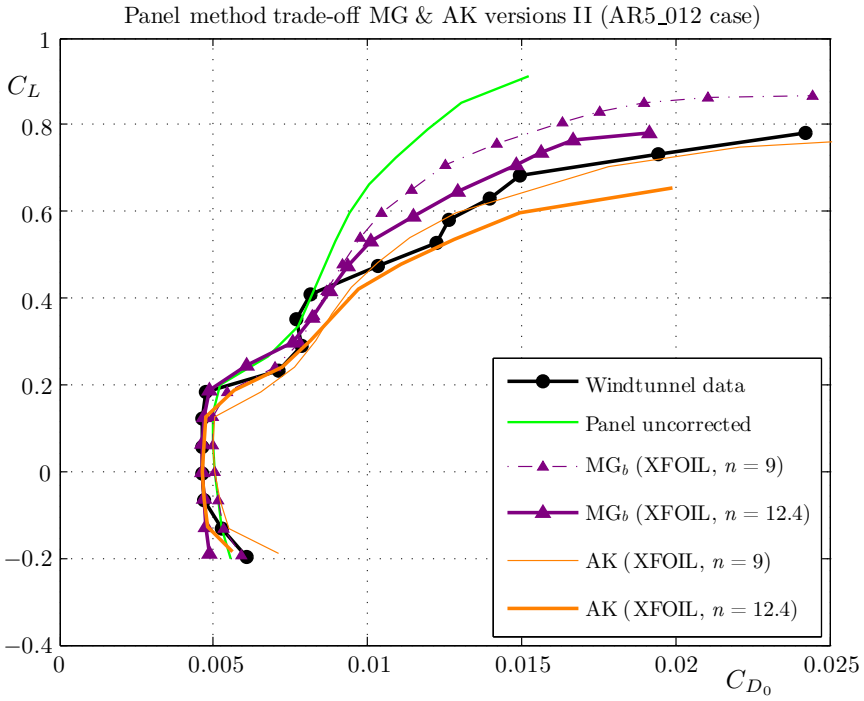

Figure B.19: The $C_L - C_{D_0}$ curves obtained from windtunnel experiments and XFLR5 simulations (Panel method versions) for the AR5_012 wing where $Re = 2.0 \cdot 10^6$.

B.3 Swept wing AR5_612

See next page.

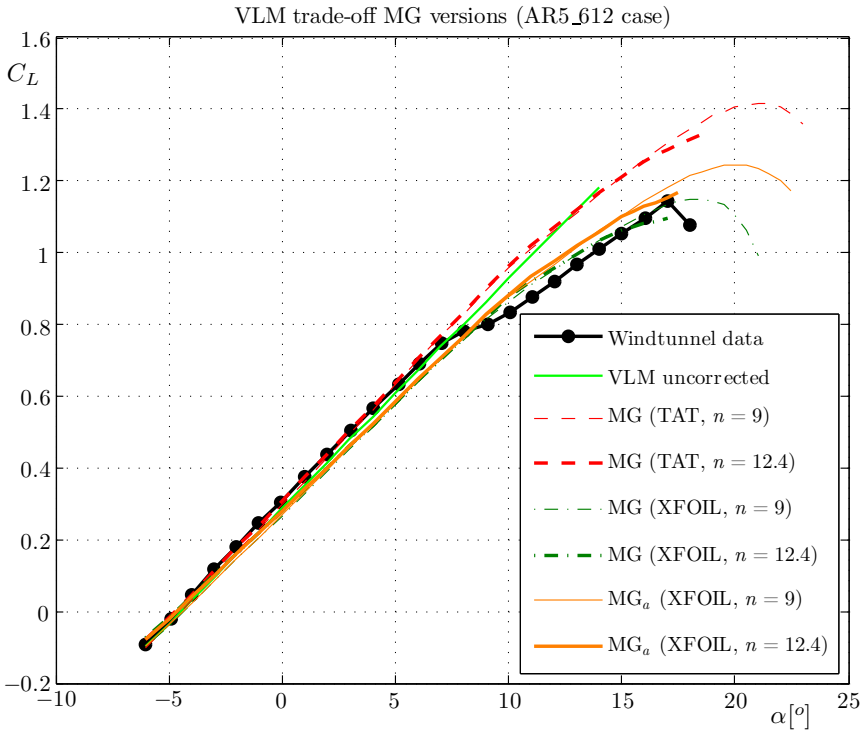

Figure B.20: The $C_L - \alpha$ curves obtained from windtunnel experiments and XFLR5 simulations (VLM MG versions) for the AR5_612 wing where $Re = 2.0 \cdot 10^6$.

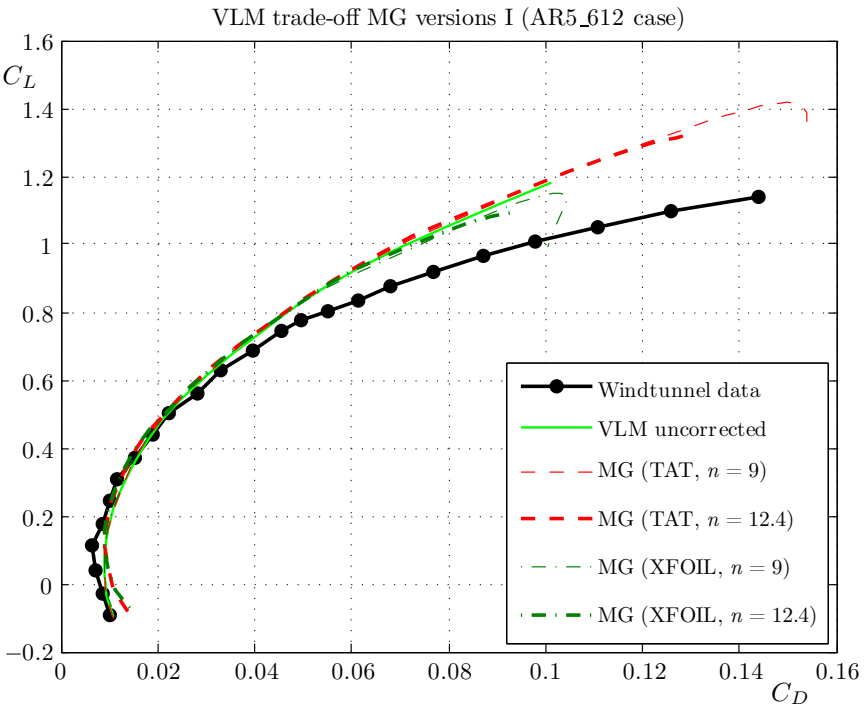

Figure B.21: The $C_L - C_D$ curves obtained from windtunnel experiments and XFLR5 simulations (VLM MG versions) for the AR5_612 wing where $Re = 2.0 \cdot 10^6$.

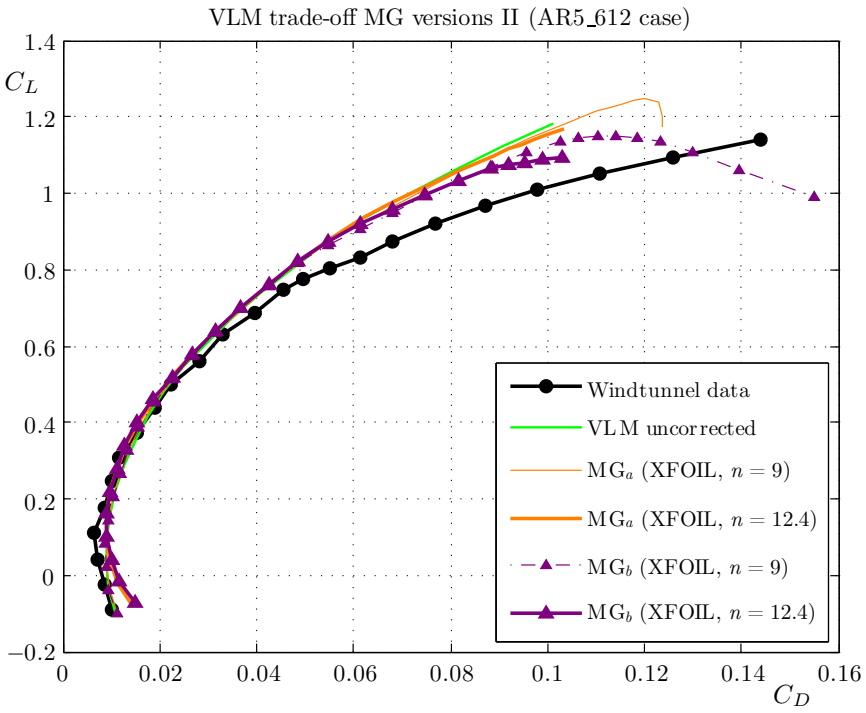

Figure B.22: The $C_L - C_D$ curves obtained from windtunnel experiments and XFLR5 simulations (VLM MG versions) for the AR5_612 wing where $Re = 2.0 \cdot 10^6$.

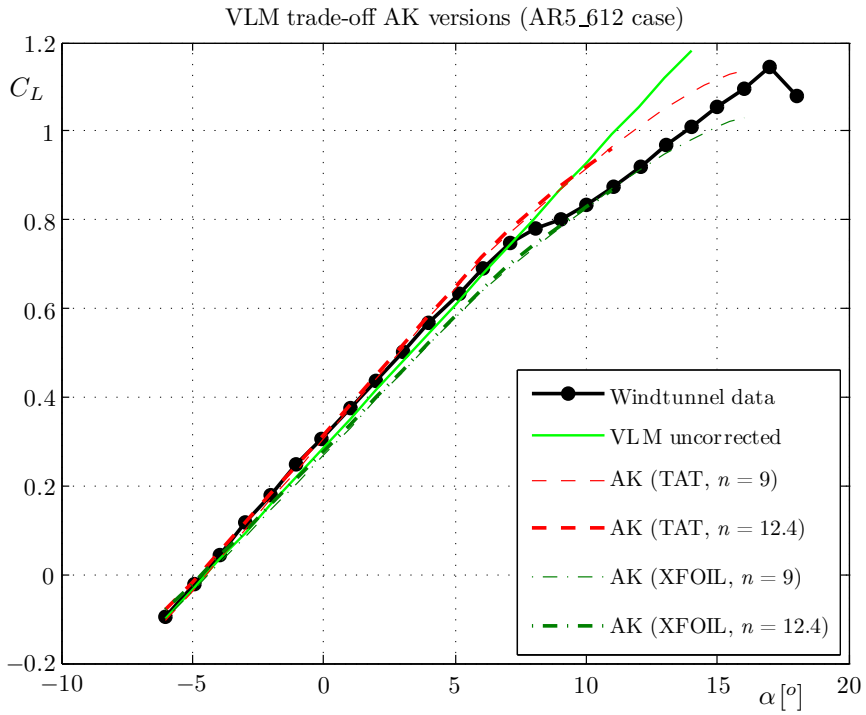

Figure B.23: The $C_L - \alpha$ curves obtained from windtunnel experiments and XFLR5 simulations (VLM AK versions) for the AR5_612 wing where $Re = 2.0 \cdot 10^6$.

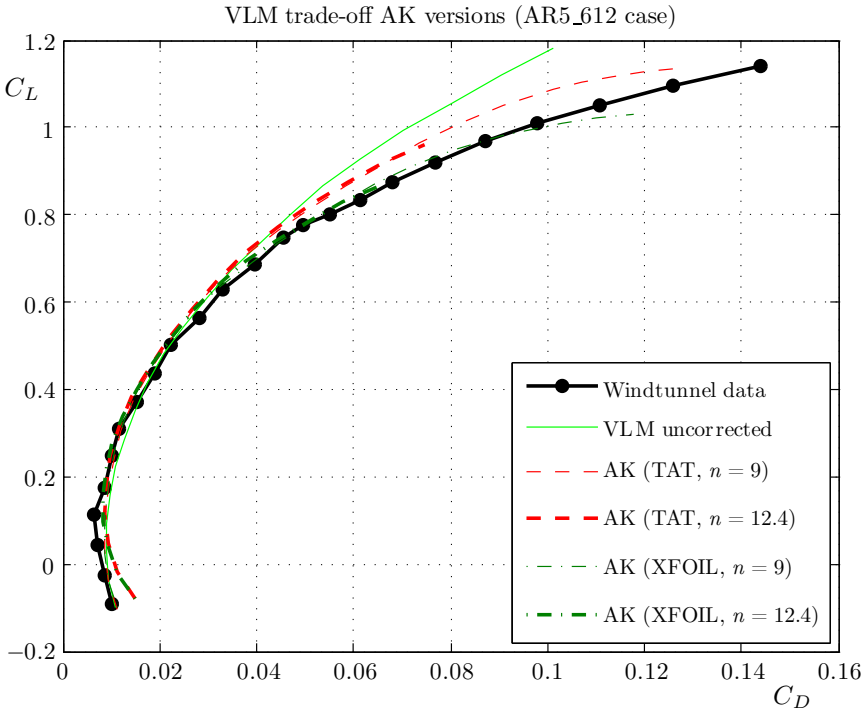

Figure B.24: The $C_L - C_D$ curves obtained from windtunnel experiments and XFLR5 simulations (VLM AK versions) for the AR5_612 wing where $Re = 2.0 \cdot 10^6$.

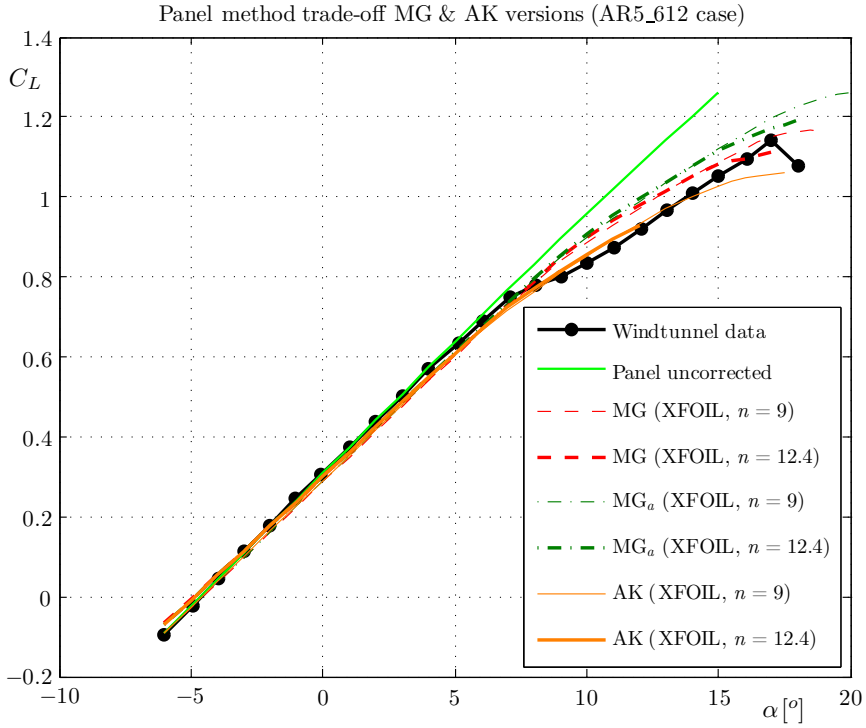

Figure B.25: The $C_L - \alpha$ curves obtained from windtunnel experiments and XFLR5 simulations (Panel method versions) for the AR5_612 wing where $Re = 2.0 \cdot 10^6$.

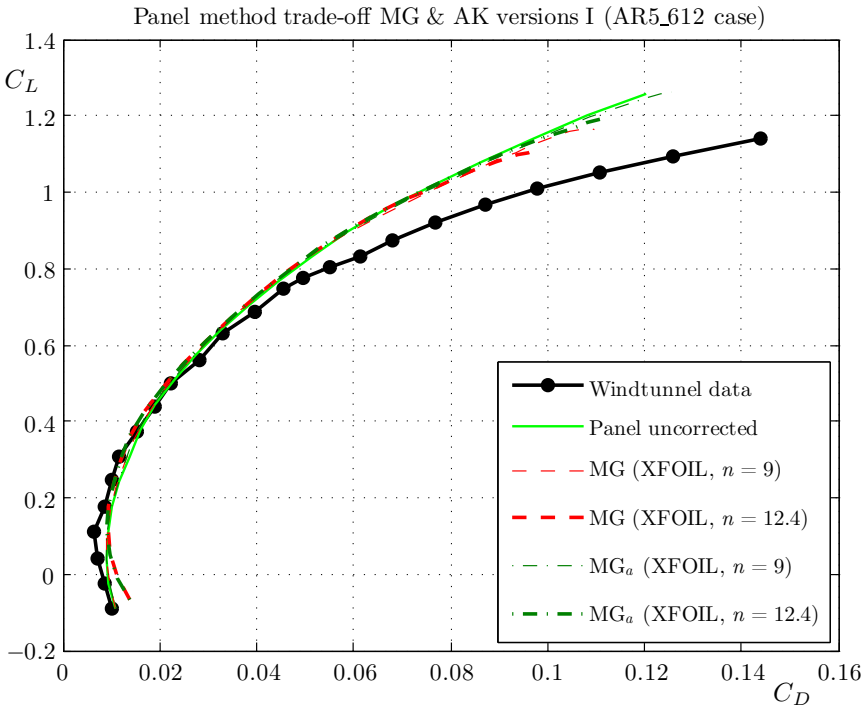

Figure B.26: The $C_L - C_D$ curves obtained from windtunnel experiments and XFLR5 simulations (Panel method versions) for the AR5_612 wing where $Re = 2.0 \cdot 10^6$.

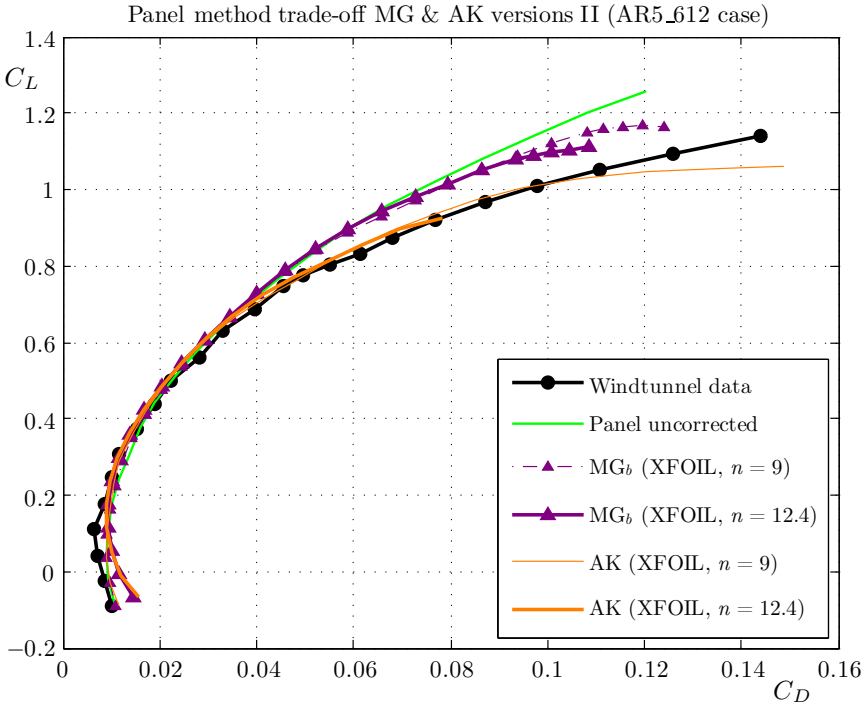

Figure B.27: The $C_L - C_D$ curves obtained from windtunnel experiments and XFLR5 simulations (Panel method versions) for the AR5_612 wing where $Re = 2.0 \cdot 10^6$.

B.4 Swept wing AR10_012

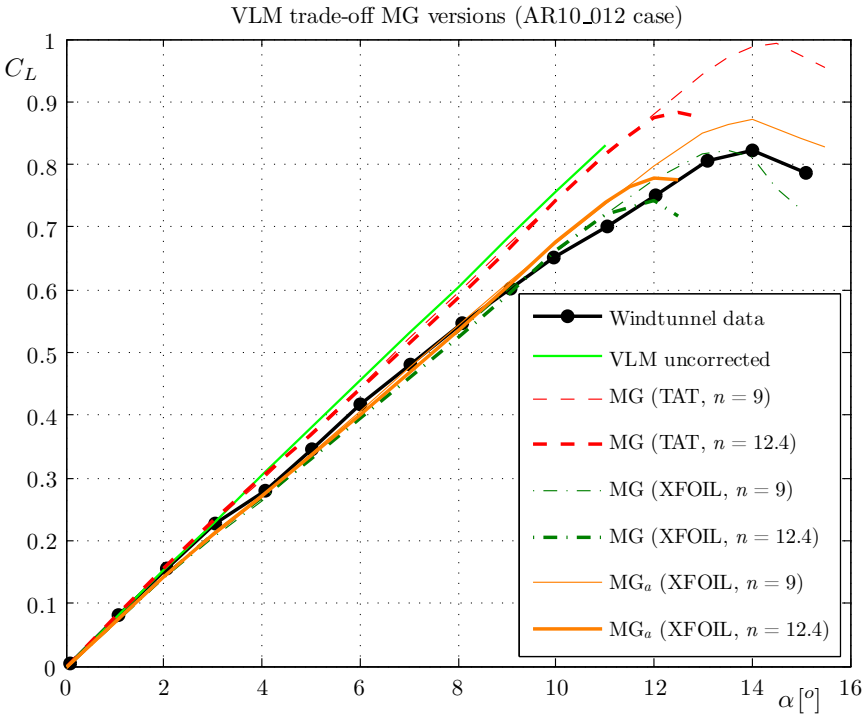

Figure B.28: The $C_L - \alpha$ curves obtained from windtunnel experiments and XFLR5 simulations (VLM MG versions) for the AR10_012 wing where $Re = 2.0 \cdot 10^6$.

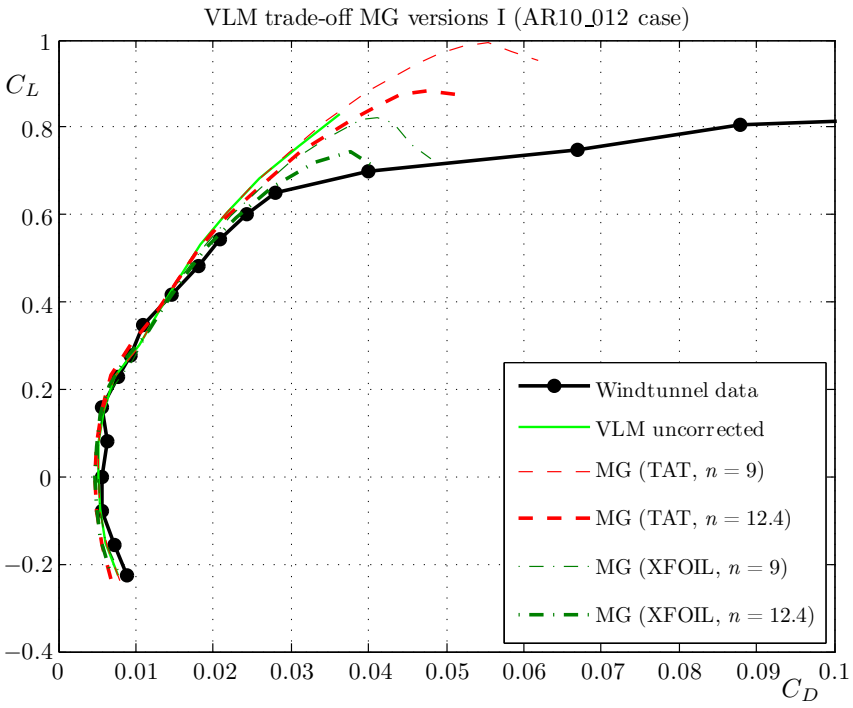

Figure B.29: The $C_L - C_D$ curves obtained from windtunnel experiments and XFLR5 simulations (VLM MG versions) for the AR10_012 wing where $Re = 2.0 \cdot 10^6$.

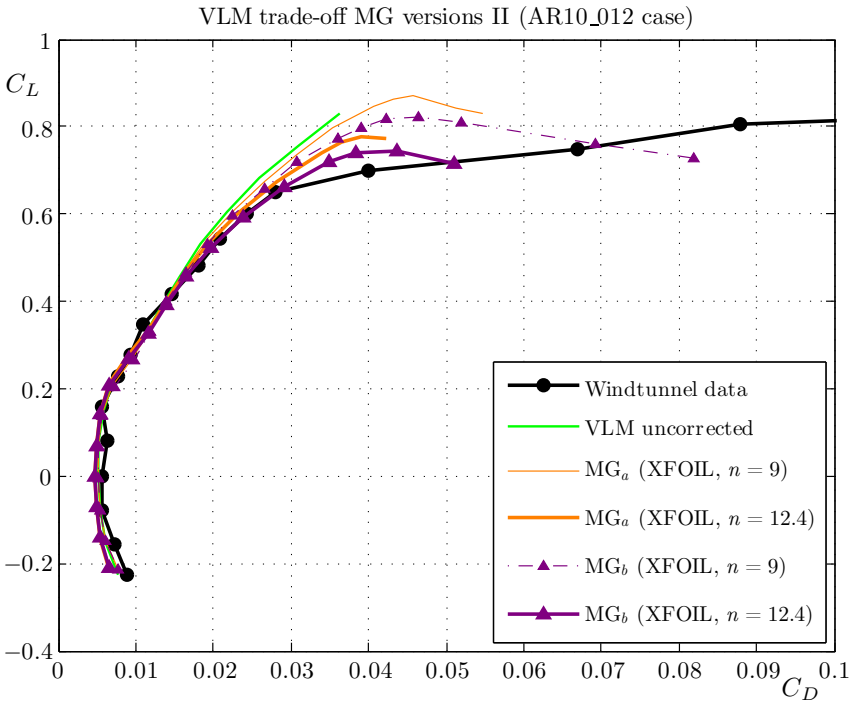

Figure B.30: The $C_L - C_D$ curves obtained from windtunnel experiments and XFLR5 simulations (VLM MG versions) for the AR10_012 wing where $Re = 2.0 \cdot 10^6$.

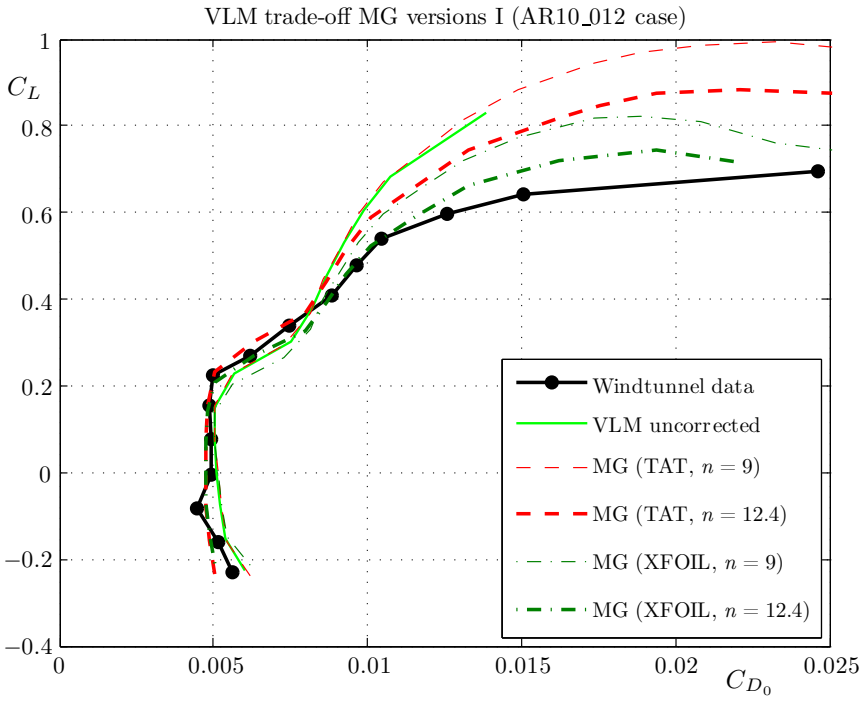

Figure B.31: The $C_L - C_{D_0}$ curves obtained from windtunnel experiments and XFLR5 simulations (VLM MG versions) for the AR10_012 wing where $Re = 2.0 \cdot 10^6$.

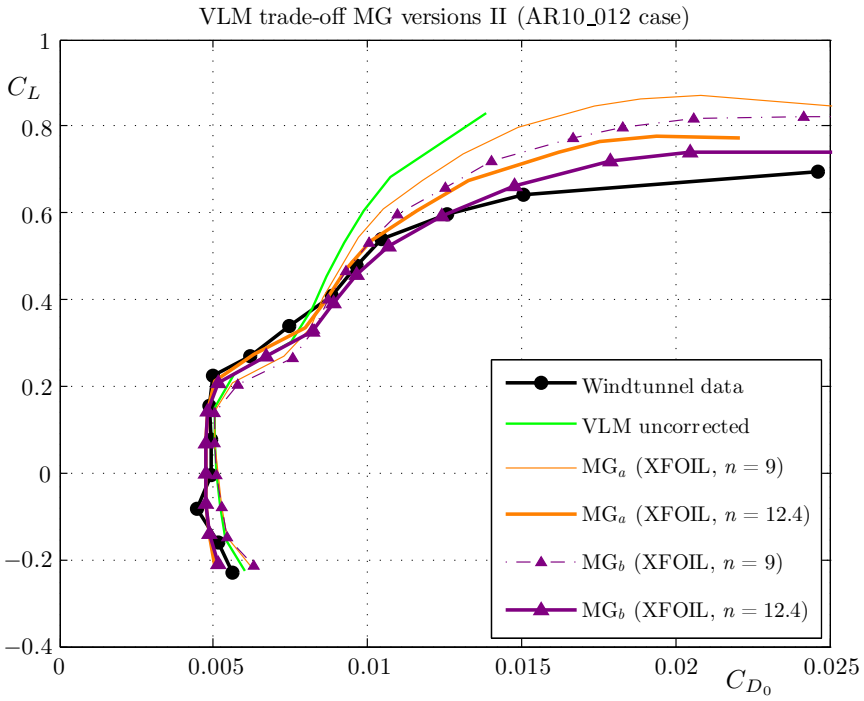

Figure B.32: The $C_L - C_{D_0}$ curves obtained from windtunnel experiments and XFLR5 simulations (VLM MG versions) for the AR10_012 wing where $Re = 2.0 \cdot 10^6$.

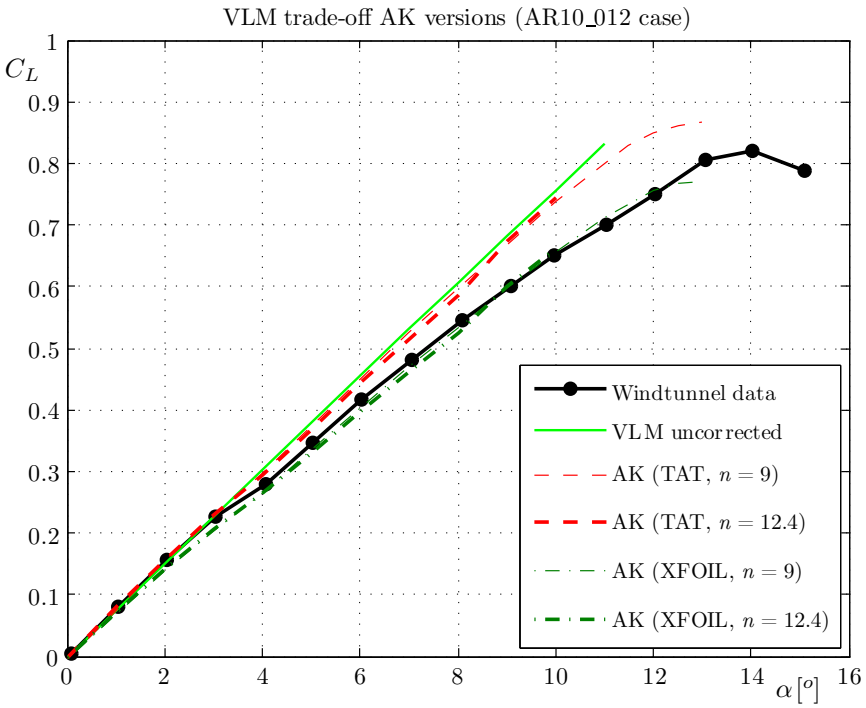

Figure B.33: The $C_L - \alpha$ curves obtained from windtunnel experiments and XFLR5 simulations (VLM AK versions) for the AR10_012 wing where $Re = 2.0 \cdot 10^6$.

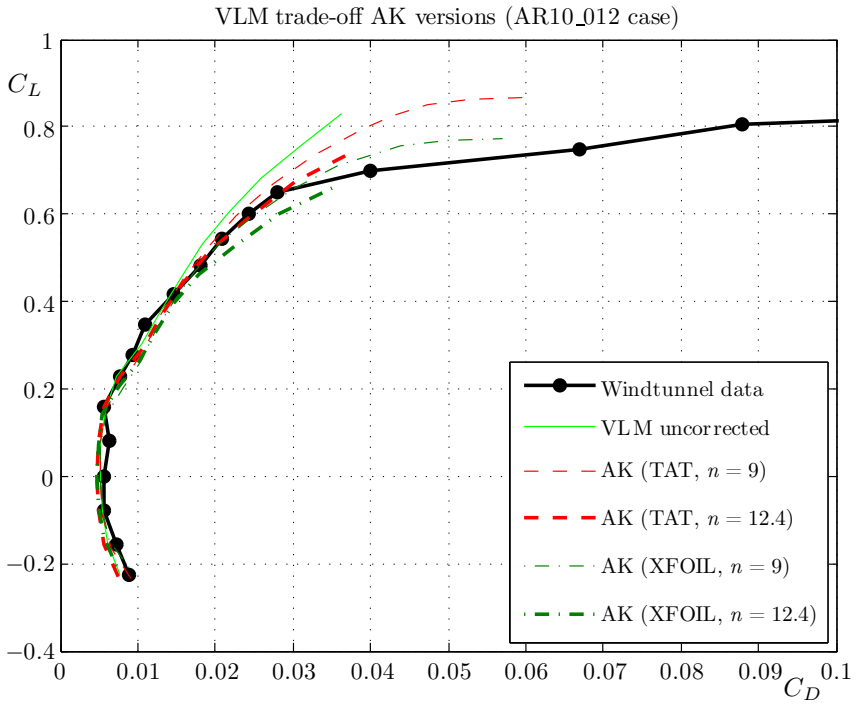

Figure B.34: The $C_L - C_D$ curves obtained from windtunnel experiments and XFLR5 simulations (VLM AK versions) for the AR10_012 wing where $Re = 2.0 \cdot 10^6$.

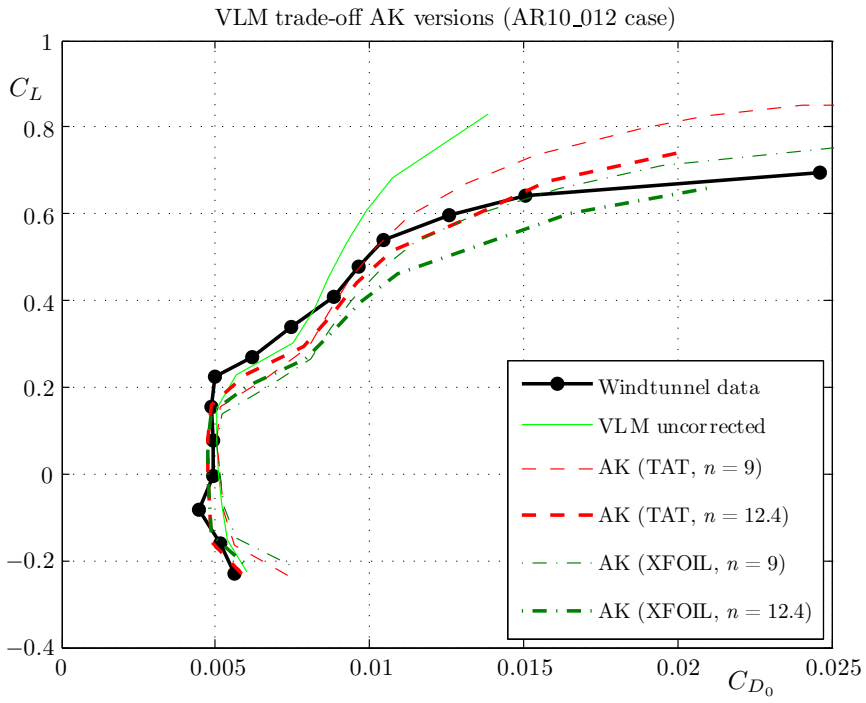

Figure B.35: The $C_L - C_{D_0}$ curves obtained from windtunnel experiments and XFLR5 simulations (VLM AK versions) for the AR10_012 wing where $Re = 2.0 \cdot 10^6$.

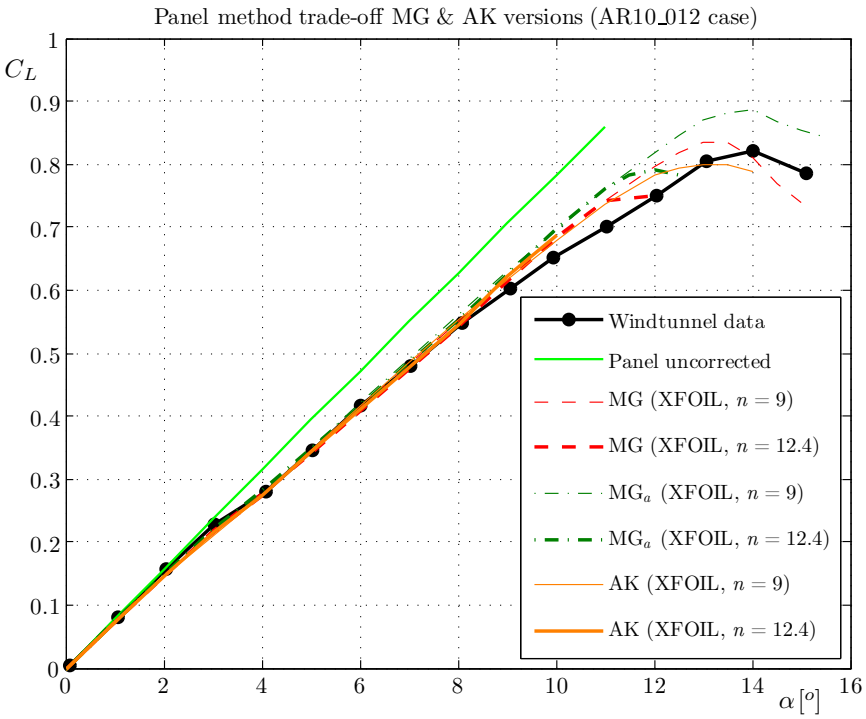

Figure B.36: The $C_L - \alpha$ curves obtained from windtunnel experiments and XFLR5 simulations (Panel method versions) for the AR10_012 wing where $Re = 2.0 \cdot 10^6$.

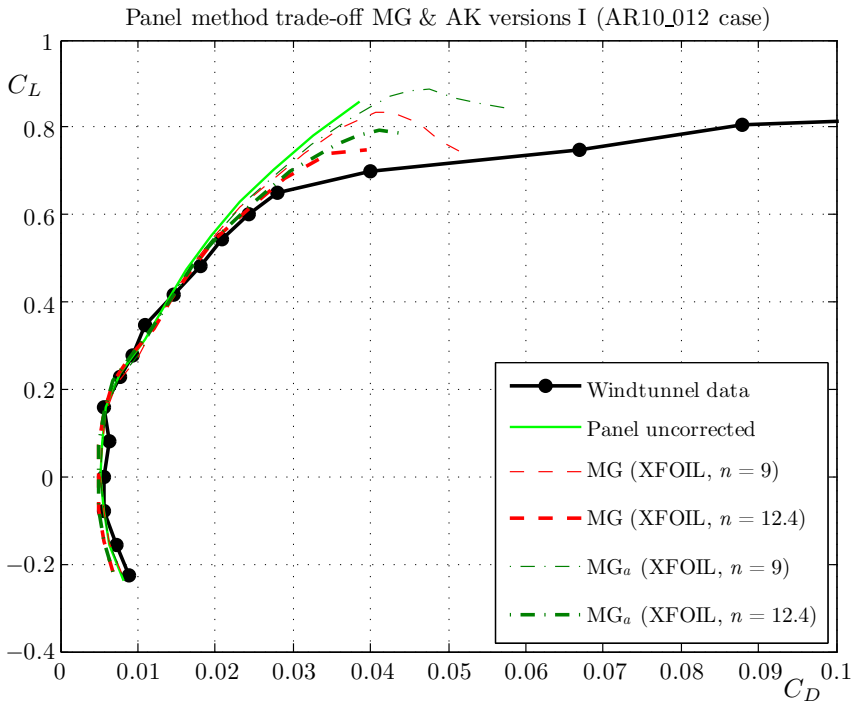

Figure B.37: The $C_L - C_D$ curves obtained from windtunnel experiments and XFLR5 simulations (Panel method versions) for the AR10_012 wing where $Re = 2.0 \cdot 10^6$.

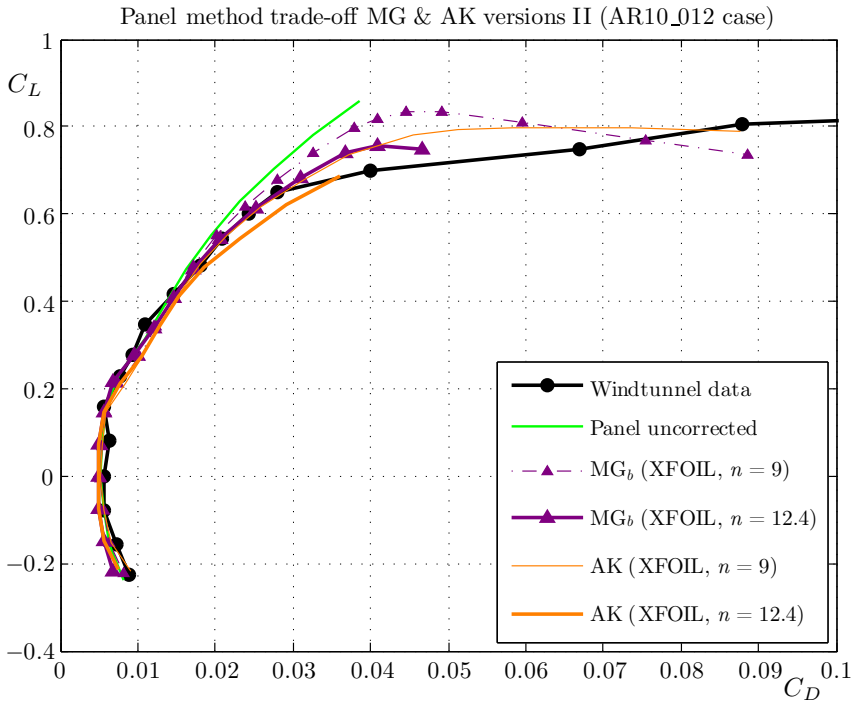

Figure B.38: The $C_L - C_D$ curves obtained from windtunnel experiments and XFLR5 simulations (Panel method versions) for the AR10_012 wing where $Re = 2.0 \cdot 10^6$.

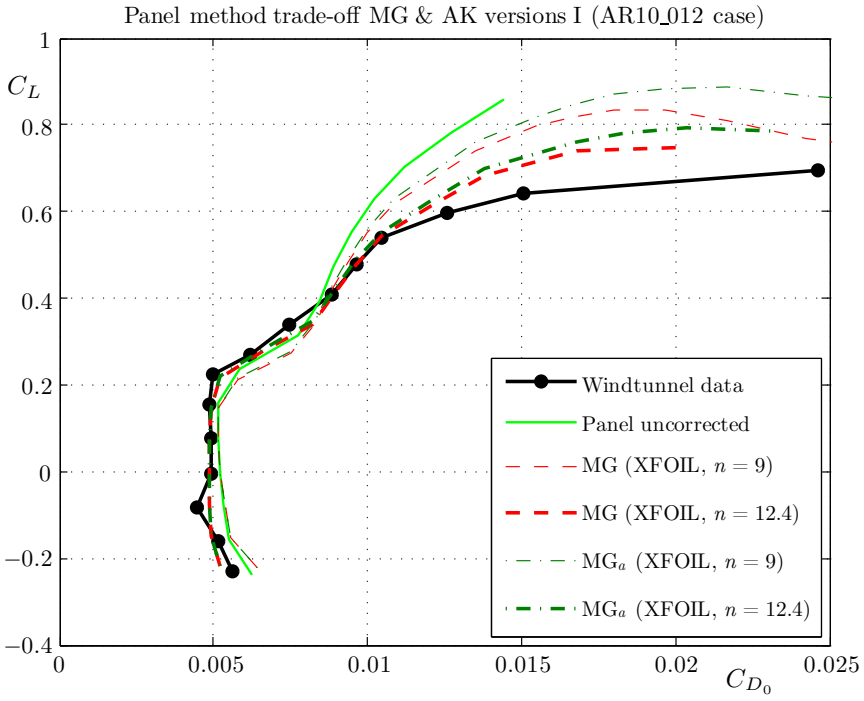

Figure B.39: The $C_L - C_{D_0}$ curves obtained from windtunnel experiments and XFLR5 simulations (Panel method versions) for the AR10_012 wing where $Re = 2.0 \cdot 10^6$.

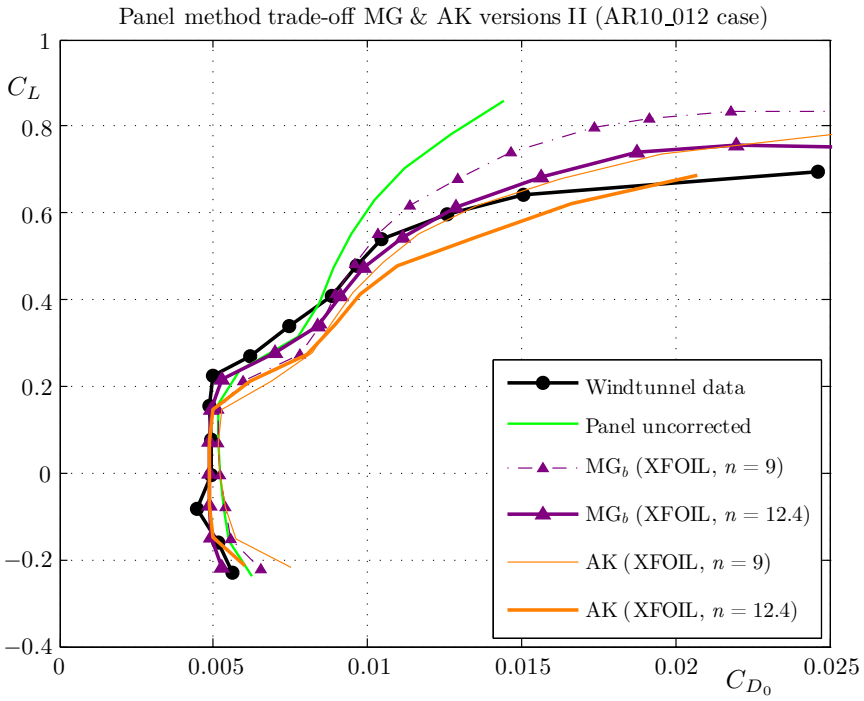

Figure B.40: The $C_L - C_{D_0}$ curves obtained from windtunnel experiments and XFLR5 simulations (Panel method versions) for the AR10_012 wing where $Re = 2.0 \cdot 10^6$.

B.5 Swept wing AR10_612

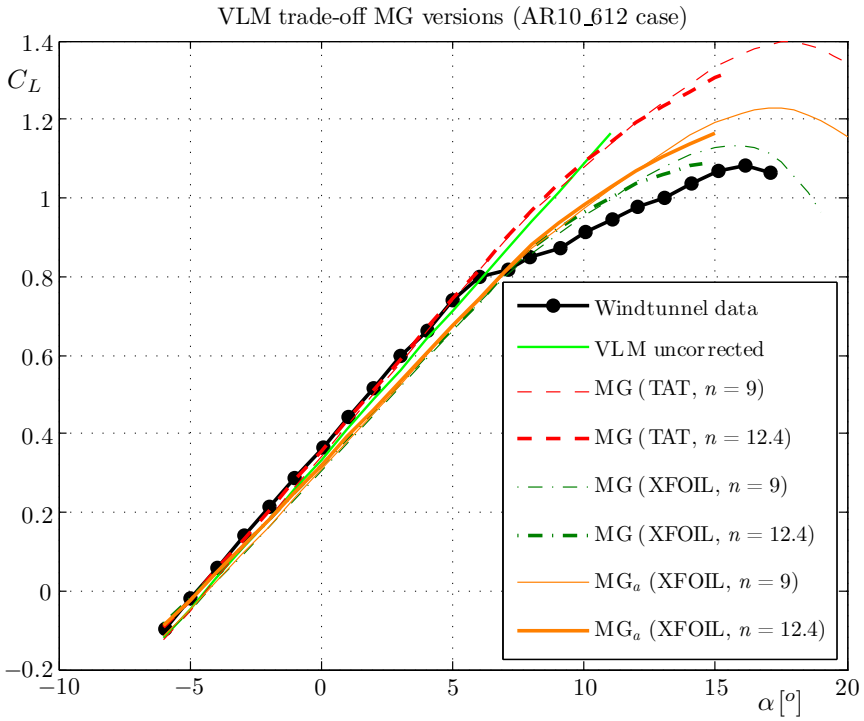

Figure B.41: The $C_L - \alpha$ curves obtained from windtunnel experiments and XFLR5 simulations (VLM MG versions) for the AR10_612 wing where $Re = 2.0 \cdot 10^6$.

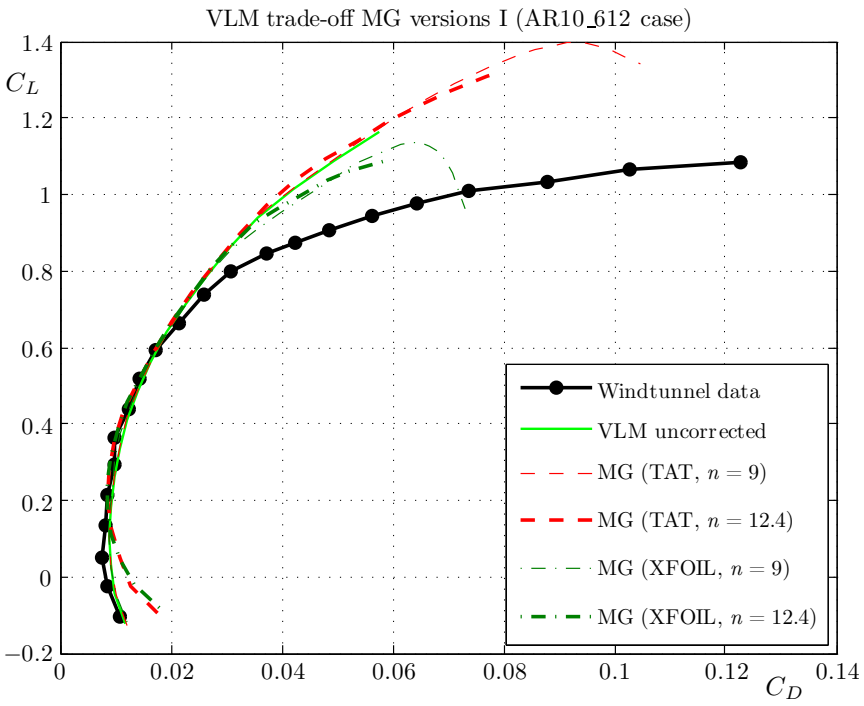

Figure B.42: The $C_L - C_D$ curves obtained from windtunnel experiments and XFLR5 simulations (VLM MG versions) for the AR10_612 wing where $Re = 2.0 \cdot 10^6$.

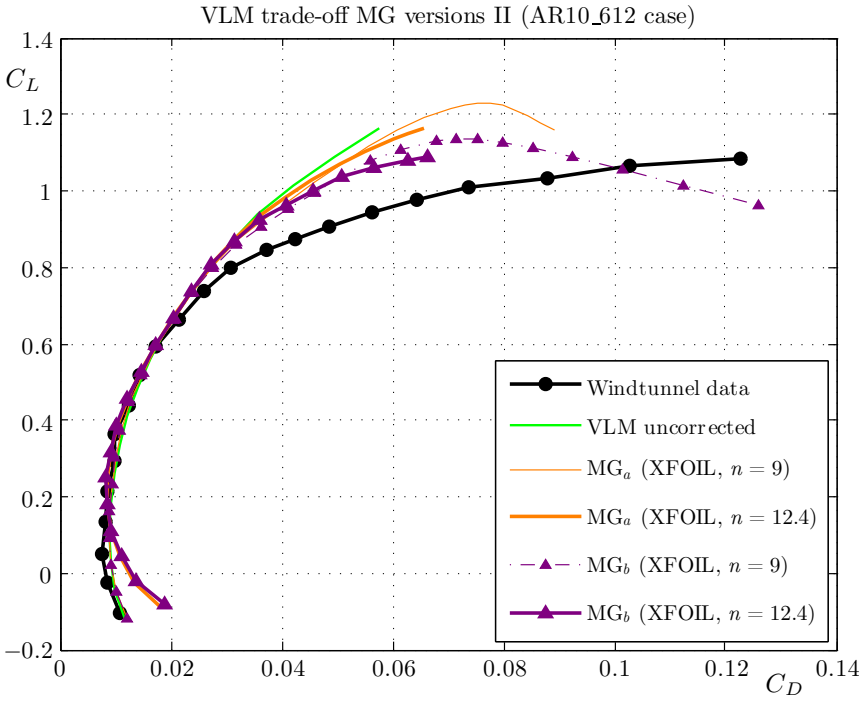

Figure B.43: The $C_L - C_D$ curves obtained from windtunnel experiments and XFLR5 simulations (VLM MG versions) for the AR10_612 wing where $Re = 2.0 \cdot 10^6$.

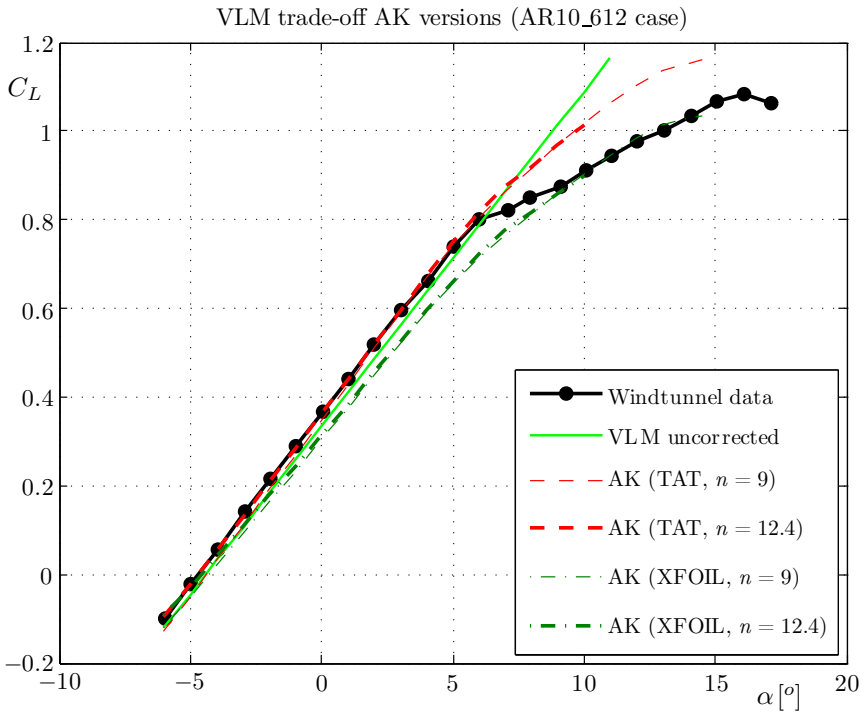

Figure B.44: The $C_L - \alpha$ curves obtained from windtunnel experiments and XFLR5 simulations (VLM AK versions) for the AR10_612 wing where $Re = 2.0 \cdot 10^6$.

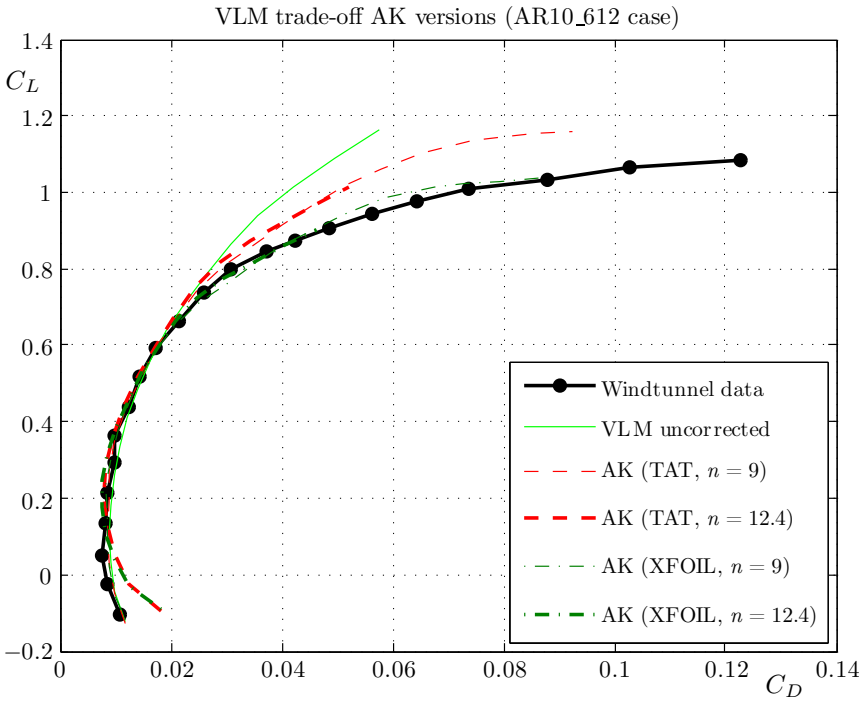

Figure B.45: The $C_L - C_D$ curves obtained from windtunnel experiments and XFLR5 simulations (VLM AK versions) for the AR10_612 wing where $Re = 2.0 \cdot 10^6$.

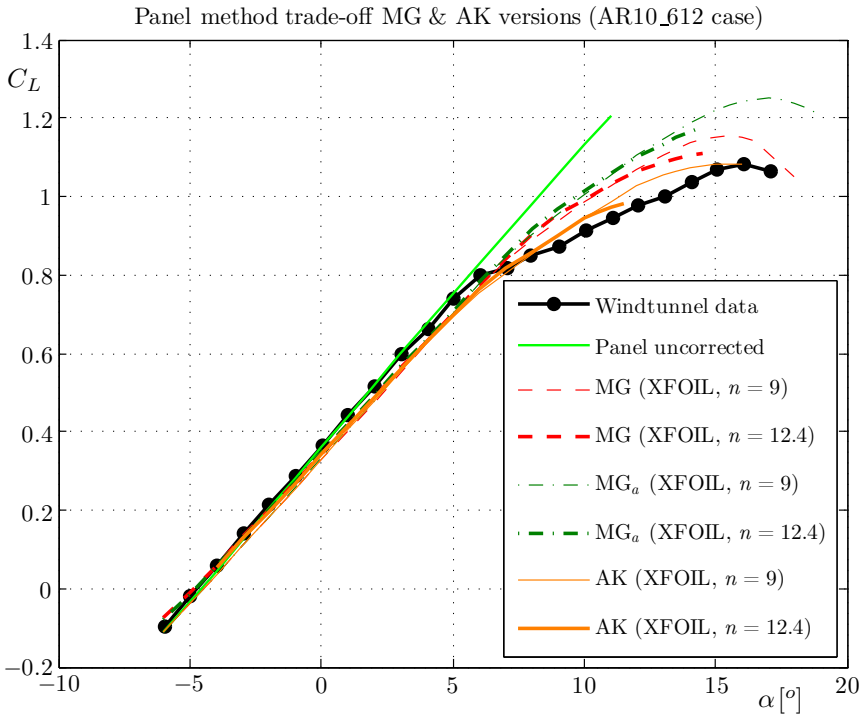

Figure B.46: The $C_L - \alpha$ curves obtained from windtunnel experiments and XFLR5 simulations (Panel method versions) for the AR10_612 wing where $Re = 2.0 \cdot 10^6$.

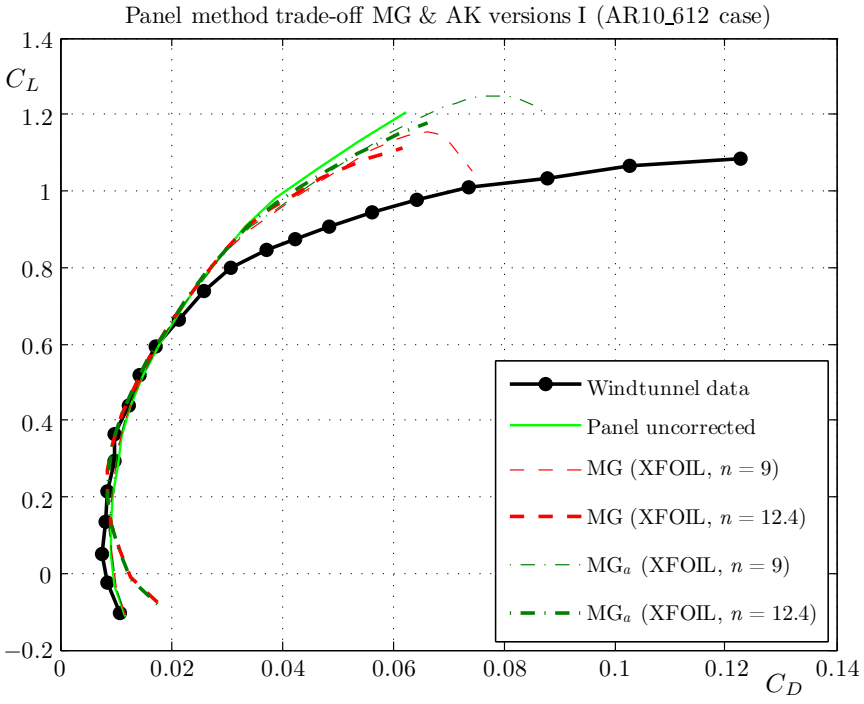

Figure B.47: The $C_L - C_D$ curves obtained from windtunnel experiments and XFLR5 simulations (Panel method versions) for the AR10_612 wing where $Re = 2.0 \cdot 10^6$.

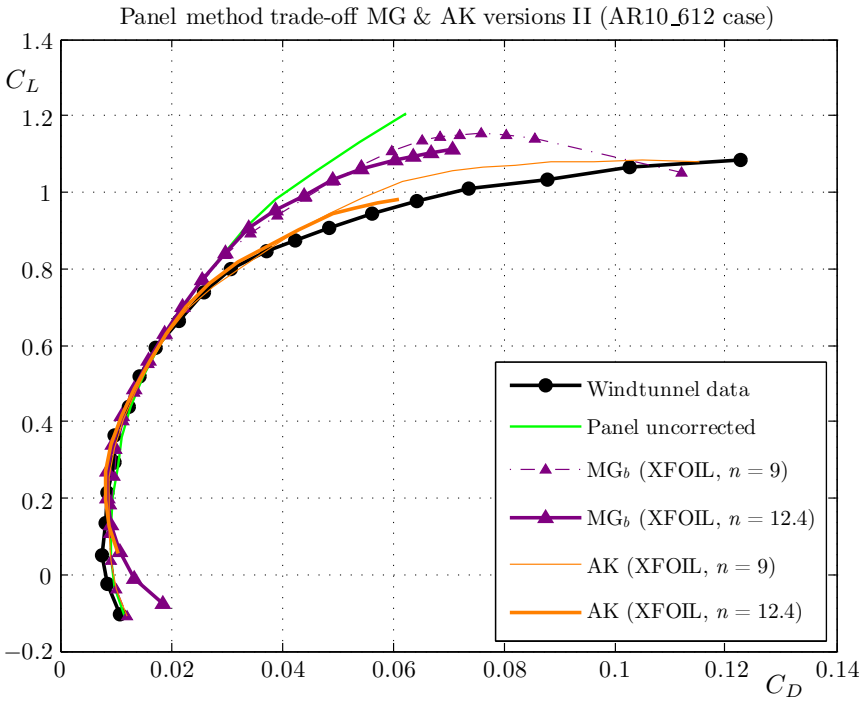

Figure B.48: The $C_L - C_D$ curves obtained from windtunnel experiments and XFLR5 simulations (Panel method versions) for the AR10_612 wing where $Re = 2.0 \cdot 10^6$.

Appendix C

Simulation results final versions

This appendix contains the remaining simulation results (see section 5.4) of the validation cases performed with the versions MG_b and AK of the adapted XFLR5 program.

C.1 Flat wing

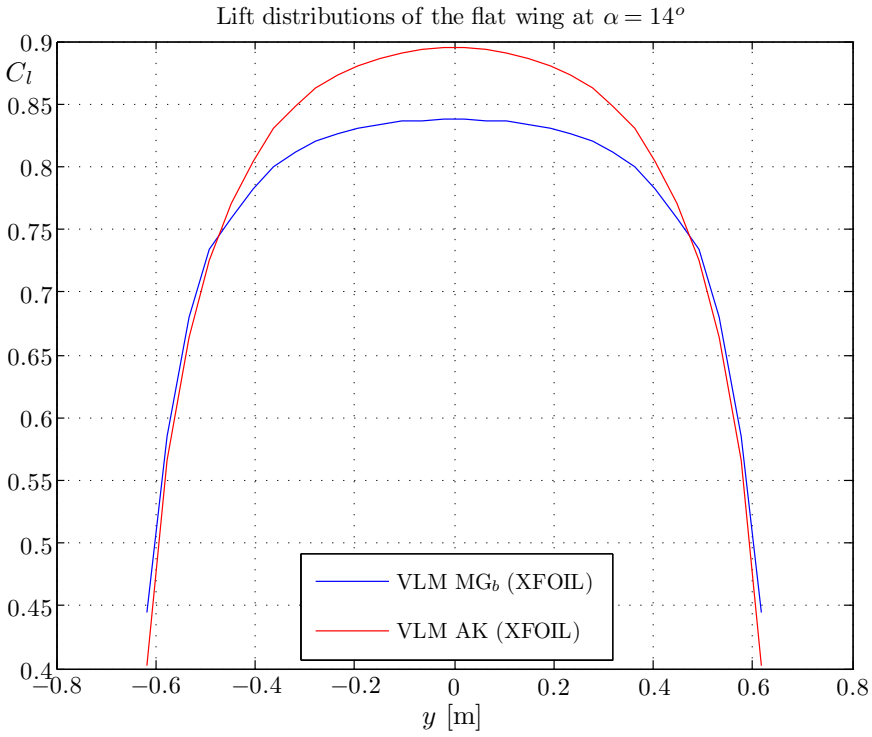

Figure C.1: The $C_l - y$ distribution obtained from XFLR5 simulations for the flat wing with $\alpha = 14^o$.

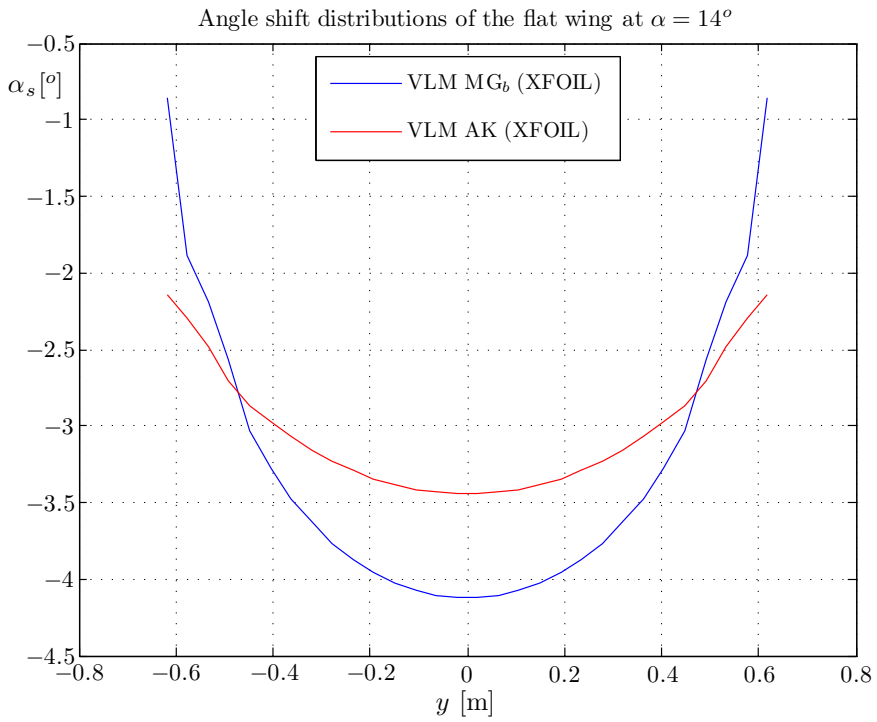

Figure C.2: The $\alpha_s - y$ distribution obtained from XFLR5 simulations for the flat wing with $\alpha = 14^o$.

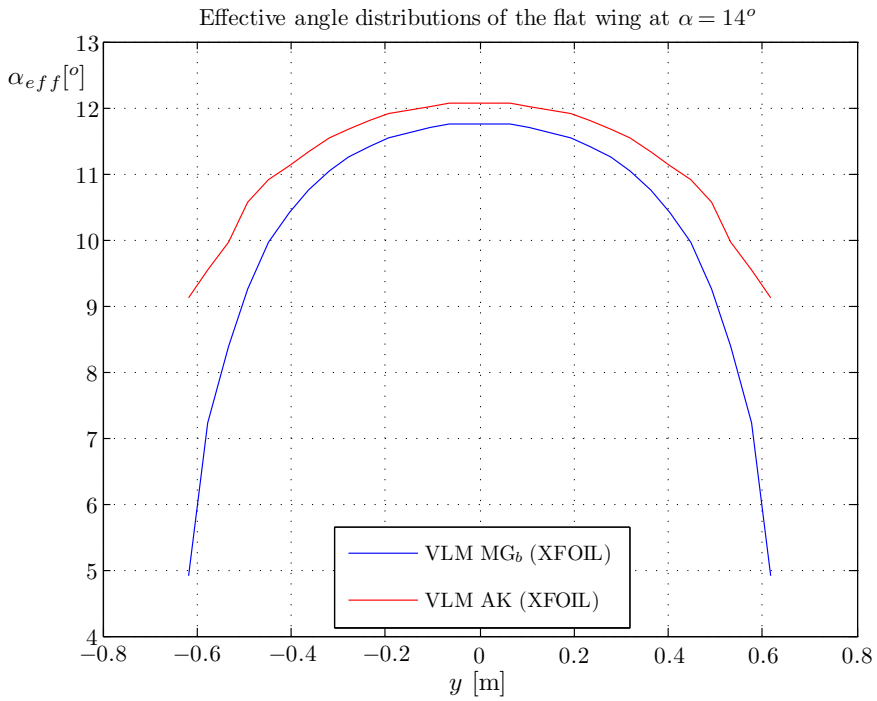

Figure C.3: The $\alpha_{eff} - y$ distribution obtained from XFLR5 simulations for the flat wing with $\alpha = 14^o$.

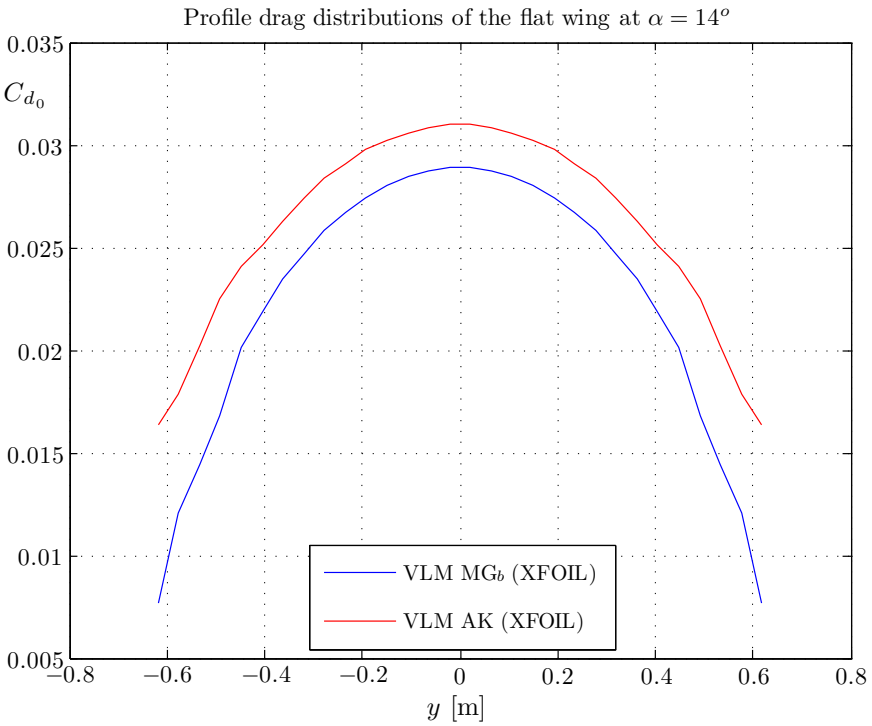

Figure C.4: The $C_{d_0} - y$ distribution obtained from XFLR5 simulations for the flat wing with $\alpha = 14^o$.

C.2 Swept wing AR5_012

See next page.

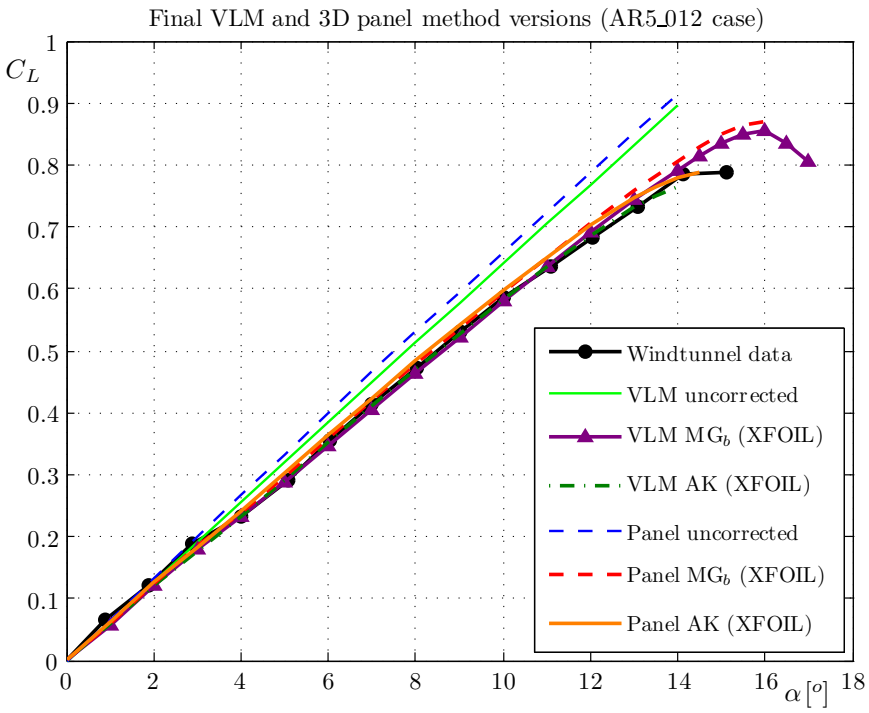

Figure C.5: The $C_L - \alpha$ curve obtained from windtunnel experiments and XFLR5 simulations of the AR5_012 wing where $Re = 2.0 \cdot 10^6$.

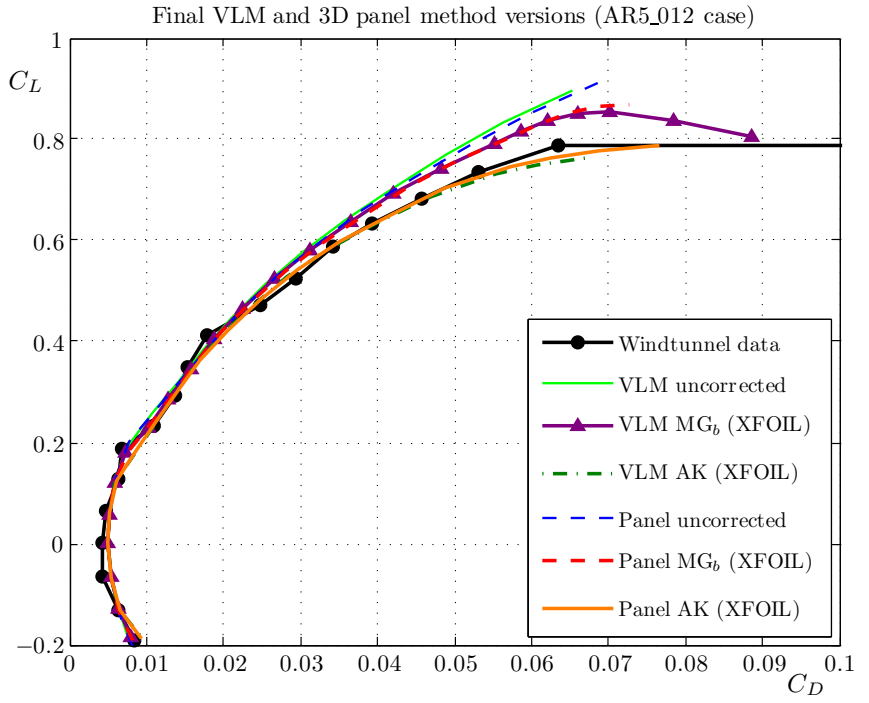

Figure C.6: The $C_L - C_D$ curve obtained from windtunnel experiments and XFLR5 simulations of the AR5_012 wing where $Re = 2.0 \cdot 10^6$.

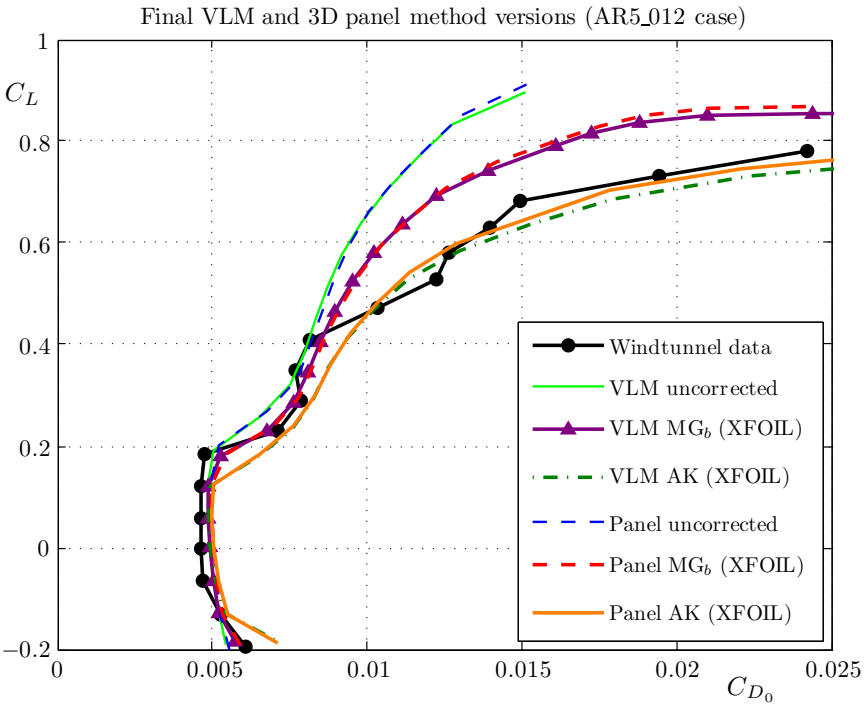

Figure C.7: The $C_L - C_{D_0}$ curve obtained from windtunnel experiments and XFLR5 simulations of the AR5_012 wing where $Re = 2.0 \cdot 10^6$.

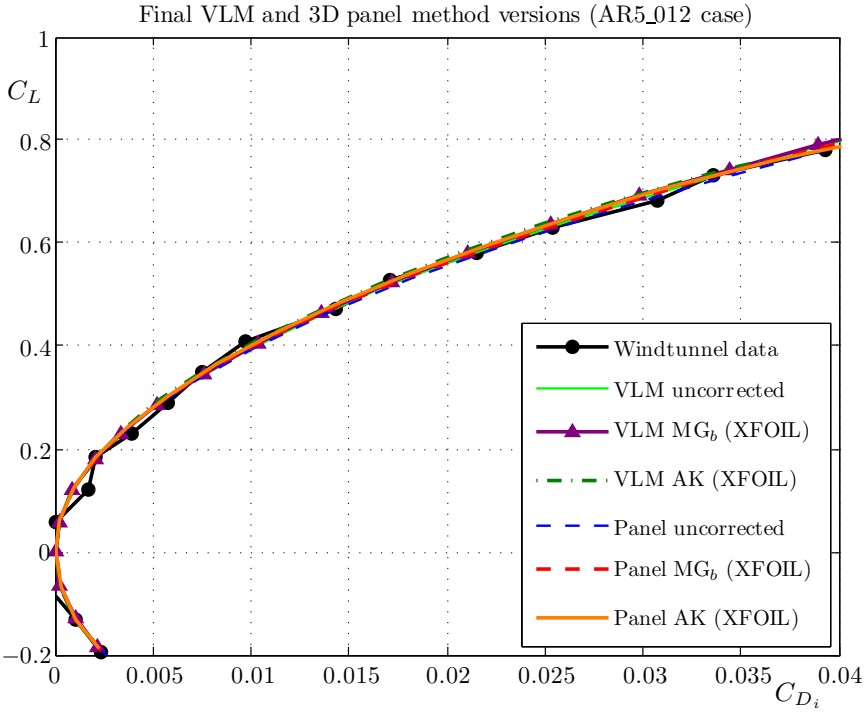

Figure C.8: The $C_L - C_{D_i}$ curve obtained from windtunnel experiments and XFLR5 simulations of the AR5_012 wing where $Re = 2.0 \cdot 10^6$.

C.3 Swept wing AR5_612

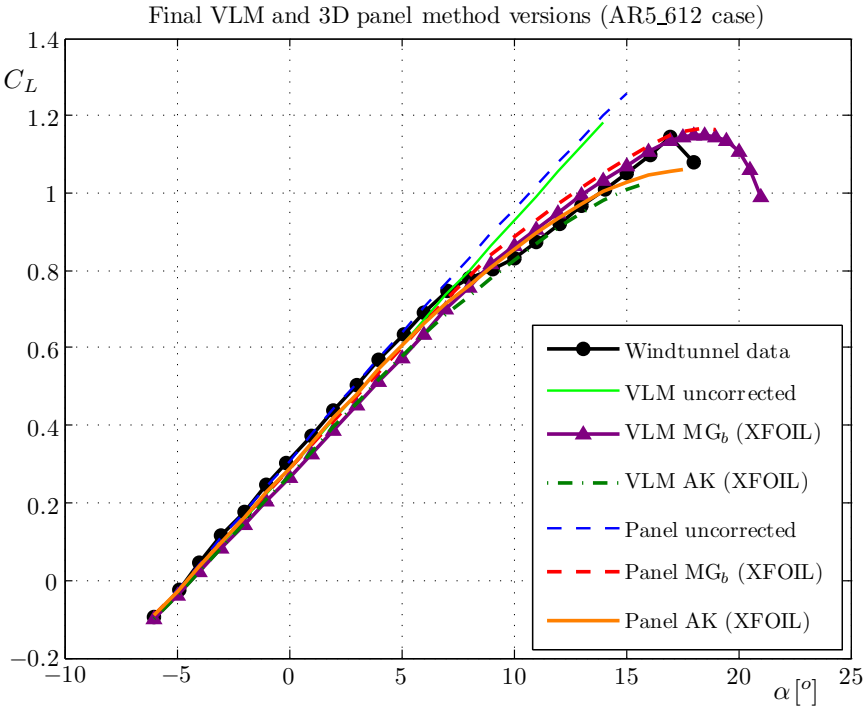

Figure C.9: The $C_L - \alpha$ curve obtained from windtunnel experiments and XFLR5 simulations of the AR5_612 wing where $Re = 2.0 \cdot 10^6$.

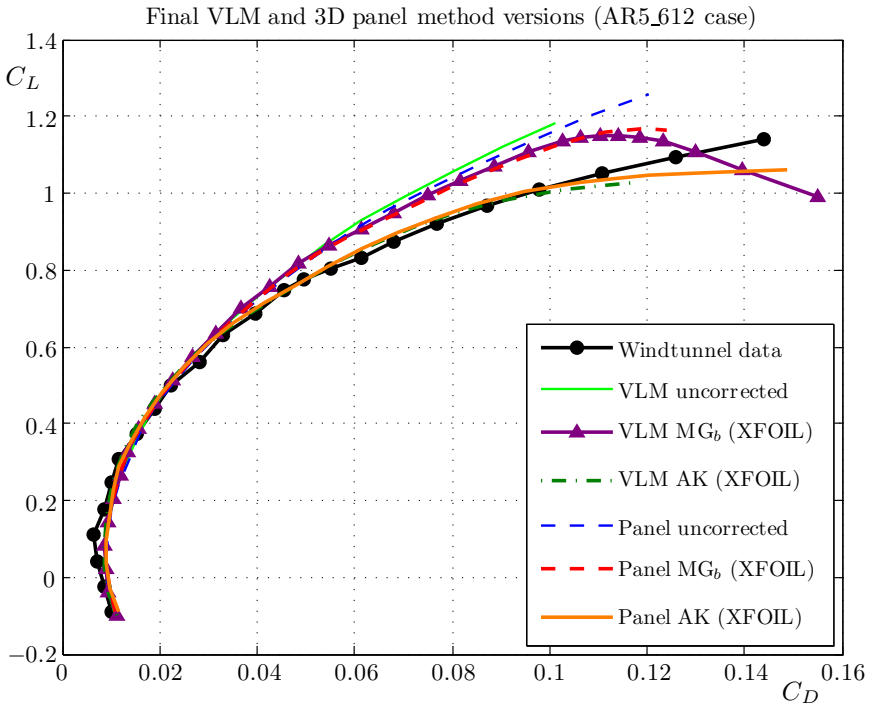

Figure C.10: The $C_L - C_D$ curve obtained from windtunnel experiments and XFLR5 simulations of the AR5_612 wing where $Re = 2.0 \cdot 10^6$.

C.4 Swept wing AR10_612

See next page.

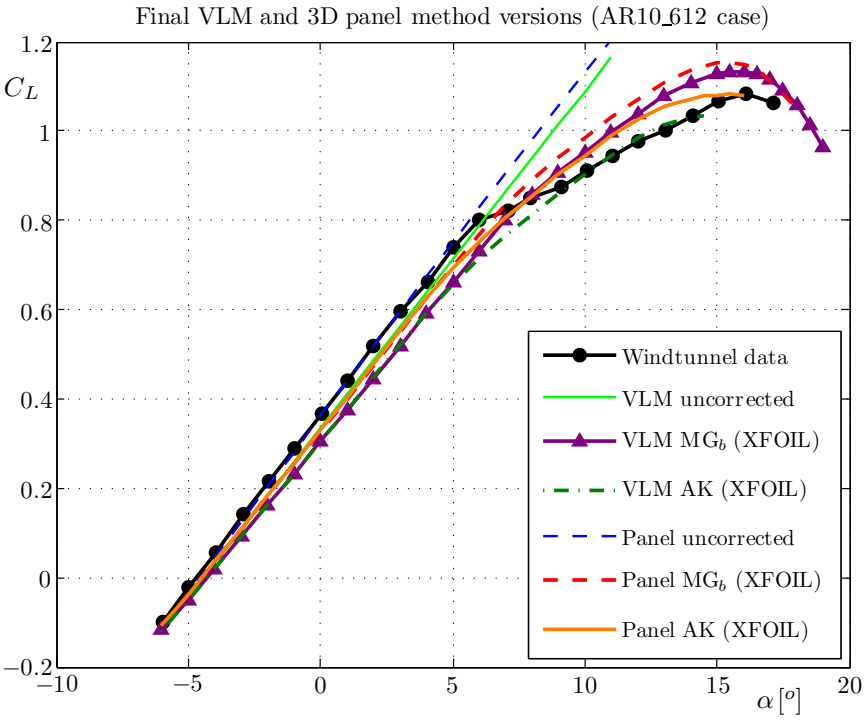

Figure C.11: The $C_L - \alpha$ curve obtained from windtunnel experiments and XFLR5 simulations of the AR10_612 wing where $Re = 2.0 \cdot 10^6$.

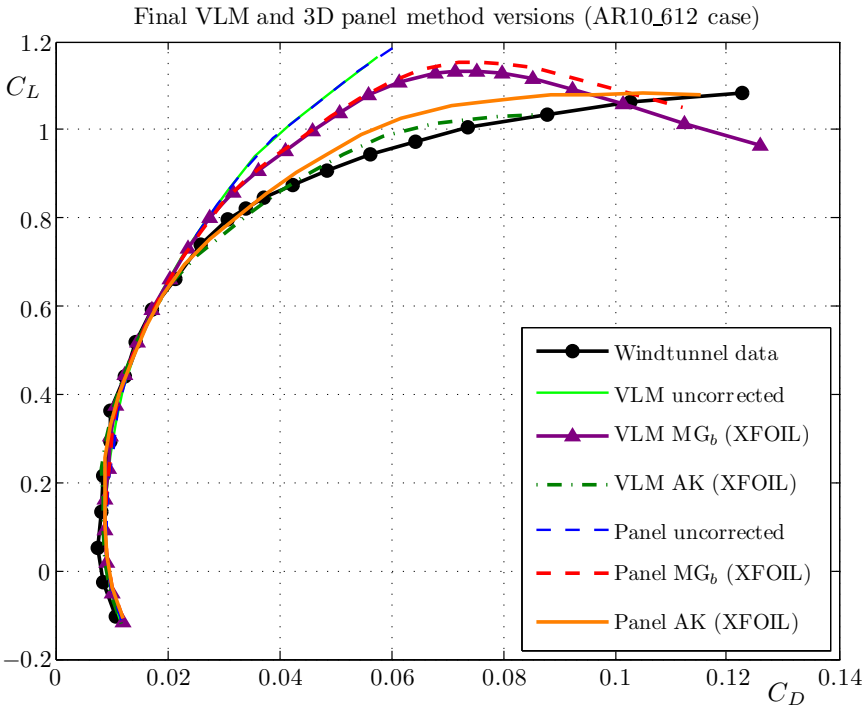

Figure C.12: The $C_L - C_D$ curve obtained from windtunnel experiments and XFLR5 simulations of the AR10_612 wing where $Re = 2.0 \cdot 10^6$.